Development and Implementation of State Variable Based User Materials in Computational Plasticity

Gerhardus J. Jansen van Rensburg

Development and Implementation of State Variable Based User Materials in Computational Plasticity

by

Gerhardus J. Jansen van Rensburg

This thesis is submitted in partial fulfillment of the requirements for the degree

Philosophiae Doctor (Mechanical Engineering)

in the

Faculty of Engineering, the Built Environment and Information Technology

University of Pretoria

Pretoria

South Africa

2016

Abstract

Title:	Development and Implementation of State Variable Based User Materials in Computational Plasticity
Author:	Gerhardus Jacobus Jansen van Rensburg
Supervisors:	Prof. S. Kok Dr. D.N. Wilke

The Finite Element Method is a powerful tool that can be used to test, improve or better understand an industrially relevant problem. There are numerous Finite Element Analysis (FEA) software packages that operate either in the commercial, open source or research space. Different application specific codes also have specialised model formulations. Most software packages have a comprehensive list of material models already implemented. If a different material model is required, some form of user material can often be implemented and linked to the software package.

In some cases the effective implementation and testing of a user implemented material requires knowledge on the effect and handling of strain formulations, element technologies and the desired material behaviour. With sophisticated material models available in the research space, this thesis focuses on the identification and implemen-

tation of existing computational plasticity models for use within FEA.

The effect of different strain formulation choices is first illustrated and discussed using different sample problems. Three different FEA software packages are also compared before discussion and implementation of a general numerical framework for corotated hypo-elastoplasticity in isotropic and combined hardening. The numerical framework allows expansion to include different, more sophisticated hardening behaviour by simply altering the scalar equation used to update the von Mises yield surface.

The Mechanical Threshold Stress (MTS) material model is implemented within the hypo-elastoplastic numerical framework. Material parameter identification is investigated using linear regression on data followed by numerical optimisation. The MTS model is a rate and temperature dependent state variable based material model. The model is tuned to fit imperfect cemented carbide data in compression, where material test frame compliance or some eccentricity caused inhomogeneous deformation through the test section of the specimen. The characterised model is then used on a sample problem to investigate the plastic deformation in the cemented carbide anvils during the High Pressure, High Temperature (HPHT) synthesis of diamond.

Further extensions, built on the dislocation density based modelling theory of the MTS model, are investigated by selecting an alternate form of the state dependent variable. A dislocation density ratio is used instead of the original stress like variable in the MTS model. The evolution of this internal state variable is altered, along with additional state dependent variables, to include additional deformation and thermal mechanisms. The model extensions in the case of rate and temperature dependent cyclic deformation as well as multiple waves of recrystallisation are discussed and implemented. The recrystallisation and through thickness microstructural variation of a High Strength, Low Alloy (HSLA) steel are finally investigated during the process of industrial hot rolling or roughing simulations.

To my wife Lize,

my parents,

family and friends,

for all their love and support.

Acknowledgements

I would like to thank the Advanced Mathematical Modelling competency area for giving me the opportunity and funding to do my Ph.D. I would like to thank my manager Dr. Onno Ubbink in particular as well as my research supervisors at the University of Pretoria, Prof. Schalk Kok and Dr. Nico Wilke for their insights and suggestions.

Contents

List of Figures

List of Tables

Chapter 1

Introduction

This thesis contains some of the work done while on a Ph.D. studentship contract at the Council for Scientific and Industrial Research (CSIR) in South Africa. The Advanced Mathematical Modelling (AMM) competency area within the CSIR Modelling and Digital Science operating unit focuses on various industrial applications using mathematical sciences and scientific computing.

It is common practise in industry to only use material models already built into Finite Element Analysis (FEA) software packages. This limits software functionality. It is possible however to investigate and model a wide range of material response through the implementation and proper material parameter identification of a user material subroutine. Proper implementation and use of these user subroutines require extensive knowledge of finite element technologies, strain formulations, materials as well as time for adequate testing and verification. Due to the lack of competence in this regard and time required to implement a user material from scratch, industry often chooses to stick to the trusted material models implemented within a software package of its choice.

Within AMM, the CSIR and even the larger South African context, a lack of material modelling competency and specific project requirements drove much of the work done in this thesis. For this reason, the work done in this document is presented in the hope that it would contribute to improved modelling capability in computational plasticity. All of the user materials implemented are also included in the thesis, so that it may be freely used, learnt from or improved upon in the spirit of an open source

philosophy.

There are sophisticated and well studied models in the research environment that do not form part of the standard material libraries in FEA software. From a Mechanical Engineering background, a lot of focus and attention is given in this thesis to the identification of the proper material models available or necessary for a specific problem. The state dependent plasticity models used in this thesis can be seen as built on the same dislocation density based modelling theory.

The focus in this thesis is not on the development of new and unique material models but the rigorous numerical implementation of existing models or a combination of existing ideas. This thesis therefore covers the theory where possible while the main focus is on proper implementation and testing of the model.

1.1 Structure

The structure of this document starts with a general user material framework to model von Mises elastoplasticity within a finite element environment. Different material models can be implemented into this framework. Various physical phenomena is modelled by selecting different forms of the kinetic and internal state variable evolution equations.

Two industry relevant problems are considered in this study following specific projects completed and modelling needs identified. The first problem considers the plastic deformation of a high strength cemented carbide. The material response is modelled using the temperature and strain rate dependent Mechanical Threshold Stress (MTS) material model. The second problem is the industrial simulation of a hot rolling process in which temperatures exceed the recrystallisation temperature. Here it is critical that one considers material softening that includes recrystallisation and thermal recovery. A brief general outline of the Chapters contained within this document is now presented.

1.1.1 Chapter 2: Verification of the User Material Framework

In Chapter 2, different strain formulations in computational plasticity are demonstrated. This is done using a modified Cook's membrane sample problem with linear hardening plasticity. The effect of the different strain formulations in plasticity is demonstrated for cases where a reasonable deformation is applied and small strain plasticity is no longer valid. The compression of an axi-symmetric billet with barrelling and rollover is also modelled to investigate the different strain formulations in a case where a significant amount of deformation is present.

Comparisons are made for the same axi-symmetric billet analysis modelled using three finite element solvers namely Abaqus 6.11 (2011b), CalculiX 2.8 (Dhondt and Wittig, 1998) and Code_Aster 11.3 (Électricité de France, 2012). Each of these finite element software packages use a slightly different strain formulation in large deformation plasticity. A satisfactory agreement between the corotational hypo-elastoplastic formulation of Abaqus and the fully hyper-elastoplastic formulation used in Code_Aster is observed. The results obtained using the hyper-elastoplastic formulation of CalculiX differs slightly from that of Code_Aster. This could be due to the fact that the yield function in CalculiX is evaluated using the second Piola-Kirchhoff stress measure while Code_Aster uses the Kirchhoff stress.

User defined material models are possible in all three software packages by linking a Fortran material model subroutine. In all three packages the user material layout native to Abaqus can be linked. Code_Aster makes use of the subroutine in either the reinitialised small strain plastic or logarithmic hypo-elastoplastic strain formulations. CalculiX on the other hand transforms its total strain vector into a logarithmic form of the strain increment. A six dimensional strain vector is passed into the user material subroutine containing principal strain ε_{kk} and engineering shear strain $\gamma_{ij,i\neq j} = \varepsilon_{ij} + \varepsilon_{ji}$ components.

The general elastoplastic user material framework is discussed for isotropic and combined hardening. Numerical implementation of the material framework in a corotational hypo-elastoplastic sense is discussed and the implementations validated against the native Abaqus large strain plasticity formulations. The corotational hypo-elastoplastic implementation can be used as foundation for other state variable based material formulations. The framework is therefore designed to be modular. In subsequent

chapters, a different model can be implemented by changing the content of the hardening subroutine. A reader familiar with general large strain elastoplastic formulations is encouraged to skip ahead to Chapter 3.

1.1.2 Chapter 3: Temperature and Rate Effects

The linear isotropic strain hardening model of Chapter 2 is replaced by the temperature and strain rate dependent Mechanical Threshold Stress (MTS) model in Chapter 3. The kinetic equation leading to the form of the MTS scaling functions as well as the development of the microstructure evolution equation in the form of the Voce-law are discussed. Apart from the Voce-law, the mechanical threshold stress internal state variable can also be evolved using different versions of the evolution equation. Numerical implementation of the MTS model is discussed and the analytical sensitivities required for proper convergence within the isotropic user material framework are derived. The MTS model is finally fit to experimental data using a scalar model or material point simulation. The experimental data, material point simulation and detailed finite element analyses using the MTS hardening function in the isotropic hardening user material framework are also compared.

1.1.3 Chapter 4: Characterising Imperfect Compression Data for Cemented Carbides

In Chapter 4, the MTS model is applied to cemented Tungsten Carbide data. Experimental data for cemented Tungsten Carbide is available for different material grades at different temperatures. In the room temperature data, the imperfect compression of the material specimen, possibly due to test frame compliance, is visible with a clear variation in strain gauge data around the circumference of the test section of the specimen. In this chapter, the use of a finite element analysis to simulate approximate experimental conditions and time varying boundary conditions are discussed to improve the accuracy with which the MTS material parameter values may be identified.

Simultaneous estimation of the material parameters as well as the time varying boundary conditions are investigated, using finite element analyses within the optimisation loop. This is illustrated on a virtual problem so that the known material

response can be compared to the response estimated by inverse analysis. From the investigation the procedure seems satisfactory in accurately determining the material property values, but at great computational cost. An alternative characterisation procedure is also investigated using an extended and calibrated point integration setup to promising effect.

The tungsten carbide data used in this chapter is proprietary information and subject to an ongoing memorandum of understanding. For this reason most of the figure axes in this chapter are scaled or normalised and the specific alloy compositions or carbide particulate sizes are not reported. The chapter serves only as an illustration of improved characterisation using imperfect hardmetal compression data. It is mainly demonstrated on virtual experimental data in this document with characterisation on the actual data reserved for a confidential document. A six axis multi-anvil press simulation is used to investigate the plastic deformation in the cemented Tungsten Carbide anvils during the High Pressure, High Temperature (HPHT) synthesis of diamond.

1.1.4 Chapter 5: Dislocation Density Based Modelling Extensions

An alternative choice on internal state variable, the dislocation density ratio, is chosen to replace the evolving internal stress like variable of the original mechanical threshold stress model in Chapter 5. The model implementation using the alternative formulation of the temperature and rate dependent model of Chapter 3 is now considered using the dislocation density ratio. Within the new modelling environment, various extensions are discussed and implemented to include further physical phenomena present during metal forming.

The inclusion of geometrically necessary dislocations and stage IV hardening is achieved by including an additional internal state variable to represent the average slip plane lattice incompatibility. Extending the microstructural evolution equation to include thermal or static recovery of statistical dislocations is also included. By viewing the microstructure as a system of channels or regions of low dislocation density, separated by parallel narrow walls with a high density of segmented edge dislocations, cyclic effects are also included.

To model cyclic effects, a back stress and additional internal state variable is considered. The additional internal state variable represents the density of dislocations trapped in the walls but partially recoverable upon stress reversal. Both back stress and partially recoverable dislocation density ratio internal state variables have their own evolution equations and are effected by load reversal. The dislocation density ratio based model with cyclic behaviour is implemented numerically into the combined hardening model framework validated in Chapter 2. The characterisation of the dislocation density based combined hardening model is finally illustrated on digitised experimental data for two different metal alloys.

An extension on the isotropic dislocation density ratio model is also covered to include recrystallisation. Some of the foundation theory on recrystallisation modelling is first discussed as well as the assumptions made in the current modelling approach. The model describes multiple waves of recrystallisation and each recrystallised or unrecrystallised volume fraction has its own set of internal state variables. The numerical implementation as well as choices made to keep track of, initialise or shift internal state variables as needed at the onset or completion of a specific wave of recrystallisation are discussed. The recrystallisation model is finally calibrated to dynamic recrystallisation data on Cobalt and Copper.

1.1.5 Chapter 6: Roughing of a Steel Alloy

Austenite grain growth is an important factor that determines the final microstructure and mechanical properties of the product. The dislocation density based model with recrystallisation is used in Chapter 6 to investigate the through-thickness microstructural variation due to different roll reduction schedules. The behaviour of a microalloyed C-Mn-Nb-Ti-V steel is modelled during hot rolling or roughing. Stress-strain data obtained from different cylindrical test specimens, subjected to different deformation schedules are used in the material parameter identification.

The through thickness microstructural variation is estimated by linking a normal grain growth model to the mechanical response. The grain size of the original material volume fraction as well as each subsequent wave of recrystallised material is determined and combined as a volume fraction averaged grain size estimate per integration point.

1.1.6 Chapter 7: Conclusions

Some suggestions for future work are included in Chapter 7. The contributions of this work are also summarised.

1.1.7 Appendices

All of the developed user material subroutines are included in the Appendices. Appendix D serves as an extension to the material characterisation performed in Chapter 4 while Appendices G to I are used for figures related to Chapter 6.

Chapter 2

Verification of the User Material Framework

The main aim of this chapter is to implement and verify a generic elastoplastic material framework. Different material responses can be modelled within this framework by implementing other hardening subroutines based on specific choices of kinetic equations or equations for the evolution of internal state variables. Readers familiar with the numerical implementation of plasticity should be familiar with the work covered in this chapter and could skip ahead. However, for the sake of sound and thorough documentation of the work, this chapter is included to serve as a source of the relevant theory and implementation.

In this chapter, various strain formulations in computational plasticity are compared for different boundary value problems. In an attempt to make the work more general, different finite element packages are also compared. Investigating different strain formulations and simulation environments gives a more holistic view on elastoplastic modelling. This provides a basis from which to make decisions. Software accessibility, ease of implementation or validity of different formulations under an expected degree of deformation could be a deciding factor for which route to follow in modelling a boundary value problem of interest.

The first strain formulation comparisons are done by modelling linear work hardening on a version of Cook's membrane problem for small strain plasticity, hyperelastoplasticity and logarithmic hypo-elastoplasticity in Code_Aster 11.3 (Électricité

de France, 2012). The Cook's membrane problem is a popular benchmark problem where small strain plasticity is no longer valid due to the magnitude of deformation. A second strain formulation comparison is done by modelling the compression of a cylindrical test specimen up to about 120% true axial strain. The second sample problem is more complex with rollover present at the contact surface as would be expected if material testing is performed in this manner. This axi-symmetric test problem therefore requires a strain formulation that effectively describes geometric effects.

In Section 2.2, a comparison is made between the built in elastoplastic formulations in Abaqus 6.11 (2011b) and CalculiX 2.8 (Dhondt and Wittig, 1998) against the hyperelastoplastic formulation in Code_Aster 11.3. The same test problem setup for an axi-symmetric billet with rollover is modelled in the three different software packages. The von Mises stress as well as the displacement field values are extracted at the same 1281 nodal locations for comparison. The comparison between the Code_Aster results to that of Abaqus shows on average a 0.6781% difference despite using different strain formulations. The largest average difference is observed between the Code_Aster and CalculiX results at 1.166%.

In Section 2.3, the elastoplastic material framework that is implemented into an Abaqus user material Fortran subroutine is discussed. This section includes the development of the material consistent tangent and numerical implementation for the purely isotropic hardening case as well as combined hardening. The results obtained using the user material subroutine is verified against the built in elastoplastic model by modelling a slender beam subject to varying boundary conditions in Abaqus.

2.1 Comparison example using different strain formulations

2.1.1 Cook's membrane

Cook's membrane is a common test problem used to assess finite elements in combined bend and shear with moderate distortion, usually using linear elastic materials. Although it was first used by Cook (1974) to test an improved two dimensional finite element formulation, it has also been proposed as a benchmark in finite strain plastic-

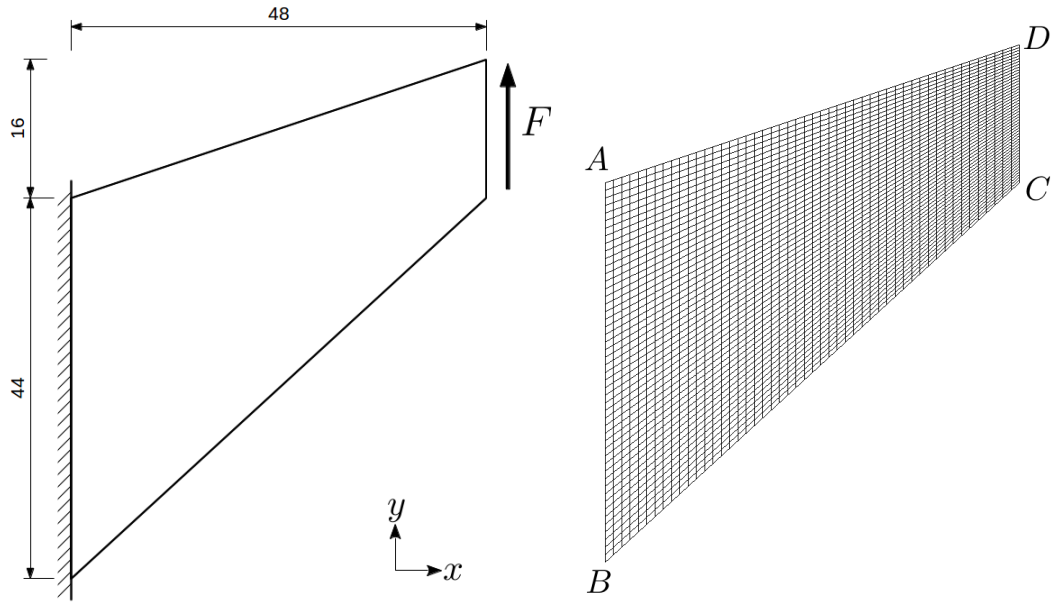

Figure 2.1: The Cook's membrane problem modelled to compare the different finite strain plasticity formulations. (a) The geometry and setup as well as (b) the discretisation using 50×50 elements. In (b) the four corner nodes are labelled to ease subsequent discussion.

ity by Simo and Armero (1992) and used by Glaser and Armero (1997). Authors such as Elguedj et al. (2008), Auricchio et al. (2005) as well as Mathisen et al. (2011) to name a few, have also used Cook's membrane as a benchmark in nonlinear elasticity and plasticity using isogeometric formulations.

In this comparison the membrane geometry in Figure 2.1(a) is discretised into a 50×50 mesh of linear, four noded elements as seen in Figure 2.1(b). The test problem is modelled in Code_Aster, using plane strain elements with full integration. Each element therefore has 4 Gauss integration points (2×2 Gauss quadrature) and is modelled using a thickness of 1mm. The artificial material modelled has an elastic stiffness $E = 1\text{GPa}$ and a Poisson's ratio of $\nu = 0.25$.

The plastic behaviour is modelled with using a linear strain hardening model. The isotropic von Mises yield surface is evolved using a univariate description of the total

equivalent plastic strain α. In this model the isotropic yield stress is given by

$$\sigma_{\mathrm{Y}} = \sigma_0 + K\alpha, \tag{2.1}$$

where σ_0 is the initial yield stress and K the strain hardening modulus. In the Cook's membrane problem, an initial yield stress of $\sigma_0 = 10$MPa and linear strain hardening modulus of $K = 100$MPa is used.

The left most nodes in Figure 2.1(b) are fixed. On the right most node set, a vertical force is applied per node. In this comparison, a force of $F_y = 3$N is applied to each of the 51 nodes, in 50 loading increments.

The analysis is performed using four different strain formulations. In the first case, the small strain plasticity formulation is used. In this formulation there is no distinction between the current or reference configuration. A second case is modelled, again using the small strain formulation, but using a reactualised geometry for each load increment. This means that the mesh is updated at the start of each increment using the converged displacement solution of the previous increment. A third simulation uses the hyper-elastoplastic formulation of Simo and Miehe (1992). This formulation takes a multiplicative approach to elastoplastic coupling based on observations from crystal plasticity. The hyper-elastoplastic formulation is assumed to be the most accurate and is therefore treated as the benchmark solution used for comparison. A fourth formulation modelled is the logarithmic hypo-elastoplastic formulation of Miehe et al. (2002), where the logarithmic form of the right Cauchy-Green strain tensor is additively decomposed into elastic and plastic components.

The equivalent plastic strain contours between 0 and 0.1 can be seen on the deformed membrane geometry in Figure 2.2 for the four different cases modelled. To facilitate a comparison to the results using the hyper-elastoplastic formulation as benchmark, the same contours in Figure 2.2 are superimposed as lines onto the colour contours of the benchmark result in Figure 2.3. In Figure 2.3 the contour lines for equivalent plastic strain in increments of 0.01 up to 0.09 are displayed, with overlayed filled contours of the hyper-elastoplastic result, all displayed on the undeformed configuration.

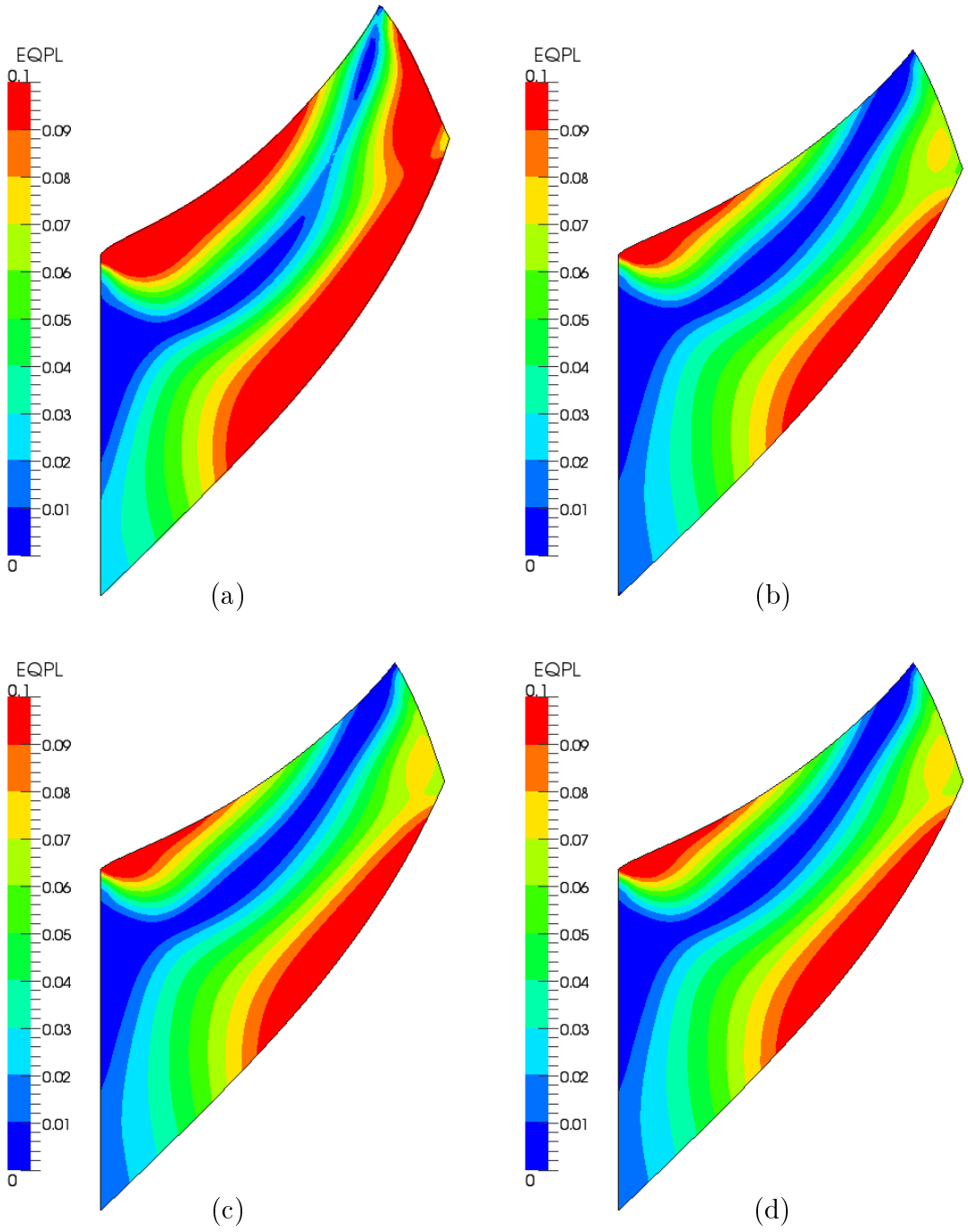

Figure 2.2: The equivalent plastic strain contours for the Cook's membrane test problem using the (a) small strain plasticity formulation with (b) reactualisation of the geometry. The results for the (c) hyper-elastoplastic and (d) logarithmic elastoplastic formulations are seen to compare very well.

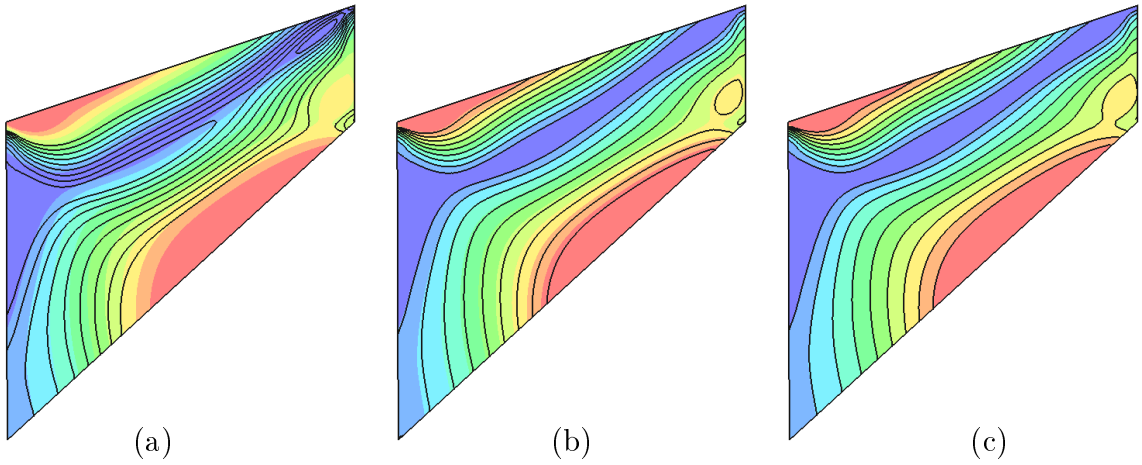

(a) (b) (c)

Figure 2.3: The undeformed geometry with hyper-elastoplastic filled contours for the equivalent plastic strains as in Figure 2.2. Contour lines correspond to (a) the small strain plasticity formulation with (b) reactualisation of the geometry as well as (c) logarithmic elastoplastic formulation.

	Equivalent Plastic Strain			x Displacement		y Displacement		Average
	A	B	C	C	D	C	D	Difference
Small Strain	0.2359	0.0251	0.0720	-2.9571	-11.936	14.945	16.053	39.187%
Updated Mesh	0.1998	0.0092	0.0614	-3.6496	-10.060	11.029	10.371	6.1913%
Logarithmic	0.1814	0.0112	0.0658	-3.5735	-10.031	11.330	10.585	0.7014%
Hyper-elastoplastic	0.1833	0.0116	0.0659	-3.5819	-10.034	11.329	10.585	-

Table 2.1: Equivalent plastic strain and deflection values extracted at selected nodal locations labelled in Figure 2.1(b).

For further comparison, the total equivalent plastic strain values at nodes A, B and C as well as the displacements at nodes C and D labelled in Figure 2.1(b) are also given in Table 2.1.

The small strain formulation is not consistent and even at these moderate strains a fair amount of tip enlargement and overestimated displacement is visible in Figure 2.2(a) compared to the other solutions. The plastic response also seems to be overestimated when comparing the results obtained using the other formulations. If the plastic strains and displacement values given in Table 2.1 are compared to those of the hyper-elastoplastic results, an average difference of 39.19% is observed.

While still using the small strain plastic formulation, reactualising the geometry at each of the 50 load increments created a result closer to the actual solution. This is evident when comparing Figure 2.2(b) to Figure 2.2(c) or by inspecting Figure 2.3(b). In Table 2.1, the 39.19% error using the small strain formulation is reduced to 6.19% by updating the nodal coordinates at the end of each time step in this case. A drawback of this method however is that it is not fully objective. Each incremental solution is determined from the previous updated mesh, meaning the solution may be strongly affected by the size of the increments. The stresses, strains, and other internal state variables are also not properly rotated throughout the solution. It is therefore possible that the incremental mistakes could accumulate to make up a large part of the solution in the presence of larger deformations compared to the other formulations.

For this test case with moderate geometric effects, the hyper-elastoplastic and logarithmic formulations compare very well. The contours in Figure 2.3(c) and extracted values in Table 2.1 are closely matched compared to the results obtained using other strain formulations. An average difference of 0.7% is observed when comparing the plastic strains and displacement values given in Table 2.1 to those of to the hyper-elastoplastic results.

2.1.2 Compression of a cylindrical specimen

In this test case, a cylinder with a height to diameter ratio of 2:1 is modelled subject to a large amount of axial strain. Figure 2.4(a) illustrates a cylinder with a height of 10mm and diameter of 5mm between two anvils. One anvil is assumed fixed while the other is subject to a force or pressure displacing it a specified amount at some specified velocity.

Code_Aster is again used to compare the small strain plasticity, hyper-elastoplasticity and logarithmic hypo-elastoplastic formulations. A boundary value problem is set up to model a 5mm $\times$ 2.5mm quarter axi-symmetric section of the test specimen using a 20×20 mesh of quadratic elements. The artificial material modelled has an elastic stiffness $E = 1$GPa, Poisson's ratio of $\nu = 0.25$, initial yield stress of $\sigma_0 = 50$MPa and linear strain hardening modulus of $K = 100$MPa assigned to all of the elements.

The nodal degrees of freedom associated with the axis of symmetry is constrained

in the radial or x direction while the nodes corresponding to the middle of the test specimen are constrained in the axial direction. A 7mm long line is used to model the contact surface of the upper anvil, assumed to be rigid. The line has a starting point at $\{x, y\} = \{0, 5\}$ and end point at $\{7, 5\}$, and is therefore in contact with the line segments associated with the upper face of the test specimen at the start of the simulation. Possible contact is defined between the rigid line and outer surface of the test specimen so that barrelling and rollover may be handled during the compression. An illustration of the axi-symmetric boundary value problem setup is presented in Figure 2.4(b). While the rigid line starts off already in contact with the billet in the simulation, the line is displayed above the billet in Figure 2.4(b) to show them individually. The red lines illustrate the two surfaces where contact is checked and allowed. For convenience of subsequent discussion and comparison, the four corner nodes are again labelled.

The discrete Lagrangian contact formulation in Code_Aster is used with hard or impenetrable contact normal to the surface while friction is handled using a Coulomb friction coefficient of $\mu_C = 0.2$ assuming there is suitable lubricant between the anvil and material sample. Over the course of the simulation, the rigid line is displaced 3.5mm downward resulting in a total true axial strain of $100 \times \ln(1 - 3.5/5) \approx 120\%$. The displacement is applied as a linear ramp over the course of the simulation using automatic time stepping between 0 and 1 with a maximum allowable step size of 0.1 and a minimum of 1×10^{-8}.

Figure 2.5 shows the solution to the boundary value problem at time $t = 1$ using the different formulations. The black wireframe is as a result of the hyper-elastoplastic formulation while the red and blue wireframes are as a result of the logarithmic and small strain elastoplastic formulations respectively.

As expected, the small strain formulation generates an unrealistic solution considering the difference in the final volumes of the three formulations in Figure 2.5. The equivalent plastic strain contours are presented in Figure 2.6 while the von Mises equivalent stress values are given in Figure 2.7. The von Mises stresses are scaled between the initial yield value of 50MPa and 200MPa. For all three cases, the maximum stress value is reported at the corner node of the element associated with the initial roll over due to excessive distortion. For the small strain formulation an interpolated value

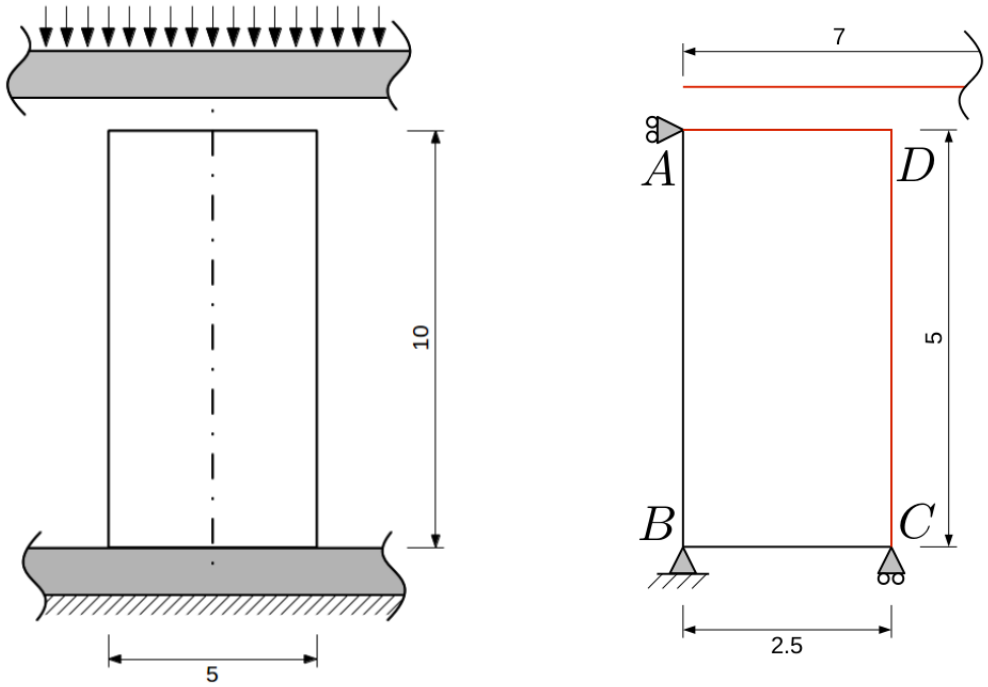

(a) (b)

Figure 2.4: (a) Axial compression of a cylindrical test specimen with (b) the axi-symmetric boundary value problem setup. In (b) the four corner nodes are labelled to ease subsequent discussion.

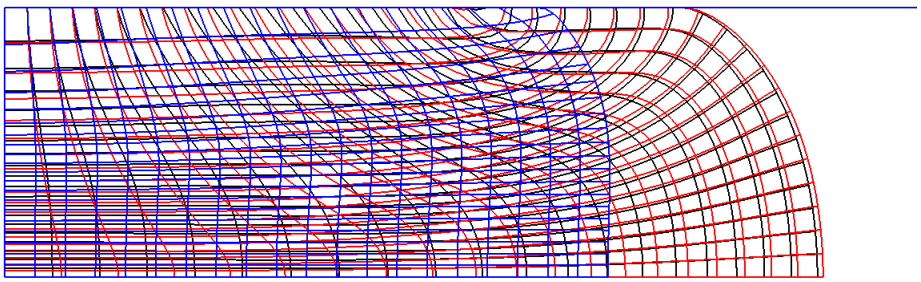

Figure 2.5: Resulting deformations of the three different strain formulations on the cylindrical test specimen boundary value problem with isotropic plasticity. The blue mesh indicates the small strain solution while red is the logarithmic hypo-elastoplastic solution and black the hyper-elastoplastic solution.

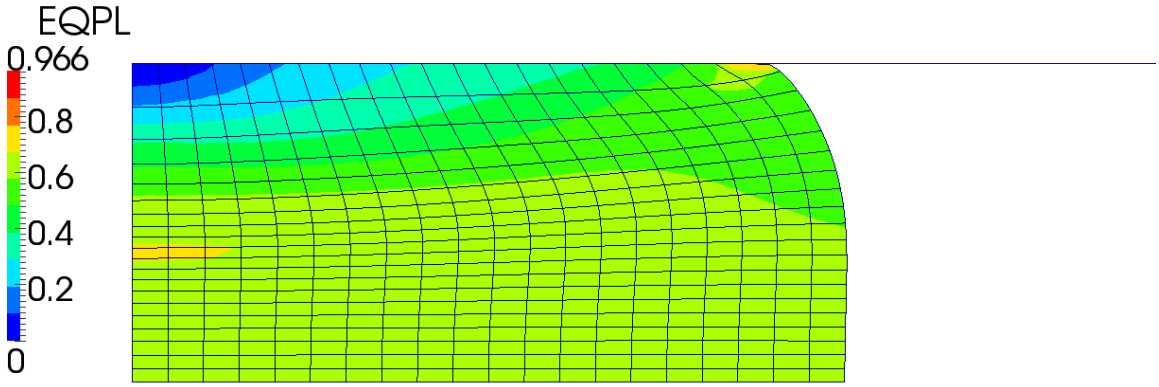

(a)

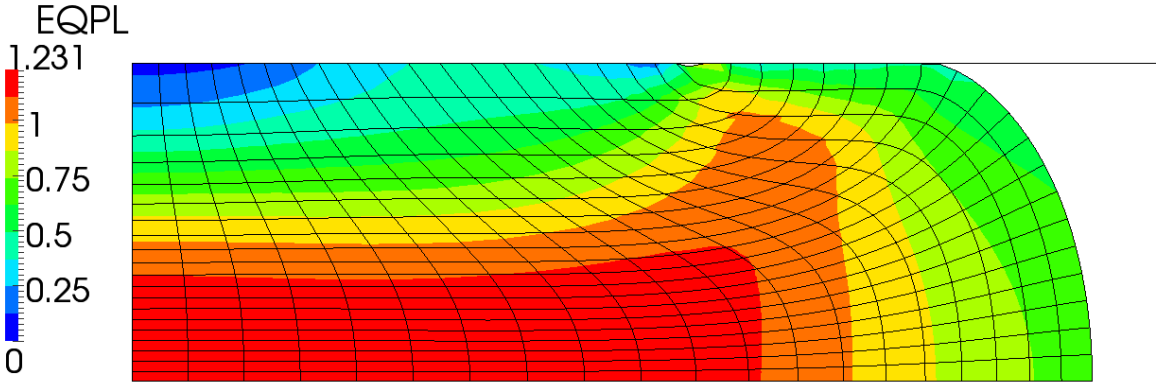

(b)

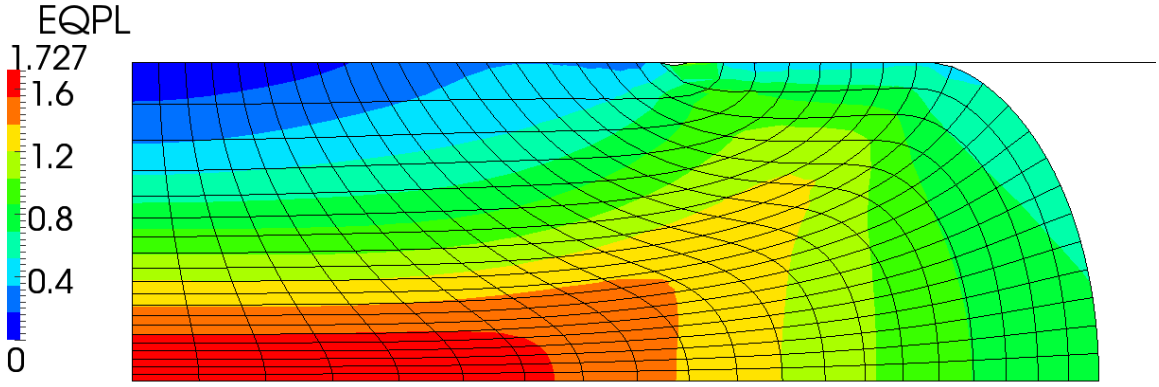

(c)

Figure 2.6: Equivalent plastic strains for the compressed cylindrical test specimen using the (a) small strain (b) hyper- and (c) logarithmic elastoplastic formulations.

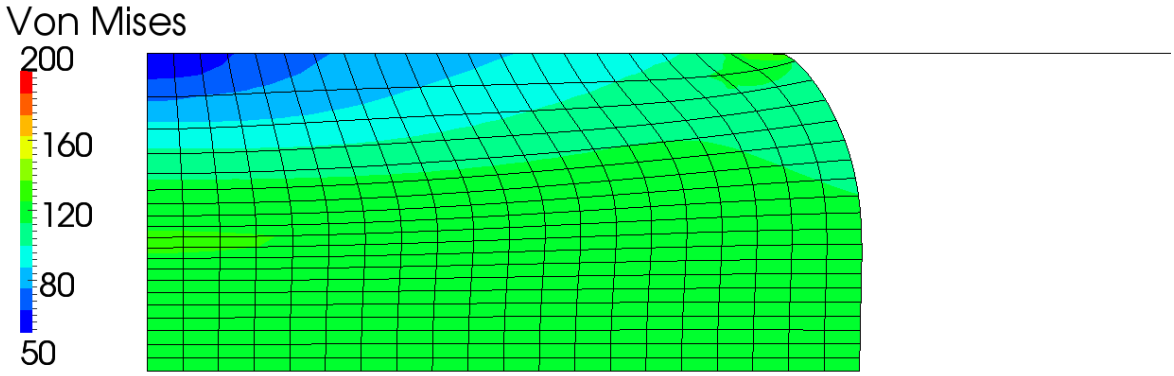

(a)

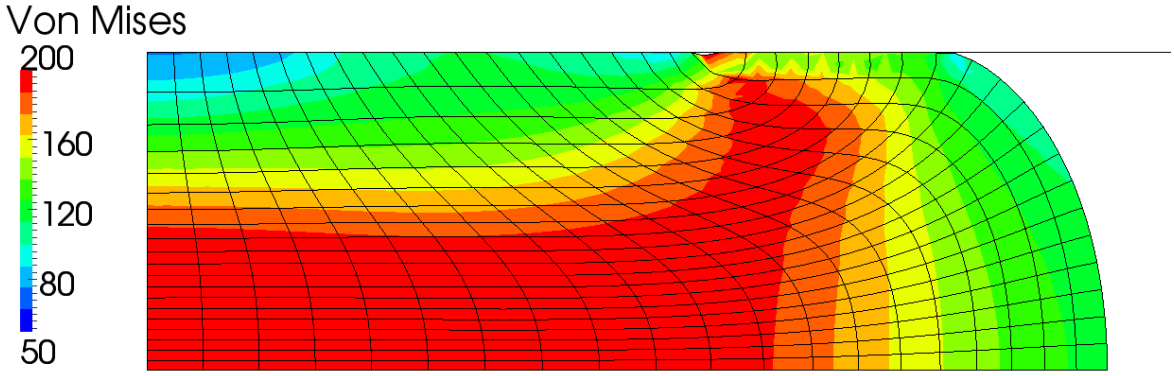

(b)

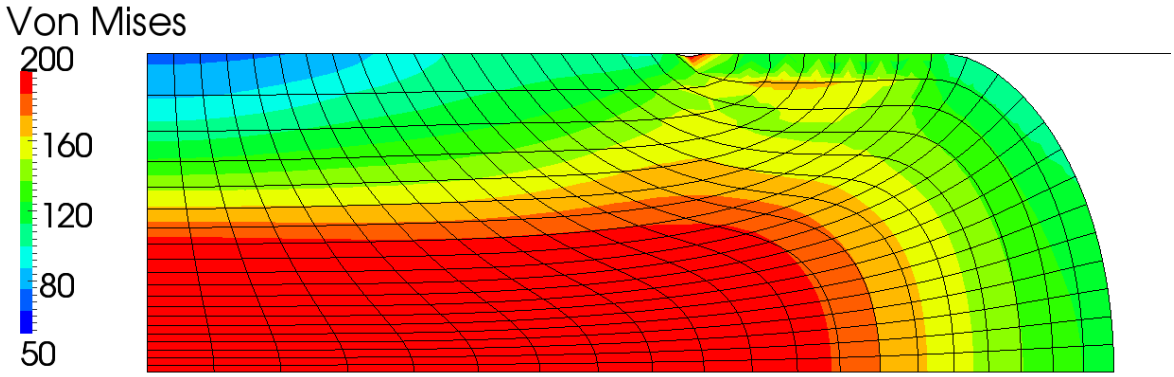

(c)

Figure 2.7: Von Mises equivalent stress values between 50MPa and 200MPa for the compressed cylindrical test specimen using the (a) small strain (b) hyper- and (c) logarithmic elastoplastic formulations.

of 158.57MPa is reported while the hyper-elastoplastic formulation reports a value of 363.08MPa and 281.07MPa in case of the logarithmic formulation. The upper limit of 200MPa is simply chosen to better compare the results visually without giving much importance to these concentrated nodal values.

The results for the Cook's membrane problem, that was subjected to moderate strains, compared well for the hyper-elastoplastic and logarithmic cases. This test sample shows the variation between these formulations given larger deformations, where in some cases elements also undergo substantial rotation relative to one another. A similar test problem is again modelled, this time in three different boundary value problem solvers for comparison on the native formulations used in large deformation plasticity.

2.2 Software package comparison

This section compares the built in elastoplastic formulations for Abaqus 6.11 and CalculiX 2.8 in the presence of geometric effects as well as the hyper-elastoplastic formulation using Code_Aster 11.3. In all three packages an Abaqus user material, coded as a Fortran subroutine, can be linked.

A cylinder with a height to diameter ratio of 2:1 is again modelled subject to a large axial strain, as depicted in Figure 2.4. In the three software packages, the axi-symmetric problem is set up and and solved using the same linear strain hardening material parameters.

A boundary value problem is set up in this section to model a 5mm$\times$2.5mm quarter axi-symmetric section of the test specimen using a 20×20 mesh of quadratic elements. To make the roll over easier to solve, the upper right square element is replaced with two triangular elements. For this comparison, the material is modelled using an elastic stiffness of $E = 10$GPa, Poisson's ratio of $\nu = 0.3$, initial yield stress of $\sigma_0 = 50$MPa and linear strain hardening modulus of $K = 100$MPa.

CalculiX does not have the option of a rigid line or surface to model the anvil. The anvil is therefore modelled using a single element 5mm long in the radial direction and 1mm high in the axial direction. Contact is defined between the lower surface of the anvil element and outer surface of the test specimen so that barrelling and rollover may

again be handled during the compression. Hard normal contact is chosen in Abaqus and friction is assumed using a coefficient $\mu_C = 0.2$. CalculiX does not have the option for hard contact and so it is modelled using a spring contact formulation with a spring stiffness of $K_{\text{spring}} = 50\text{GPa}$. The discrete Lagrangian contact formulation in Code_Aster is again used as in Section 2.1.2.

Over the course of the simulation, a downward axial displacement of 3.5mm is prescribed to the two lower nodes of the anvil element. The resulting von Mises equivalent stress is displayed for comparison at the end of the simulation, in Figure 2.8. These stress results are limited between 50MPa and 200MPa to allow easier comparison. The von Mises stress values extracted at the corner nodes labelled in Figure 2.4(b) as well as the displacement in the radial direction are given in Table 2.2.

Despite some local variations, the hyper-elastoplastic result in Figure 2.8(c) seems in good agreement to the hypo-elastoplastic, Jaumann corotational formulation intrinsically used by Abaqus in Figure 2.8(a).

Although the results obtained using CalculiX have the same approximate stress distributions, there is a clearer distinction between Figure 2.8(b) and the other figures. According to the CalculiX documentation, the native formulation used for isotropic plasticity in the presence of large strain or geometric effects is modelled using the hyper-elastoplastic formulation described by Simo and Hughes (1997). If we assume that the CalculiX results should be closer to that of Figure 2.8(c), a possible reason for the observed variation from the other two results could be due to the alternative spring contact formulation used. The variation could also be attributed to a slightly different element formulation or treatment of the yield surface hardening function.

The quadratic meshes contain a total of 1281 nodes. For a quantitative comparison, the Von Mises stresses as well as the radial and axial displacements at all 1281 nodal

	Von Mises stress				Radial displacement	
	A	*B*	*C*	*D*	*C*	*D*
Abaqus	50.803	213.08	138.02	194.81	2.1578	0.61400
CalculiX	78.304	209.16	138.30	195.53	2.1507	0.63447
Code_Aster	51.996	214.36	138.51	199.07	2.1593	0.62628

Table 2.2: Von Mises stress and displacement values at selected locations

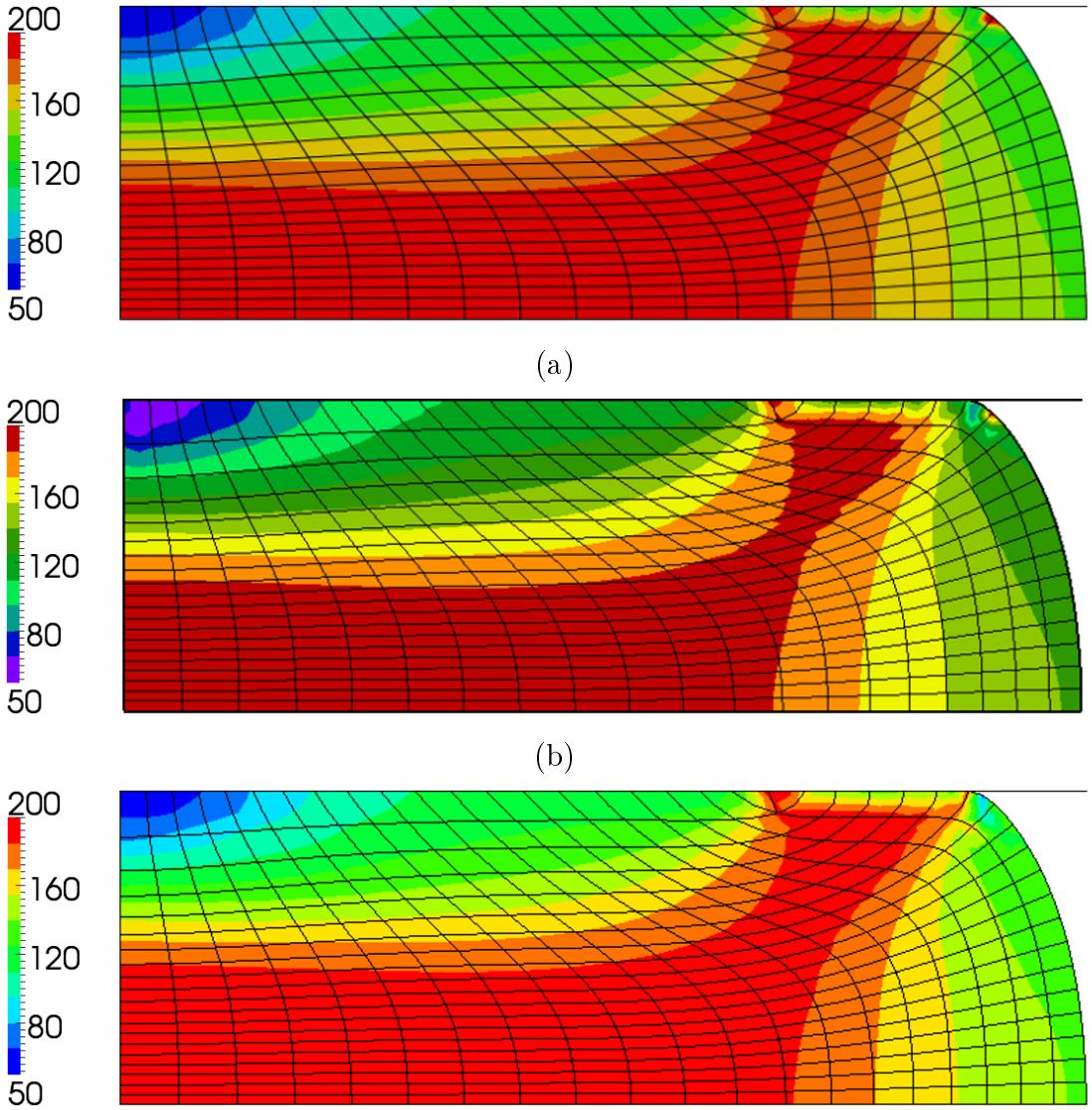

Figure 2.8: Von Mises equivalent stress values between 50MPa and 200MPa for the compressed cylindrical test specimen. The results are obtained from (a) Abaqus (b) CalculiX and (c) the hyper-elastoplastic formulation in Code_Aster.

locations are extracted and compared.

The average difference as a percentage of both quantities compared is calculated over all $N = 1281$ nodal locations using

$$\text{Average \% difference}(\boldsymbol{\phi}, \boldsymbol{\varphi}) = \frac{200}{N} \sum_{i}^{N} \left| \frac{\phi_i - \varphi_i}{\phi_i + \varphi_i} \right|, \tag{2.2}$$

where $\boldsymbol{\phi}$ and $\boldsymbol{\varphi}$ are the two vectors containing the quantities compared.

The average differences when comparing the Abaqus, CalculiX and Code_Aster results are given in Table 2.3. The von Mises stresses between Abaqus and CalculiX compare the best at a 1.17% difference while the largest difference is 2.18% when comparing the CalculiX results to that of Code_Aster. The displacement solution using Abaqus and Code_Aster compare well with a 0.65% difference in the radial direction and less than 0.1% difference in the axial direction. Comparing all 3843 extracted values the Abaqus and Code_Aster solution are within 0.68%. While there are a large number of reasons why the solutions could vary, the solution using the three different software packages compare favourably with an average variation below 1.2%.

Abaqus, as a commercial software package, is extensively validated while CalculiX and Code_Aster are both research codes. The verification using the three different packages to solve the same representative problem in this subsection is mainly aimed at illustrating reasonable variation while concluding that both the hyper-elastoplastic and corotational hypo-elastoplastic formulations are appropriate choices.

A general elastoplastic user material framework is discussed in the following section for isotropic and combined (isotropic and kinematic) hardening. Theory and implementation of the Abaqus material framework in a corotational hypo-elastoplastic sense are discussed.

	Von Mises stress	Radial displacement	Axial displacement	Average
Abaqus - CalculiX	1.1679	1.5792	0.2508	0.9993
Abaqus - Code_Aster	1.2856	0.6519	0.0966	0.6781
CalculiX - Code Aster	2.1773	1.1546	0.1663	1.1661

Table 2.3: Average percentage difference in the von Mises stress field and displacement solution evaluated at 1281 nodal locations.

2.3 Incremental hypo-elastoplasticity: an Abaqus user material framework

The results of the Abaqus native formulation, where the corotational Jaumann stress rate is used to obtain a hypo-elastoplastic formulation, and those of the hyper-elastoplastic formulation in Code_Aster compare well, considering Figure 2.8. This section therefore focuses on the relevant theory and implementation of a hypo-elastoplastic framework for both purely isotropic as well as an extension to combined isotropic and kinematic hardening plasticity into an Abaqus user material subroutine.

In this section, a review on some basic continuum mechanics is presented as may be found in many books on the subject, see for example *"Nonlinear Solid Mechanics: A Continuum Approach for Engineering"* by Holzapfel (2000). Much of the theory is also contained in *"Computational Inelasticity"* by Simo and Hughes (1997) or taken from pages 757 to 818 of the Abaqus 6.11 Theory Manual (2011a).

2.3.1 Deformation theory

If $\mathcal{B}_0$, an open bounded set in $\mathbb{R}^3$, is the reference configuration of a continuum body with particles labelled by $\boldsymbol{X} \in \mathcal{B}_0$, a smooth deformation is defined by a one-to-one mapping:

$$\boldsymbol{\varphi} : \mathcal{B}_0 \to \mathcal{B} \subset \mathbb{R}^3. \tag{2.3}$$

Here $\boldsymbol{X}$ is mapped by $\boldsymbol{\varphi}$ to $\boldsymbol{x} \in \mathcal{B}$, a point in the current configuration $\mathcal{B} = \boldsymbol{\varphi}(\mathcal{B}_0)$. Therefore $\boldsymbol{x} = \boldsymbol{\varphi}(\boldsymbol{X}, t)$ at time t, as seen in Figure 2.9.

The deformation gradient at time t, $\boldsymbol{F}(\boldsymbol{X}, t)$ is the derivative of the deformation (Simo and Hughes, 1997)

$$\boldsymbol{F}(\boldsymbol{X}, t) := \frac{\partial \boldsymbol{x}}{\partial \boldsymbol{X}} = \frac{\partial \boldsymbol{\varphi}(\boldsymbol{X}, t)}{\partial \boldsymbol{X}}. \tag{2.4}$$

Interpenetrability of matter further means that the determinant of the deformation gradient (Simo and Hughes, 1997)

$$J(\boldsymbol{X}) = \det[\boldsymbol{F}(\boldsymbol{X})] > 0. \tag{2.5}$$

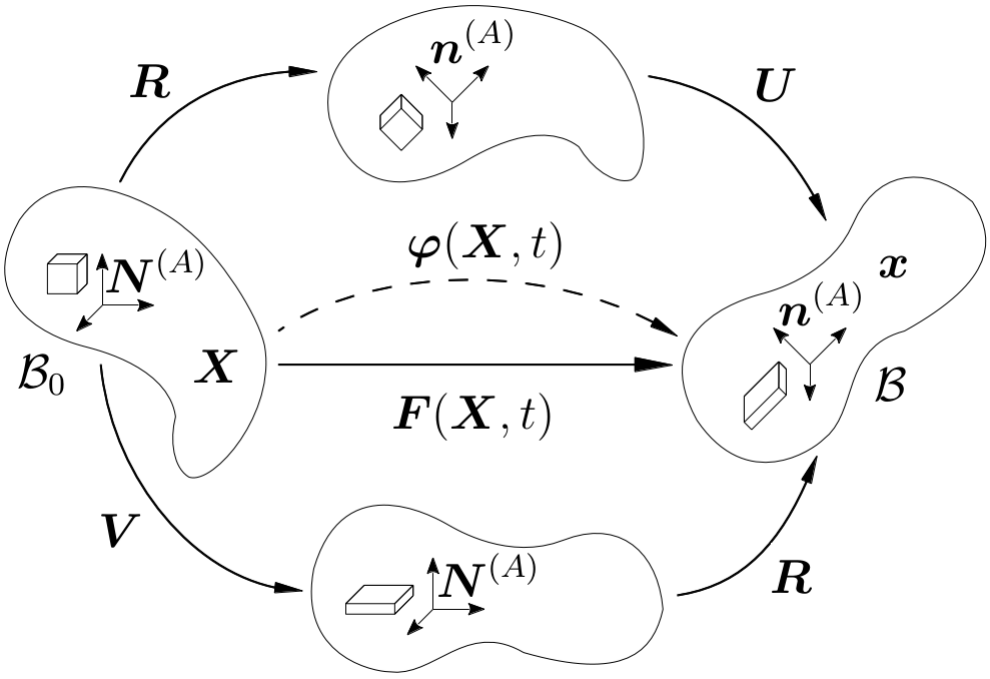

Figure 2.9: The deformation gradient, adapted from Simo and Hughes (1997).

The deformation gradient may be decomposed into a rigid and nonrigid part as is visible in Figure 2.9. If $\boldsymbol{R}$ is a pure rigid body rotation with the property $\boldsymbol{R}^{\mathsf{T}} = \boldsymbol{R}^{-1}$, $\boldsymbol{U}$ is the right stretch tensor and $\boldsymbol{V}$ the left stretch tensor, the deformation gradient may be decomposed into (Simo and Hughes, 1997)

$$\boldsymbol{F} = \boldsymbol{R} \cdot \boldsymbol{U} \qquad \text{or} \qquad \boldsymbol{F} = \boldsymbol{V} \cdot \boldsymbol{R}. \tag{2.6}$$

First consider rigid body rotation. Each unit vector $\boldsymbol{N}$ on the original solid body $\mathcal{B}_0$ is rotated to the unit normal in the current configuration through

$$\boldsymbol{n} = \boldsymbol{R} \cdot \boldsymbol{N}, \tag{2.7}$$

where $\boldsymbol{n}$ therefore becomes the principal stretch direction in the Eulerian frame (on $\mathcal{B}$). Given three associated orthogonal directions, the total rigid body rotation may be

constructed by sum of the dyadic products of the principal directions

$$\boldsymbol{R} = \sum_{A=I}^{III} \boldsymbol{n}^{(A)} \otimes \boldsymbol{N}^{(A)}. \tag{2.8}$$

Spectral decomposition of the deformation gradient further takes the form (Simo and Hughes, 1997)

$$\boldsymbol{F} = \sum_{A=I}^{III} \lambda^{(A)} \boldsymbol{n}^{(A)} \otimes \boldsymbol{N}^{(A)}, \tag{2.9}$$

where $\lambda^{(A)}$ is the stretch associated with principal direction $\boldsymbol{n}^{(A)}$ in the Eulerian reference frame. The right and left stretch tensors are further given by

$$\boldsymbol{U} = \sum_{A=I}^{III} \lambda^{(A)} \boldsymbol{N}^{(A)} \otimes \boldsymbol{N}^{(A)} \qquad \text{and} \qquad \boldsymbol{V} = \sum_{A=I}^{III} \lambda^{(A)} \boldsymbol{n}^{(A)} \otimes \boldsymbol{n}^{(A)}. \tag{2.10}$$

Using Equation (2.6), these tensors are related through the rotation by

$$\boldsymbol{U} = \boldsymbol{R}^{\mathsf{T}} \cdot \boldsymbol{F} = \boldsymbol{R}^{\mathsf{T}} \cdot \boldsymbol{V} \cdot \boldsymbol{R}. \tag{2.11}$$

2.3.2 Displacement and velocity

We may have a displacement $\boldsymbol{u}$ such that the coordinates $\boldsymbol{x}$ on the deformed configuration are related to the coordinates $\boldsymbol{X}$ on the undeformed configuration by

$$\boldsymbol{x} = \boldsymbol{X} + \boldsymbol{u}. \tag{2.12}$$

The deformation gradient according to Equation (2.4) can now be determined with

$$\boldsymbol{F} = \frac{d\boldsymbol{x}}{d\boldsymbol{X}} = \frac{d\left(\boldsymbol{X} + \boldsymbol{u}\right)}{d\boldsymbol{X}} = \boldsymbol{I} + \nabla_{\boldsymbol{X}} \boldsymbol{u}, \tag{2.13}$$

where $\nabla_{\boldsymbol{X}} \boldsymbol{u}$ is known as the displacement gradient. If the velocity of a material particle is $\dot{\boldsymbol{u}} = \partial_t \boldsymbol{x}$, we can similarly have a velocity gradient. The velocity difference between neighbouring particles in the current configuration, an infinitesimal distance $d\boldsymbol{x}$ apart

using $d\boldsymbol{x} = \boldsymbol{F} \cdot d\boldsymbol{X}$ from Equation (2.4) is:

$$d\dot{\boldsymbol{u}} = \nabla_{\boldsymbol{x}}\dot{\boldsymbol{u}} \cdot d\boldsymbol{x} = \nabla_{\boldsymbol{x}}\dot{\boldsymbol{u}} \cdot \boldsymbol{F} \cdot d\boldsymbol{X} \quad \text{or} \quad \frac{d\dot{\boldsymbol{u}}}{d\boldsymbol{X}} = \nabla_{\boldsymbol{x}}\dot{\boldsymbol{u}} \cdot \boldsymbol{F}, \tag{2.14}$$

where $\nabla_{\boldsymbol{x}}\dot{\boldsymbol{u}}$ is the velocity gradient in the current configuration $\mathcal{B}$. It can also be determined directly:

$$\frac{d\dot{\boldsymbol{u}}}{d\boldsymbol{X}} = \frac{\partial}{\partial t}\left(\frac{d\boldsymbol{x}}{d\boldsymbol{X}}\right) = \frac{\partial}{\partial t}\left(\boldsymbol{F}\right) = \dot{\boldsymbol{F}}. \tag{2.15}$$

Comparing these two equations the expression for the spatial velocity gradient is (Simo and Hughes, 1997):

$$\begin{aligned} \nabla_{\boldsymbol{x}}\dot{\boldsymbol{u}} \cdot \boldsymbol{F} &= \dot{\boldsymbol{F}} \\ \nabla_{\boldsymbol{x}}\dot{\boldsymbol{u}} &= \dot{\boldsymbol{F}} \cdot \boldsymbol{F}^{-1}. \end{aligned} \tag{2.16}$$

The velocity gradient is commonly split into a symmetric part known as the rate of deformation tensor ($\boldsymbol{d} = \boldsymbol{d}^{\mathsf{T}}$) and a skew symmetric part known as the spin matrix ($\boldsymbol{w} = -\boldsymbol{w}^{\mathsf{T}}$). This decomposition means that

$$\boldsymbol{d} = \frac{1}{2}\left[\nabla_{\boldsymbol{x}}\dot{\boldsymbol{u}} + \nabla_{\boldsymbol{x}}^{\mathsf{T}}\dot{\boldsymbol{u}}\right] \qquad \text{and} \qquad \boldsymbol{w} = \frac{1}{2}\left[\nabla_{\boldsymbol{x}}\dot{\boldsymbol{u}} - \nabla_{\boldsymbol{x}}^{\mathsf{T}}\dot{\boldsymbol{u}}\right]. \tag{2.17}$$

2.3.3 Incremental solution update in Abaqus

Given a converged solution to the boundary value problem at time step t, a solution update

$$\delta\boldsymbol{u} = \boldsymbol{\varphi}\left(\boldsymbol{X}, t + \delta t\right) - \boldsymbol{\varphi}\left(\boldsymbol{X}, t\right) = \boldsymbol{x}_{t+\delta t} - \boldsymbol{x}_t \tag{2.18}$$

to an incremental change or time step δt is generally required. The average material rotation over an increment can be constructed using the multiplicative decomposition of the rotation tensor. From the work by Hughes and Winget (1980), assume that a rotation somewhere in the current increment can be determined from

$$\boldsymbol{R}_{t+\alpha\delta t} = \delta\boldsymbol{R}\left(\beta\right) \cdot \boldsymbol{R}_t \Rightarrow \delta\boldsymbol{R}\left(\beta\right) = \boldsymbol{R}_{t+\beta\delta t} \cdot \boldsymbol{R}_t^{\mathsf{T}}. \tag{2.19}$$

The scalar value $0 \leq \beta \leq 1$ indicates where the calculation takes place. A value of $\beta = 0$ is associated with values at the start of the increment t while a value of 1 is associated with the end of the increment $t + \delta t$. For notational brevity, the full rotation during an increment is simply $\delta \boldsymbol{R} = \boldsymbol{R}_{t+\delta t} \cdot \boldsymbol{R}_t^{\mathsf{T}}$ while at the start of the increment $\delta \boldsymbol{R}(0) = \boldsymbol{R}_t \cdot \boldsymbol{R}_t^{\mathsf{T}} = \boldsymbol{I}$. For each rotational increment, the deformation basis or principal stretch direction is updated. All vectors and tensors can be rotated by this incremental rotation. For example,

$$\widetilde{\boldsymbol{n}}_t = \delta \boldsymbol{R} \cdot \boldsymbol{n}_t \qquad \text{and} \qquad \widetilde{\boldsymbol{\sigma}}_t = \delta \boldsymbol{R} \cdot \boldsymbol{\sigma}_t \cdot \delta \boldsymbol{R}^{\mathsf{T}} \tag{2.20}$$

are a rotated normal vector and rotated stress tensor at the start of the calculation under the imposed incremental rotation respectively. In Abaqus, rotated variables are passed to constitutive routines that further update them subject to various constitutive effects. The velocity gradient at any time in the increment $\nabla_{\boldsymbol{x}} \dot{\boldsymbol{u}}(\alpha)$, is rotated to the current deformation basis using the instantaneous rotation in Equation (2.19) as well as the full rotation increment. The tensor is first rotated back to the basis at the start of the increment and then rotated forward to the end. The rotated velocity gradient at any point during the increment time, as seen in the current coordinate system is therefore

$$\nabla_{\boldsymbol{x}} \dot{\widetilde{\boldsymbol{u}}}(\beta) = \delta \boldsymbol{R} \cdot \left(\delta \boldsymbol{R}^{\mathsf{T}}(\beta) \cdot \nabla_{\boldsymbol{x}} \dot{\boldsymbol{u}}(\beta) \cdot \delta \boldsymbol{R}(\beta) \right) \cdot \delta \boldsymbol{R}^{\mathsf{T}}. \tag{2.21}$$

Using Equation (2.21), an expression for the instantaneous rate of deformation tensor in Equation (2.17) as rotated to the final coordinate system becomes

$$\widetilde{\boldsymbol{d}}(\beta) = \frac{1}{2} \left[\nabla_{\boldsymbol{x}} \dot{\widetilde{\boldsymbol{u}}}(\beta) + \nabla_{\boldsymbol{x}}^{\mathsf{T}} \dot{\widetilde{\boldsymbol{u}}}(\beta) \right]. \tag{2.22}$$

Decomposing the total deformation increment as in Equation (2.6) so that $\delta \boldsymbol{F}(\beta) = \delta \boldsymbol{R}(\beta) \cdot \delta \boldsymbol{U}(\beta)$ and using Equation (2.16) for the instantaneous velocity gradient:

$$\begin{aligned} \nabla_{\boldsymbol{x}} \dot{\boldsymbol{u}}(\beta) &= \delta \dot{\boldsymbol{F}}(\beta) \cdot \delta \boldsymbol{F}^{-1}(\beta) \\ &= \left(\delta \dot{\boldsymbol{R}}(\beta) \cdot \delta \boldsymbol{U}(\beta) + \delta \boldsymbol{R}(\beta) \cdot \delta \dot{\boldsymbol{U}}(\beta) \right) \cdot \left(\delta \boldsymbol{U}^{-1}(\beta) \cdot \delta \boldsymbol{R}^{\mathsf{T}}(\beta) \right) \\ &= \delta \dot{\boldsymbol{R}}(\beta) \cdot \delta \boldsymbol{R}^{\mathsf{T}}(\beta) + \delta \boldsymbol{R}(\beta) \cdot \delta \dot{\boldsymbol{U}}(\beta) \cdot \delta \boldsymbol{U}^{-1}(\beta) \cdot \delta \boldsymbol{R}^{\mathsf{T}}(\beta). \end{aligned} \tag{2.23}$$

Within Abaqus, integration of the rotated rate of deformation tensor in Equation (2.22) over the entire increment gives the total strain update $\delta\boldsymbol{\varepsilon}$ for the current configuration. Using Equations (2.21) and (2.23), the strain increment is determined by

$$\begin{aligned}\delta\boldsymbol{\varepsilon} &= \int_0^1 \widetilde{\boldsymbol{d}}\,(\beta)\,d\beta \\ &= \frac{1}{2}\delta\boldsymbol{R}\cdot\int_0^1 \delta\boldsymbol{R}^{\mathsf{T}}\,(\beta)\cdot\left[\nabla_{\boldsymbol{x}}\dot{\boldsymbol{u}}\,(\beta)+\nabla_{\boldsymbol{x}}^{\mathsf{T}}\dot{\boldsymbol{u}}\,(\beta)\right]\cdot\delta\boldsymbol{R}\,(\beta)\,d\beta\cdot\delta\boldsymbol{R}^{\mathsf{T}} \\ &= \frac{1}{2}\delta\boldsymbol{R}\cdot\int_0^1 \left[\delta\dot{\boldsymbol{U}}\,(\beta)\cdot\delta\boldsymbol{U}^{-1}\,(\beta)+\delta\boldsymbol{U}^{-1}\,(\beta)\cdot\delta\dot{\boldsymbol{U}}\,(\beta)\right]d\beta\cdot\delta\boldsymbol{R}^{\mathsf{T}}. \qquad (2.24)\end{aligned}$$

Using spectral decomposition of the stretch tensors in Equation (2.10), the instantaneous right stretch tensor is

$$\delta\boldsymbol{U}\,(\beta)=\sum_{A=I}^{III}\left[1+\beta\left(\delta\lambda^{(A)}-1\right)\right]\boldsymbol{N}^{(A)}\otimes\boldsymbol{N}^{(A)}. \qquad (2.25)$$

If the instantaneous time increment is $\beta\delta t$, the time derivative of the right stretch tensor is

$$\delta\dot{\boldsymbol{U}}\,(\beta)=\frac{1}{\delta t}\frac{\partial\boldsymbol{U}\,(\beta)}{\partial\beta}=\frac{1}{\delta t}\sum_{A=I}^{III}\left(\delta\lambda^{(A)}-1\right)\boldsymbol{N}^{(A)}\otimes\boldsymbol{N}^{(A)}, \qquad (2.26)$$

while the inverse using the instantaneous stretch increment is

$$\delta\boldsymbol{U}^{-1}\,(\beta)=\sum_{A=I}^{III}\left[\frac{1}{1+\beta\left(\delta\lambda^{(A)}-1\right)}\right]\boldsymbol{N}^{(A)}\otimes\boldsymbol{N}^{(A)}. \qquad (2.27)$$

The integral part of Equation (2.24) can be determined using Equations (2.25) to (2.27):

$$\begin{aligned}&\frac{1}{2}\int_0^1\left[\delta\dot{\boldsymbol{U}}\,(\beta)\cdot\delta\boldsymbol{U}^{-1}\,(\beta)+\delta\boldsymbol{U}^{-1}\,(\beta)\cdot\delta\dot{\boldsymbol{U}}\,(\beta)\right]d\beta \\ &\qquad=\int_0^1\sum_{A=I}^{III}\left[\frac{\left(\delta\lambda^{(A)}-1\right)}{1+\beta\left(\delta\lambda^{(A)}-1\right)}\right]\boldsymbol{N}^{(A)}\otimes\boldsymbol{N}^{(A)}d\beta\end{aligned}$$

$$= \sum_{A=I}^{III} \ln(\delta\lambda^{(A)}) \boldsymbol{N}^{(A)} \otimes \boldsymbol{N}^{(A)} \tag{2.28}$$

since $\int_0^1 \frac{\left(\delta\lambda^{(A)}-1\right)}{1+\beta\left(\delta\lambda^{(A)}-1\right)} d\beta = \ln\left(1+\beta\left(\delta\lambda^{(A)}-1\right)\right)\Big|_0^1 = \ln\left(\delta\lambda^{(A)}\right)$. Equation (2.24) in terms of the incremental logarithmic strain increment is therefore:

$$\begin{aligned} \delta\boldsymbol{\varepsilon} &= \delta\boldsymbol{R} \cdot \left[\sum_{A=I}^{III} \ln(\delta\lambda^{(A)}) \boldsymbol{N}^{(A)} \otimes \boldsymbol{N}^{(A)}\right] \cdot \delta\boldsymbol{R}^{\mathsf{T}} \\ &= \sum_{A=I}^{III} \ln(\delta\lambda^{(A)}) \boldsymbol{n}^{(A)} \otimes \boldsymbol{n}^{(A)} \\ &= \ln(\delta\boldsymbol{V}). \end{aligned} \tag{2.29}$$

As long as the stretch at any time during the increment has the same principal directions as the total stretch increment, Abaqus assumes that a logarithmic incremental strain provides the integral of the strain rate or rate of deformation. In Abaqus, the logarithmic strain increment formulation as described above is used as an input to the material constitutive subroutine and solved using a corotational description of the relevant tensors such as the strain, plastic strain, stress and back stress.

2.3.4 Hypo-elastoplasticity

In hypo-elastoplasticity, the material constitutive response is integrated objectively by using a rotation neutralised description of the spatial evolution equations. The formulation can be explained by first introducing an orthogonal tensor $\boldsymbol{\Lambda}$. Following Simo and Hughes (1997), this tensor has the following properties:

$$\boldsymbol{\Lambda}|_{t=0} = \boldsymbol{I}, \qquad \dot{\boldsymbol{\Lambda}} = \hat{\boldsymbol{\omega}} \cdot \boldsymbol{\Lambda}, \tag{2.30}$$

where $\hat{\boldsymbol{\omega}} = -\hat{\boldsymbol{\omega}}^{\mathsf{T}}$ is a skew symmetric tensor. Using this orthogonal tensor, the rotated local configurations

$$\boldsymbol{D} = \boldsymbol{\Lambda}^{\mathsf{T}} \cdot \boldsymbol{d} \cdot \boldsymbol{\Lambda} \qquad \text{and} \qquad \boldsymbol{\Sigma} = \boldsymbol{\Lambda}^{\mathsf{T}} \cdot \boldsymbol{\sigma} \cdot \boldsymbol{\Lambda} \tag{2.31}$$

are introduced as the rotated rate of deformation tensor $\boldsymbol{D}$ and rotated Cauchy stress tensor $\boldsymbol{\Sigma}$. The time derivative of the rotated Cauchy stress tensor gives

$$\begin{aligned}\dot{\boldsymbol{\Sigma}} &= \boldsymbol{\Lambda}^{\mathsf{T}} \cdot \dot{\boldsymbol{\sigma}} \cdot \boldsymbol{\Lambda} + \dot{\boldsymbol{\Lambda}}^{\mathsf{T}} \cdot \boldsymbol{\sigma} \cdot \boldsymbol{\Lambda} + \boldsymbol{\Lambda}^{\mathsf{T}} \cdot \boldsymbol{\sigma} \cdot \dot{\boldsymbol{\Lambda}} \\ &= \boldsymbol{\Lambda}^{\mathsf{T}} \cdot \left[\dot{\boldsymbol{\sigma}} + \hat{\boldsymbol{\omega}}^{\mathsf{T}} \cdot \boldsymbol{\sigma} + \boldsymbol{\sigma} \cdot \hat{\boldsymbol{\omega}}\right] \cdot \boldsymbol{\Lambda} \\ &= \boldsymbol{\Lambda}^{\mathsf{T}} \cdot \left[\dot{\boldsymbol{\sigma}} - \hat{\boldsymbol{\omega}} \cdot \boldsymbol{\sigma} + \boldsymbol{\sigma} \cdot \hat{\boldsymbol{\omega}}\right] \cdot \boldsymbol{\Lambda} \\ &= \boldsymbol{\Lambda}^{\mathsf{T}} \cdot \mathring{\boldsymbol{\sigma}} \cdot \boldsymbol{\Lambda} \end{aligned} \tag{2.32}$$

with $\mathring{\boldsymbol{\sigma}}$ now a corotated objective Cauchy stress rate relative to the axes with spin $\hat{\boldsymbol{\omega}}$. The objective stress rate may follow from the choice of the skew symmetric spatial tensor. Choosing $\hat{\boldsymbol{\omega}} = \boldsymbol{w}$, the spin tensor associated with the velocity gradient in Equation (2.17) effectively recovers the Jaumann rate while the choice of $\hat{\boldsymbol{\omega}} = \dot{\boldsymbol{R}} \cdot \boldsymbol{R}^{\mathsf{T}}$ results in the Green-Naghdi rate (Simo and Hughes, 1997). In most cases, Abaqus natively uses the Jaumann rate.

The hypo-elastoplastic formulation assumes the additive decomposition of the rate of deformation or strain rate

$$\boldsymbol{D} = \boldsymbol{D}^{\mathrm{e}} + \boldsymbol{D}^{\mathrm{p}} \qquad \text{or} \qquad \boldsymbol{d} = \boldsymbol{d}^{\mathrm{e}} + \boldsymbol{d}^{\mathrm{p}}. \tag{2.33}$$

From this assumption, material rate constitutive equations are given by

$$\mathring{\boldsymbol{\sigma}} = \boldsymbol{\mathcal{C}} : \boldsymbol{d}^{\mathrm{e}} \tag{2.34}$$

where the material tensor $\boldsymbol{\mathcal{C}}$ can take the same form as in the small strain formulation with

$$\mathcal{C}_{ijkl} = \left(\kappa - \frac{2}{3}\mu\right)\delta_{ij}\delta_{kl} + 2\mu\delta_{ik}\delta_{jl} \tag{2.35}$$

for example. In this equation $\kappa > 0$ is the bulk modulus; μ is the shear modulus and δ_{ij} represents Kronecker's delta ($\delta_{ii} = 1$, $\delta_{i,j\neq i} = 0$). κ and μ are related to the elastic modulus E and Poisson's ratio ν through

$$\kappa = \frac{\nu E}{(1+\nu)(1-2\nu)} \qquad \text{and} \qquad \mu = \frac{E}{2(1+\nu)}. \tag{2.36}$$

2.3.5 Isotropic Hardening

From Equation (2.33), the rotated instantaneous rate of deformation tensor is decomposed additively:

$$\widetilde{\boldsymbol{d}} = \widetilde{\boldsymbol{d}}^{\mathrm{e}} + \widetilde{\boldsymbol{d}}^{\mathrm{p}} \quad \Rightarrow \quad \dot{\boldsymbol{\varepsilon}} = \widetilde{\boldsymbol{d}} \quad \Rightarrow \quad \delta\boldsymbol{\varepsilon} = \delta\boldsymbol{\varepsilon}^{\mathrm{e}} + \delta\boldsymbol{\varepsilon}^{\mathrm{p}}. \tag{2.37}$$

The stress tensor is updated incrementally using the Hughes-Winget formula (1980):

$$\boldsymbol{\sigma}_{t+\delta t} = \widetilde{\boldsymbol{\sigma}}_t + \boldsymbol{\mathcal{C}} : \delta\boldsymbol{\varepsilon}^{\mathrm{e}}, \tag{2.38}$$

where $\widetilde{\boldsymbol{\sigma}}_t$ is the corotated stress tensor at the start of the increment in Equation (2.20) and $\boldsymbol{\mathcal{C}}$ is the material tensor. Using the incremental strains, the integrated corotational strains are

$$\varepsilon_{ij}\big|_{t+\delta t} = \widetilde{\varepsilon}^{\mathrm{e}}_{ij}\big|_t + \widetilde{\varepsilon}^{\mathrm{p}}_{ij}\big|_t + \delta\varepsilon^{\mathrm{e}}_{ij} + \delta\varepsilon^{\mathrm{p}}_{ij}. \tag{2.39}$$

with $\widetilde{\boldsymbol{\varepsilon}}_t = \delta\boldsymbol{R} \cdot \boldsymbol{\varepsilon}_t \cdot \delta\boldsymbol{R}^{\mathsf{T}}$ as in Equation (2.20). In associated flow, the von Mises yield function means that there is no volumetric plastic strain. The strain is therefore split into a volumetric $\varepsilon_{\mathrm{vol}}\boldsymbol{I}$ and deviatoric strain tensor $\boldsymbol{\varepsilon}'$ component where

$$\varepsilon_{\mathrm{vol}} = \varepsilon_{kk} \quad \text{and} \quad \varepsilon'_{ij} = \varepsilon_{ij} - \frac{1}{3}\delta_{ij}\varepsilon_{kk}. \tag{2.40}$$

The deviatoric stress may be expressed as a function of the deviatoric elastic strain component

$$\sigma'_{ij} = 2\mu\varepsilon^{\mathrm{e}\,\prime}_{ij}. \tag{2.41}$$

Plastic deformation in the materials considered is volume preserving. Given that the trace of the plastic strain is zero and there is no pressure dependent plastic deformation, the yield only depends on the deviatoric component of the stress tensor $\boldsymbol{\sigma}'$. The first invariant of the deviatoric stress $I_1(\boldsymbol{\sigma}') = \sigma'_{kk} = 0$, meaning the yield can not be a function of the first invariant. The equivalent stress measure used in the formulation of the Huber - von Mises yield criterion or J_2 isotropic plasticity is the second invariant of the deviatoric stress tensor. The equivalent stress is defined in terms of the second

invariant of the deviatoric stress as

$$\begin{aligned} \sigma_{\mathrm{vM}} &= \sqrt{3I_2\left(\boldsymbol{\sigma}'\right)} \\ &= \sqrt{\frac{3}{2}\sigma'_{ij}\sigma'_{ij}} \end{aligned} \tag{2.42}$$

known as the von Mises stress. Isotropic plasticity requires that the material satisfy a uniaxial-stress plastic-strain strain-rate relationship. If the material is rate independent, the yield condition is now defined in three dimensional isotropic plasticity as $f(\boldsymbol{\sigma}, \alpha) = \sigma_{\mathrm{vM}} - \sigma_{\mathrm{Y}}(\alpha) \leq 0$, i.e.

$$f(\boldsymbol{\sigma}, \alpha) = \sqrt{\frac{3}{2}}\left\|\boldsymbol{\sigma}'\right\| - \sigma_{\mathrm{Y}}(\alpha) \qquad \text{or} \qquad f(\boldsymbol{\sigma}, \alpha) = \left\|\boldsymbol{\sigma}'\right\| - \sqrt{\frac{2}{3}}\sigma_{\mathrm{Y}}(\alpha). \tag{2.43}$$

In these equations, σ_{Y} is the effective yield stress and α the equivalent plastic strain. From the consistency condition, with $\gamma \geq 0$ the absolute value of the slip rate:

$$\gamma\dot{f}(\sigma) = 0 \quad \text{if} \quad f(\sigma) = 0 \quad \Longrightarrow \quad \dot{\boldsymbol{\varepsilon}}^{\mathrm{p}} = \gamma\frac{\partial}{\partial\boldsymbol{\sigma}}f\left(\boldsymbol{\sigma}, \alpha\right) = \gamma\boldsymbol{n}, \tag{2.44}$$

with $\boldsymbol{n}$ the direction of plastic flow normal to the yield surface. Since plastic flow is only a function of the deviatoric stress component:

$$n_{ij} = \frac{\sigma'_{ij}}{\left\|\boldsymbol{\sigma}'\right\|}. \tag{2.45}$$

The plastic strain rate tensor can be written in terms of the equivalent plastic strain rate and stresses to take the form of the Lévy-von Mises equation for the flow rule

$$\begin{aligned} \dot{\varepsilon}^{\mathrm{p}}_{ij} &= \gamma n_{ij} \\ &= \sqrt{\frac{3}{2}}\dot{\alpha}\frac{\sigma'_{ij}}{\left\|\boldsymbol{\sigma}'\right\|} \\ &= \frac{3}{2}\dot{\alpha}\frac{\sigma'_{ij}}{\sigma_{\mathrm{vM}}}. \end{aligned} \tag{2.46}$$

The yield stress may also be temperature and rate dependent, or depend on the evolution of other internal variables of state, as discussed in subsequent chapters. If the

plastic flow is rate dependent, the equivalent plastic strain rate could be determined from a kinetic equation

$$\dot{\alpha} = h\left(\sigma_{\mathrm{Y}}, \delta\alpha, \boldsymbol{\chi}\right) \tag{2.47}$$

where $h\left(\bullet\right)$ is a known function dependent on the yield stress, strain increment as well as other variables $\boldsymbol{\chi}$. Using backward Euler fully implicit integration gives the equation

$$\delta\alpha = \delta t\; h\left(\sigma_{\mathrm{Y}}, \delta\alpha, \boldsymbol{\chi}\right), \tag{2.48}$$

that may be inverted to give the equivalent yield stress as a function of the equivalent plastic strain at the end of the increment. The rate independent as well as the integrated rate dependent elastoplastic model can therefore be given here by the general uniaxial form

$$\sigma_{\mathrm{vM}} = \sigma_{\mathrm{Y}}\left(\delta\alpha, \boldsymbol{\chi}\right) \tag{2.49}$$

during plastic flow. Integration is performed by applying the fully implicit backward Euler method to the flow rule in Equation (2.44) so that an incremental change in plasticity is given by

$$\delta\varepsilon^{\mathrm{p}}_{ij} = \dot{\varepsilon}^{\mathrm{p}}_{ij}\delta t = \delta\gamma n_{ij}. \tag{2.50}$$

Taking the incremental deviatoric elastic strain

$$\delta\varepsilon^{\mathrm{e}\,\prime}_{ij} = \delta\varepsilon'_{ij} - \delta\varepsilon^{\mathrm{p}}_{ij} = \delta\varepsilon'_{ij} - \delta\gamma n_{ij}, \tag{2.51}$$

the deviatoric stress calculated incrementally by taking the equivalent plastic strain into account is

$$\begin{aligned}
\sigma'_{ij} &= 2\mu\varepsilon^{\mathrm{e}\,\prime}_{ij} \\
&= 2\mu\left(\widetilde{\varepsilon}^{\mathrm{e}\,\prime}_{ij}\big|_t + \delta\varepsilon^{\mathrm{e}\,\prime}_{ij}\right) \\
&= 2\mu\left(\widetilde{\varepsilon}^{\mathrm{e}\,\prime}_{ij}\big|_t + \delta\varepsilon'_{ij} - \delta\gamma n_{ij}\right).
\end{aligned} \tag{2.52}$$

By taking the definition of the associated flow direction in Equation (2.46), the equation becomes

$$\left(1 + \frac{3\mu}{\sigma_{\mathrm{vM}}}\delta\alpha\right)\sigma'_{ij} = 2\mu\left(\widetilde{\varepsilon}^{\mathrm{e}\,\prime}_{ij}\big|_t + \delta\varepsilon'_{ij}\right). \tag{2.53}$$

Assuming that the full strain increment is elastic, this introduces the trial deviatoric elastic strain state

$$\varepsilon'^{\,\text{trial}}_{ij} = \widetilde{\varepsilon}^{\text{e}\,\prime}_{ij}\Big|_t + \delta\varepsilon'_{ij} \quad \text{and} \quad \sigma'^{\,\text{trial}}_{ij} = 2\mu\varepsilon'^{\,\text{trial}}_{ij}. \tag{2.54}$$

By substituting this trial elastic stress state and taking the inner product of Equation (2.53) we have a relationship to construct a residual equation in the case for a nonlinear yield condition in three dimensions:

$$\begin{aligned}
\left(1+\frac{3\mu}{\sigma_{\text{vM}}}\delta\alpha\right)^2 \sigma'_{ij}\sigma'_{ij} &= \sigma'^{\,\text{trial}}_{ij}\sigma'^{\,\text{trial}}_{ij} \\
\left(1+\frac{3\mu}{\sigma_{\text{vM}}}\delta\alpha\right)^2 \frac{2}{3}\sigma^2_{\text{vM}} &= \sigma'^{\,\text{trial}}_{ij}\sigma'^{\,\text{trial}}_{ij} \\
\left(\sigma_{\text{vM}}+3\mu\delta\alpha\right)^2 &= \frac{3}{2}\sigma'^{\,\text{trial}}_{ij}\sigma'^{\,\text{trial}}_{ij} \\
\sigma_{\text{vM}}+3\mu\delta\alpha &= \sqrt{\frac{3}{2}\sigma'^{\,\text{trial}}_{ij}\sigma'^{\,\text{trial}}_{ij}} \\
\sigma_{\text{vM}}+3\mu\delta\alpha &= \sigma^{\text{trial}}_{\text{vM}}.
\end{aligned} \tag{2.55}$$

This equation is now formulated in terms of the trial von Mises stress $\sigma^{\text{trial}}_{\text{vM}}$. Using the general uniaxial requirement for rate independent and rate dependent plasticity set up in Equation (2.49), Equation (2.55) is recast as a residual equation to solve the equivalent plastic strain increment that would result in $\sigma_{\text{vM}} = \sigma_{\text{Y}}$ upon convergence. The residual equation is

$$\mathcal{R}_f\left(\delta\alpha\right) = \sigma^{\text{trial}}_{\text{vM}} - 3\mu\delta\alpha - \sigma_{\text{Y}}\left(\delta\alpha\right). \tag{2.56}$$

Equation (2.56) is solved by Newton's method:

$$\left\{\delta\alpha\right\}^{k+1} = \left\{\delta\alpha\right\}^{k} - \frac{\mathcal{R}_f\left(\left\{\delta\alpha\right\}^k\right)}{\mathcal{D}\mathcal{R}_f\left(\left\{\delta\alpha\right\}^k\right)}, \tag{2.57}$$

where

$$\mathcal{D}\mathcal{R}_f\left(\left\{\delta\alpha\right\}^k\right) = -3\mu - \left[\frac{d\sigma_{\text{Y}}}{d\delta\alpha}\right]^k \tag{2.58}$$

until convergence is achieved. Once the equivalent plastic strain increment is known, the solution is fully defined with $\sigma_{\text{vM}} = \sigma_{\text{Y}}$, meaning the relationship between the deviatoric stress components and deviatoric strain components in the case of incremental elastoplasticity is

$$\sigma'_{ij} = \frac{2\mu}{1 + 3\mu\delta\alpha/\sigma_{\text{vM}}} \varepsilon'^{\,\text{trial}}_{ij}. \tag{2.59}$$

2.3.6 Consistent Tangent Formulation

Taking the variational form of Equation (2.53) with respect to all quantities at the end of the time increment gives

$$\left(1 + \frac{3\mu}{\sigma_{\text{vM}}}\delta\alpha\right)\partial\sigma'_{ij} + \sigma'_{ij}\frac{3\mu}{\sigma_{\text{vM}}}\left(\partial\delta\alpha - \frac{\delta\alpha}{\sigma_{\text{vM}}}\partial\sigma_{\text{vM}}\right) = \partial\sigma'^{\,\text{trial}}_{ij}. \tag{2.60}$$

Now let us first focus on the second term of Equation (2.60). From Equation (2.49) in variational form follows

$$\partial\sigma_{\text{vM}} = \mathcal{K}\partial\delta\alpha \quad \text{where} \quad \mathcal{K} = \frac{\partial\sigma_{\text{Y}}}{\partial\delta\alpha}. \tag{2.61}$$

From Equation (2.55), we get:

$$\begin{aligned} \partial\sigma_{\text{vM}} + 3\mu\partial\delta\alpha &= \partial\sigma^{\text{trial}}_{\text{vM}} \\ \partial\sigma_{\text{vM}} &= \partial\sigma^{\text{trial}}_{\text{vM}} - 3\mu\partial\delta\alpha. \end{aligned} \tag{2.62}$$

Combining these expressions means we have a variational from for the equivalent plastic strain in terms of the elastic trial von Mises stress:

$$\partial\delta\alpha = \frac{1}{3\mu + \mathcal{K}}\partial\sigma^{\text{trial}}_{\text{vM}}. \tag{2.63}$$

From the trial elastic state:

$$\partial\sigma^{\text{trial}}_{\text{vM}} = \frac{3}{2\sigma^{\text{trial}}_{\text{vM}}}\sigma'^{\,\text{trial}}_{kl}\partial\sigma'^{\,\text{trial}}_{kl} \quad \text{and} \quad \partial\sigma'^{\,\text{trial}}_{kl} = 2\mu\partial\varepsilon'^{\,\text{trial}}_{kl}. \tag{2.64}$$

If we first focus on the second term of Equation (2.60):

$$\begin{aligned}
\sigma'_{ij}\frac{3\mu}{\sigma_{\mathrm{vM}}}\left(\partial\delta\alpha - \frac{\delta\alpha}{\sigma_{\mathrm{vM}}}\partial\sigma_{\mathrm{vM}}\right) &= \sigma'_{ij}\frac{3\mu}{\sigma_{\mathrm{vM}}}\left[\left(1-\frac{\delta\alpha}{\sigma_{\mathrm{vM}}}\mathcal{K}\right)\partial\delta\alpha\right] \\
&= \sigma'_{ij}\frac{3\mu}{\sigma_{\mathrm{vM}}}\left[\left(1-\frac{\delta\alpha}{\sigma_{\mathrm{vM}}}\mathcal{K}\right)\frac{1}{3\mu+\mathcal{K}}\partial\sigma_{\mathrm{vM}}^{\mathrm{trial}}\right] \\
&= \sigma'_{ij}\frac{3\mu}{\sigma_{\mathrm{vM}}}\left[\left(1-\frac{\delta\alpha}{\sigma_{\mathrm{vM}}}\mathcal{K}\right)\frac{3\mu}{3\mu+\mathcal{K}}\frac{\sigma'_{kl}{}^{\mathrm{trial}}}{\sigma_{\mathrm{vM}}^{\mathrm{trial}}}\partial\varepsilon'_{kl}{}^{\mathrm{trial}}\right].
\end{aligned} \tag{2.65}$$

Noting that in associated flow the flow directions are

$$n_{ij} = \frac{\sigma'_{ij}}{\sigma_{\mathrm{vM}}} = \frac{\sigma'_{ij}{}^{\mathrm{trial}}}{\sigma_{\mathrm{vM}}^{\mathrm{trial}}}, \tag{2.66}$$

the expression is further simplified as

$$\begin{aligned}
\sigma'_{ij}\frac{3\mu}{\sigma_{\mathrm{vM}}}\left(\partial\delta\alpha - \frac{\delta\alpha}{\sigma_{\mathrm{vM}}}\partial\sigma_{\mathrm{vM}}\right) &= \left[\left(3\mu-\frac{3\mu\delta\alpha}{\sigma_{\mathrm{vM}}}\mathcal{K}\right)\frac{3\mu}{3\mu+\mathcal{K}}\right]n_{ij}n_{kl}\partial\varepsilon'_{kl}{}^{\mathrm{trial}} \\
&= \left[3\mu-\left(1+\frac{3\mu}{\sigma_{\mathrm{vM}}}\delta\alpha\right)\frac{\mathcal{K}}{1+\mathcal{K}/3\mu}\right]n_{ij}n_{kl}\partial\varepsilon'_{kl}{}^{\mathrm{trial}}.
\end{aligned} \tag{2.67}$$

Substituting the relative expressions, it is possible to rewrite Equation (2.60) as

$$\left(1+\frac{3\mu}{\sigma_{\mathrm{vM}}}\delta\alpha\right)\partial\sigma'_{ij} + \left[3\mu-\left(1+\frac{3\mu}{\sigma_{\mathrm{vM}}}\delta\alpha\right)\frac{\mathcal{K}}{1+\mathcal{K}/3\mu}\right]n_{ij}n_{kl}\partial\varepsilon'_{kl}{}^{\mathrm{trial}} = 2\mu\partial\varepsilon'_{ij}{}^{\mathrm{trial}}. \tag{2.68}$$

In order to write the result in terms of only the trial and final yield function value, consider that upon convergence, from Equation (2.56):

$$\begin{aligned}
\sigma_{\mathrm{vM}}^{\mathrm{trial}} - 3\mu\delta\alpha - \sigma_{\mathrm{Y}} &= 0 \\
3\mu\delta\alpha + \sigma_{\mathrm{Y}} &= \sigma_{\mathrm{vM}}^{\mathrm{trial}} \\
1+\frac{3\mu}{\sigma_{\mathrm{Y}}}\delta\alpha &= \frac{\sigma_{\mathrm{vM}}^{\mathrm{trial}}}{\sigma_{\mathrm{Y}}}.
\end{aligned} \tag{2.69}$$

Considering that $\sigma_{\text{vM}} = \sigma_{\text{Y}}$ upon convergence:

$$\partial\sigma'_{ij} = 2\mu\frac{\sigma_{\text{Y}}}{\sigma_{\text{vM}}^{\text{trial}}}\partial\varepsilon'^{\,\text{trial}}_{ij} + \left[\frac{\mathcal{K}}{1+\mathcal{K}/3\mu} - 3\mu\frac{\sigma_{\text{Y}}}{\sigma_{\text{vM}}^{\text{trial}}}\right] n_{ij}n_{kl}\partial\varepsilon'^{\,\text{trial}}_{kl}. \tag{2.70}$$

For all cases where three direct strains are defined, the material stiffness is completed by the hydrostatic pressure component.

$$\partial\sigma_{ij} = \partial\sigma'_{ij} - \delta_{ij}\partial p \tag{2.71}$$

where $\partial p = \kappa\partial\varepsilon_{kk}$.

Computing the deviatoric strain component

$$\partial\varepsilon'_{ij} = \partial\varepsilon_{ij} - \frac{1}{3}\delta_{ij}\delta_{kl}\partial\varepsilon_{kl}, \tag{2.72}$$

and substituting it into the relevant locations yields

$$\partial\sigma_{ij} = \kappa\delta_{ij}\partial\varepsilon_{kk} + 2\mu\frac{\sigma_{\text{Y}}}{\sigma_{\text{vM}}^{\text{trial}}}\left(\partial\varepsilon_{ij} - \frac{1}{3}\delta_{ij}\partial\varepsilon_{kk}\right) + \left[\frac{\mathcal{K}}{1+\mathcal{K}/3\mu} - 3\mu\frac{\sigma_{\text{Y}}}{\sigma_{\text{vM}}^{\text{trial}}}\right] n_{ij}n_{kl}\partial\varepsilon_{kl}. \tag{2.73}$$

Finally, the solution is written as

$$\partial\sigma_{ij} = \lambda^*\delta_{ij}\partial\varepsilon_{kk} + 2\mu^*\partial\varepsilon_{ij} + \left(\frac{\mathcal{K}}{1+\mathcal{K}/3\mu} - 3\mu^*\right) n_{ij}n_{kl}\partial\varepsilon_{kl}, \tag{2.74}$$

where

$$\mu^* = \mu\frac{\sigma_{\text{Y}}}{\sigma_{\text{vM}}^{\text{trial}}}, \quad \text{and} \quad \lambda^* = \kappa - \frac{2}{3}\mu^*. \tag{2.75}$$

2.3.7 Combined Hardening

For the combined hardening case, kinematic hardening is included along with the isotropic formulation. The equivalent von Mises stress is now

$$\varsigma_{\text{vM}} = \sqrt{\frac{3}{2}\varsigma_{ij}\varsigma_{ij}} \tag{2.76}$$

where the effective stress $\varsigma_{ij} = \sigma'_{ij} - q_{ij}$ is now used. q_{ij} is the moving centre of the yield surface or back stresses. The associated flow direction in Equation (2.45) is now

$$n_{ij} = \frac{\varsigma_{ij}}{\varsigma_{\mathrm{vM}}}. \tag{2.77}$$

The evolution equation for the back stresses in terms of the Prager-Ziegler (Prager, 1956; Ziegler, 1959) linear kinematic work hardening model is

$$\dot{q}_{ij} = \frac{2}{3}\mathcal{K}\dot{\varepsilon}^{\mathrm{p}}_{ij} = \mathcal{K}\dot{\alpha}n_{ij} \tag{2.78}$$

in three dimensions. In a more general setting, we can introduce a back stress function $\sigma_{\mathrm{B}}(\delta\alpha)$. If $\delta\sigma_{\mathrm{B}}(\delta\alpha)$ represents incremental kinematic hardening, the incremental change in the back stress is

$$\delta q_{ij} = \delta\sigma_{\mathrm{B}} n_{ij}. \tag{2.79}$$

In the combined hardening implementation, the back stress is also corotated as with the other variables in Equation (2.20)

$$\boldsymbol{q}_{t+\delta t} = \widetilde{\boldsymbol{q}}_t + \delta\boldsymbol{q}. \tag{2.80}$$

Considering rate independence, the general uniaxial condition in Equation (2.49) is now

$$\varsigma_{\mathrm{vM}} = \sigma_{\mathrm{Y}}(\delta\alpha) \quad \text{where} \quad \varsigma_{\mathrm{vM}} = \sigma_{\mathrm{vM}} - \sigma_{\mathrm{B}}(\delta\alpha). \tag{2.81}$$

In the combined hardening case, the trial elastic state in Equation (2.54) is extended by first freezing the back stresses:

$$q^{\mathrm{trial}}_{ij} = q_{ij}|_t \quad \text{and} \quad \varsigma^{\mathrm{trial}}_{ij} = \sigma^{\mathrm{trial}\prime}_{ij} - q^{\mathrm{trial}}_{ij}. \tag{2.82}$$

If the effective uniaxial stress is $\sigma_{\mathrm{vM}} = \sigma_{\mathrm{Y}} + \sigma_{\mathrm{B}}$, Equation (2.55) becomes:

$$\sigma_{\mathrm{Y}} + \sigma_{\mathrm{B}}|_{t+\delta t} + 3\mu\delta\alpha = \varsigma^{\mathrm{trial}}_{\mathrm{vM}} + \sigma_{\mathrm{B}}|_t, \tag{2.83}$$

meaning the residual equation in combined hardening is

$$\mathcal{R}_f\left(\delta\alpha\right) = \varsigma_{\mathrm{vM}}^{\mathrm{trial}} - 3\mu\delta\alpha - \sigma_{\mathrm{Y}} - \delta\sigma_{\mathrm{B}}. \tag{2.84}$$

This equation is solved again by Newton's method where now

$$\mathcal{DR}_f\left(\left\{\delta\alpha\right\}^k\right) = -3\mu - \mathcal{K}^k - \mathcal{H}^k \quad \text{with} \quad \mathcal{K} = \frac{d\sigma_{\mathrm{Y}}}{d\delta\alpha} \quad \text{and} \quad \mathcal{H} = \frac{d\delta\sigma_{\mathrm{B}}}{d\delta\alpha}. \tag{2.85}$$

It is visible that the elastoplastic tangent modulus $\mathcal{K}$ in the isotropic case is simply replaced by a combined elastoplastic tangent modulus $\mathcal{K}^* = \mathcal{K} + \mathcal{H}$. The consistent tangent in the combined isotropic and kinematic hardening elastoplastic formulation is therefore given for the three dimensional case as

$$\partial\sigma_{ij} = \lambda^*\delta_{ij}\partial\varepsilon_{kk} + 2\mu^*\partial\varepsilon_{ij} + \left(\frac{1}{1+\mathcal{K}^*/3\mu} - 3\mu^*\right) n_{ij}n_{kl}\partial\varepsilon_{kl} \tag{2.86}$$

where

$$\mu^* = \mu\frac{\sigma_{\mathrm{Y}} + \delta\sigma_{\mathrm{B}}}{\sigma_{\mathrm{vM}}^{\mathrm{trial}}}, \quad \lambda^* = \kappa - \frac{2}{3}\mu^* \quad \text{and} \quad \mathcal{K}^* = \frac{d\sigma_{\mathrm{Y}}}{d\delta\alpha} + \frac{d\delta\sigma_{\mathrm{B}}}{d\delta\alpha}. \tag{2.87}$$

2.3.8 Numerical Implementation

The generic isotropic and combined material frameworks are implemented into an Abaqus user material (`UMAT`) subroutine. This Fortran subroutine is called at all material calculation points of elements where a specific material is assigned. This subroutine can use or update solution dependent state variables. The use of an Abaqus user material subroutine is outlined in Section 1.1.40 of the Abaqus user subroutine reference manual.

Abaqus makes use of engineering strains in Voigt notation. The incremental strain vector in three dimensions is therefore

$$\texttt{DSTRAN} = \left\{\delta\varepsilon\right\} = \left\{\delta\varepsilon_{11}, \delta\varepsilon_{22}, \delta\varepsilon_{33}, \delta\gamma_{23}, \delta\gamma_{13}, \delta\gamma_{12}\right\}^{\mathsf{T}} \tag{2.88}$$

where $\delta\gamma_{23} = \delta\varepsilon_{23} + \delta\varepsilon_{32}$ for example. In the stress and strain arrays, as well as the consistent tangent matrix `DDSDDE`, the `NDI` direct components are stored first, followed by the `NSHR` engineering shear components. In three dimensions, `NDI`=3, `NSHR`=3 and `DDSDDE` is a 6×6 matrix.

The stresses are used as an input and output to the subroutine where the input stress vector is already given in the corotational frame of Equation (2.20) if geometric nonlinearities are taken into account. The utility subroutine `ROTSIG` is further available within the user material subroutine to calculate corotated vectors as needed. In the implemented combined hardening subroutine for example, corotated back stresses are obtained by using the `ROTSIG` utility subroutine.

In Appendix A, the numerical implementation of the fully isotropic user material framework using linear strain hardening is provided. Given that the model developments in subsequent chapters include temperature and rate effects, as well as solution dependent state variables, provision is already made within the general framework. The `NSTATV` state variables in the `STATEV` array is first duplicated into a temporary `TEMPSTATV` array. A shear modulus is then determined from a `SHEARMOD` subroutine before the trial elastic state is determined and elastic material consistent tangent is assembled.

Given the initial assumption that the equivalent plastic strain increment is zero, the yield stress is evaluated using the `FISOTROPIC` subroutine for the isotropic case. This subroutine takes the equivalent plastic strain increment, time increment, temperature as well as the material property and state variable arrays as input and returns the isotropic yield stress σ_{Y} as well as the sensitivity $\mathcal{K}$ in Equation (2.61). It also potentially updates the temporary state variables as required.

If the yield condition is violated, the implementation uses Newton-Raphson to determine the equivalent plastic strain increment as given in Equation (2.57). The stress vector is updated using the yield stress and hydrostatic pressure while the consistent tangent matrix `DDSDDE` is updated according to Equation (2.74) in the presence of plastic flow. Upon convergence, the state variable array is updated to take the values of the converged temporary state variable array.

The linear isotropic strain hardening implementation in Appendix A requires four material properties (`NPROPS`=4) given as input by the `PROPS` array. The first two material properties are the shear modulus μ and Poisson's ratio ν, followed by the initial yield stress σ_0 and linear strain hardening modulus K. The `SHEARMOD` subroutine simply returns the property values subject to $\nu \leq 0.4999$ in this case since the shear modulus is assumed to be temperature independent. The `FISOTROPIC` subroutine first

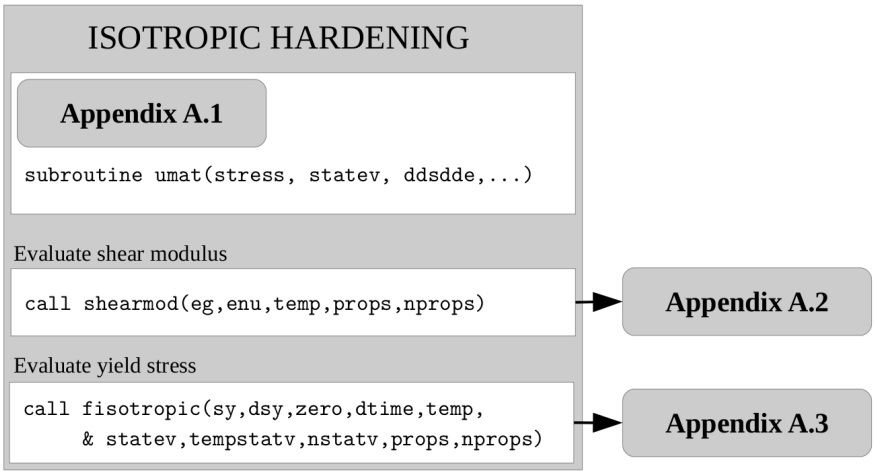

Figure 2.10: The isotropic hardening user material.

calculates the total equivalent plastic strain before calculating the yield stress. The total equivalent plastic strain at the start of the increment is stored in the first entry of the state variable array and at the end of the increment in `TEMPSTATV`.

A simple flow chart showing the location of the subroutines called by the isotropic hardening user material in Appendix A.1 is given in Figure 2.10. In the linear work hardening case for this chapter, the user material framework calls the subroutines in Appendix A.2 and Appendix A.3. In subsequent chapters, calls to the `SHEARMOD` and `FISOTROPIC` subroutines are associated with different files. In each new development, an updated layout will accompany the explanation to convey the modular implementation of the framework.

The combined hardening material framework is provided in Appendix B. As in the isotropic case, the state variables are again updated from a temporary state variable array while the `SHEARMOD` subroutine also accommodates a temperature dependent shear modulus. In the combined hardening case, the first `NDI+NSHR` entries in the `STATEV` and `TEMPSTATV` arrays contain the back stresses, corotated using the `ROTSIG` utility subroutine over the rotation increment `DROT`. A subroutine `CYCLREVERSAL` is introduced here to act on the state variables if cyclic reversal occurs. Load reversal is checked in the current implementation by comparing the dot product of the current effective stress and converged effective stress of the previous iteration or time step.

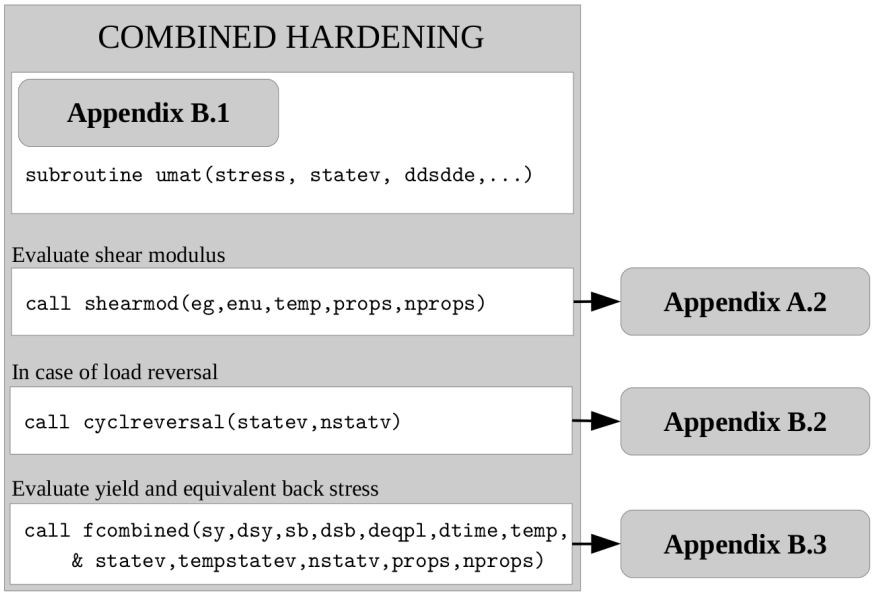

Figure 2.11: The combined hardening user material.

Instead of the `FISOTROPIC` subroutine in the isotropic hardening case, the combined hardening subroutine calls an `FCOMBINED` subroutine. Within `FCOMBINED`, the isotopic yield stress σ_{Y} and sensitivity $\mathcal{K}$ is determined as well as the back stress σ_{B} and equivalent plastic strain sensitivity $\mathcal{H}$. As in the isotropic case, it also potentially updates the temporary state variables.

The linear combined strain hardening implementation in Appendix B requires five material properties (`NPROPS`=5) given as input by the `PROPS` array. The first four are the same as in the isotropic case while the fifth material property is the linear hardening modulus for the equivalent back stress $\mathcal{H}$. Given that the first six entries in the state variable arrays are used for the back stresses in the three dimensional case, the total equivalent plastic strain is stored in the seventh entry for the combined linear hardening implementation in Appendix B. As in the isotropic case, Figure 2.11 shows a layout of the appended subroutines called by the combined user material.

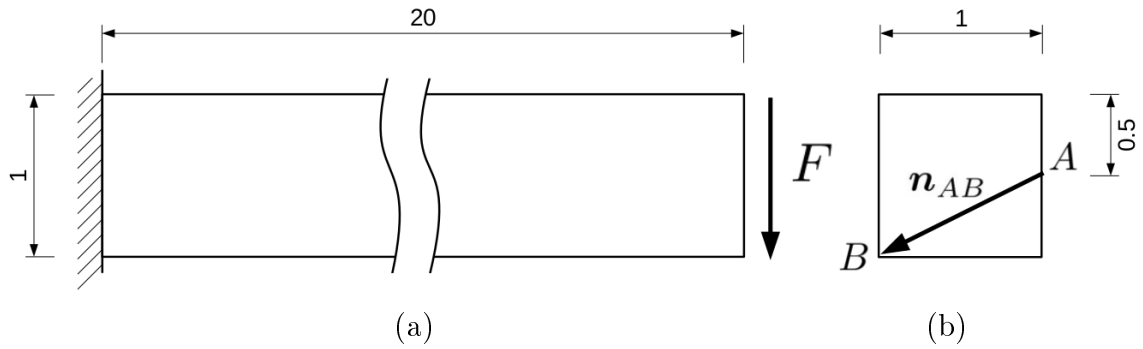

Figure 2.12: (a) The slender beam test problem with fixed and surface traction boundary conditions. (b) The direction of the traction force is defined by two nodes A and B on the traction surface.

2.4 Material Framework Verification

To verify the user material subroutines implemented in Appendix A and B, a simple test problem is simulated in Abaqus and compared using the internal plastic formulation and user material subroutines. The test problem is modelled using only isotropic hardening and only kinematic hardening. The difference in response illustrates two extremes of material modelling to highlight the importance and effect of each mechanism. The aim of this section is to quantify the response of each hardening mechanism in isolation, and in addition to verify the UMAT responses against the built in responses.

A slender beam with a square section of 1×1mm and a length of 20mm is modelled with 160 eight noded brick elements. Each element has an initial dimension of $0.5 \times 0.5 \times 0.5$mm. The one side of the beam is fixed while the other side is subjected to a transient surface traction as illustrated in Figure 2.12(a). The traction direction is defined by two nodes on the traction surface labelled A and B in Figure 2.12(b). The initial direction of the traction force is in the $\{x, y, z\}$ direction $\{0, -0.447214, 0.894427\}$.

The test problem is evaluated over a 200s period using automatic time stepping with a maximum time step size of 1s. The magnitude of the periodic surface traction starts at 0N, ramping linearly to 1N at 50s before reversing to -1N at 150s and then the traction is removed again so that it has a magnitude of 0N at 200s which is the end of the analysis. The magnitude of the traction force over time is plotted in Figure 2.13.

The purely isotropic user material subroutine is tested using a shear modulus value

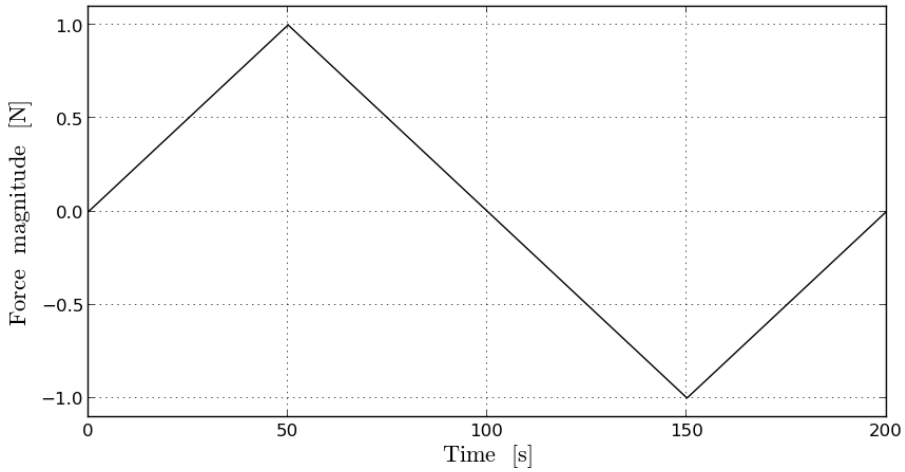

Figure 2.13: Magnitude of the traction force

of $\mu = 4$GPa and Poisson's ratio $\nu = 0.25$ along with an initial yield stress $\sigma_0 = 50$MPa and linear strain hardening modulus $K = 100$MPa. The results are compared to an Abaqus simulation using the `*ELASTIC` card and values of 10GPa for the Elastic modulus $E = 2\mu(1+\nu)$ and $\nu = 0.25$. The `*PLASTIC` card is then used where the response is defined using the two points $(50., 0.)$ and $(150., 1.)$ for the stress as a function of equivalent plastic strain.

The implementation of the combined hardening user subroutine is tested for the kinematic hardening case using a material with the same elastic properties, but yield defined using an initial yield stress $\sigma_0 = 50$MPa, linear strain hardening modulus $K = 0$MPa and linear hardening modulus for the back stress $H = 100$MPa. The Abaqus input file for the isotropic case is modified by simply changing the `*PLASTIC` card to `*PLASTIC,HARDENING=KINEMATIC` and leaving the definition of the stress as a function of equivalent plastic strain as well as the rest of the input file as is.

In Figures 2.14 to 2.23, the equivalent von Mises stresses are displayed on the deformed beam for the isotropic and kinematic hardening cases using the built in Abaqus plasticity formulations. At the start of the simulation, the beam is stress and deformation free. At 30s the force magnitude is 0.6N and the beam has experienced little deformation as visible in Figure 2.14. The base of the beam then acts as a plastic hinge so that the beam undergoes a large amount of deformation up to the 50s/1N

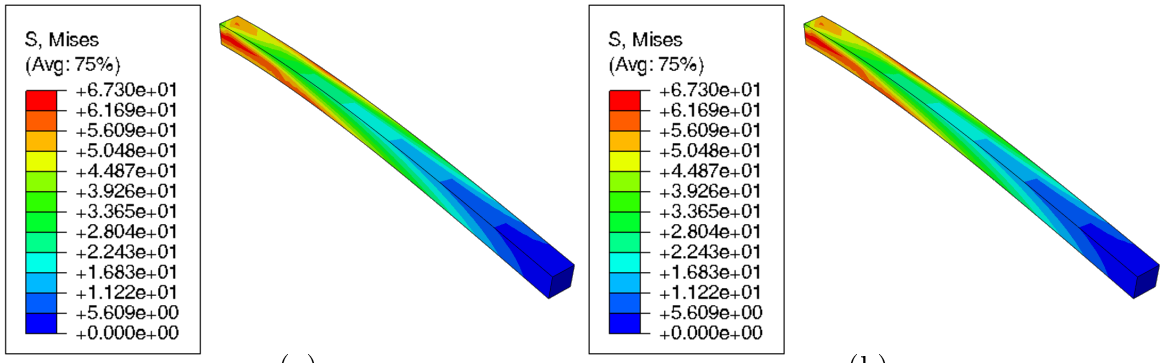

(a) (b)

Figure 2.14: Verification example at 30s for the (a) Isotropic and (b) Kinematic Case

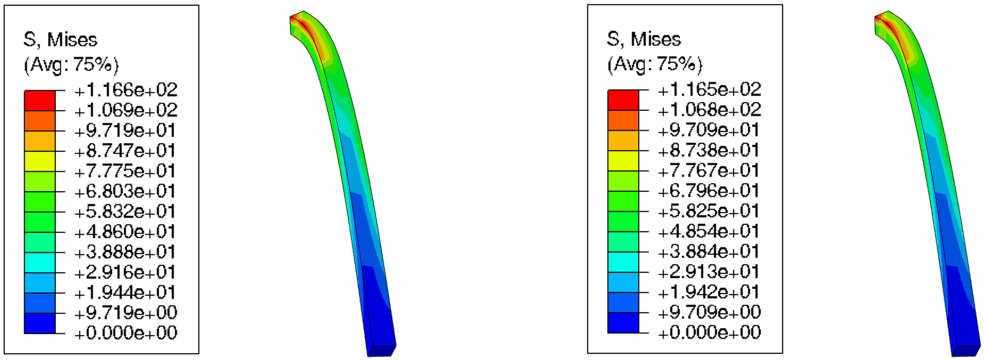

(a) (b)

Figure 2.15: Verification example at 40s for the (a) Isotropic and (b) Kinematic Case

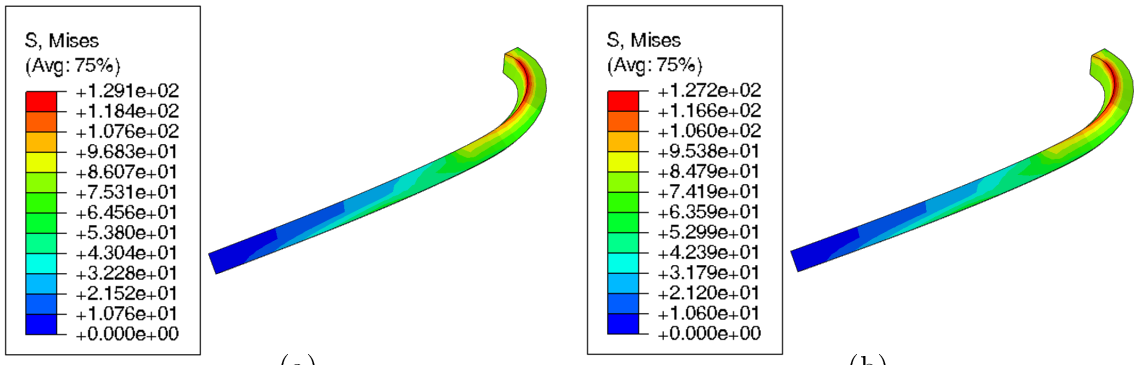

(a) (b)

Figure 2.16: Verification example at 50s for the (a) Isotropic and (b) Kinematic Case

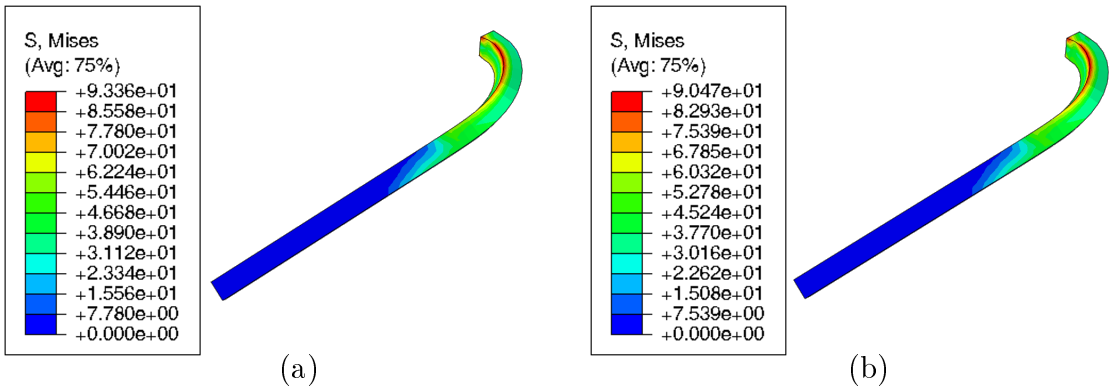

Figure 2.17: Verification example at 100s for the (a) Isotropic and (b) Kinematic Case

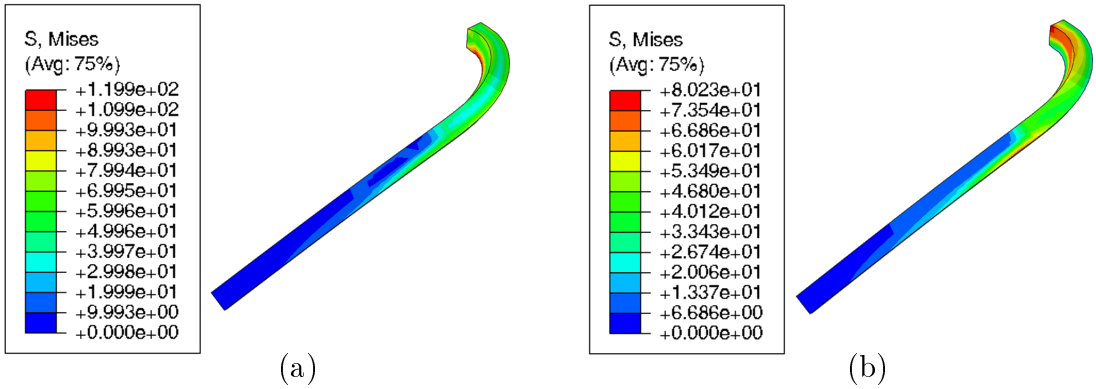

Figure 2.18: Verification example at 120s for the (a) Isotropic and (b) Kinematic Case

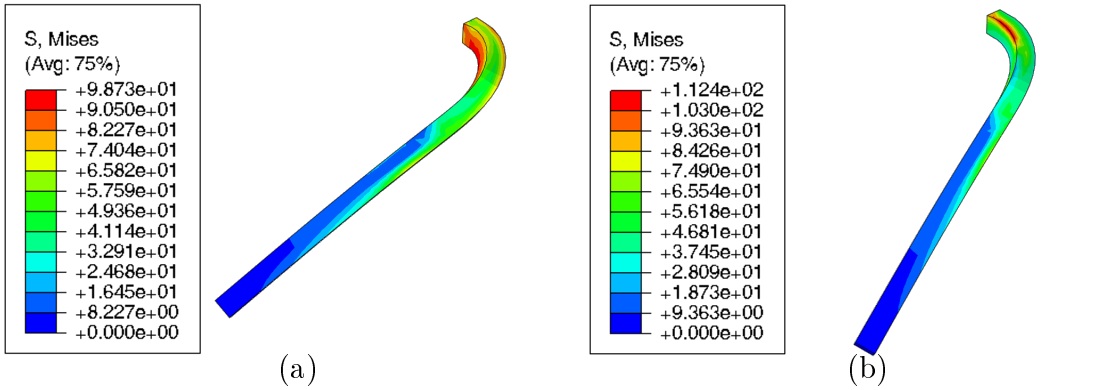

Figure 2.19: Verification example at 130s for the (a) Isotropic and (b) Kinematic Case

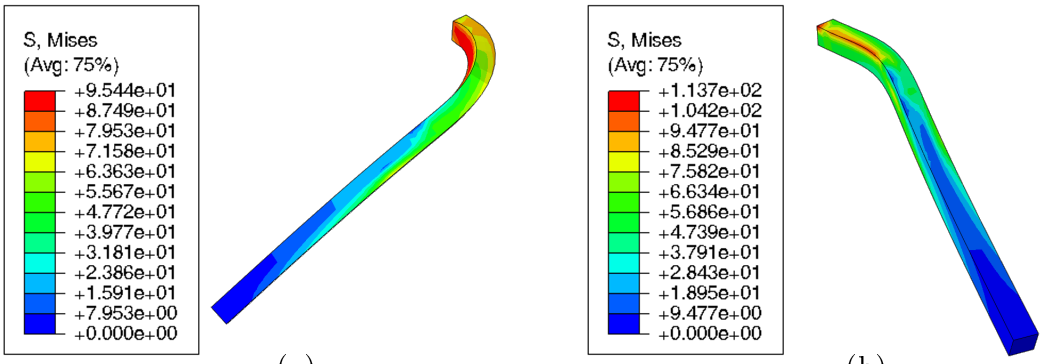

Figure 2.20: Verification example at 135s for the (a) Isotropic and (b) Kinematic Case

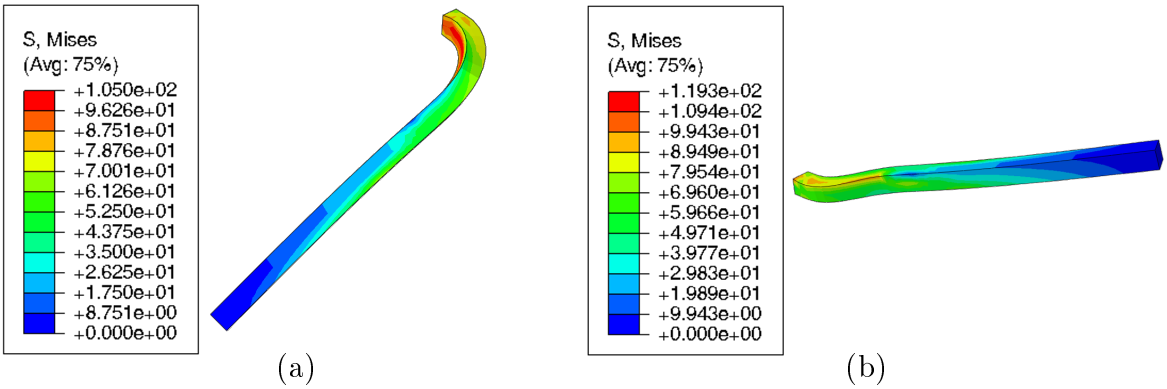

Figure 2.21: Verification example at 140s for the (a) Isotropic and (b) Kinematic Case

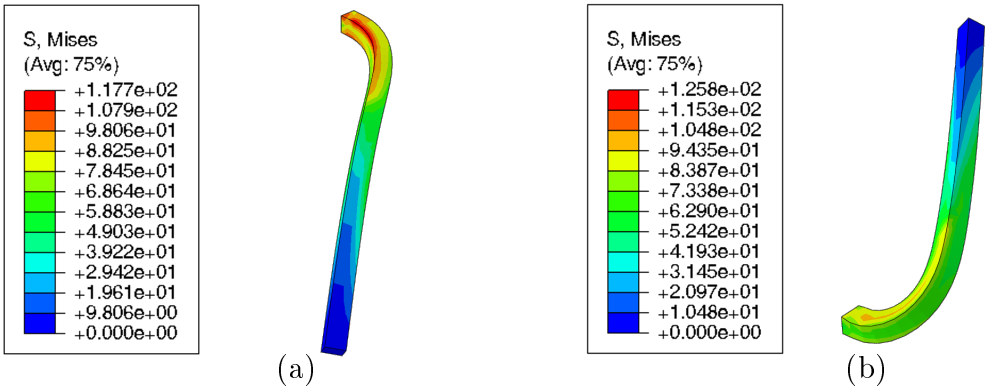

Figure 2.22: Verification example at 150s for the (a) Isotropic and (b) Kinematic Case

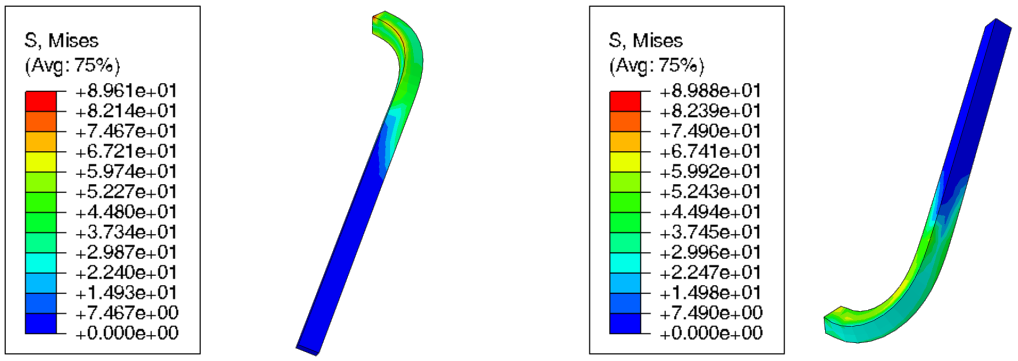

(a) (b)

Figure 2.23: Verification example at 200s for the (a) Isotropic and (b) Kinematic Case

mark as seen when comparing Figures 2.15 and 2.16. At 100s in Figure 2.17, the residual force has been completely removed. The maximum von Mises stress from the scalar bar in Figure 2.17(a) is 93.36MPa in the isotropic case compared to 90.47MPa in Figure 2.17(b) meaning the results are not exactly the same in the isotropic and kinematic cases. Up to this point, an increasing von Mises yield surface versus a shifting yield surface results in similar results.

The load is reversed from 100s in Figure 2.18 to the 150s mark in Figure 2.22. The response upon load reversal differs significantly when comparing the two cases. The isotropic hardening reduces the probability of further plastic deformation lower due to the growing yield surface, whereas the kinematic hardening case has a lower yield value upon load reversal and a plastic hinge is again responsible for the severe deformation in the opposite direction as seen in Figures 2.19 to 2.22. At 200s, the surface traction is again removed resulting in the final deformed beams in Figure 2.23.

The solutions using the implemented user materials are obtained and compared to the Abaqus solution. The objectivity of the implementation is also checked by solving a rotated version of the problem using the user materials. In this case an x axis rotation of $-30°$

$$R_x\left(-30°\right) = \begin{bmatrix} 1 & 0 & 0 \\ 0 & \cos\left(-30°\right) & -\sin\left(-30°\right) \\ 0 & \sin\left(-30°\right) & \cos\left(-30°\right) \end{bmatrix} = \begin{bmatrix} 1 & 0 & 0 \\ 0 & 0.866 & 0.5 \\ 0 & -0.5 & 0.866 \end{bmatrix} \tag{2.89}$$

is applied to both the purely isotropic and purely kinematic test problems before performing the simulation.

In Figure 2.24, the equivalent plastic strains at the end of the simulation using the (a) internal formulation and (b) user material subroutine are compared. In Figure 2.24(c), the equivalent plastic strain using the user material subroutine on the rotated problem is presented. The maximum equivalent plastic strain in Figures 2.24(a) is 0.5090 compared to 0.5091 in Figures 2.24(b) and again 0.5090 in Figures 2.24(c). Apart from this very slight variation, the contours are essentially the same in the three cases.

In Figure 2.25, the equivalent plastic strains at the end of the simulation using the (a) internal formulation and (b) user material subroutine are again compared for the kinematic hardening case. Figure 2.25(c) again presents the equivalent plastic strain using the user material subroutine on the rotated problem. Here, the maximum equivalent plastic strain values of 0.9304, 0.9304 and 0.9305 and contours are again essentially the same in the three cases with only slight variations.

The displacement of the centre of the surface traction tip over the entire 200s is plotted in Figure 2.26 for the isotropic hardening case. The black dots are the values of the displacement components at the various time steps using the internal Abaqus material formulation while the lines represent the three components of the displacement vector over time using the user material subroutine. In Table 2.4, the final displacement values in Figure 2.26 as well as those for the rotated problem are given. Comparing the user material to the internal Abaqus solution, there is a 0.0394% difference while there is a 0.0007% difference when the rotated problem is compared to the Abaqus solution.

Considering the comparisons in Figures 2.24 and 2.26 as well as the almost negligible

	ABAQUS	UMAT	$-30°$ ROTATED	
			Extracted	Back rotated
x Displacement	-11.109	-11.100	-11.109	-11.109
y Displacement	-8.9116	-8.9102	-0.7437	-8.9118
z Displacement	13.948	13.945	16.535	13.948

Table 2.4: Comparison of centre tip displacement over the simulation time for the isotropic material subroutine validation.

variation reported in Table 2.4, the isotropic user material subroutine implemented in Appendix A appears to be accurate and the integration objective for use in large deformation elastoplasticity.

The traction surface centre tip displacement over the entire 200s is also plotted for the kinematic hardening case in Figure 2.27. The black dots are the values of the displacement components at the various time steps using the internal Abaqus material formulation while the lines again represent the three components of the displacement vector over time, now using the user material subroutine implemented in Appendix B.

In Table 2.5, the final displacement values in Figure 2.27 as well as those for the rotated kinematic hardening case are given. Using the five significant numbers chosen to populate Table 2.27 , there is no visible variation between the solutions.

Considering the comparisons in Figures 2.25 and 2.27 as well as the virtually identical solutions reported in Table 2.5, the handling of kinematic effects are accurate and the integration is objective so that the user material subroutine may be used in large deformation elastoplasticity.

This section instills confidence in the implemented elastoplastic material framework for both the isotropic and kinematic strain hardening components. The framework serves as foundation for subsequent models developed in this thesis by simply replacing the linear strain hardening subroutines by a different `FISOTROPIC` or `FCOMBINED` subroutine. The material response is altered in the next chapter for example to include temperature and strain rate effects by implementing the Mechanical Threshold Stress model (Follansbee and Kocks, 1998).

	ABAQUS	UMAT	$-30°$ ROTATED	
			Extracted	Back rotated
x Displacement	-23.612	-23.612	-23.612	-23.612
y Displacement	8.4407	-8.4407	-0.1791	-8.4407
z Displacement	-14.976	-14.976	-17.189	-14.976

Table 2.5: Comparison of centre tip displacement over the simulation time for the kinematic material subroutine validation.

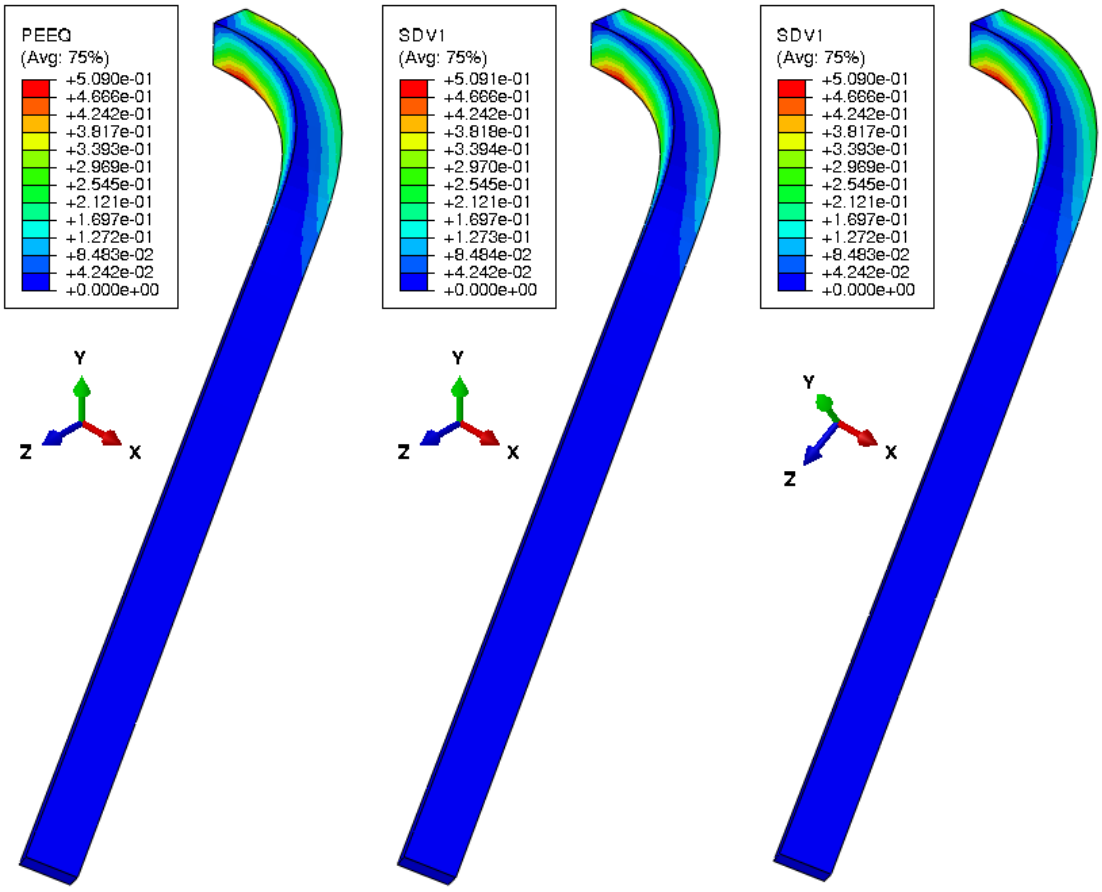

(a) (b) (c)

Figure 2.24: Equivalent plastic strains obtained using (a) the internal Abaqus isotropic hardening and (b) user material subroutine. (c) The rotated problem equivalent plastic strains using the user material.

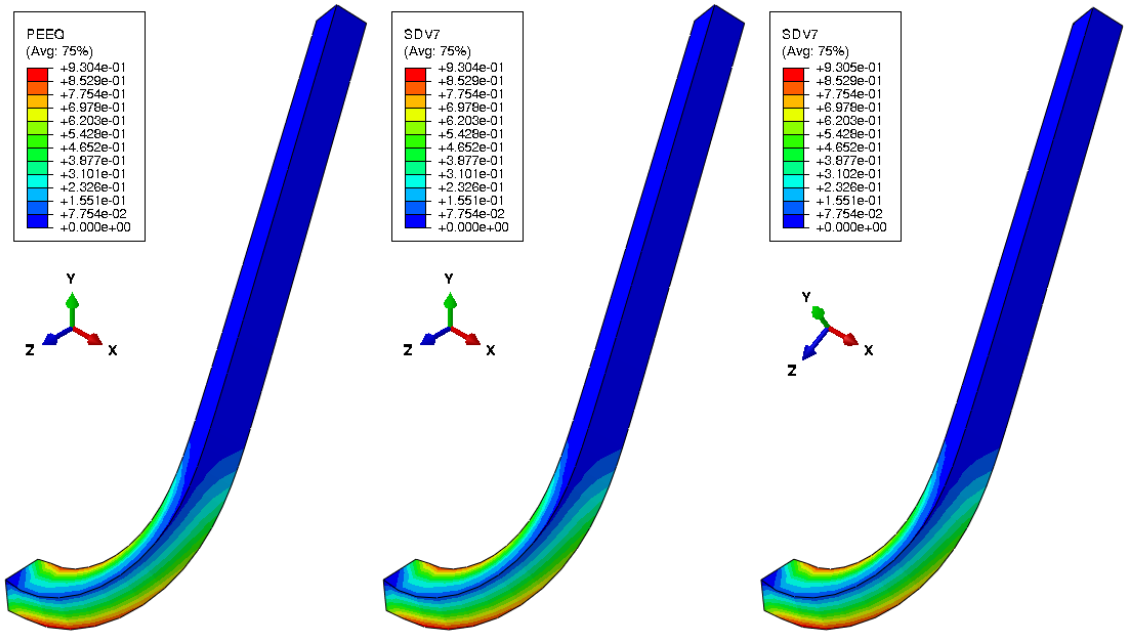

(a) (b) (c)

Figure 2.25: Equivalent plastic strains obtained using (a) the internal Abaqus kinematic hardening and (b) user material subroutine. (c) The rotated problem equivalent plastic strains using the user material.

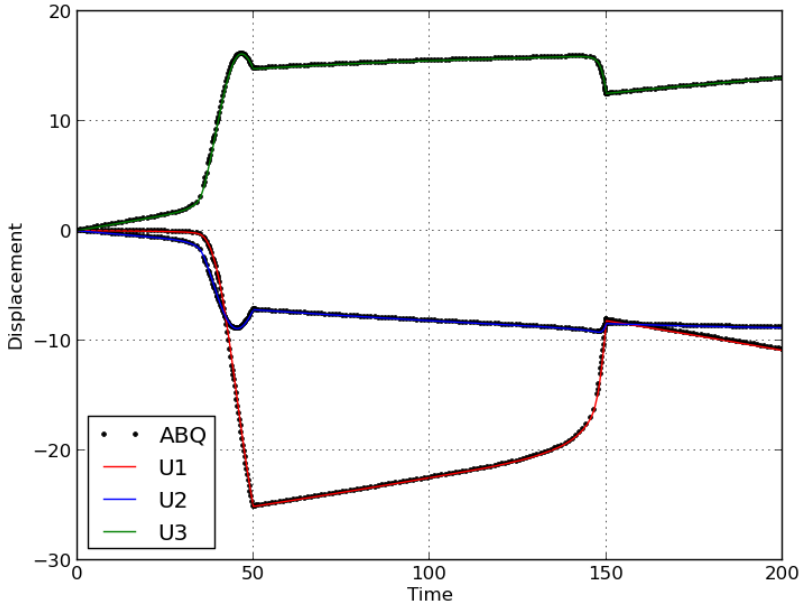

Figure 2.26: Centre tip displacement over the simulation time for the isotropic material subroutine validation.

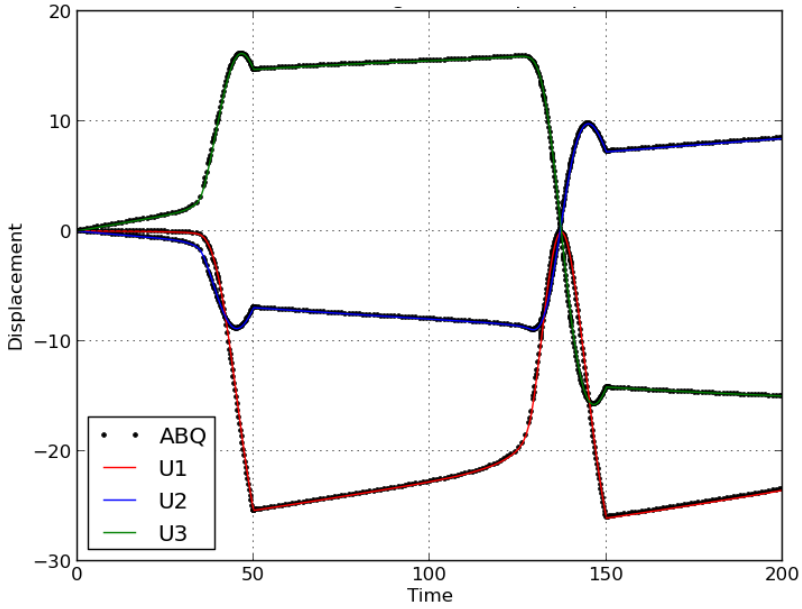

Figure 2.27: Centre tip displacement over the simulation time for the kinematic material subroutine validation.

Chapter 3

Temperature and Strain Rate Effects

In all the examples and implementation of Chapter 2, simple linear strain hardening or back stress evolution is used. Real metals however do not have a perfect transition from elastic to a linear strain hardening behaviour.

In this chapter, the development of the Mechanical Threshold Stress (MTS) model is discussed using material test data of Oxygen free high conductivity Copper (OFHC Cu) as an example. In Figure 3.1, some test data on OFHC Cu is demonstrated as obtained by Tanner et al. (1999). In their tests, material samples were compressed while maintaining a constant strain rate and temperature.

Figure 3.1 shows the material response for OFHC Cu at room temperature for strain rates of $0.0004s^{-1}$, $0.01s^{-1}$, $0.1s^{-1}$ and $1s^{-1}$; material responses at 134°C and 202°C for a strain rate of $0.0004s^{-1}$; and the material response at 269°C for a strain rate of $0.01s^{-1}$, $0.1s^{-1}$ and $1s^{-1}$ respectively. Although their data set is far more extensive, only these nine temperature and strain rate dependent response curves are used in the hardening range of interest in this chapter. The data curves used here are selected given that this chapter does not include very high strain rates (in the impact or ballistics range) or material softening effects (thermal recovery or recrystallisation). The Mechanical Threshold Stress model is described and implemented in this chapter as an extension to the isotropic user material framework implemented into an Abaqus user subroutine in Appendix A.

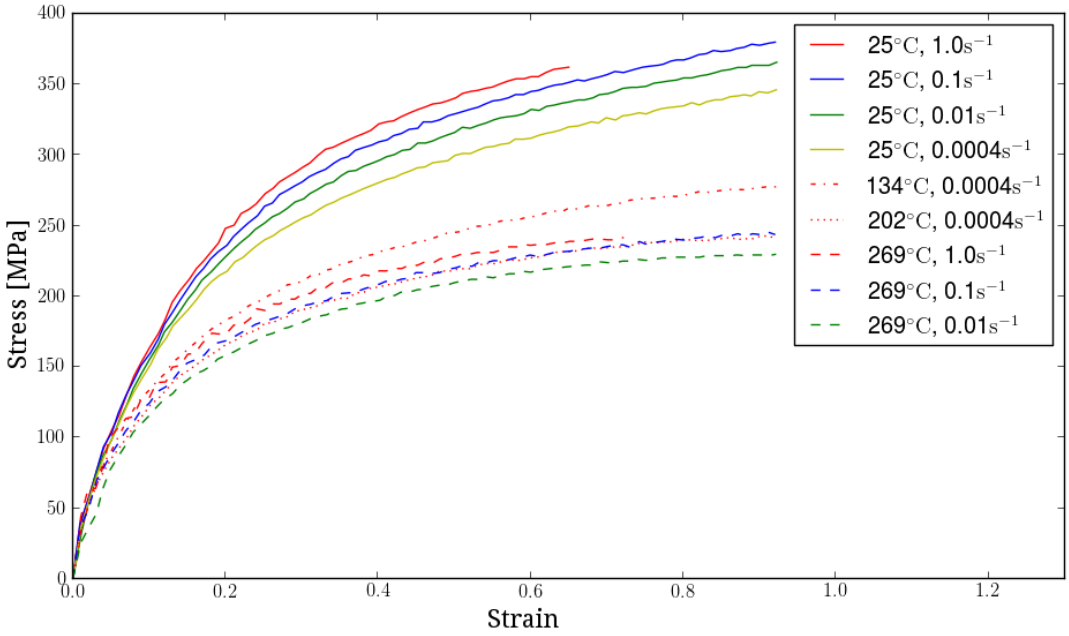

Figure 3.1: Oxygen free high conductivity Copper data obtained by Tanner et al. (1999).

3.1 The Kinetic Equation

Model specifics can first enter into play through a particular form of the kinetic equation. In the kinetic equation, equivalent plastic strain rate and the equivalent stress are related, reducing the problem of constitutive modelling to a scalar operation (Estrin, 1996). The role the kinetic equation plays in the model framework is explained by referring back to Equation (2.47)

From the work by Kocks (1976), a suitable mathematical form for $h(\bullet)$ in Equation (2.47) is the power-law. If $\dot{\alpha}$ represents the equivalent plastic strain rate $\dot{\bar{\varepsilon}}^{\mathrm{p}}$, then

$$\dot{\alpha} = \dot{\varepsilon}_0 \left(\frac{\sigma}{\hat{\sigma}} \right)^m . \tag{3.1}$$

In Equation (3.1), $\hat{\sigma}$ is an internal stress like variable representing the material state or threshold stress. This internal state variable can be dependent on temperature, incremental plastic strain or other internal variables of state. The equation also contains two additional material parameters $\dot{\varepsilon}_0$ and m. The factor $\dot{\varepsilon}_0$ is proportional to the

density of mobile dislocations and can be modelled as a constant (Estrin and Mecking, 1984; Kocks, 1976, 1987; Mecking and Kocks, 1981).

Considering the thermodynamics and kinetics of slip, Kocks et al. (1975) models m using

$$m = \frac{V\sigma}{k_{\mathrm{B}}T}. \tag{3.2}$$

The temperature dependence of the plastic strain rate is then included with V the activation volume, k_{B} the Boltzmann constant and T the absolute temperature.

In the work by Follansbee and Kocks (1998), an alternate variant of the kinetic equation in Equation (3.1), in which the Arrhenius form is preserved is

$$\dot{\alpha} = \dot{\varepsilon}_0 \exp\left[-\frac{\triangle G_0}{k_{\mathrm{B}}T}\left(1 - \left(\frac{\sigma}{\hat{\sigma}}\right)^p\right)^q\right]. \tag{3.3}$$

Here, $\triangle G_0$ is the value of the Gibbs free activation energy at zero stress while the exponents p and q are statistical constants that characterise the shape of the obstacle profile ($0 \leq p \leq 1$, $1 \leq q \leq 2$). The exponents provide the required shape of the equivalent plastic strain rate versus stress curve.

Given that the microstructure evolves during plastic deformation, a separate equation is needed to model the evolution of $\hat{\sigma}$. In general form following Kocks (1976), this can be written as

$$\frac{d\hat{\sigma}}{d\alpha} = \theta(\hat{\sigma}, \dot{\alpha}, T). \tag{3.4}$$

The introduction of this microstructural evolution equation suggests that the rate of change in $\hat{\sigma}$ is affected by its current value subject to some rate and temperature sensitivity. A concrete form of the evolution of $\hat{\sigma}$ completes the constitutive formulation.

3.2 Kocks-Mecking work hardening

The development of the microstructure evolution equation in Equation (3.4) associated with the Mechanical Threshold Stress model starts with reviewing the Kocks-Mecking work hardening theory (Kocks et al., 1975; Kocks, 1976; Mecking, 1977). Dislocation density, ρ, is introduced as a microstructural variable of state through the introduction of the threshold stress with the relationship

$$\hat{\sigma} = \frac{1}{2} M \mu_r b \sqrt{\rho}. \tag{3.5}$$

Here, M is the average Taylor factor that accounts for the polycrystallinity of the material (Kocks, 1976). $M = \sigma/\tau = \gamma^{\mathrm{p}}/\varepsilon^{\mathrm{p}}$ relates the shear stress τ and plastic shear strain γ^{p} to the axial stress σ and axial plastic strain ε^{p}. We however use α and $\dot{\alpha}$ for the scalarised equivalent plastic strain and strain rate instead of the one dimensional values ε^{p} and $\dot{\varepsilon}^{\mathrm{p}}$, so in this case $M\alpha = \gamma^{\mathrm{p}}$.

In Equation (3.5), μ_r is a reference value of the elastic shear modulus and b is the length of the Burger's vector. The evolution of the threshold stress in the presence of plastic strain is developed from the evolution of the dislocation density.

The two main occurrences in the evolution of dislocation density is storage ($d\rho^{(+)}$) and recovery ($d\rho^{(-)}$), either with respect to a plastic strain increment or time. The general form of an infinitesimal incremental change in dislocation density is expressed here as

$$d\rho = \sum d\rho^{(+)} - \sum d\rho^{(-)}. \tag{3.6}$$

It is possible to have multiple storage and recovery terms to account for the various mechanisms of dislocation density evolution. In this chapter however, only the two main terms associated with the storage and recovery of forest dislocations are covered.

The first observation regarding the evolution of dislocation density is the assumption that a mobile dislocation moves, on average, a distance L (the mean free path) before it is either immobilised or annihilated. This mean free path is assumed much smaller than the grain size of the material. The storage term considering this observation can be expressed by noticing that a shear strain increment $d\gamma^{\mathrm{p}} = M d\alpha$ can be expressed in terms of an immobilisation of mobile dislocations after travelling the distance of the mean free path $bLd\rho$. A storage increment in the dislocation density with respect to a plastic strain increment is therefore given by

$$d\rho^{(+)} = \frac{M}{bL}\, d\alpha. \tag{3.7}$$

The mean free path between obstacles in this modelling approach is considered as a statistical measure of forest dislocations and is proportional to obstacle spacing,

resulting in a possible modification of the storage term to

$$d\rho^{(+)} = Mk_1\sqrt{\rho}\, d\alpha \tag{3.8}$$

where k_1 is a constant that accounts for the proportionality of $L \propto 1/\sqrt{\rho}$.

Dislocations are stored on the glide plane at impenetrable obstacles. They are assumed to be annihilated when they leave the glide plane. The source of these annihilations is either the cross-slip of screw dislocations or the climb of edge dislocations. According to Estrin (1996), the cross-slip of screw dislocations is more prevalent at low temperature ranges while the climb of edge dislocations is more prevalent in the high temperature range that starts somewhere between half and two thirds of the material melting temperature. During the deformation of moderate to low Stacking Fault Energy (SFE) materials, like OFHC Copper, cross-slip onto different glide planes are inhibited by dislocations (Chaboche, 2008). This means that in some cases the observed annihilation of dislocations may in fact be attributed to different deformation mechanisms. Use of the Kocks-Mecking theory and model derivatives in this thesis does not take into account the explicit role of Stacking Fault Energy in the material crystalline structure. Material parameters can be tuned to get as close as possible to an observed material response even if the exact deformation mechanism is not explicitly modelled or taken into account.

Dislocation annihilation reactions result in dynamic recovery rates that is quadratic in dislocation density with respect to the time derivative while it is linear in ρ in terms of a derivative with respect to strain (Estrin, 1996). A dynamic recovery component in the incremental dislocation density evolution equation can be included as

$$d\rho^{(-)} = Mk_2(\dot{\alpha}, T)\, \rho\, d\alpha. \tag{3.9}$$

The recovery coefficient k_2 is strain rate and temperature dependent. Combining Equations (3.8) and (3.9), the Kocks-Mecking work hardening theory is obtained for the evolution of dislocation density in the presence of plastic strain:

$$\frac{d\rho}{d\alpha} = Mk_1\sqrt{\rho} - Mk_2(\dot{\alpha}, T)\, \rho. \tag{3.10}$$

Nabarro et al. (1964) observed experimentally that the flow stress $\hat{\tau}$ at a given dislocation density, can be calculated for a specific temperature and strain rate through the equation

$$\hat{\tau} = \hat{\tau}_a + \alpha \mu_r b \sqrt{\rho}, \tag{3.11}$$

where $\hat{\tau}_a$ is the athermal portion of the flow stress. Through the relationship for the threshold stress in Equation (3.5), and the addition of a constant initial yield stress value $\hat{\sigma}_a = M\hat{\tau}_a$ at a given dislocation density, the yield stress σ_{Y} for a reference temperature and strain rate may be calculated using

$$\sigma_{\mathrm{Y}}(T) = \hat{\sigma}_a + \hat{\sigma}_T, \tag{3.12}$$

where $\hat{\sigma}_T$ is now the thermal component of the yield stress.

Again using the relationship in Equation (3.5), the evolution of the thermal component of the threshold stress in the presence of plastic strain is given by

$$\frac{d\hat{\sigma}_T}{d\alpha} = \frac{M\mu b}{4\sqrt{\rho}} \frac{d\rho}{d\alpha}. \tag{3.13}$$

Now substituting Equation (3.10):

$$\frac{d\hat{\sigma}_T}{d\alpha} = \frac{M^2 \mu b k_1}{4} - \frac{M^2 \mu b k_2(\dot{\alpha}, T)\sqrt{\rho}}{4}, \tag{3.14}$$

or in terms of the thermal component of the threshold stress:

$$\frac{d\hat{\sigma}_T}{d\alpha} = \frac{M^2 \mu b k_1}{4} - \frac{M k_2(\dot{\alpha}, T)\hat{\sigma}_T}{2}. \tag{3.15}$$

If the new parameters

$$\theta_0 = \frac{M^2 \mu b k_1}{4} \qquad \text{and} \qquad \hat{\sigma}_s(\dot{\alpha}, T) = \frac{2\theta_0}{M k_2(\dot{\alpha}, T)} \tag{3.16}$$

are introduced, Equation (3.15) can be written in terms of the Voce-law (Kocks et al., 1998; Mourad et al., 2013)

$$\frac{d\hat{\sigma}_T}{d\alpha} = \theta_0 \left(1 - \frac{\hat{\sigma}_T}{\hat{\sigma}_s}\right) \tag{3.17}$$

where θ_0 is now the initial hardening rate and $\hat{\sigma}_s(\dot{\alpha}, T)$ is the temperature and strain rate dependent saturation stress.

3.3 The Mechanical Threshold Stress Model

The Mechanical Threshold Stress (MTS) model (Follansbee and Kocks, 1998) was developed to describe the post yielding behaviour of metals. It has demonstrated the ability to accurately model the effect of temperature and plastic strain rate on the post yielding behaviour of metals.

In the MTS model, the internal material variable representing the material state ($\hat{\sigma}$) is regarded as the mechanical threshold as explained in the previous subsection. This threshold value represents a theoretical maximum flow stress at 0K. The material flow stress, σ_{Y}, is obtained in this framework by scaling the mechanical threshold to accommodate rate and temperature dependence. The yield stress in Equation (3.12) was for a specific reference or threshold temperature. The MTS model on the other hand uses temperature and rate dependent scaling factors to construct an expression for the yield stress over a range of temperatures and strain rates.

Following Equation (3.11), the threshold flow stress is separated into an athermal $\hat{\sigma}_a$ and k different thermal components $\hat{\sigma}_T^k$,

$$\hat{\sigma} = \hat{\sigma}_a + \sum_k \hat{\sigma}_T^k. \tag{3.18}$$

The athermal component $\hat{\sigma}_a$ characterises the rate-independent interactions of dislocations with long-range barriers. The thermal components $\hat{\sigma}_T^k$ characterise the rate-dependent interactions of dislocations with short-range obstacles that can be overcome with the assistance of thermal activation (Follansbee and Kocks, 1998).

At different temperatures T and plastic strain rates $\dot{\alpha}$, the contributions to the flow stress σ_k are related to their threshold counterparts $\hat{\sigma}_k$ through the scaling functions $S_k(\dot{\alpha}, T)$, so that

$$\sigma_k = \hat{\sigma}_k \frac{\mu(T)}{\mu_r} S_k(\dot{\alpha}, T). \tag{3.19}$$

Here, $\mu(T)$ and μ_r indicate the current and reference shear modulus values. The inter-

action kinetics for short-range obstacles are described using an Arrhenius expression while a phenomenological relation is used for the free energy function of stress (Kocks et al., 1975).

Considering the scaling relationship between the flow stress and theoretical threshold values of a material, the equivalent flow stress σ_{Y} is expressed as

$$\frac{\sigma_{\mathrm{Y}}}{\mu} = \frac{\hat{\sigma}_a}{\mu} + \sum_k \frac{\sigma_k}{\mu} = \frac{\hat{\sigma}_a}{\mu} + \sum_k S_k(\dot{\alpha}, T)\frac{\hat{\sigma}_k}{\mu_r}. \tag{3.20}$$

In this model implementation, the same model to describe the temperature dependence of the shear modulus is used as previously applied in conjunction with the Kocks-Mecking work hardening theory (see for example Goto et al., 2000; Kok et al., 2002 and Banerjee, 2007). The temperature dependence of the shear modulus is expressed using the model developed by Varshni (1970), which reads

$$\mu(T) = \mu_r - \frac{D_r}{\exp\left({}^{T_r}/_{T}\right) - 1}. \tag{3.21}$$

Here μ_r, D_r are empirically obtained parameters. T_r has to be well below the temperatures used while T is the absolute temperature.

The scaling functions of the threshold stress components $S_k(\dot{\alpha}, T)$ are derived from the kinetic equation in Equation (3.3) and take the form

$$S_k(\dot{\alpha}, T) = \left[1 - \left(\frac{k_{\mathrm{B}}T}{g_{0k}\mu b^3}\ln\frac{\dot{\varepsilon}_{0k}}{\dot{\alpha}}\right)^{1/q_k}\right]^{1/p_k}, \tag{3.22}$$

where g_{0k} is the normalised activation energy for dislocations to overcome the obstacles. In the standard MTS model there are two thermal components, i.e. $\hat{\sigma}_k$, $k = 1, 2$. Using the notation $\hat{\sigma}_1 = \hat{\sigma}_i$ and $\hat{\sigma}_2 = \hat{\sigma}_\varepsilon$, the flow stress relation in Equation (3.20) changes to

$$\frac{\sigma_{\mathrm{Y}}}{\mu} = \frac{\hat{\sigma}_a}{\mu} + S_i(\dot{\alpha}, T)\frac{\hat{\sigma}_i}{\mu_r} + S_\varepsilon(\dot{\alpha}, T)\frac{\hat{\sigma}_\varepsilon}{\mu_r}. \tag{3.23}$$

In Equation (3.23), $\hat{\sigma}_i$ describes the non-evolving thermal portion of the yield stress and $\hat{\sigma}_\varepsilon$ describes the evolving interaction of mobile dislocations with the forest dislocation structure.

While Equation (3.23) describes the kinetics of the Mechanical Threshold Stress framework, an equation for the evolution of $\hat{\sigma}_\varepsilon$ is needed to complete the constitutive formulation. With $\hat{\sigma}_\varepsilon$ the evolving component of the threshold stress, the extension to the general form of Equation (3.4) is

$$\frac{d\hat{\sigma}_\varepsilon}{d\alpha} = \theta(\hat{\sigma}_\varepsilon, \dot{\alpha}, T) = \theta_0 - \theta_r(\hat{\sigma}_\varepsilon, \dot{\alpha}, T), \tag{3.24}$$

where θ_0 is now the hardening due to dislocation accumulation and θ_r is the dynamic recovery rate. The functional form of the hardening rate θ can be chosen to fit experimental data. Using the Kocks-Mecking theory of the previous subsection, Equation (3.24) can have the functional form of the Voce law in Equation (3.17). Popular choices for alternative formulations as used by Chen and Gray (1996), Follansbee and Kocks (1998) as well as Goto et al. (2000) is the hyperbolic tangent or power law forms

$$\theta = \theta_0 \left(1 - \frac{\tanh\left[\frac{a\hat{\sigma}_\varepsilon}{\hat{\sigma}_{\varepsilon s}}\right]}{\tanh(a)}\right) \qquad \text{or} \qquad \theta = \theta_0 \left(1 - \frac{\hat{\sigma}_\varepsilon}{\hat{\sigma}_{\varepsilon s}}\right)^a. \tag{3.25}$$

The parameter a is a fitted constant with $a = 1$ applied to the second formulation resulting in Equation (3.17). θ_0 assumes the role of the initial hardening rate and $\hat{\sigma}_{\varepsilon s}(\dot{\alpha}, T)$ is the threshold saturation stress as defined by the Kocks-Mecking theory in Equation (3.16). The hardening rate θ decreases with strain and saturates. Following the work of Chen and Gray (1996), the threshold saturation stress $\hat{\sigma}_{\varepsilon s}(\dot{\alpha}, T)$ is a function of both strain rate and temperature, through

$$\ln \frac{\dot{\alpha}}{\dot{\varepsilon}_{0\varepsilon s}} = \frac{g_{0\varepsilon s}\mu b^3}{k_{\mathrm{B}} T} \ln \frac{\hat{\sigma}_{\varepsilon s}}{\hat{\sigma}_{0\varepsilon s}}, \tag{3.26}$$

where $\dot{\varepsilon}_{0\varepsilon s}$, $g_{0\varepsilon s}$ and $\hat{\sigma}_{0\varepsilon s}$ are empirically obtained constants. Other formulations of the evolution equation are also possible within the Mechanical Threshold Stress model. Instead of a constant value, temperature and rate dependence can be included to the dislocation accumulation parameter as done by Mourad et al. (2013):

$$\theta_0 = A_0 + A_1 \log(\dot{\alpha}) + A_2\sqrt{\dot{\alpha}} - A_3 T + A_4 T^{-A_5}. \tag{3.27}$$

It is then also possible to extend the response beyond the saturation level by formally including stage IV hardening. One such modification used by Goto et al. (2000) is

$$\theta = \theta_0 \left[1 - \tanh\left(\frac{a\hat{\sigma}_\varepsilon}{\hat{\sigma}_{\varepsilon s}}\right)\right] + \theta_{IV} \tanh\left(\frac{a\hat{\sigma}_\varepsilon}{\hat{\sigma}_{\varepsilon s}}\right), \tag{3.28}$$

where a constant strain hardening rate of θ_{IV} is based on the experimental observation of linear hardening during stage IV.

3.4 Numerical Implementation

Extending the isotropic user material framework in Appendix A, the Mechanical Threshold Stress model is implemented numerically by the incrementally objective integration of the hypoelastic(visco)plastic constitutive equations similar to that of Mourad et al. (2013).

The temperature dependent shear modulus following Equation (3.21) is returned by calling the `SHEARMOD` subroutine presented in Appendix C.1. The elastic properties μ_r, D_r and T_r in Equation (3.21) as well as Poisson's ratio ν are passed to the material subroutine using the first four entries in the `PROPS` array of user defined material properties. The subroutine returns the shear modulus at the current temperature along with Poisson's ratio to evaluate the trial elastic state. For Equation (3.21) to return a valid shear modulus value, the current temperature should exceed the reference value $T > T_r$. A logical check is therefore coded so that should $T \leq T_r$, the reference shear modulus value is returned $\mu = \mu_r$.

The Mechanical Threshold Stress model is also implemented into an isotropic hardening subroutine `FISOTROPIC` that is called by the Abaqus user material subroutine in place of the linear hardening version of the previous chapter. The yield stress function `FISOTROPIC` for the MTS model is attached in Appendix C.2. Figure 3.2 shows the layout of the appended subroutines called by Appendix A.1 in this implementation.

As in the linear hardening case presented in the previous chapter, the trial elastic state is evaluated by assuming that there is no additional equivalent plastic strain in the current increment, i.e. $\delta\alpha = 0$. This means that an initial equivalent plastic strain rate $\dot{\alpha} = {}^{\delta\alpha}/_{\delta t} = 0$ would be assumed for the trial elastic stress state. A zero

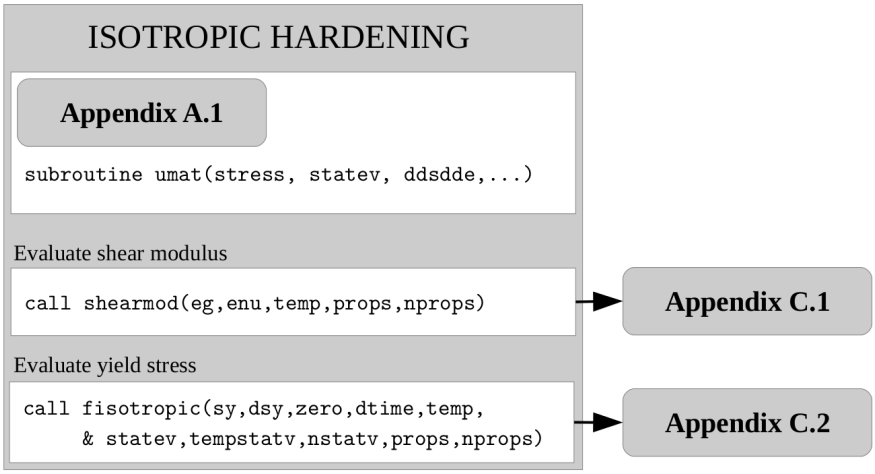

Figure 3.2: The Mechanical Threshold Stress isotropic hardening user material.

plastic strain rate assumption causes problems when evaluating the scaling functions in Equation (3.22). For this reason, the same reasoning as that of Mourad et al. (2013) is followed. In the numerical implementation of Appendix C, a minimum allowable equivalent plastic strain rate $\dot{\alpha}_{\min} = 10^{-10}$ is assigned. Given the incremental equivalent plastic strain and time step as inputs to the `FISOTROPIC` subroutine, the strain rate used in the calculations where needed is determined by

$$\dot{\alpha} = \max\left(\frac{\delta\alpha}{\delta t}, \dot{\alpha}_{\min}\right). \tag{3.29}$$

In addition to the strain increment and the time step to estimate the strain rate, `FISOTROPIC` is given the temperature at the end of the increment and a converged value for the evolving thermal stress component at the start of the increment $\hat{\sigma}_{\varepsilon}|_t$. It then computes and returns the candidate threshold stress value at the end of the increment $\hat{\sigma}_{\varepsilon}|_{t+\delta t}$, yield stress $\sigma_{\mathrm{Y}}|_{t+\delta t}$ and sensitivities. These values are determined using fully implicit backward Euler integration.

The numerical implementation uses a single state variable `STATEV(1)` = $\hat{\sigma}_{\varepsilon}|_t$ at the start of the increment. The converged value of the evolving thermal stress at the end of the current increment `TEMPSTATEV(1)` = $\hat{\sigma}_{\varepsilon}|_{t+\delta t}$ is then returned upon a call to the `FISOTROPIC` subroutine for the next iteration.

3.4.1 Determining the evolving thermal stress

Backward Euler implicit integration is first used to determine the value of the evolving thermal stress component ($\hat{\sigma}_\varepsilon$) at the end of a specific time step. The plastic strain rate, duration of the time increment and temperature over the time increment are taken into account. The evolving thermal stress component at time $t + \delta t$ is given by

$$\hat{\sigma}_\varepsilon|_{t+\delta t} = \hat{\sigma}_\varepsilon|_t + \delta\alpha\theta(\hat{\sigma}_\varepsilon|_{t+\delta t}, \dot{\alpha}|_{t+\delta t}, T|_{t+\delta t}) = \hat{\sigma}_\varepsilon|_t + \delta\alpha\ \theta|_{t+\delta t}\,. \tag{3.30}$$

In this implementation, the value of $\theta|_{t+\delta t}$ is computed from either the hyperbolic tangent or power law form of Equation (3.25) at the end of the increment into consideration. The implicit integration is done using Netwon-Raphson given an initial guess $\hat{\sigma}_\varepsilon|_{t+\delta t} = \hat{\sigma}_\varepsilon|_t$ and a residual equation based on Equation (3.30). The residual equation and derivative to solve the evolving thermal stress component are

$$\mathcal{R}_{\hat{\sigma}_\varepsilon} = \hat{\sigma}_\varepsilon|_{t+\delta t} - \hat{\sigma}_\varepsilon|_t - \delta\alpha\ \theta|_{t+\delta t} \qquad \text{and} \qquad \mathcal{D}\mathcal{R}_{\hat{\sigma}_\varepsilon} = 1 - \delta\alpha\ \left.\frac{d\theta}{d\hat{\sigma}_\varepsilon}\right|_{t+\delta t}\,. \tag{3.31}$$

If the hyperbolic tangent form of the hardening law in Equation (3.25) is chosen, the derivative of the hardening law with respect to the evolving thermal stress component is

$$\frac{d\theta}{d\hat{\sigma}_\varepsilon} = \frac{-a\theta_o}{\hat{\sigma}_{\varepsilon s}\tanh(a)\cosh^2\left(\frac{a\hat{\sigma}_\varepsilon}{\hat{\sigma}_{\varepsilon s}}\right)}. \tag{3.32}$$

In the power law case on the other hand, the derivative is

$$\frac{d\theta}{d\hat{\sigma}_\varepsilon} = \frac{-a\theta_0}{\hat{\sigma}_{\varepsilon s}}\left(1 - \frac{\hat{\sigma}_\varepsilon}{\hat{\sigma}_{\varepsilon s}}\right)^{a-1}\,. \tag{3.33}$$

3.4.2 Analytical Gradients

The sensitivity of the calculated yield stress using Equation (3.23), given a different equivalent plastic strain increment as input, is required to solve the equivalent plastic strain increment. This is done using Equations (2.57) and (2.58) in the user material framework implemented in Appendix A. From Equation (3.23), the yield stress at the

end of the current increment is

$$\sigma_{\mathrm{Y}}|_{t+\delta t} = \hat{\sigma}_a + \frac{\mu\left(T|_{t+\delta t}\right)}{\mu_r}\left(S_i|_{t+\delta t}\,\hat{\sigma}_i + S_\varepsilon|_{t+\delta t}\,\hat{\sigma}_\varepsilon|_{t+\delta t}\right). \tag{3.34}$$

The derivative of the yield stress with respect to the equivalent plastic strain increment can be determined from the chain rule

$$\frac{d\sigma_{\mathrm{Y}}}{d\delta\alpha} = \frac{\mu}{\mu_r}\left[\frac{\partial S_i}{\partial\dot{\alpha}}\frac{d\dot{\alpha}}{d\delta\alpha}\hat{\sigma}_i + \frac{\partial S_\varepsilon}{\partial\dot{\alpha}}\frac{d\dot{\alpha}}{d\delta\alpha}\hat{\sigma}_\varepsilon + S_\varepsilon\left(\frac{\partial\hat{\sigma}_\varepsilon}{\partial\delta\alpha} + \frac{\partial\hat{\sigma}_\varepsilon}{\partial\dot{\alpha}}\frac{d\dot{\alpha}}{d\delta\alpha}\right)\right], \tag{3.35}$$

where $d\dot{\alpha}/d\delta\alpha = 1/\delta t$ when $\delta\alpha > 0$ following from Equation (3.29).

The Arrhenius expression in Equation (3.22) is used for the MTS scaling functions. The partial derivatives of these scaling functions with respect to the equivalent plastic strain rate can be determined from

$$\frac{\partial S_k}{\partial\dot{\alpha}} = \frac{\Gamma_k}{p_k q_k\dot{\alpha}}\left[1 - \left(\Gamma_k \ln\left(\frac{\dot{\varepsilon}_{0k}}{\dot{\alpha}}\right)\right)^{\frac{1}{q_k}}\right]^{\frac{1-p_k}{p_k}}\left[\Gamma_k \ln\left(\frac{\dot{\varepsilon}_{0k}}{\dot{\alpha}}\right)\right]^{\frac{1-q_k}{q_k}} \tag{3.36}$$

with Γ_T^k given by

$$\Gamma_k = \frac{k_{\mathrm{B}}T}{g_{0k}\mu b^3}. \tag{3.37}$$

Given the implicit definition of the evolving thermal stress component at the end of the increment in Equation (3.30), the partial derivative with respect to the incremental equivalent plastic strain is

$$\frac{\partial\,\hat{\sigma}_\varepsilon|_{t+\delta t}}{\partial\delta\alpha} = \theta|_{t+\delta t} + \delta\alpha\frac{\partial\,\theta|_{t+\delta t}}{\partial\delta\alpha}. \tag{3.38}$$

Now, using the chain rule

$$\frac{\partial\theta}{\partial\delta\alpha} = \frac{\partial\theta}{\partial\hat{\sigma}_\varepsilon}\frac{\partial\hat{\sigma}_\varepsilon}{\partial\delta\alpha}. \tag{3.39}$$

The partial derivative of the hardening formulation with respect to the evolving thermal stress component $\partial\theta/\partial\hat{\sigma}_\varepsilon$ is given by Equation (3.32) for the hyperbolic tangent and by Equation (3.33) for the power law case. The partial derivative of the thermal stress component with respect to the incremental plastic strain is then given by

$$\frac{\partial\ \hat{\sigma}_{\varepsilon}|_{t+\delta t}}{\partial \delta\alpha} = \frac{\theta|_{t+\delta t}}{\left(1 - \delta\alpha\ \frac{d\theta}{d\hat{\sigma}_{\varepsilon}}\Big|_{t+\delta t}\right)}. \tag{3.40}$$

Similarly, the partial derivative of the evolving thermal stress component at the end of the increment with respect to the equivalent plastic strain rate is computed from Equation (3.30) to give

$$\frac{\partial\ \hat{\sigma}_{\varepsilon}|_{t+\delta t}}{\partial \dot{\alpha}} = \delta\alpha \frac{\partial\ \theta|_{t+\delta t}}{\partial \dot{\alpha}}. \tag{3.41}$$

The final result follows from the chain rule:

$$\frac{\partial \theta}{\partial \dot{\alpha}} = \frac{\partial \theta}{\partial \hat{\sigma}_{\varepsilon}} \frac{\partial \hat{\sigma}_{\varepsilon}}{\partial \dot{\alpha}} + \frac{\partial \theta}{\partial \hat{\sigma}_{\varepsilon s}} \frac{\partial \hat{\sigma}_{\varepsilon s}}{\partial \dot{\alpha}}. \tag{3.42}$$

In both hardening formulations (Equations (3.32) and (3.33)) under consideration, the evolving thermal stress component over saturation stress fraction $\hat{\sigma}_{\varepsilon}/\hat{\sigma}_{\varepsilon s}$ is used, i.e.

$$\frac{\partial \theta}{\partial \hat{\sigma}_{\varepsilon s}} = -\frac{\hat{\sigma}_{\varepsilon}}{\hat{\sigma}_{\varepsilon s}} \frac{\partial \theta}{\partial \hat{\sigma}_{\varepsilon}}. \tag{3.43}$$

Substitution into Equation (3.41) leads to

$$\frac{\partial\ \hat{\sigma}_{\varepsilon}|_{t+\delta t}}{\partial \dot{\alpha}} = \delta\alpha\ \frac{d\theta}{d\hat{\sigma}_{\varepsilon}}\Big|_{t+\delta t} \frac{\partial\ \hat{\sigma}_{\varepsilon}|_{t+\delta t}}{\partial \dot{\alpha}} - \delta\alpha \frac{\hat{\sigma}_{\varepsilon}|_{t+\delta t}}{\hat{\sigma}_{\varepsilon s}|_{t+\delta t}}\ \frac{d\theta}{d\hat{\sigma}_{\varepsilon}}\Big|_{t+\delta t} \frac{\partial\ \hat{\sigma}_{\varepsilon s}|_{t+\delta t}}{\partial \dot{\alpha}}. \tag{3.44}$$

From Equation (3.44) and the derivative of the saturation stress in Equation (3.26) with respect to the equivalent plastic strain rate we obtain

$$\frac{\partial\ \hat{\sigma}_{\varepsilon}|_{t+\delta t}}{\partial \dot{\alpha}} = \delta\alpha\ \frac{d\theta}{d\hat{\sigma}_{\varepsilon}}\Big|_{t+\delta t} \left(\delta\alpha\ \frac{d\theta}{d\hat{\sigma}_{\varepsilon}}\Big|_{t+\delta t} - 1\right)^{-1} \frac{\Gamma_{\varepsilon s} \hat{\sigma}_{0\varepsilon s}\ \hat{\sigma}_{\varepsilon}|_{t+\delta t}}{\dot{\varepsilon}_{0\varepsilon s}\ \hat{\sigma}_{\varepsilon s}|_{t+\delta t}} \left(\frac{\dot{\alpha}}{\dot{\varepsilon}_{0\varepsilon s}}\right)^{\Gamma_{\varepsilon s}-1}, \tag{3.45}$$

with

$$\Gamma_{\varepsilon s} = \frac{k_{\mathrm{B}} T}{g_{0\varepsilon s} \mu b^3}. \tag{3.46}$$

The gradients and numerical implementation of the model in Appendix C is now tested. This is done using an arbitrary set of material parameters and a single call to a one dimensional version of the user material framework that also uses the subroutine in Appendix C.

The value of the residual equation, analytical gradient as well as the estimated equivalent plastic strain increment is reported for each iteration. A central finite difference estimate of the sensitivity is also calculated within the one-dimensional test environment by perturbing the estimated plastic strain by 10^{-8}.

For this test, the material parameters for a purely virtual material are used:

- The elastic property values of $\mu_r = 10\text{GPa}$, $D_r = 100\text{MPa}$ and $T_r = 180\text{K}$ in Equation (3.21) and a Poisson's ratio of $\nu = 0.3$ are used.

- The stress values in Equation (3.23) are chosen as $\hat{\sigma}_a = 5\text{MPa}$, $\hat{\sigma}_i = 1\text{MPa}$ and $\hat{\sigma}|_{\alpha=0} = 0\text{MPa}$.

- The scaling functions in Equation (3.22) are modelled using parameter values $k_\text{B}/g_{0\varepsilon}b^3 = k_\text{B}/g_{0i}b^3 = 0.8\text{MPa/K}$, $p_\varepsilon = p_i = q_\varepsilon = q_i = 1$ and $\dot{\varepsilon}_{0\varepsilon} = \dot{\varepsilon}_{0i} = 10^7\text{s}^{-1}$.

- The implementation is tested using the power law hardening formulation in Equation (3.25b) with $\theta_0 = 1\text{GPa}$ and $a = 2$.

- The saturation stress property values in Equation (3.26) are chosen as $\hat{\sigma}_{0\varepsilon s} = 500\text{MPa}$, $k_\text{B}/g_{0\varepsilon s}b^3 = 2.5\text{MPa/K}$ and $\dot{\varepsilon}_{0\varepsilon s} = 10^{10}\text{s}^{-1}$.

Assuming a time increment $\delta t = 1\text{s}$, temperature of $T = 300\text{K}$ and one dimensional incremental strain $\delta\varepsilon = 0.1$, the residual value, equivalent plastic strain and sensitivities for each iteration in the solution loop are given in Table 3.1. The first iteration has no finite difference estimated sensitivity since there is no yield stress value associated with $\delta\alpha = -10^{-8}$.

The function call results in a resolved von Mises yield stress of $\sigma_\text{Y} = 21.329\text{MPa}$ and evolving thermal stress value $\hat{\sigma}_\varepsilon = \texttt{STATEV(1)} = 31.726\text{MPa}$. Out of the 0.1 total strain increment, the plastic strain increment is $\delta\alpha = 0.0992$ as seen in Table 3.1. According to the convergence of the residual and by comparison of the analytical sensitivity to the finite difference approximation in Table 3.1, the gradients are correctly derived and numerically implemented.

Iteration	Residual	Plastic Increment	Analytical Sensitivity	Finite Difference Estimate
1	2565.3224	0.	7.5E8	-
2	2564.4506	3.42041E-6	22222.308	22222.308
3	1176.8253	5.35342E-2	132.33881	132.33882
4	1.2973122	9.91192E-2	83.037994	83.037985
5	8.59911E-7	9.91695E-2	83.003841	83.003844
6	2.1316E-13	9.91695E-2	83.003841	83.003826

Table 3.1: Test on the convergence of the Mechanical Threshold Stress material subroutine in Appendix C.

3.5 Characterisation to Experimental Data

In this section, the Mechanical Threshold Stress model is first characterised using systematic linear regression, each time removing some of the unknown material parameters by linear regression or making assumptions on a specific material parameter to allow this approach. This is a classical method to obtain the material parameter values associated with the MTS model as done in the papers by Goto et al. (2000); Kocks (2001); Banerjee (2007) and Banerjee and Bhawalkar (2008) to name a few. The resulting material parameter values are then tuned using numerical optimisation for a better fit between the model predicted response and the data.

In the work by Tanner and McDowell (1999) from where the stress strain data in Figure 3.1 is obtained, the temperature dependent shear modulus of OFHC Cu is captured by the function

$$\mu(T) = 1000\left[47.093 - \left(0.1429 + 0.0002763T^2\right)^{0.5}\right] \text{MPa}. \tag{3.47}$$

From Tanner's Ph.D. Thesis (1998), and using Equation (3.47), there are two values for the Copper shear modulus at five different temperatures: $\mu\,(25°\text{C}) = \{42, 42.13\}$; $\mu\,(269°\text{C}) = \{38.11, 38.08\}$; $\mu\,(405°\text{C}) = \{35.94, 35.82\}$; $\mu\,(541°\text{C}) = \{33.46, 33.36\}$ and $\mu\,(691°\text{C}) = \{31.37, 31.07\}$ in units of GPa. A reference temperature of $T_r = 200\text{K}$ is selected and a linear regression is performed to fit the shear modulus data points to Equation (3.21). The result is depicted in Figure 3.3. From the intersection of the line with the ordinate axis, the reference shear modulus is $\mu_r = 49.91\text{GPa}$ while the slope corresponds to $D_r = 3.29\text{GPa}$.

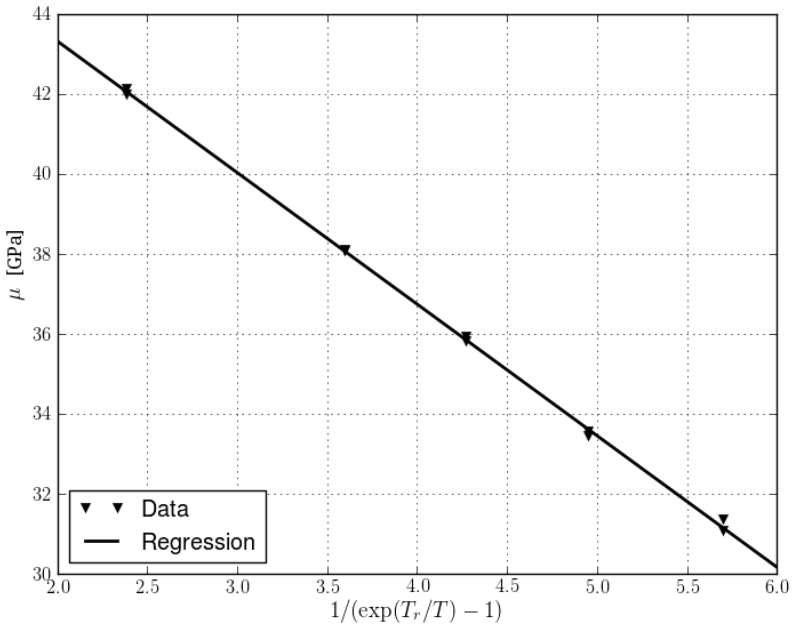

Figure 3.3: Linear regression through temperature dependent shear modulus data points obtained from Tanner et al. (1999).

The stress strain curves in Figure 3.1 are manipulated by removing the elastic strain from the total strains using the temperature dependent shear values. The elastic strain $\varepsilon^{\mathrm{e}} = \sigma/E = \sigma/\left[2\mu\left(1+\nu\right)\right]$ is subtracted at each digitised data point where we assume that $\nu = 1/3$ as reported by Tanner (1998). On a plot of the stress as a function of the remaining plastic strain, the yield stress for each data curve is interpolated from the data assuming the initial yield stress corresponds to the stress value at $\varepsilon^{\mathrm{p}} = 0.005$ as seen in Figure 3.4. The area of interest in the figure typically only shows part of the curves as a result of one or two data points apart from the origin resulting in what could be observed as a kink in the respective curves.

In this material parameter fit, the athermal yield stress component in Equation (3.23) is assumed $\hat{\sigma}_a = 0\mathrm{MPa}$. We therefore assume that the yield stress values in Figure 3.4 are as a result of the constant thermal yield stress component $\hat{\sigma}_i$ and the associated temperature and strain rate dependent scaling function $S_i\left(\dot{\alpha}, T\right)$ in Equation (3.23).

As done by many authors who use the Mechanical Threshold Stress model, a linear regression is performed on the temperature and rate dependent yield stress values in

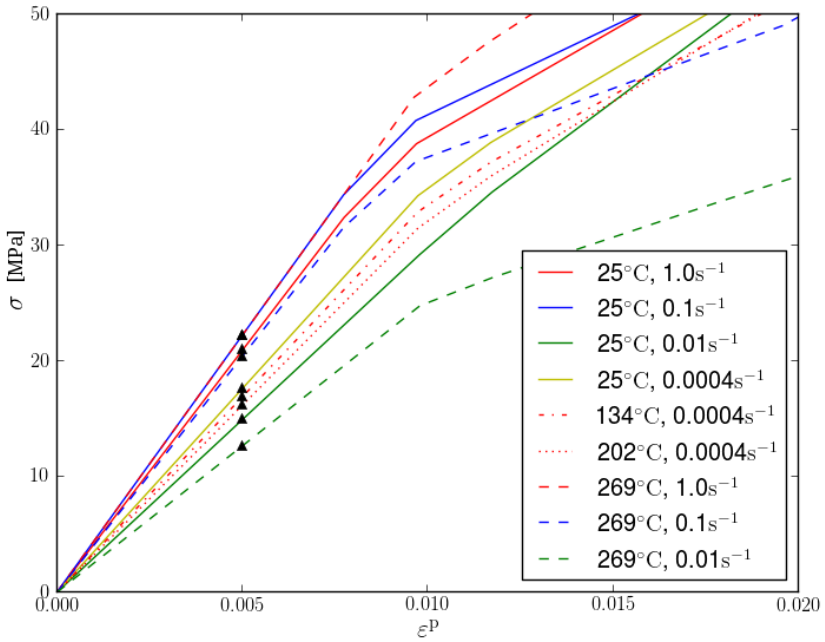

Figure 3.4: Assumed initial yield stress values interpolated from the stress versus plastic strain curves of the OFHC Cu data in Figure 3.1.

Figure 3.4 by fitting a line through the data points with values of $[T/\mu \ \ln(\dot{\varepsilon}_{i0}/\dot{\alpha})]^{1/q_i}$ on the $x-$axis and values of $[(\sigma_{\mathrm{Y}} - \hat{\sigma}_a)/\mu]^{p_i}$ on the $y-$axis.

Given the general linear regression form $y = A_i x + B_i$, we obtain the material parameters from

$$a_{0i} = \left(\frac{-B_i}{A_i}\right)^{q_i} \qquad \text{where} \qquad a_{0i} = \frac{g_{0i} b^3}{k_{\mathrm{B}}}. \tag{3.48}$$

In Equation (3.48) a_{0i} is introduced as a convenient grouping of material parameters with values typically reported in K/MPa. The reference stress value is also determined from $\hat{\sigma}_i = \mu_r A_i^{1/p_i}$.

In this characterisation, the values $p_i = q_i = 1$ and $\dot{\varepsilon}_{i0} = 10^7 \mathrm{s}^{-1}$ are assumed resulting in the modified Arrhenius Fisher plot displayed in Figure 3.5. From this plot, the resulting equivalent material parameters are determined as $a_{0i} = 1.523\mathrm{K/MPa}$ and constant thermal stress component $\hat{\sigma}_i = 23.29\mathrm{MPa}$. In Figure 3.5, there is an unsatisfactory description of the data using linear regression. This is likely due to the fact that the yield stress itself is not adequately captured. As seen in Figure 3.4, the

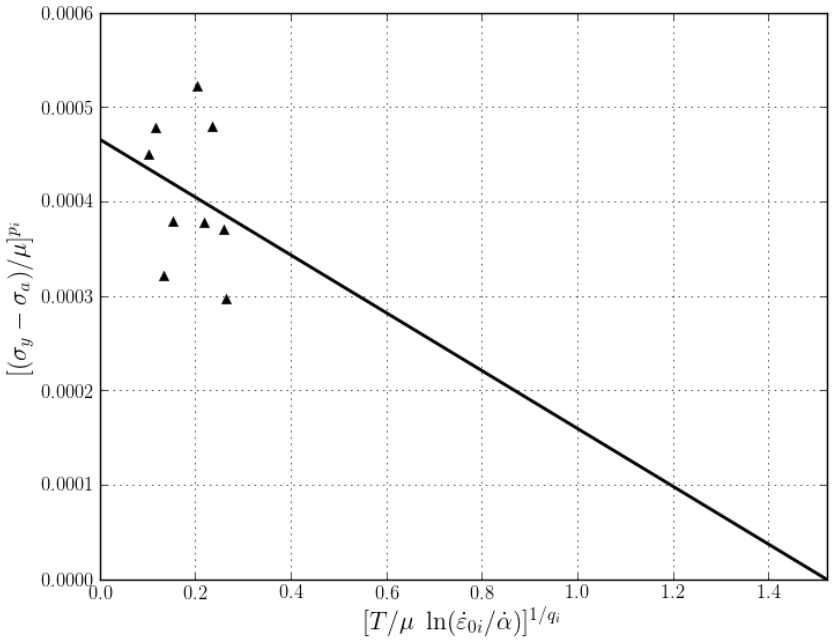

Figure 3.5: Linear regression to determine $\hat{\sigma}_i$ and $a_{0i} = (g_{0i}b^3)/k_{\mathrm{B}}$.

yield stress is effectively estimated by simple interpolation on the first two data points.

The next step in the material characterisation is to characterise the rate of change in the remainder of the stress as a function of the evolving thermal stress component as well as temperature and rate dependent threshold stress. The scaling function and already observed contributions are first removed from the stress-strain data. In this section, we assume that $a_{0\varepsilon} = 2\mathrm{K/MPa}$ where $a_{0\varepsilon}$ is again a convenient grouping of the Boltzmann constant (k_{B}), Burger's vector length (b) and normalised activation energy ($g_{0\varepsilon}$) in the evolving thermal stress scaling function as in Equation (3.48). The values of the statistical quantities $p_\varepsilon = q_\varepsilon = 1$ are also assumed along with $\dot{\varepsilon}_{0\varepsilon} = 10^7\mathrm{s}^{-1}$.

The stress-strain data is modified by removing the scaled constant thermal stress component $S_i\hat{\sigma}_i$ and applying the evolving thermal stress component scaling function values S_ε based on the assumptions mentioned above at each data point. The rate of change with respect to the plastic strain is then associated with the hardening function in Equation (3.24).

The rate of change as a function of the remaining evolving thermal stress is given in Figure 3.6. The hardening curves θ as a function of the remaining evolving stress $\hat{\sigma}_\varepsilon$

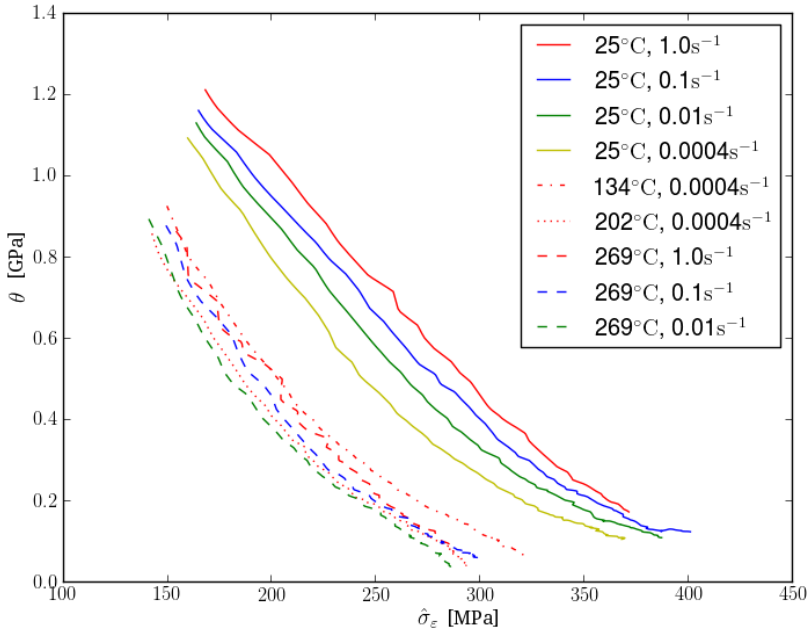

Figure 3.6: Hardening rate θ as a function of the residual stress $\hat{\sigma}_\varepsilon$.

is used to determine an appropriate temperature and rate dependent saturation stress value.

The saturation stress in each case is approximated by fitting a line through the entire curve in Figure 3.6 and reading off the intersection with the abscissa or $x-$axis. Saturation stress values of 395.81MPa, 407.18MPa, 394.86MPa and 376.29MPa are estimated from the room temperature curves given in descending strain rate order. A saturation stress of 326.19MPa is determined from the 134°C, 0.0004s^{-1} curve and 297.62MPa from the 202°C, 0.0004s^{-1} curve. Saturation stress values of 296.68MPa, 301.28MPa and 289.43MPa are estimated for the 269°C curves. Using Equation (3.26), values of the reference saturation stress $\hat{\sigma}_{0\varepsilon s}$ and lumped material parameter $a_{0\varepsilon s} = g_{0\varepsilon s} b^3/k_{\mathrm{B}}$ as in Equation (3.48) is again determined using a modified Arrhenius Fisher plot and linear regression. After estimating the temperature and strain rate dependent saturation stress values $\hat{\sigma}_{\varepsilon s}$ from Figure 3.6, a linear regression is performed on $[T/\mu \ \ln(\dot{\varepsilon}_{0\varepsilon s}/\dot{\alpha})]$ versus $[\ln(\hat{\sigma}_{\varepsilon s})]$. Assuming here that $\dot{\varepsilon}_{0\varepsilon s} = 10^{10}\mathrm{s}^{-1}$, the modified Arrhenius Fisher plot is displayed in Figure 3.7 resulting in $\hat{\sigma}_{0\varepsilon s} = 528.86\mathrm{MPa}$ and $a_{0\varepsilon s} = 0.5696\mathrm{K/MPa}$.

Assuming the material response follows the Voce hardening law in Equation (3.17),

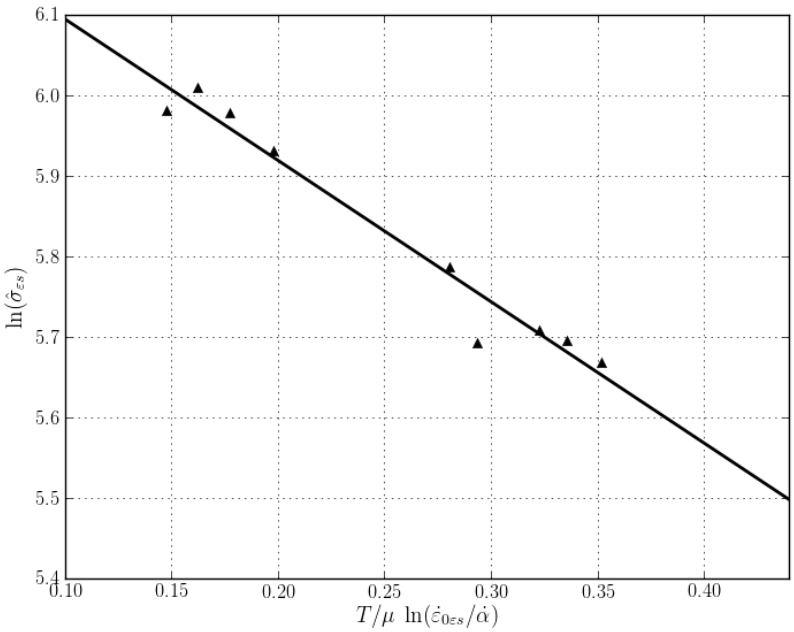

Figure 3.7: Linear regression to determine $\hat{\sigma}_{0\varepsilon s}$ and $a_{0\varepsilon s} = (g_{0\varepsilon s} b^3)/k_{\mathrm{B}}$.

the hardening curves in Figure 3.6 are now plotted against the saturation stress scaled values $\hat{\sigma}_{\varepsilon}/\hat{\sigma}_{\varepsilon s}$ in Figure 3.8(a). Fitting a line through the data in a least squares sense results in $\theta_0 = 1574.83$MPa at the intersection with the ordinate axis. Using the material parameters as assumed and determined in this section with the initial evolving stress component $\hat{\sigma}_{\varepsilon}|_{t=0} = 0$MPa, the model response at each of the rates and temperatures corresponding to the experimental curves are evaluated numerically and compared to the experimental data in Figure 3.8(b).

It is possible that alternate assumptions or greater care in extracting the saturation stress values per curve for example might improve the overall fit between the modelled and experimentally observed response in Figure 3.8. Successful material parameter characterisation following the approach discussed thus far is then somewhat dependent on the experience or insights of the person performing the characterisation, which is not ideal.

Assuming that the strain hardening rather follows the modified Voce law formulations presented in Equation (3.25), an initial hardening rate $\theta_0 = 4001.02$MPa is obtained assuming $a = 2$ and the hyperbolic tangent formulation, with the results pre-

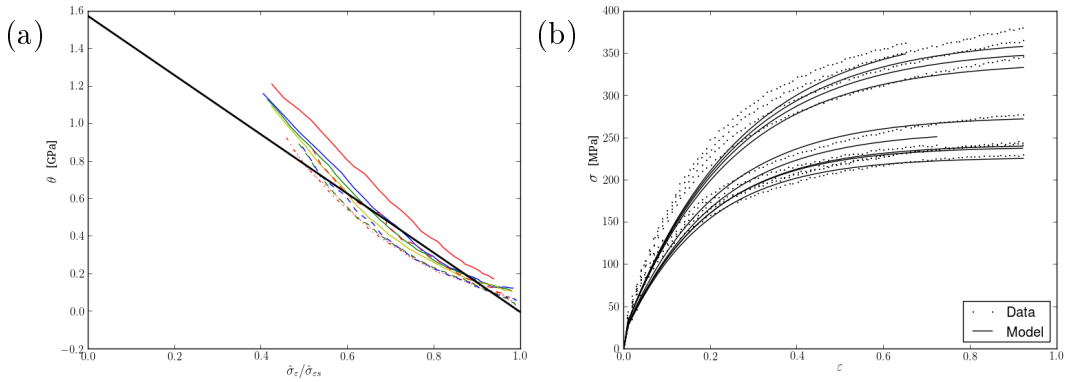

Figure 3.8: Voce formulation initial hardening $\theta_0 = 1574.83$MPa in (a) and (b) response compared to the experimental data.

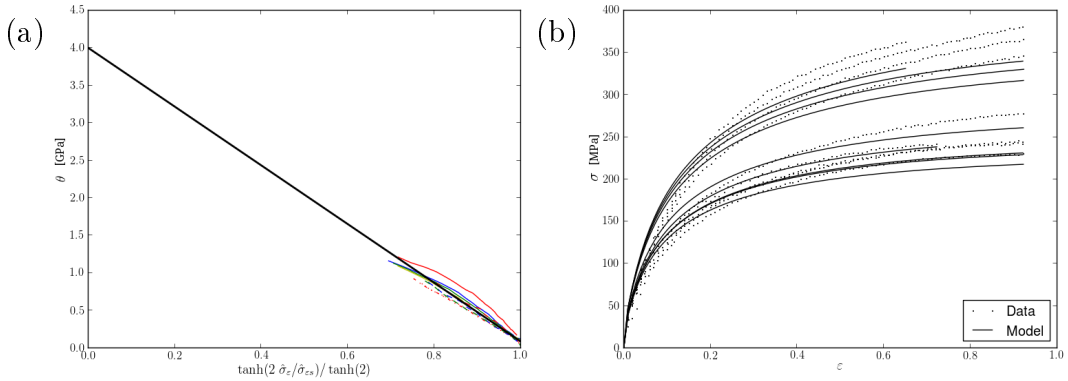

Figure 3.9: Hyperbolic tangent formulation initial hardening (a) and (b) response compared to the experimental data using $a = 2$ and $\theta_0 = 4001.02$MPa.

sented in Figure 3.9. Figure 3.10(a) shows the initial hardening rate $\theta_0 = 2566.7$MPa again obtained assuming $a = 2$, but using the power law formulation. Comparison between the model and experimental response is presented in Figure 3.10(b).

To take the material parameter characterisation a step further and make it less biased, numerical optimisation can be employed. The material parameters obtained in the three different cases are now assumed as initial conditions to an inverse problem. Six of the material parameters are varied numerically until the best fit between the model prediction and experimental data is obtained. Here, we use the downhill simplex method as implemented in the optimisation modules of the Scientific Python (SciPy) (Jones et al., 2001) libraries to perform the optimisation.

The six material parameters chosen by numerical optimisation in this chapter are

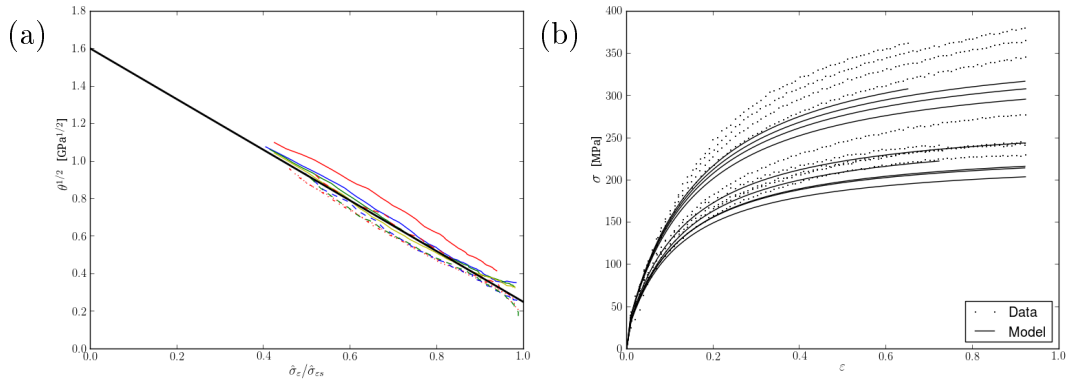

Figure 3.10: Power law formulation initial hardening (a) and (b) response compared to the experimental data using $a = 2$ and $\theta_0 = 2566.7$MPa.

the constant thermal yield stress $\hat{\sigma}_i$, the reference saturation stress $\hat{\sigma}_{0\varepsilon s}$, the grouped material quantities a_{0i}, $a_{0\varepsilon}$ and $a_{0\varepsilon s}$ as well as the initial strain hardening θ_0.
The chosen objective function is

$$f_{\text{obj}}(\mathbf{x}) = \sum_{mn} \left[\frac{\sigma_{mn} - \sigma(\varepsilon_{mn}, \mathbf{x}, \dot{\alpha}_m, T_m)}{\sigma_{mn}} \right]^2, \tag{3.49}$$

where σ_{mn} is the stress of the n^{th} data point on the m^{th} experimental data curve. The stress $\sigma(\varepsilon_{mn}, \mathbf{x}, \dot{\alpha}_m, T_m)$ is the value of the model predicted stress response at the same total strain as the data point σ_{mn} using the constant strain rate and temperature associated with the m^{th} curve and the material parameter values $\mathbf{x} = \{\hat{\sigma}_i, \hat{\sigma}_{0\varepsilon s}, a_{0i}, a_{0\varepsilon}, a_{0\varepsilon s}, \theta_0\}$.

The first inverse problem is to characterise a case that concerns the Voce hardening law in Equation (3.17) with the initial parameter values $\mathbf{x}_0 = \{23.29,\ 528.86,\ 1.523,\ 2,\ 0.5696,\ 1574.83\}$. The initial values result in an initial objective function value $f_{\text{obj}}(\mathbf{x}_0) = 5.1284$. The final objective function value as a result of 502 iterations and 770 function evaluations is $f_{\text{obj}}(\mathbf{x}^*) = 1.4863$ where $\mathbf{x}^* = \{29.79,\ 515.5,\ 1.591,\ 1.011,\ 0.7018,\ 2039.49\}$. The initial response of Figure 3.8(b) is duplicated in Figure 3.11(a) to facilitate better comparison with the optimal fit in Figure 3.11(b). The same is then done for the hyperbolic tangent and power law hardening formulations.

For the hyperbolic tangent hardening formulation, the initial parameter values are $\mathbf{x}_0 = \{23.29,\ 528.86,\ 1.523,\ 2,\ 0.5696,\ 4001.02\}$ and $f_{\text{obj}}(\mathbf{x}_0) = 6.221$. After 359 iterations and 562 function evaluations the optimisation terminated successfully with

	Voce (3.17)		**Tanh** (3.25a)		**Power** (3.25b)	
	Regression	Optimised	Regression	Optimised	Regression	Optimised
f_{obj}	5.128	1.486	6.221	0.712	8.686	0.6941
$\hat{\sigma}_i$	23.29	29.79	23.29	16.35	23.29	20.67
$\hat{\sigma}_{0\varepsilon s}$	528.86	515.5	528.86	710.9	528.86	689.12
a_{0i}	1.523	1.591	1.523	1.684	1.523	1.402
$a_{0\varepsilon}$	2	1.011	2	2.108	2	1.632
$a_{0\varepsilon s}$	0.5696	0.7018	0.5696	0.4522	0.5696	0.5011
θ_0	1574.83	2039.49	4001.02	2880.99	2566.70	2611.94
a	-	-	2	2	2	2

Table 3.2: Objective function values associated with selected initial and optimised MTS Parameters on OFHC Cu.

$f_{\text{obj}}(\mathbf{x}^*) = 0.7117$ and $\mathbf{x}^* = \{16.35,\ 710.9,\ 1.684,\ 2.108,\ 0.4522,\ 2880.99\}$.

The power law formulation on the other hand has an initial objective function value $f_{\text{obj}}(\mathbf{x}_0) = 8.6864$ where $\mathbf{x}_0 = \{23.29,\ 528.86,\ 1.523,\ 2,\ 0.5696,\ 2566.70\}$. After 410 iterations and 637 function evaluations the final material parameters are $\mathbf{x}^* = \{20.67,\ 689.12,\ 1.402,\ 1.632,\ 0.5011,\ 2611.94\}$ with $f_{\text{obj}}(\mathbf{x}^*) = 0.6941$.

The initial material parameter values are compared to the optimal material parameter values in Table 3.2. The model predicted response is also compared to the experimental data curves in Figure 3.11 for both the initial material parameter values and the optimal material parameter values. The first column of figures in Figure 3.11 shows the response for the initial material parameter values. The second column is the response as a result of material parameters determined with the help of the numerical optimisation as outlined above.

Given a reasonable initial guess for the material parameters, the downhill simplex method finds the material parameter values that best reproduce the experimental data curves with fairly little effort. It would therefore seem that the inverse problem using the MTS model is fairly well posed within the bounds evaluated and assumptions made in this chapter.

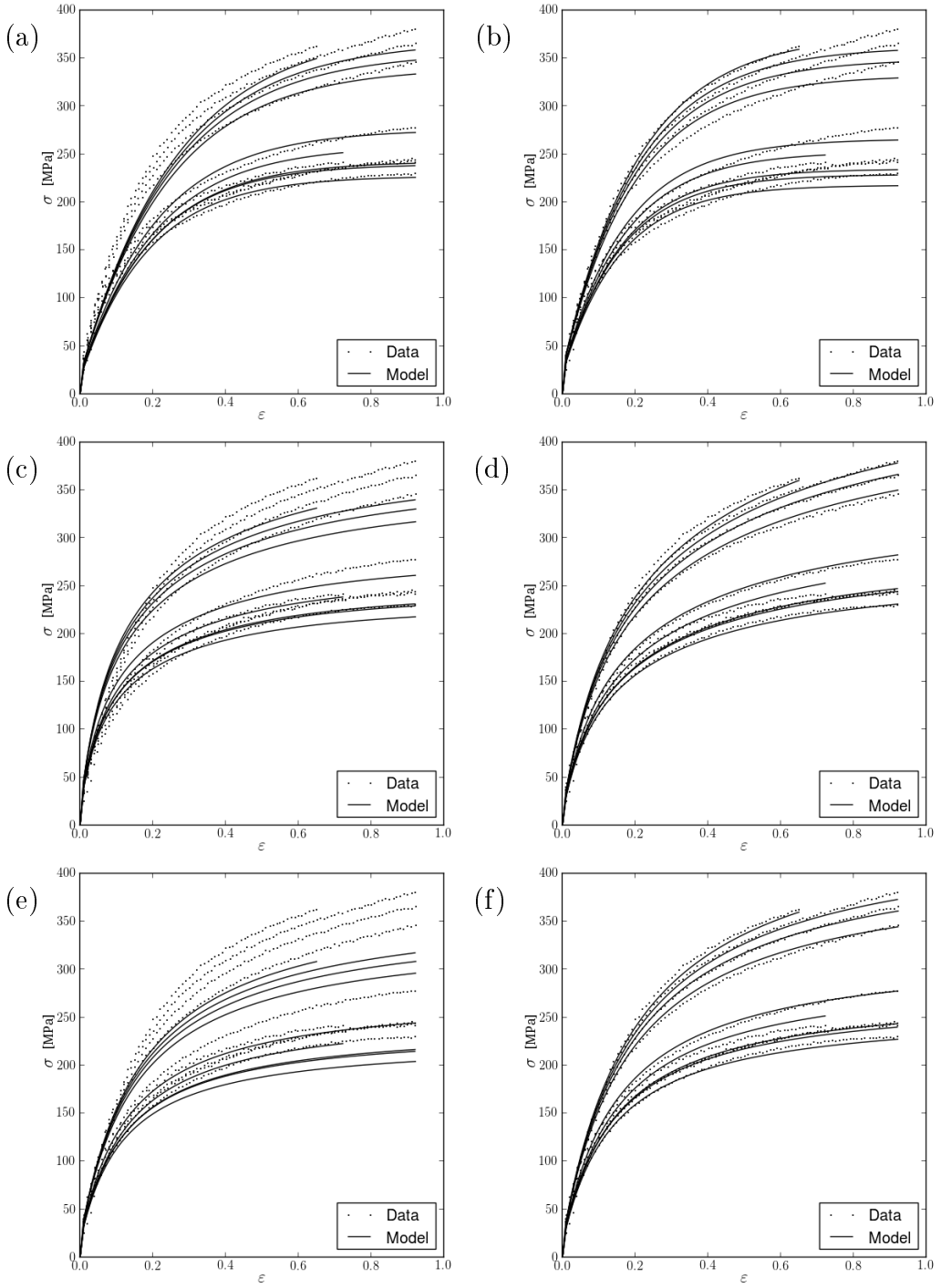

Figure 3.11: (a) Initial and (b) optimal fit for the Voce hardening formulation. (c) Initial and (d) optimal fit for the hyperbolic tangent hardening formulation with $a = 2$. (e) Initial and (f) optimal fit for the power law Voce hardening formulation with $a = 2$.

3.6 Temperature and rate dependent compression of a cylindrical test specimen

Up to this point in the chapter, a single point integration is performed using a one dimensional version of the material model framework calling the isotropic hardening subroutine in Appendix C. The following section illustrates the difference in the material point simulator compared to a finite element analysis of axi-symmetric billet compression as in Sections 2.1.2 and 2.2.

In this section, the problem is set up following Figure 2.4(b) in Abaqus. The billet is modelled using a 20×20 grid of quadratic axi-symmetric elements while a rigid analytical plane is used for the anvil contact surface. Hard normal contact between the billet and anvil is modelled with a Coulomb friction coefficient $\mu_C = 0.2$.

Four different problems are simulated that correspond to the experimental test data for 1s^{-1} and 0.0004s^{-1} at 298K, 0.0004s^{-1} at 407K and 0.01s^{-1} at 542K. The billet section modelled has a radius of 2.5mm and a half length of 5mm, meaning a 100% reduction in length corresponds to a anvil displacement of $5\text{mm} \times (\exp(-1) - 1) = -3.1606\text{mm}$. This displacement is applied over 1s in the 1s^{-1} case, 100s in the 0.01s^{-1} case and 2500s in the 0.0004s^{-1} in 100 increments.

The material parameters for OFHC Cu characterised using the power law hardening form with $a = 2$ in the last column of Table 3.1 is used since it produced the smallest objective function value (f_{obj} =0.6941). These material property values are:

- The elastic property values of $\mu_r = 49.91\text{GPa}$, $D_r = 3.29\text{GPa}$ and $T_r = 200\text{K}$ in Equation (3.21) and a Poisson's ratio of $\nu = 1/3$ are used.
- The stress values in Equation (3.23) are $\hat{\sigma}_a = 0\text{MPa}$, $\hat{\sigma}_i = 20.67\text{MPa}$ and $\hat{\sigma}_\varepsilon|_{\alpha=0} = 0\text{MPa}$.
- The scaling function values in Equation (3.22) are chosen as $a_{0i} = g_{0i}b^3/k_{\text{B}} = 1.402\text{K/MPa}$, $a_{0\varepsilon} = g_{0\varepsilon}b^3/k_{\text{B}} = 1.632\text{K/MPa}$, $p_\varepsilon = p_i = q_\varepsilon = q_i = 1$ and $\dot{\varepsilon}_{0\varepsilon} = \dot{\varepsilon}_{0i} = 10^7\text{s}^{-1}$.
- The power law hardening formulation in Equation (3.25b) is used with $\theta_0 = 2611.94\text{MPa}$ and $a = 2$.

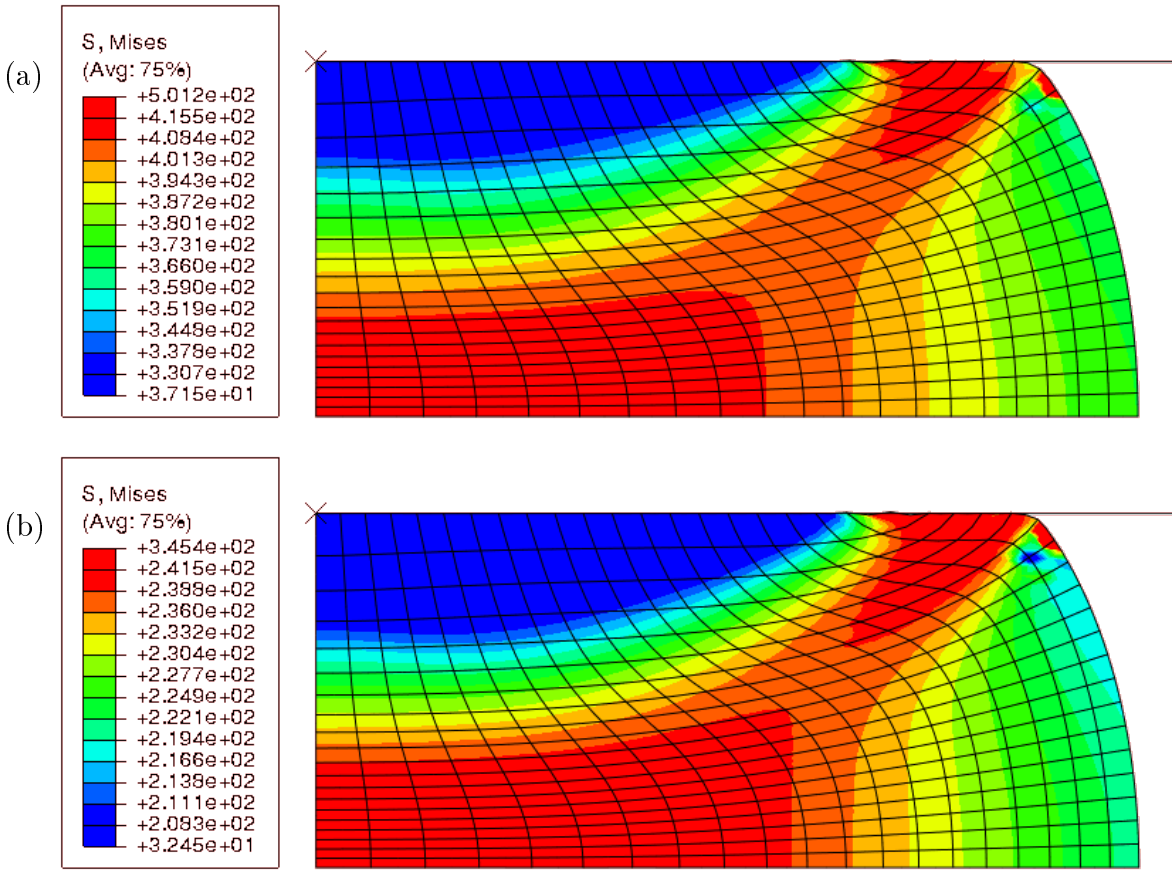

Figure 3.12: Von Mises stress distributions after 100% reduction in length for (a) 1s^{-1} at 298K and (b) 0.01s^{-1} at 542K.

- The saturation stress property values in Equation (3.26) are $\hat{\sigma}_{0\varepsilon s} = 689.12\text{MPa}$, $a_{0\varepsilon s} = g_{0\varepsilon s}b^3/k_\text{B} = 0.5011\text{K/MPa}$ and $\dot{\varepsilon}_{0\varepsilon s} = 10^{10}\text{s}^{-1}$.

In Figure 3.12, the von Mises stress distributions after 100% reduction in length is displayed for the hardest and softest of the material responses modelled. In Figure 3.12(a) the 1s^{-1} at 298K results are given while (b) is the stress distribution in the 0.01s^{-1} at 542K case.

From the Abaqus results, the engineering strain values at each increment is determined from $\epsilon = \triangle L/L_0 = u_y/5$, where u_y is the prescribed anvil displacement in the axial direction. This is transformed to the true strain value $\varepsilon_\text{true} = \ln(1+\epsilon)$. The

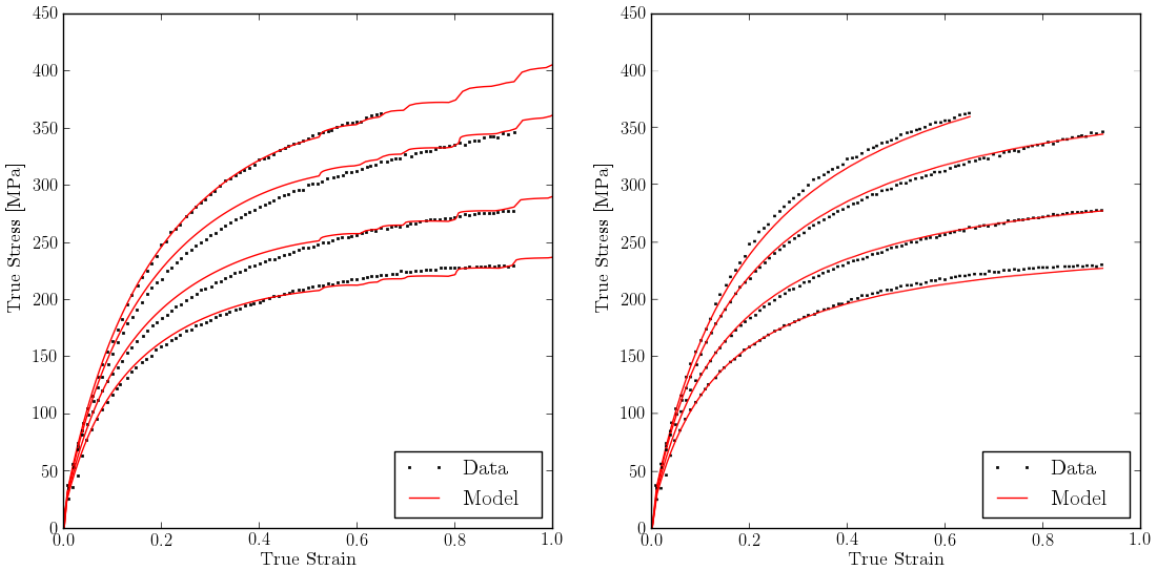

Figure 3.13: (a) Abaqus axi-symmetric simulation and (b) material point simulator using the material parameters estimated for OFHC Cu compared to the experimental test data.

total reaction force P at the mid plane nodes is also as extracted at each incremental solution. The volume preserving area assumption is further used to calculate the true stress.

The volumes $V = V_0$ means $AL = A_0L_0$ is assumed at every data point where A_0 is the initial test specimen area and L_0 the initial specimen length. The volume preserving area $A = A_0L_0/L$ is determined at each data point thanks to the known values of A_0, L_0 and current length $L = L_0 + \triangle L$ linked to the prescribed anvil displacement. The approximate true stress value at each time increment is now calculated by

$$\sigma_{\text{true}} = \frac{P}{A} = \frac{P}{A_0} \times \frac{L_0 + \triangle L}{L_0} = \frac{P}{A_0}\left(1 + \epsilon\right). \tag{3.50}$$

In Figure 3.13(a) the true stress versus true strain curves for the four cases simulated are presented. In Figure 3.13(b) the comparison between the test data and material point simulator also presented in Figure 3.11(f) is again given for convenient comparison.

The Abaqus simulation data with simple post processing to estimate the true stress - true strain data compares well to the experimental test data and material point simulator. If greater accuracy between the finite element result and experimental test data is required however, the characterisation using numerical optimisation can again be performed. This time, finite element evaluations can be performed instead of the material point integration within the objective function evaluation.

Chapter 4

Characterising Imperfect Compression Data for Cemented Carbides

Material testing usually makes use of a simple geometry subjected to a simple load case. The goal is to obtain uniform stress states so that simple analytical post processing would produce stress - strain curves. Specific standards and procedures are in place for these tests. If a compression test is performed under ideal conditions, experimental data can be used to calibrate a material model with little effort.

However, in the case of hard material compression testing, the high stiffness of the specimen compared to the effective stiffness of the test machine can result in a material test that does not conform to the ideal. In this chapter, experimental data (hydraulic cylinder displacement, load cell force data and strain gauge readings) for a number of compression tests are available at different temperatures for different grades of Cemented Tungsten Carbide (WC-Co) or hardmetal samples. The different material grades have varying particulate sizes, binder phase chemistry and percentage volume fractions. The data and work in this chapter is subject to an ongoing memorandum of understanding where the data is proprietary information and as such may not be published as is. The alloy compositions and chemistry are therefore not reported and in figures where the data is presented, the values of the ordinate axis is often removed or scaled to comply with the memorandum of understanding.

This chapter is divided into four main sections. In Section 4.1 the cemented Carbide data, the motivation for this work and the setup for a virtual experiment are

discussed. Section 4.2 investigates the inverse material parameter identification using the Mechanical Threshold Stress (MTS) material model discussed in Chapter 3 and implemented in Appendix C using finite element analysis. The finite element method is used to simulate the unideal compression tests. The effective stiffness of the testing frame is included in the model and a nonuniform axial displacement is gradually applied to the specimen as the test proceeds. This is done while keeping the average rate of displacement constant. Using the available experimental data as a reference, the current work aims to find the material model parameters, testing machine stiffness and displacement boundary conditions that best reproduce the experimental data by solving an inverse problem on virtually constructed experimental data. Instead of using a full finite element simulation per function evaluation, Appendix D also investigates point integration.

In Section 4.3 an industrial test case is modelled. In this simulation a six axis press is modelled to illustrate plastic deformation during the compression of a pyrophyllite high-pressure cell. The chapter is finally concluded in Section 4.4. This chapter serves as an illustration of characterising a material model using imperfect hard material compression data. It is mainly demonstrated on virtual experimental data in this document with characterisation on the actual data reserved for a different document that is confidential in nature.

4.1 Experimental Data

The experimental data is obtained from compression tests where 3 strain gauge readings are available at room temperature, along with hydraulic cylinder displacement and load cell data. The strain gauges are fixed to the centre of the experimental test specimen, 120° apart. Higher temperature data is also available at 150°C, 250°C, 350°C and 500°C. At these elevated temperatures however, only a single extensometer strain measurement is available.

The materials tested are used in high temperature and pressure applications. The specific application, exact material compound and grade is proprietary information and for this reason, figure axes and material parameter values will be normalised. A material test specimen similar to the one described by Dunlay et al. (1989) is used

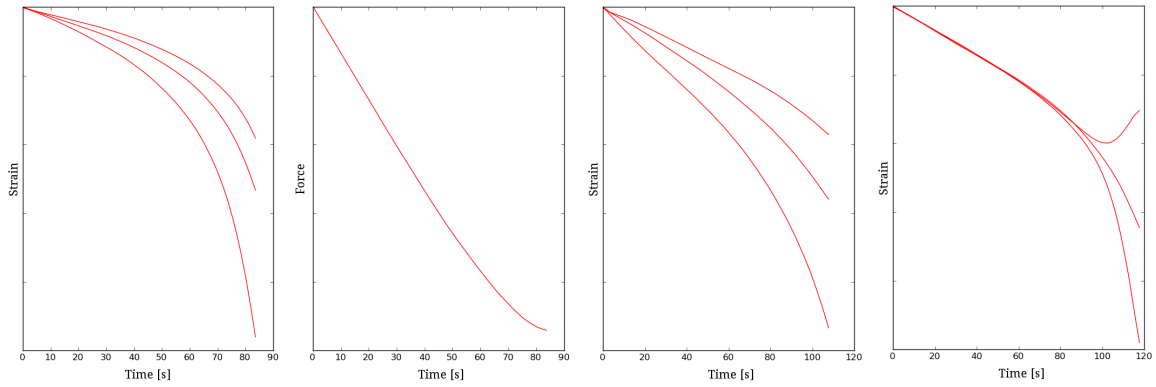

(a) (b) (c) (d)

Figure 4.1: Normalised experimental strains and load cell data at room temperature. (a) Strains recorded by the strain gauges spaced evenly around the circumference of the test section with (b) the load cell data of the same experiment. (c),(d) Strain gauge measured strains of two other experiments.

for the experimental compression tests. This compression test specimen is essentially a modified version of a conventional cylindrical tensile specimen. The length of the test section is reduced in an attempt to avoid buckling and shear deformation modes during the compression test.

One of the demanding aspects of compression tests on these hard materials is the very high compressive strength and stiffness. The testing machine stiffness, which should ideally be orders of magnitude greater than that of the specimen, is inadequate in this case. Experimental data indicates that for a typical test the hydraulic cylinder displaces 1.4mm, while the specimen test section only decreases height by about 0.4mm. Elastic deformation of the testing machine frame seems to account for the remaining 1.0mm displacement. From the strain gauge data of various room temperature compression tests seen in Figures 4.1(a), (c) and (d) there appears to be some compressive instability, eccentric load condition or equivalent bending moment present. Unfortunately, data for only a single extensometer is available at elevated temperatures. From all the room temperature data it seems plausible that the elevated temperature tests may also have experienced a similar unideal loading condition, but this cannot be taken into account due to the limited data.

In Figure 4.1, the room temperature data demonstrates that a nonuniform stress

state develops during the compression test, possibly due to compliance of the test frame. The data also indicates that the strain rate in the specimen is not constant, even though the crosshead speed of the hydraulic cylinder is.

To investigate the possible effect the nonuniform stress state would have on the accuracy of the material characterisation if ignored, the material model under isothermal conditions is characterised to the room temperature data using simple post processing. A representative material parameter set in the range of the characterised results is then used in a finite element analysis where the test specimen compression is modelled subject to ideal and unideal boundary conditions. The virtual experimental data is also described. The virtual problem setup will be used to investigate the accuracy, efficiency and potential cost of the characterisation strategies covered in this chapter.

4.1.1 Simple Room Temperature Characterisation

Strain gauge and load cell data for all five different hardmetal grades are used in this characterisation. If simple post processing of the data is performed, the average values of the strain gauges at each time step are taken as the true strain values. The load cell data divided by a volume preserving cylindrical area estimate at each time step is taken as the true stress value. A plot of the stress strain curves of the five different grades, here just named grade A to E, are given in Figure 4.2(a).

Although the different material grades vary in quite a few aspects, the elastic properties seem fairly identical when considering the room temperature data seen in Figure 4.2(b). The thick black line in this figure is associated with an elastic modulus of 636.5GPa. The expected elastic modulus range for pure Tungsten Carbide is 600-686GPa according to the AZO Materials website (2002) with a Poisson's ratio of 0.2 to 0.22. Although the materials have a mainly Cobalt binder phase varying between 5-15%, the elastic modulus of the material in compression is therefore most likely attributed to the Tungsten Carbide particles given the elastic modulus of pure Cobalt in the 209GPa range.

The maximum compressive strength and plastic deformation have a greater spread between the different material grades. Using a Young's modulus of 636.5GPa, the elastic strain component is removed from the total strain values resulting in the stress

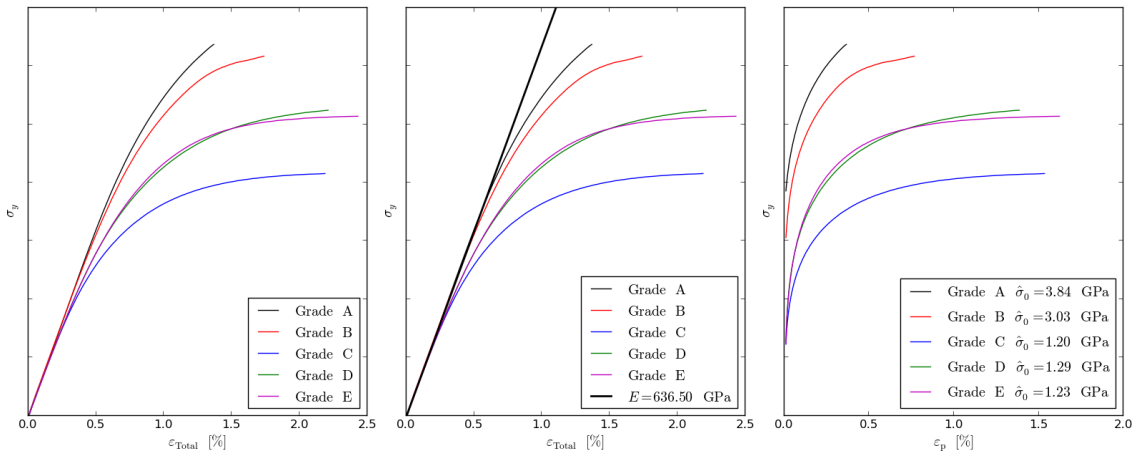

(a) (b) (c)

Figure 4.2: (a) The stress-strain relationship for the various grades of WC-Co using the averaged strains. (b) The Elastic modulus determined by a linear regression on the stress-strain data below 0.2% total strain. (c) The initial yield stress interpolated at 0.1% plastic strain.

versus plastic strain curves in Figure 4.2(c). The initial yield stress for the different material grades are then estimated as the stress value at 0.1% plastic strain.

We assume that the isothermal material model used here follows the empirical modification for the Voce law (Kocks et al., 1998; Mourad et al., 2013) as given in Equation (3.25), now reading

$$\frac{d\hat{\sigma}}{d\varepsilon_{\mathrm{p}}} = \theta_0 \left(1 - \frac{\hat{\sigma}}{\hat{\sigma}_s}\right)^a . \tag{4.1}$$

In this subsection, $\hat{\sigma}$ is not scaled with temperature and rate effects using some form of Equation (3.22) as in the full MTS model. Rather, an approximate characterisation can be done, as in Section 3.5. The hardening rate is estimated as the slope of the data in Figure 4.2(c). In Figure 4.3(a), the hardening rate for each grade is plotted on the ordinate axis with the residual stress $\hat{\sigma} = \sigma_{\mathrm{Y}} - \sigma_0$ on the abscissa. From this figure the saturation stress is determined as the approximate intersection with the abscissa in each case resulting in the values reported in the legend.

Scaling each of the residual stress values with the saturation stress so that the values on the abscissa are now $\hat{\sigma}/\hat{\sigma}_s$ results in Figure 4.3(b). On a plot of $\hat{\sigma}/\hat{\sigma}_s$ versus $d\hat{\sigma}/d\varepsilon_{\mathrm{p}}$,

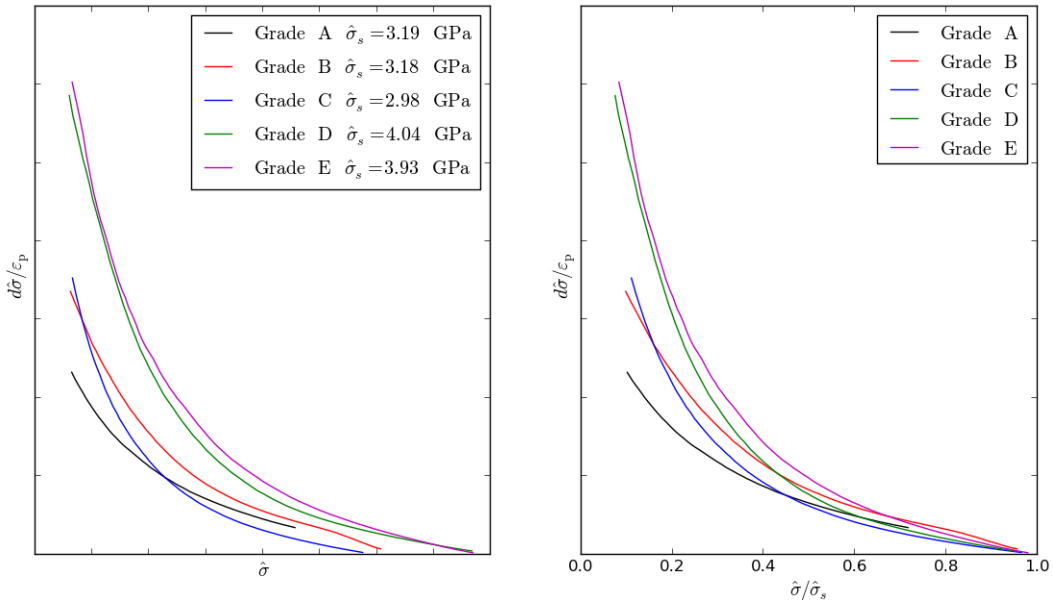

(a) (b)

Figure 4.3: (a) Hardening rate θ as a function of the residual stress $\hat{\sigma}$ and (b) residual stress over saturation stress $\hat{\sigma}/\hat{\sigma}_s$.

the ideal Voce like behaviour should be a linear decline as opposed to the shape of the curves in Figure 4.3(b). The figure would therefore suggest that there is some stage IV hardening present in the material response despite the fact that the maximum plastic strain is in the range of 1.5% to 2.5%. This is likely due to the fact that the majority of the deformation is attributed to the binder phase making up less than 15% of the total material volume.

The power law case of Equation (4.1) applied to the cemented Carbide data is illustrated in Figure 4.4. In these figures, the power 1/2 and 1/3 is applied to the estimated hardening rates in each case. The curves resulting from this procedure are straighter in comparison to those in Figure 4.3(b). This indicates that the power law modified Voce formulation should be better equipped to model the stress response over the observed plastic strain range.

The initial hardening rate is determined for each grade in the power law cases using linear regression, as illustrated in Figure 4.5(a) and (b). A line is fit through the data points in a least squares sense while the intersection with the abscissa is fixed at 1. The

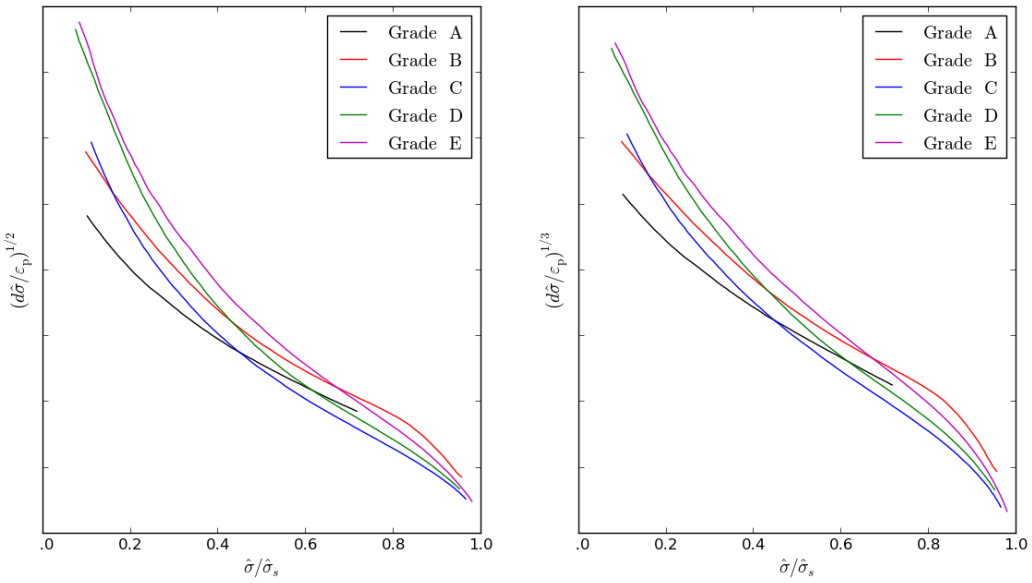

(a) (b)

Figure 4.4: Power law test on the cemented Carbide data for a power law formulation with (a) $a = 2$ and (b) $a = 3$.

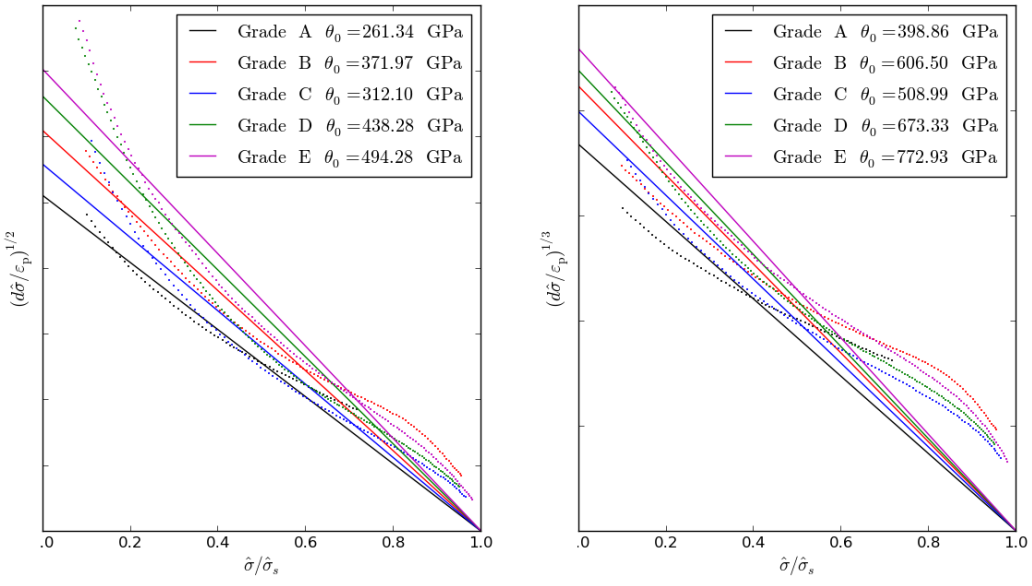

(a) (b)

Figure 4.5: The estimated initial hardening on the cemented Carbide data using linear regression for a power law formulation using (a) $a = 2$ and (b) $a = 3$.

value of the intersection with the ordinate axis is squared in (a) or cubed in (b) to give the approximate initial hardening rate θ_0. For the case $a = 2$, the initial hardening rate ranges between 261.34GPa to 494.28GPa for the different material grades while the case $a = 3$ suggests a range of 398.86GPa to 772.93GPa. The overlay of the lines with the data suggests that the initial hardening in the $a = 2$ case is underpredicted while a straight line regressed through the data in the case $a = 3$ misses the observed saturation. The characterisation does however give us an idea of the range of the material parameter values for the typically observed material response. This is now used in constructing an initial virtual experiment to investigate the possible effect the unideal experimental data would have on the material parameter characterisation.

4.1.2 Characterisation Accuracy

The characterisation accuracy is investigated by conducting two virtual experiments with the use of the finite element method. In the ideal case the test specimen is subjected to a uniform displacement that should result in the uniform stress state necessary for simple post processing of forces and displacements into stress strain curves. An imperfect test case is then simulated where a varying displacement boundary condition results in a strain distribution recovered around the circumference of the test specimen centre that is similar to the actual experimental data in Figure 4.1. The stress strain curves resulting from the same post processing is compared to investigate the potential deviation from the ideal test case.

Figure 4.6 shows the dimensions of the test specimen as it is modelled. The central 35mm of the full 120mm test specimen is modelled with a material model that has elastic properties as well as plastic behaviour using the modified Voce law of Equation (4.1). Later on in this section, the test section material is modelled using the full MTS material model. Due to the limitation of the testing frame, the full hydraulic cylinder displacement cannot simply be applied as a boundary condition to the finite element test specimen. 5mm of artificial elastic material is therefore added to the ends of the specimen. Hydraulic cylinder displacement can now be used as a boundary condition while the stiffness of the artificial material section can be changed during the inverse analysis procedure to represent the testing machine compliance. By modelling

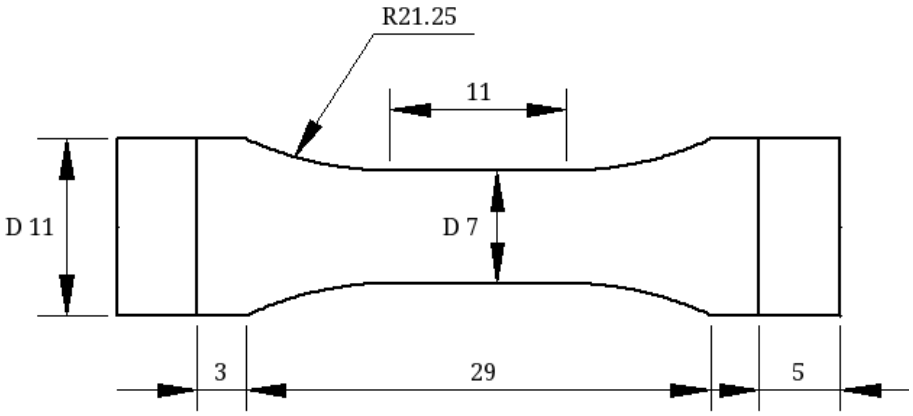

Figure 4.6: Dimensions of the test specimen modelled. Only the central 35mm of the test specimen is modelled along with a 5mm artificial elastic section on both ends to represent the test frame compliance.

it in this way, the experimental hydraulic cylinder displacement can be applied to the artificial material section. A correct choice of artificial material stiffness would then result in an effective strain rate and displacement experienced by the test specimen that best resembles the conditions experienced during the actual test.

A finite element model is set up by meshing the three dimensional geometry based on the dimensions in Figure 4.6. The analysis is performed in CalculiX (Dhondt and Wittig, 1998) using a model with 13056 degrees of freedom and of 3696 reduced integration 8 noded brick elements.

In the initial investigation, the elastic modulus of the material section is chosen as 600GPa with a Poisson's ratio of 0.21. An initial yield stress of $\sigma_0 = 2$GPa is assigned with $\hat{\sigma}|_{\varepsilon_p=0} = 0$. The post yielding behaviour of the model uses Equation (4.1) with $a = 2$ along with an initial hardening rate $\theta_0 = 600$GPa and saturation stress $\hat{\sigma}_s = 4$GPa. The artificial material sections are modelled with a Young's modulus of 30GPa and Poisson's ratio of 0.21.

Boundary conditions are applied to mimic two different test cases. The first test case models ideal compression where only a displacement in the axial direction is applied. All 3 degrees of freedom are constrained for the nodes on the one side of the model while only the two degrees of freedom associated with the radial plane of the geometry (x and z axis) are constrained on the other side of the model. A displacement of -1mm

is assigned in the axial direction (y axis) over 100 seconds in 5 second increments to simulate the course of an ideal experimental test.

To model an imperfect or virtual test case, a variation from the ideal boundary conditions is prescribed. The different strain gauge data visible in Figures 4.1(a) and (c) seem to deviate from each other early on in the experiment. From this observed difference in the strain gauge data in a single compression test, a spatially varying displacement boundary condition is included in the imperfect analysis instead of a purely uniaxial displacement. In this case the upper and lower boundaries of the model are subjected to a multi point constraint (MPC) boundary condition. Three master points are assigned on each boundary: one in the centre of the plane (x and z values equal to zero) and one at the nodes with the greatest x and z values respectively. The degrees of freedom in the x and z direction are constrained as in the ideal case while only the y values of the master nodes are prescribed explicitly. Given the prescribed displacement value at the master nodes, all other points of the boundary condition have an axial displacement subject to the MPC ensuring all the boundary nodes remain on a plane. The axial displacement of the centre bottom node is zero while the other nodes have total axial displacement values of 0.1mm and -0.1mm. The total axial displacement of the upper central node is -1mm as in the ideal case while the master nodes are assigned values of -1.1mm and -0.9mm to simulate an effective bending moment at the boundaries that are equal in size but opposite in direction. The total displacement is again applied in twenty 5 second increments.

The von Mises equivalent stress distributions at the end of the simulations are visible in Figure 4.7. In Figure 4.7(a) the stress field as a result of the ideal test case is presented where only a uniaxial displacement is prescribed. Figures 4.7(b) and (c) show the stress distribution due to the slight variation from the ideal boundary conditions as seen from the positive and negative x direction. Notice that the ideal compression test has a near uniform axial stress of 425MPa in the test section, while the axial stress in the test section of the unideal test varies between 182MPa and 479MPa.

Three elements 120° apart on the circumference of the centre of the model are chosen to represent the three strain gauge locations. The strain histories at these locations represent the data associated with the three strain gauges in the actual experiments at room temperature. The strain histories for the ideal test case is presented in Fig-

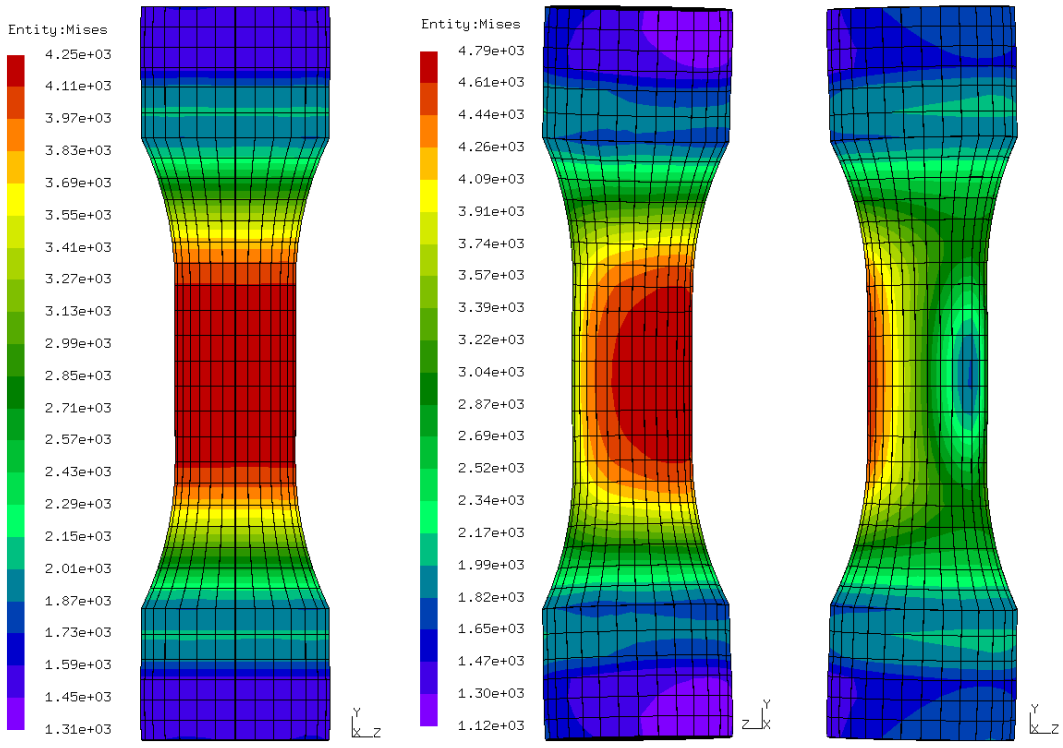

Figure 4.7: (a) von Mises equivalent stress distribution on the isothermal virtual experiment for perfect uniaxial compression. (b) Front and (c) back view of the von Mises equivalent stress distribution when a slight bend is included to mimic the true experimental strain spread with the same average axial displacement as in the perfect uniaxial compression case.

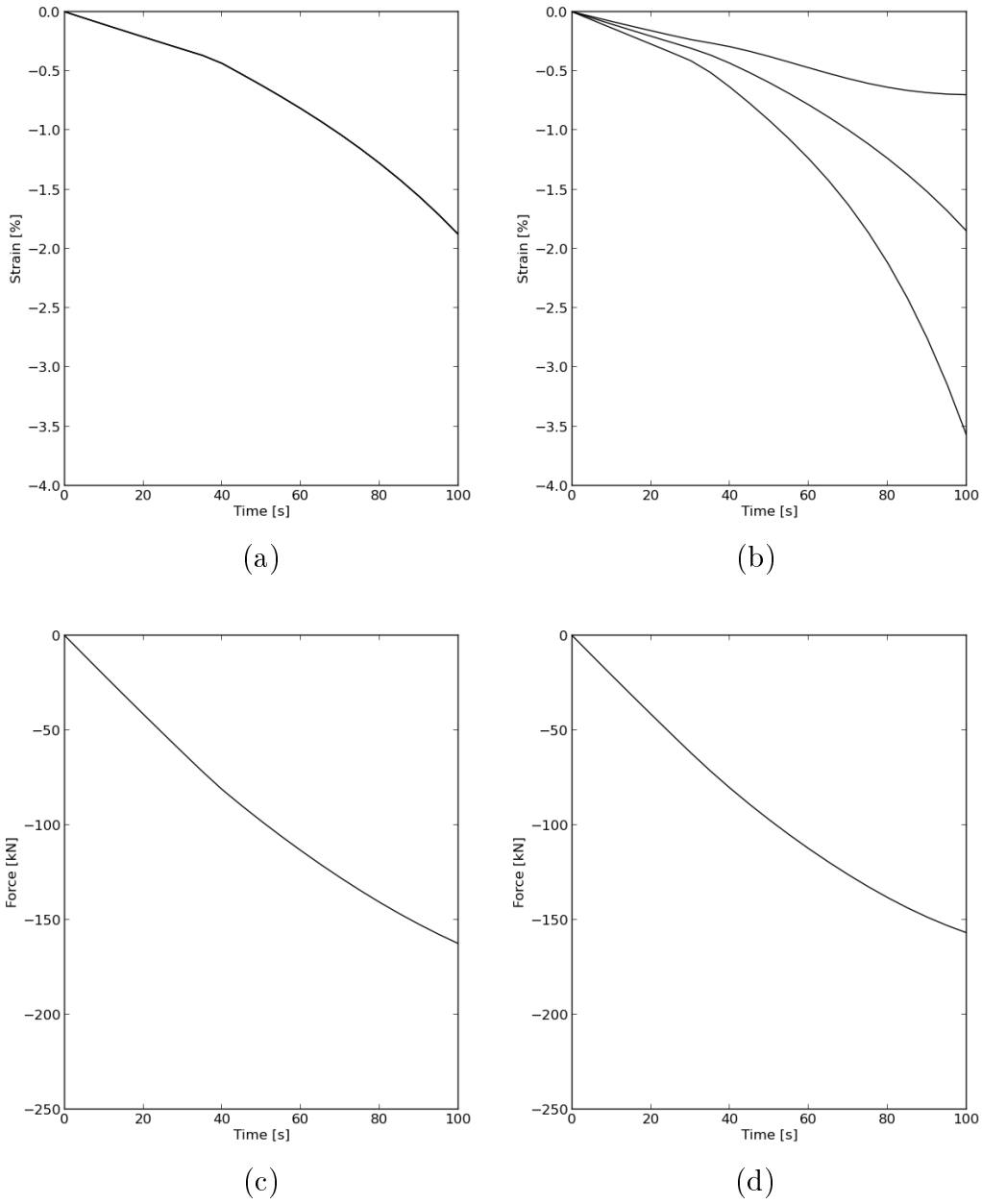

Figure 4.8: Strain history of the three strain gauge locations on the virtual experiment for the (a) ideal and (b) unideal virtual experiment simulations. Force history of the (c) ideal and (d) unideal virtual experiment simulations.

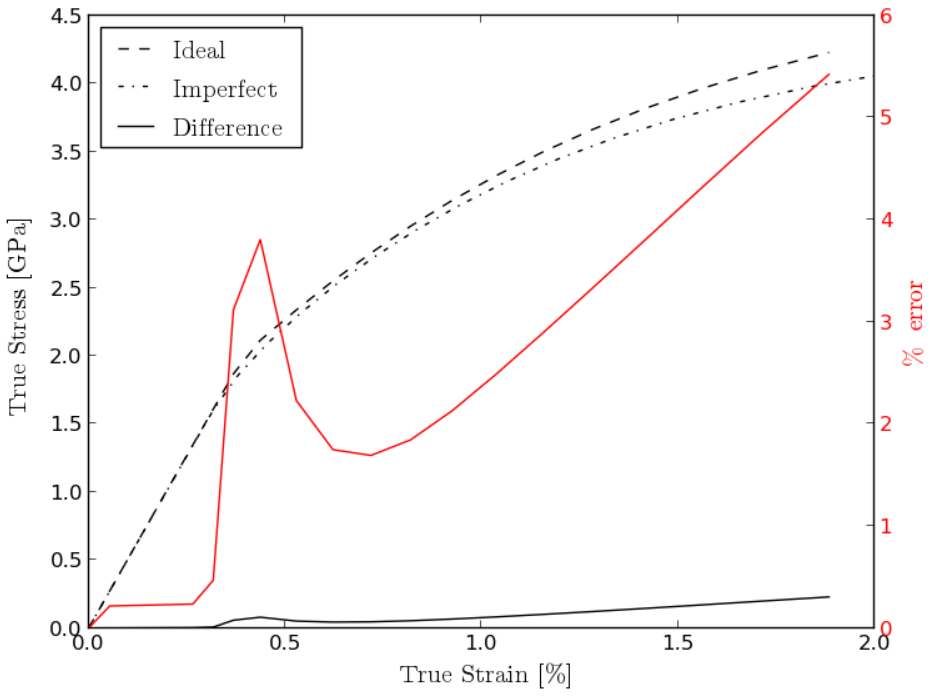

Figure 4.9: Comparison of the true stress - true strain curves obtained when simple post processing is performed on a uniformly compressed and an imperfect test simulation. The percentage error is determined by the difference between the two curves compared to the ideal test case.

ure 4.8(a) with the strain histories of the imperfect test case in Figure 4.8(b). The force histories of the two test cases are also presented in Figures 4.8(c) and (d).

The ideal and imperfect force and strain histories are used to construct stress versus strain curves, and then compared. The average of the three strain values at a specific time is taken as the engineering strain value ϵ and then transformed to the true strain value $\varepsilon_{\text{true}} = \ln(1+\epsilon)$. Assuming the material is volume preserving, the total force P, initial test specimen area A_0 and engineering strain are used as in Equation (3.50) to approximate the true stress value at each time increment using

$$\sigma_{\text{true}} = \frac{P}{A_0}(1+\epsilon)\,. \tag{4.2}$$

In Figure 4.9, the true stress - true strain curves resulting from the typical post

processing is given along with the percentage error when the curve using the imperfect test case is compared to that resulting from ideal uniform compression. The curves are similar in the elastic region while the initial yield prediction in the imperfect test case is off by about 4%. At the end of the curves there is a fairly constant increase in error with increased strain of about 2% per 1% increase in total strain. The maximum error in this case is in the range of about 5% with total strain values below 2%. If it is necessary to characterise the material model with errors below this magnitude, a different strategy should be followed to achieve the desired precision.

4.1.3 Finite element based inverse analysis

Following the investigation in the previous subsection, a general boundary value problem setup is constructed and used here to characterise the material properties of one of the material grades. The MTS material parameters are determined by an inverse analysis using a finite element simulation in Abaqus. The material response is provided by the MTS user material subroutine. The material parameters and boundary conditions are sought that best replicate the experimental data using the same model as constructed from Figure 4.6 in the previous subsection. The inverse analysis is performed by comparing the experimental data to the results of a finite element analysis at 25°C and 500°C.

Given the added artificial elastic material sections, the hydraulic cylinder displacement is used as an average uniaxial displacement boundary condition while the stiffness of the artificial material section can be changed during the inverse analysis procedure. A correct choice of artificial material stiffness would result in an effective strain rate and displacement experienced by the test specimen that best resembles the conditions experienced during the actual test. Instead of the MPC boundary conditions of the initial investigation, the spatially varying displacement field applied to the artificial material section in this instance is applied using a user displacement subroutine in Abaqus. The boundary condition at a given time step is now defined by the two boundary properties illustrated in Figures 4.10(a), (b) and (c). If the axial direction is chosen as the y axis in the finite element analysis, a top face node n experiences a y

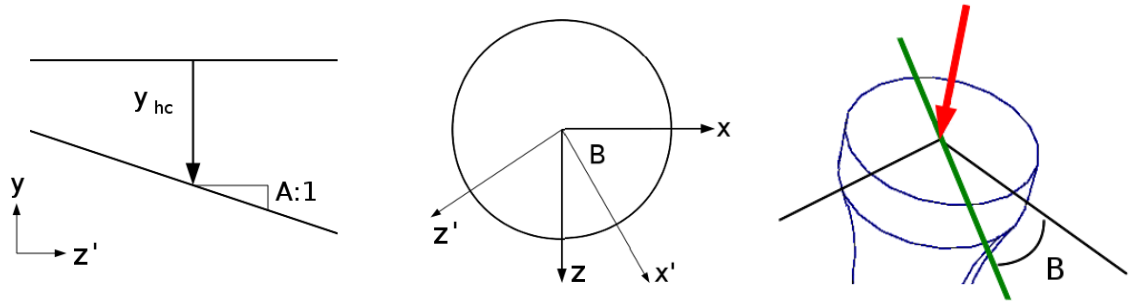

(a) (b) (c)

Figure 4.10: The two variables A and B that are used to describe the boundary displacement at a specific time. (a) The maximal gradient of the displacement variation is associated with the variable A. (b,c) The angle B defines the neutral axis where the axial displacement is equal to the average displacement.

displacement of the form

$$y_n = A(t)\left[\sin(B(t))z_n + \cos(B(t))x_n\right] + y_{hc}(t), \tag{4.3}$$

where t is the current fraction of time, $t \in [0, 1]$ and $y_{hc}(t)$ is the experimental hydraulic cylinder displacement as a function of this time fraction. x_n and z_n are the x and z coordinates of node n. The displacement field variation $A(t)$ and angle of the neutral axis $B(t)$ can also change as a function of the time fraction. In this characterisation however the angle (and so the neutral axis of the bending moment) would remain constant while the displacement field variation is linear over time $A(t) = At$. Similarly, the y displacement field at a bottom face node is determined by

$$y_n = -A(t)\left[\sin(B(t))z_n + \cos(B(t))x_n\right]. \tag{4.4}$$

By modelling the top and bottom displacement fields in this way, an equal and opposite equivalent bending moment can be approximated at a specific fraction of the total time.

From the data no constant thermal stress component $\hat{\sigma}_i$ is assumed. The constant thermal stress component of the mechanical threshold stress definition in Equation (3.23) therefore falls away. Neither k_B nor b are used anywhere other than the relationships $k_B/g_{0\varepsilon}b^3$ in Equation (3.22) and $k_B/g_{0\varepsilon_s}b^3$ in Equation (3.26), so these two

Parameter	Definition	Type	Value
$\hat{\sigma}_a$	Equation (3.18)	Variable	
$\hat{\sigma}_{0\varepsilon s}$	Equation (3.26)	Variable	
$k_B/g_{0\varepsilon}b^3$	Equation (3.22)	Variable	
$k_B/g_{0\varepsilon S}b^3$	Equation (3.26)	Variable	
θ_0	Equation (3.25)	Variable	
μ_r	Equation (3.21)	Variable	
D_r	Equation (3.21)	Variable	
$\hat{\sigma}_\varepsilon\|_{t=0}$	Equation (3.23)	Constant	0MPa
T_r	Equation (3.21)	Constant	200K
$\dot{\varepsilon}_0$	Equation (3.22)	Constant	$10^6 s^{-1}$
$\dot{\varepsilon}_{0\varepsilon s}$	Equation (3.26)	Constant	$10^6 s^{-1}$
q_ε	Equation (3.22)	Constant	1
p_ε	Equation (3.22)	Constant	$^2/_3$
a	Equation (3.25)	Constant	2

Table 4.1: List of MTS material parameters regarded as either constant or optimisation variables for use in the inverse analysis.

relationships are treated as single variables, as in Equation (3.48). In this parameter identification the hyperbolic tangent form of the hardening law in Equation (3.25) is used. A list of the MTS material parameters used as optimisation variables and constant parameters during this inverse material parameter characterisation is given in Table 4.1.

The seven MTS material parameters are determined along with an artificial material stiffness at 25°C and 500°C respectively. Including the two boundary condition variables A and B, 11 variables need to be determined by the inverse analysis.

The optimisation is performed using the unconstrained optimisation algorithm `fmin`, available via the `scipy.optimize` (Jones et al., 2001) module in Python. `fmin` is an implementation of the downhill simplex algorithm. Although the `scipy.optimize` module does give access to arguably better numerical optimisation algorithms, this is a very robust algorithm that only requires function value evaluations without additional gradient information.

The objective function used in the inverse analysis optimisation procedure compares the results of a finite element simulation to experimental curves in a mean squared

fashion. Given a set of parameter values, a room temperature analysis is set up which includes the displacement field boundary conditions of Equations (4.3) and (4.4), as well as the artificial material stiffness. This problem is then solved using Abaqus.

The logarithmic strains at the three locations spread evenly around the centre circumference of the finite element test specimen are then compared to the strain gauge data as a function of time. The load cell data is also compared to the total vertical reaction force at the top face. The 500°C/773K experiment is assumed to have occurred under ideal circumstances, since only a single set of strain data is available for comparison. A quarter model of the schematic visible in Figure 4.6 is used in this case. The same uniaxial displacement over time is used as extracted from the hydraulic cylinder displacement data for the 773K simulation. The average logarithmic strain of the central element set and reaction force at the top face is then compared to the strain and load cell data for the corresponding experiment. The inverse parameter characterisation is done on the material test for the room temperature results depicted in Figures 4.1(a) and (b). The converged results are displayed in Figures 4.11 and 4.12 respectively.

In Figures 4.11(a) and (b) as well as the actual strains over time in Figure 4.12(a), it is visible that minimal bending is necessary to approximately replicate the distribution of strains around the central circumference of the test section. The six curve fits in Figure 4.12(a) and (b) match well but could be improved. The mismatch is likely due to inadequate parametrisation of the boundary conditions, in this case assumed as constants in Equations (4.3) and (4.4), or an inadequate work hardening form. The parameter identification required 1'156 function evaluations to converge. Each function evaluation required approximately 45s, making the inverse parameter identification an expensive exercise if done using the finite element procedure (≈15h using a single processor).

If the work hardening form is assumed adequate, a proper parametrisation of the boundary conditions would further improve the material parameter estimation. However, the proper parametrisation is also unknown. One concern of this approach is that a better fit to the experimental data might not necessarily imply a better approximation of the material stress-strain curve. It is conceivable that the complex boundary condition allows a better fit to the data, but that both the true stress-strain curve and

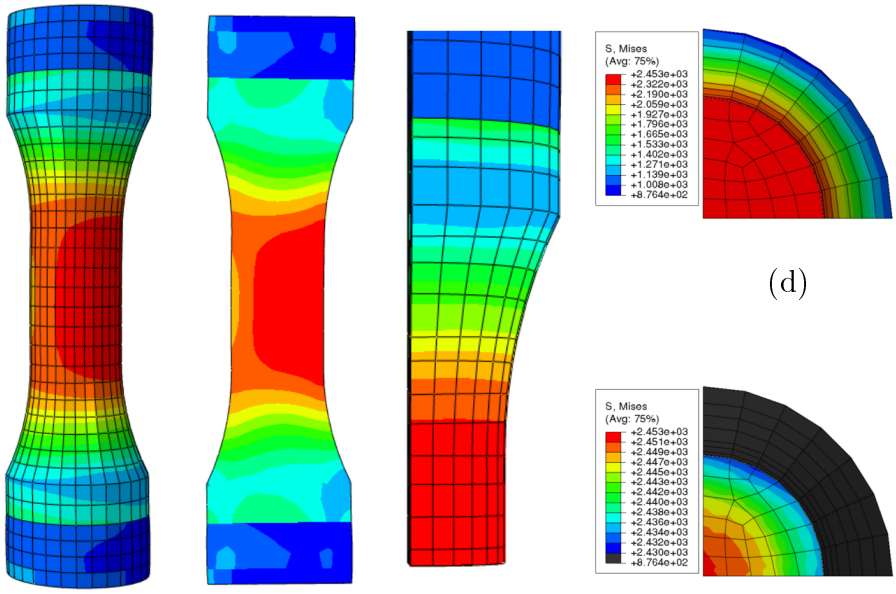

Figure 4.11: (a) External and (b) centre section view of FEA results showing the von Mises stresses at the end of the room temperature simulation where a bend is included in the model. (c) The upper part of the uniaxial compression quarter model for 500°C. A detail of the von Mises stress in a uniaxial compression simulation is visible in (d) with contours scaled so that the gradients can be seen in (e).

the true boundary condition are approximated with worse accuracy. In essence, the inverse problem could be ill-posed where various combinations of stress-strain curves with its associated boundary condition variation can fit the experimental data well. In addition, a more complex boundary condition parametrisation would also require additional unknowns which could result in an even more computationally expensive procedure.

In the next section, a time varying boundary parameter $A(t)$ is used to generate virtual experimental data assuming the change is not linear over time. An inverse analysis is then performed as if the shape of the more complex boundary condition is not known and approximated by a piecewise linear approximation. This is done in order to investigate the sensitivity and general invertibility of the material parameter identification problem.

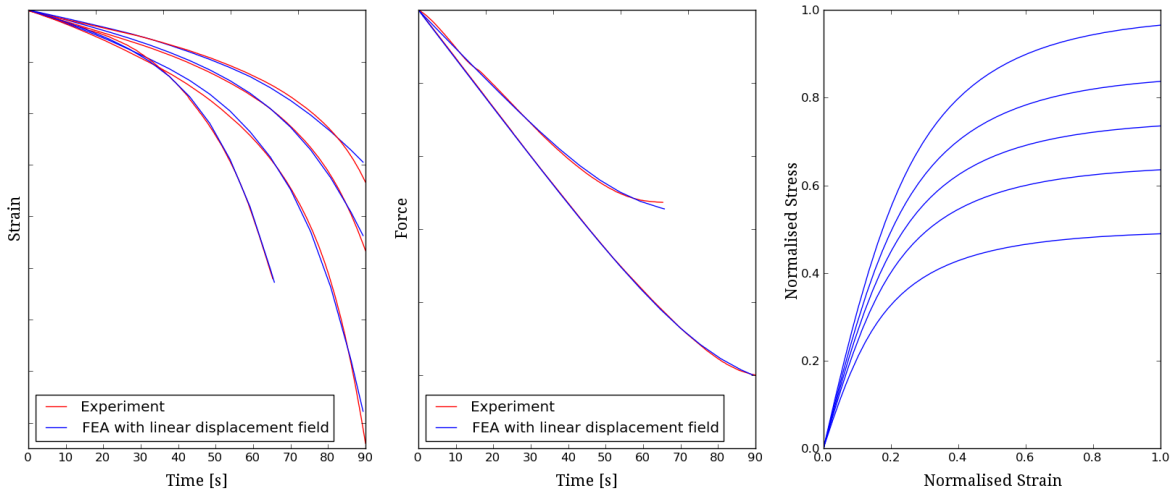

(a) (b) (c)

Figure 4.12: Resulting optimum fit of the FEA curves compared to the experimental data. (a) The three strain gauge measurements as well as the extensometer data compared to what the finite element model predicts. (b) FEA and experimental forces over time. (c) The MTS material response at 25°C, 150°C, 250°C, 350°C and 500°C for a constant strain rate of 0.0001s^{-1} given the material parameter values determined by inverse analysis.

4.2 Simultaneous Estimation of Experimental and Material Parameters

Two different displacement fields are used to set up two different virtual experiments at room temperature. These displacement fields produce strain distributions that have approximately the same order of magnitude difference at the end of the simulation as seen in the actual experimental data. Since the values of the material parameters used in the virtual experiment are known, an inverse analysis may be performed to determine the accuracy with which these known parameters and boundary conditions can be retrieved. Such an investigation gives important insight as to whether the data available is sufficient to distinguish between the effects attributed to the work hardening and the boundary conditions respectively.

As in the previous characterisation, the MTS parameter selections and variables in Table 4.1 are used for this investigation. The material is modelled using the various

parameter values obtained from the inverse material parameter estimation resulting in the fit and response of Figure 4.12.

4.2.1 Virtual Experiment Data

The two sets of virtual experimental data are obtained using the same MTS material parameters with a slightly different boundary condition on the room temperature virtual test. In both 25°C virtual experiments, the angle B is set to a constant 4.5 radians while the virtual hydraulic cylinder displacement is chosen as $y_{hc} = 1t$, $t \in [0, 1]$. The different experimental boundary conditions are obtained by different forms of $A(t)$. In the two virtual experiments, the form of $A(t)$ in Equations (4.3) and (4.4) is chosen as

$$A(t) = \frac{0.03 \times \tanh(3t)}{\tanh(3)} \quad \text{and} \quad A(t) = \frac{0.03 \times \sinh(3t)}{\sinh(3)}. \tag{4.5}$$

The curves that represent $A(t)$ as a function of the time fraction are visible in Figure 4.13. A 500°C virtual experiment is also set up. This high temperature virtual experiment is modelled as a perfect uniaxial compression test subject to a constant hydraulic cylinder displacement rate. The hydraulic cylinder displacement $y_{hc} = 1t$, $t \in [0, 1]$ is again used with a different artificial material section stiffness. After the problems are solved using Abaqus, the following virtual data is extracted from each of the 25°C results:

- The logarithmic strain history of the central test section elements closest to the 0, $^2/_3\pi$ and $^4/_3\pi$ radian locations along the test section circumference. This virtual data is chosen to represent the three strain gauges' histories in the original experiments.
- The total vertical reaction force on the top artificial material section. This is chosen to represent the experimental load cell data.

The normalised strain and force histories that result from the two forms of $A(t)$ can be seen in Figures 4.14(a) through (d). These histories are now used as virtual experimental data to further test the idea of simultaneously estimating material parameters and boundary conditions by inverse analysis. A single set of high temperature FEA results

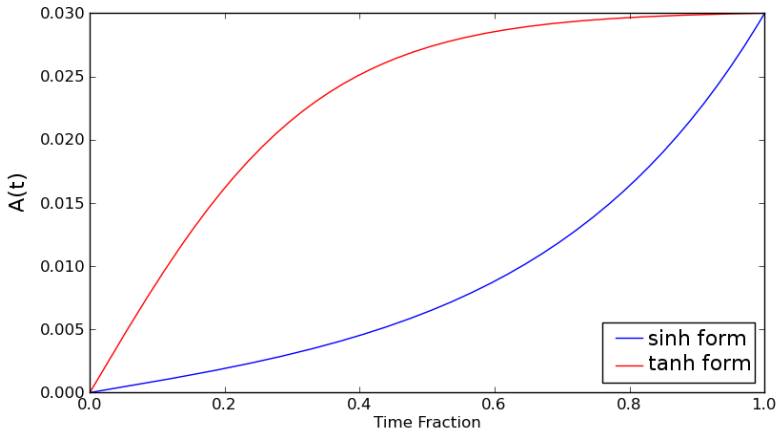

Figure 4.13: Curves selected to represent two possible forms of $A(t)$. These curves represent the definition of $A(t)$ in Equation (4.5), used for the displacement boundary conditions in the virtual experiments.

is used to represent the high temperature experimental data. The total reaction force is again used to represent the load cell data while the average of the central test section element set logarithmic strain histories are used to represent the single extensometer data of the original experiment.

4.2.2 Inverse Analysis

To test the invertibility of this type of problem, the MTS material parameters are determined by again fitting force and strain curves to the 25°C and 500°C virtual experiment data. This inverse analysis aims to recover both the elastic as well as plastic behaviour of the material along with the artificial material stiffness at the different temperatures and boundary conditions, making it a complex inverse parameter identification problem despite the seemingly simple geometry and setup.

Assuming no prior information is available on the shape of the displacement boundary condition $A(t)$ in Equation (4.5), the invertibility of the problem is inspected using a piecewise linear approximation to $A(t)$. First, a single linear time variation is used to approximate the form of $A(t)$. A piecewise linear approximation using three and six intervals is then inspected. The straight line approximation requires one unknown,

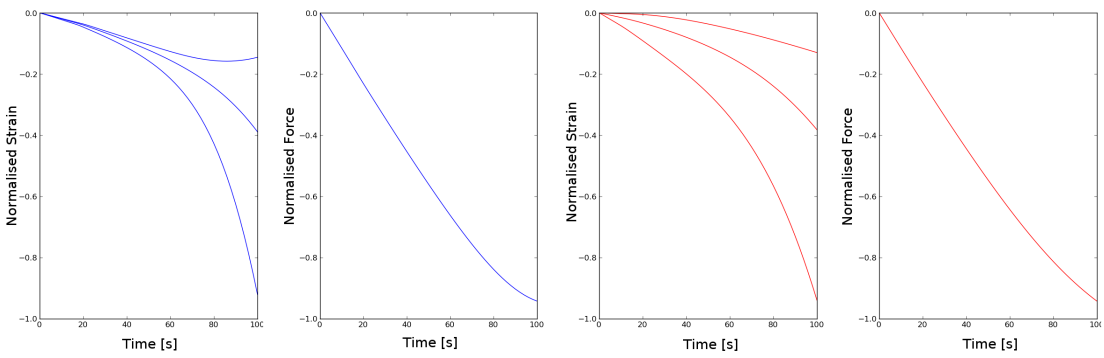

(a) (b) (c) (d)

Figure 4.14: Strain and force history of the three strain gauge locations on the virtual experiment for the (a,b) sinh and (c,d) tanh form of the $A(t)$ definition in Equation (4.5).

while the three intervals and six intervals piecewise linear approximations require three and six unknowns respectively. The optimisation is again performed using the unconstrained optimisation algorithm `fmin` as in the first case.

Given a set of material and boundary condition parameters, a 25°C finite element job is constructed and solved using Abaqus. The logarithmic strains at the same locations along the circumference of the central test section is extracted the same way as originally done to obtain virtual experiment data. These three strain histories are compared to the virtual experiment data. The total reaction force at the top surface of the inverse solution over time and that of the virtual experiment is compared. A finite element analysis for the 500°C problem is also constructed and solved. The average logarithmic strains and total force histories are again extracted from the results as were done to initially obtain the virtual experimental data and compared to its corresponding virtual experiment data set. Each of the four strain histories and two force histories are compared by first normalising it so that the absolute maximum function value is unity. The function value returned is the sum of the mean squared error of the six normalised curve comparisons.

4.2.3 Results

The form of $A(t)$ is first approximated by a single linear time varying section. In this first approximation, the $A(t)$ approximation therefore only requires a single unknown. This unknown along with the angle B, artificial material stiffness at 25°C and 500°C as well as the seven MTS material parameters are estimated simultaneously. The form of $A(t)$ is then approximated by three piecewise linear time varying sections that require an additional two unknowns.

The single line and three piecewise approximation runs were given the same initial guess for all of the corresponding parameters. The two additional parameters in the three interval piecewise linear approximation were also chosen in such a way that the initial approximation was still a straight line. In contrast, the six interval piecewise linear approximation run was continued from the three interval result, taking the parameter values at the termination of the three piece result and adding three additional points on the curve that approximates $A(t)$. Inverse analyses using this single linear approximation, three interval piecewise linear and continued six interval piecewise linear approximation to the form of $A(t)$ are performed on both the sinh and tanh boundary condition virtual experiments.

The results of the final approximation to the form of $A(t)$ in the boundary displacement description using a single, three and six interval piecewise linear approximation are presented in Figure 4.15. The normalised parameter results at the end of each optimisation run are presented in Table 4.2. Figure 4.16 shows the curves that result from the analysis using the initial parameters while Figures 4.17 through 4.19 show the inverse analysis results.

In Table 4.2 and Figure 4.17, it is visible that using too simple an approximation on the boundary condition could result in an inadequate fit and material parameters that are far from the desired accuracy. Here it seems that the material parameters are exploited to compensate for the inadequate capture of the boundary condition. This is also visible in the fit between the green dashed lines and the true material response in Figures 4.20(a) through (d).

Not surprisingly, the higher the resolution used to approximate the form of $A(t)$ in the boundary description, the better the ability to capture the true form and the material parameters. In Table 4.2 and Figure 4.20 it is also visible that an overall

	Sinh BC Virtual Experiment			**Tanh BC Virtual Experiment**		
	Piecewise Linear Approximation			Piecewise Linear Approximation		
	1 Linear	3 Linear	6 Linear	1 Linear	3 Linear	6 Linear
Variable #:	11	13	16	11	13	16
Iterations:	2,200	2'601	+ 2'444	1'395	2'602	+ 1'356
F Value						
Initial:	3.504E-2	3.504E-2	1.776E-4	8.321E-2	8.321E-2	2.017E-4
Final:	3.936E-3	1.776E-4	1.346E-5	9.121E-3	2.017E-4	5.107E-6
Parameter						
$E_{298\mathrm{K}}{}^*$	1.03226	0.99988	1.00019	0.95957	0.99953	0.99997
$E_{773\mathrm{K}}{}^*$	1.00581	1.00026	1.00200	0.93575	0.99155	0.99993
$\mu_r{}^*$	0.78729	0.99029	0.99992	1.98992	1.06192	0.99770
$D_r{}^*$	0.45060	0.97611	1.01220	1.54866	0.72243	0.99628
$\hat{\sigma}_a{}^*$	0.02085	0.97637	0.98440	1.18953	0.29522	1.01126
$\hat{\sigma}_{0\varepsilon s}{}^*$	1.15135	0.99636	0.99641	1.27623	1.15835	0.99869
$\theta_0{}^*$	2.85187	1.04099	1.02566	0.29879	1.22473	0.99488
$k_{\mathrm{B}}/g_{0\varepsilon}b^{3*}$	0.25332	1.10369	1.04966	0.30701	0.83581	0.95063
$k_{\mathrm{B}}/g_{0\varepsilon S}b^{3\ *}$	3.22614	0.96475	1.10172	0.17437	0.52390	0.99750

Table 4.2: Normalised parameter identification results and details of the inverse analyses performed on the sinh and tanh virtual experiments.

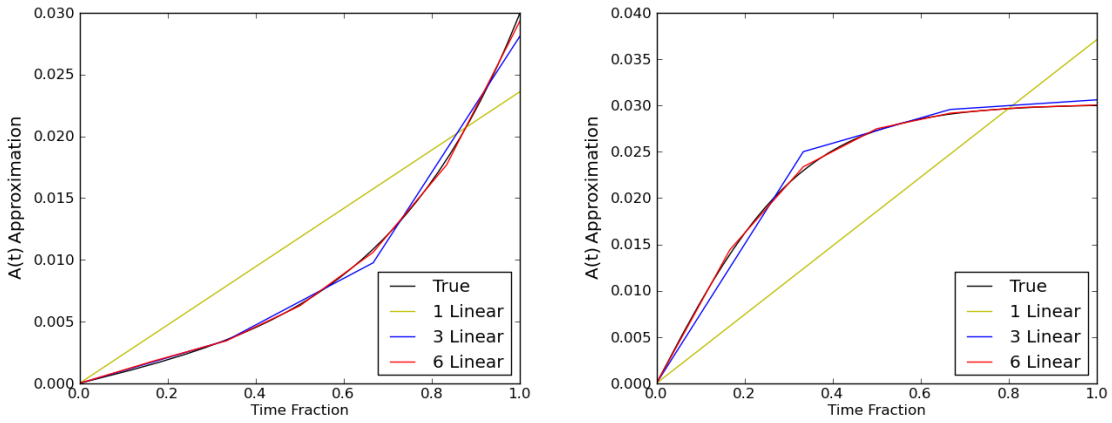

(a) (b)

Figure 4.15: The two forms of $A(t)$, used in the virtual experiment displacement boundary condition compared to the optimum approximations found by using either a single line, three or six piecewise linear approximation. (a) The sinh and (b) tanh virtual experiment results.

improvement on the accuracy of the material parameter identification is achieved when the inverse analysis has the ability to better capture the true boundary condition. Good correspondence is visible between the true material response (black lines) and that determined at the end of the six interval piecewise linear approximation (red dashed lines) in Figure 4.20.

In this work it seems that the inverse problem does not present major issues in simultaneously determining the material properties and test conditions. Although the actual form of the displacement boundary condition that would best replicate the experimental data is unknown, it has been demonstrated that a piecewise linear approximation can produce sufficient accuracy.

Ideally, a fine boundary condition parametrisation should be utilised during the identification of material parameters on real experimental data. This however introduces additional unknowns and could make the optimisation a time consuming procedure. An extended integration point based inverse material parameter identification is considered as an alternative to the full finite element based inverse analysis in Appendix D. This method makes use of three cylinder approximations with a linearly

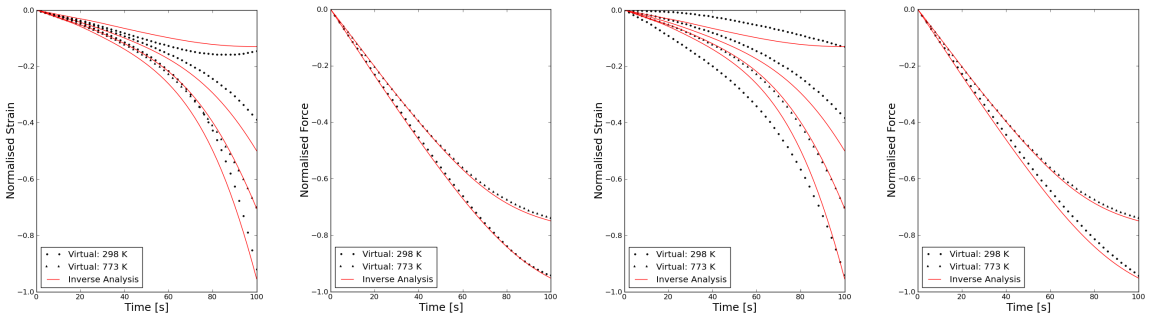

(a) (b) (c) (d)

Figure 4.16: Initial fit on the sinh and tanh virtual experimental data. (a) The strain history and (b) force history fit on the sinh virtual experiment. (c) The strain history and (d) force history fit on the tanh virtual experiment.

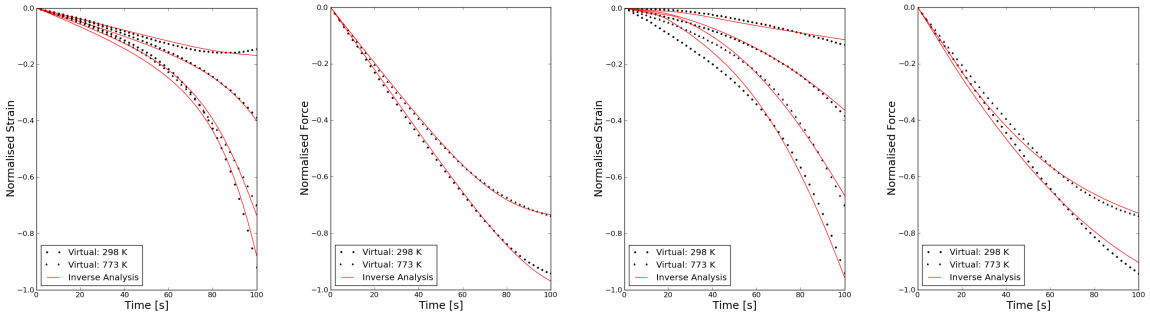

(a) (b) (c) (d)

Figure 4.17: Resulting optimum fit determined by inverse analysis on the sinh and tanh virtual experimental data using a linear approximation of $A(t)$. (a) The strain history and (b) force history fit on the sinh virtual experiment. (c) The strain history and (d) force history fit on the tanh virtual experiment.

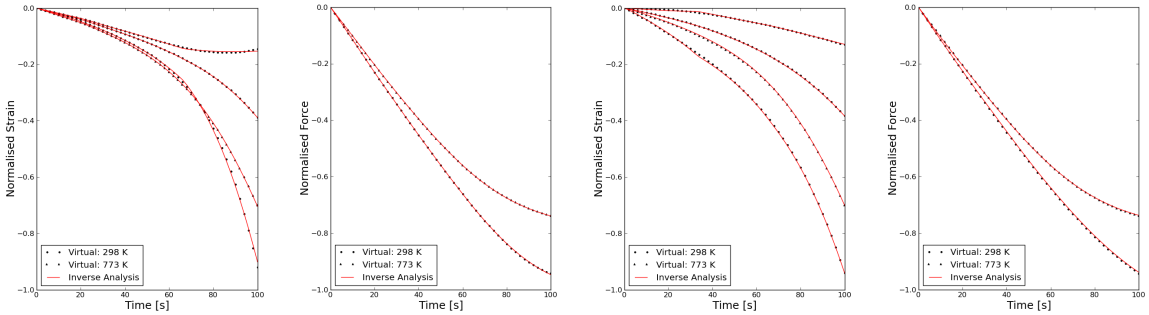

(a) (b) (c) (d)

Figure 4.18: Resulting optimum fit determined by inverse analysis on the sinh and tanh virtual experimental data using a three piecewise linear approximation of $A(t)$. (a) The strain history and (b) force history fit on the sinh virtual experiment. (c) The strain history and (d) force history fit on the tanh virtual experiment.

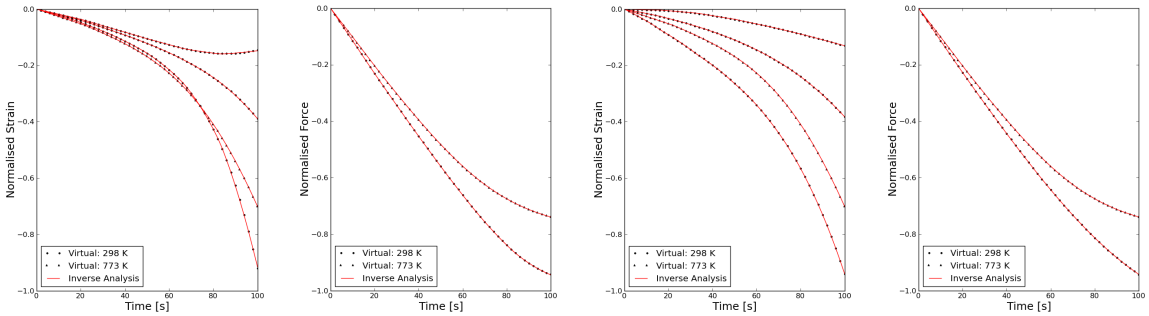

(a) (b) (c) (d)

Figure 4.19: Resulting optimum fit determined by inverse analysis on the sinh and tanh virtual experimental data using a six piecewise linear approximation of $A(t)$. (a) The strain history and (b) force history fit on the sinh virtual experiment. (c) The strain history and (d) force history fit on the tanh virtual experiment.

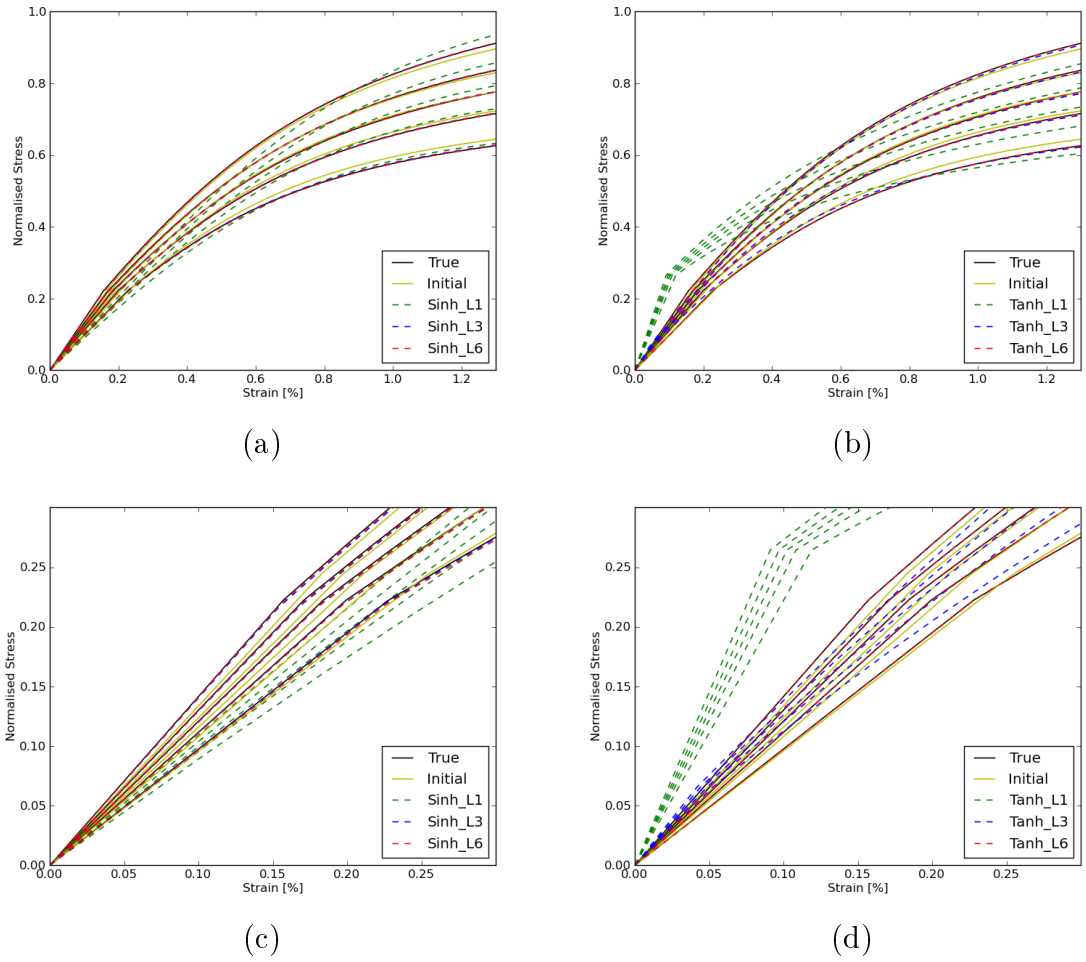

Figure 4.20: The MTS material response at 25°C, 150°C, 250°C, 350°C and 500°C for a constant strain rate of $0.0001s^{-1}$. (a) The various materials approximated using the sinh form of $A(t)$ virtual experiment with detail of the initial yield stress in (c). (b) The various materials approximated using the tanh form of $A(t)$ virtual experiment with detail of the initial yield stress in (d). The approximated material responses are plotted over the response of the actual material with known property values in black.

interpolated strain field through the test section using the experimental data values at each data point. The three cylinder point integration method in Appendix D provides a less time intensive option than using the full finite element procedure and results in characterised material behaviour that is closer to the true response than the simple post-processing alternative.

4.3 Compression of a high pressure high temperature capsule

With the temperature and rate dependent response of the cemented Carbide material characterised, plastic deformation of these materials during an industrial process can now be modelled. As an example, the plastic deformation in the anvils during the compression of a Pyrophyllite high-pressure capsule is modelled in this section.

A cubic-anvil high pressure apparatus (CHPA) is modelled following the work done by Li et al. (2007) and Han et al. (2009). The CHPA makes use of six cubic anvils, actuated by three pairs of hydraulic rams. The anvils have a square tip, forming a cubic cavity during operation. In reality, a preformed capsule or capsule-gasket assembly is compressed in this cavity during the high pressure high temperature (HPHT) synthesis of diamond or manufacture of diamond hardened tools (see for example Wang et al., 2010 or Sano-Furukawa et al., 2014).

The purpose of the capsule is to transmit the applied pressure to a specific area of interest and is therefore made from a pressure transmitting medium such as Magnesium oxide and Pyrophyllite (Wang et al., 2011). A typical preformed capsule, anvil and six axis assembly is displayed in Figure 4.21.

The anvil dimensions in Han et al. (2009) are modelled in this example. In their finite element simulation, the anvil geometry is split into four sections and a single section modelled using perfect plasticity. Li et al. (2007) modelled an octant of the full assembly. They assigned linear elastic behaviour to the anvils while investigating the deformation and pressure distribution in the capsule. The anvil material in this work is modelled using the calibrated MTS model. This allows insight into possible failure mechanisms of the anvils.

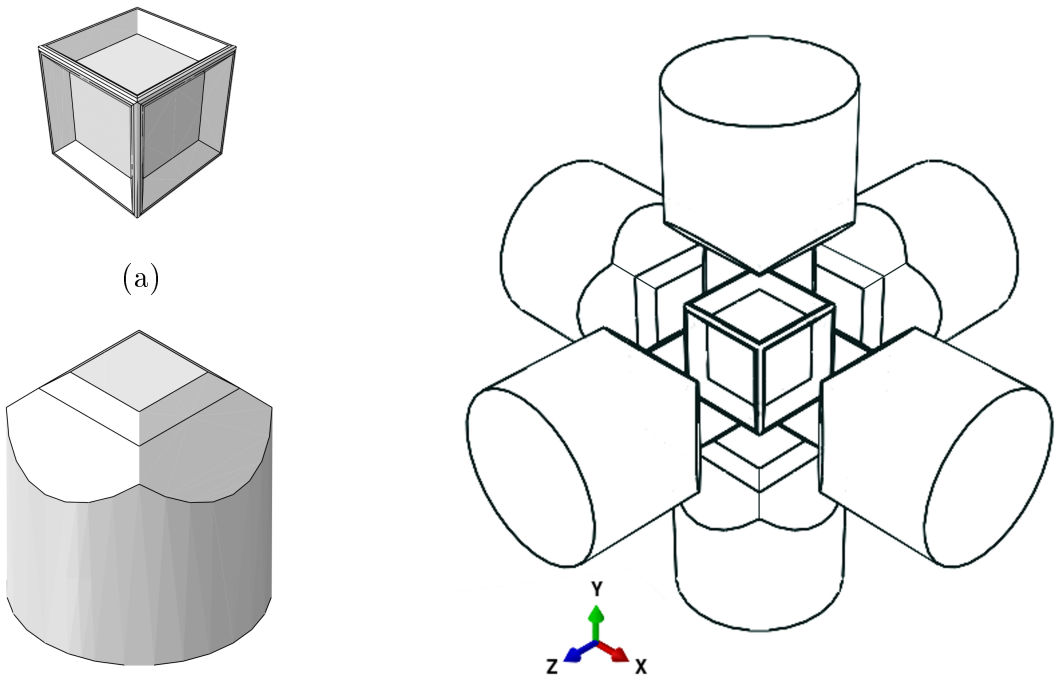

(a) (b) (c)

Figure 4.21: (a) High pressure capsule, (b) anvil design and (c) six axis assembly of the CHPA.

A 120mm long anvil section is modelled with a radius of 60mm and 44×44mm anvil size. The anvil is bevelled at 41.5° followed by an edge at 46°relative to the anvil working surface. The anvil dimensions are displayed in Figure 4.22(a). The capsule is 55×55×55mm without the gasket and has an overall dimension of 70×70×70mm with the gasket included. The capsule is preformed with the same material used for capsule and gasket. The dimensions of the anvil preformed capsule is visible in Figure 4.22(b).

4.3.1 Model

According to Fontanari et al. (2006), the yield behaviour of Pyrophyllite follows the Mohr-Coulomb model

$$\tau = c - \sigma \cdot \tan(\phi), \tag{4.6}$$

where τ is the shear stress, σ the normal stress, c is the cohesive strength of the material and ϕ the angle of internal friction. The Mohr-Coulomb model is a standard model

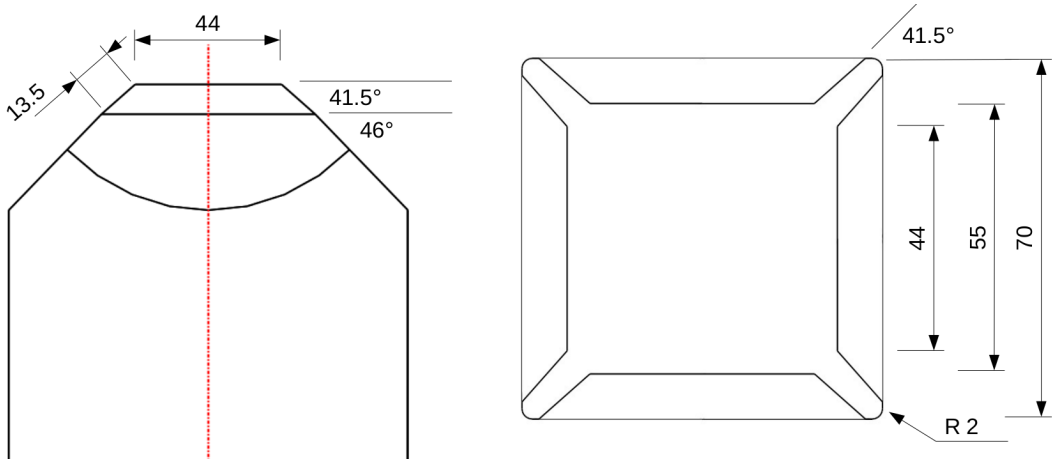

Figure 4.22: Dimensions of the (a) cemented Carbide anvil and (b) Pyrophyllite capsule.

available in Abaqus and can therefore be used to model the capsule in this study using material parameter values to represent Pyrophyllite.

In our simulation a bulk modulus of 220GPa and Poisson's ratio of 0.12 is assumed, taken from the work by Li et al. (2007). The elastic modulus modelled is therefore $E = 3\kappa\,(1 - 2\nu) = 3 \times 220 \times (1 - 0.24) = 501.6$GPa. Further following the study done by Li et al. (2007), a cohesive strength value of 13.87MPa, angle of internal friction equal to 20.68° and dilation angle of 0° is further used to model the capsule.

The cemented Tungsten Carbide anvils are modelled using the user material framework with the MTS hardening subroutine. The material parameter values obtained from the inverse material parameter estimation resulting in the fit and response of Figure 4.12 is again used in this study. The example problem is modelled assuming a uniform temperature of 1000K throughout the anvil.

An octant of the full assembly is modelled to exploit the symmetry of the problem. The quarter anvil geometry is represented using 14209 ten noded tetrahedral elements (C3D10) while an eighth of the preformed capsule is modelled using 2156 reduced integration linear brick elements (C3D8R). An isometric and side view of the meshed assembly are visible in Figure 4.23.

Three hard normal contact interactions are defined between a master surface on the

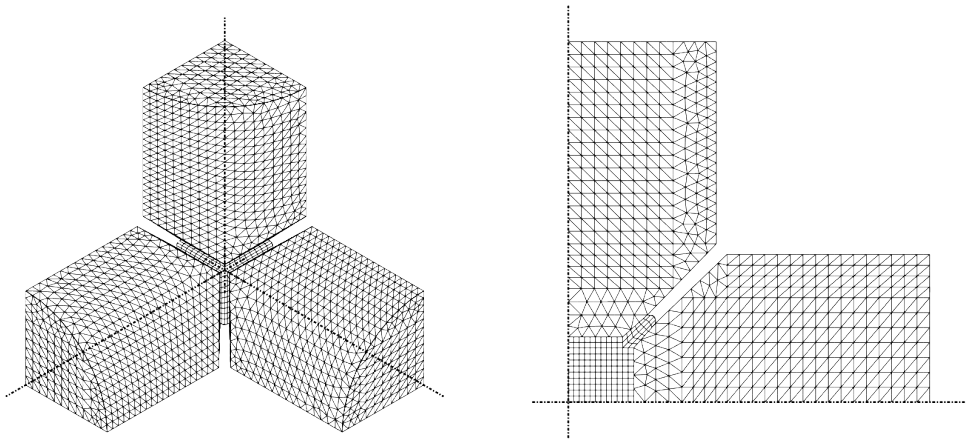

(a) (b)

Figure 4.23: Mesh of the cubic-anvil high pressure apparatus assembly. (a) Isometric view and (b) side view of the meshed octant representation.

anvil section and and slave surface on the associated side of the high-pressure capsule. Again following Li et al. (2007), a contact friction coefficient of $\mu_{\text{frict}} = 0.75$ is further attributed to the interaction between the anvil and capsule.

The z direction displacements on the xy plane are constrained for the nodes associated with that symmetry plane. This is also done for the y direction in the xz and x direction in the yz planes. The applied force boundary condition at the application surface of the anvil geometries are prescribed in Abaqus as a total distributed load boundary condition.

A linear ramp from 0N to 2000kN is applied to the end of each quarter anvil geometry over 3000 seconds, solved using automatic time stepping with an initial step size of 1s and maximum allowable step size of 30s. The results are obtained in 108 solution increments.

4.3.2 Results

Results of the finite element simulation are displayed in Figure 4.24 for the end of the CHPA compression modelled. The maximum von Mises stresses in this example are in the range of 1.77GPa to 1.93GPa in Figure 4.24(a). According to Figures 4.24(a) and (c), the highest stresses and plastic deformation happen around the centre of the anvil

below the bevel depth at about 18mm to 30mm below the surface of the anvil.

In Figure 4.24(b) the stress values along the centre of the anvil are given. This is plotted as a function of the distance from the anvil working surface. Figure 4.24(b) can therefore be seen as a plot of the values at the bottom of the anvil in Figure 4.24(a) with the distance from the contact surface used as the x axis. In this figure a maximum von Mises stress of 1.92GPa is reported at a distance of approximately 24mm below the contact surface.

Figure 4.24(d) shows the stress gradients on the surface of the anvil. The gradients on the face vary from 236.76MPa at the centre of the face to 1.08GPa at the edge and 1.22GPa at the corner of the anvil working surface.

The pressure distribution in the capsule is inhomogeneous according to Figure 4.25(a), with pressures ranging from 2.42GPa in the centre to 2.15GPa at the surface in the $\boldsymbol{n}_x = \{1, 0, 0\}$ or x direction. In Figure 4.25(b) the pressure values are plotted from the centre of the capsule in three directions for a better visualisation of the pressure distribution, namely:

- the x direction or $\boldsymbol{n}_x = \{1, 0, 0\}$,
- the xy direction or $\boldsymbol{n}_{xy} = \left\{\sqrt{1/2}, \sqrt{1/2}, 0\right\}$ and
- the xyz direction or $\boldsymbol{n}_{xyz} = \left\{\sqrt{1/3}, \sqrt{1/3}, \sqrt{1/3}\right\}$.

This plot again shows the inhomogeneity in the pressure distribution with the x and xy values directly comparable to the contour values in the same direction in Figure 4.25(a). According to Figure 4.25(b), there is a fairly homogeneous pressure for a radius of approximately 5mm from the centre of the capsule at 2.42GPa. The pressure drops to about 2.15GPa at the centre of the anvil surface and peaks at about 2.77GPa at a distance of 26.57mm in the xyz direction, i.e. $\{x, y, z\} = \{18.8, 18.8, 18.8\}$.

The ideal setup should result in a more homogeneous pressure throughout the pressure distribution medium with minimal plastic deformation in the anvil. Different anvil and capsule geometries as well as capsules assembled from different materials (Wang et al. (2010) use a capsule assembled from various components made from Pyrophyllite, Steel, Dolomite, Graphite, Molybdenum and MgO for example) can be tested and developed while also including the temperature and rate dependent plastic

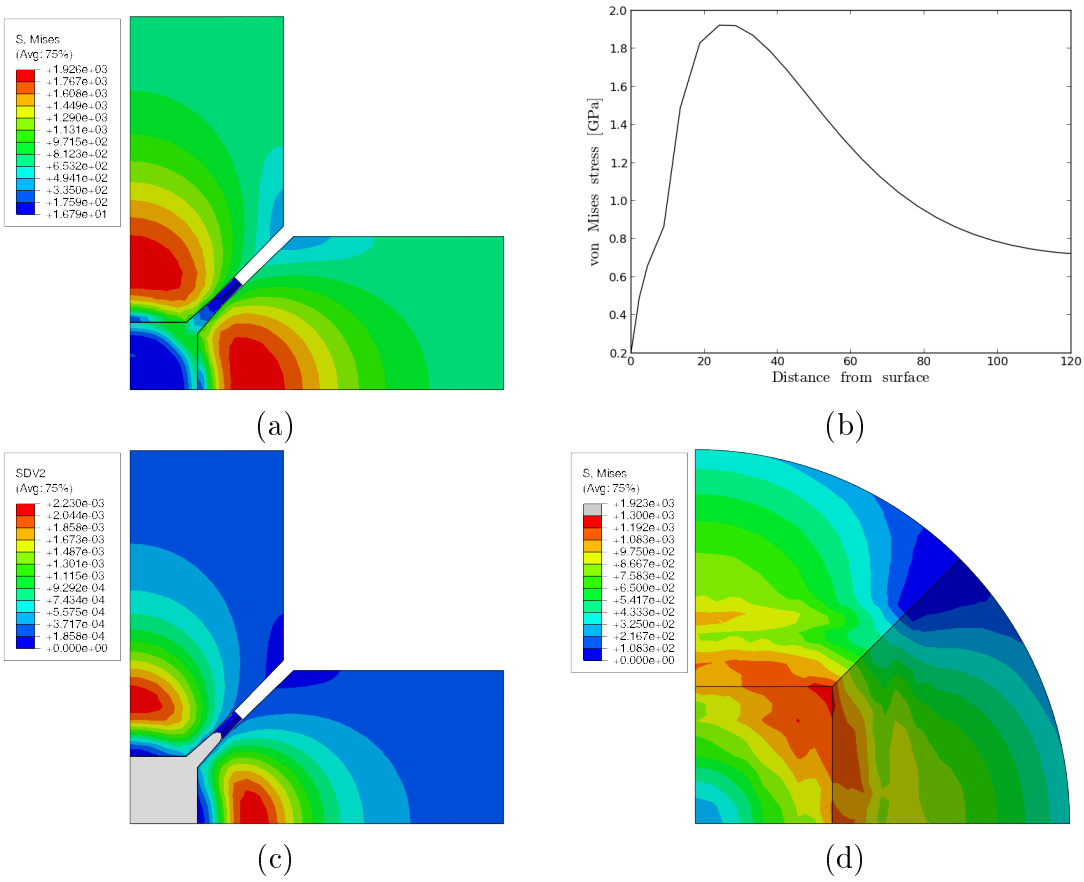

Figure 4.24: Results obtained from a finite element analysis on an octant of the CHPA assembly modelled. (a) Von Mises stress contours in the yz plane. (b) Von Mises stress values in the centre of the anvil plotted as a function of distance from the working surface. (c) Equivalent plastic deformation in the yz plane. (d) Von Mises stress viewed from the anvil working surface.

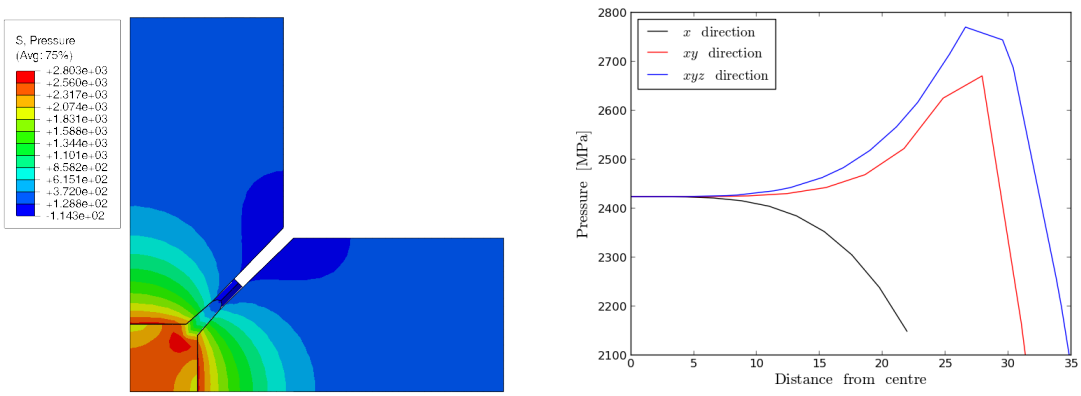

(a) (b)

Figure 4.25: Pressure distribution (a) in the assembly modelled and (b) along specific directions in the high pressure capsule.

deformation of the cemented Carbide anvil using the MTS model with parameter values identified in this chapter. This however is not included in the scope of this thesis with subsequent chapters rather investigating and implementing additional material models and problems.

4.4 Conclusions

The focus of the work done in this chapter was directed at the improved characterisation of hardmetal material parameter values in the case of non-ideal experimental test data.

In this chapter, the concept of simultaneous material and time varying boundary value estimation is introduced and investigated using finite element analyses within the optimisation loop. From the investigation the proposed procedure seems satisfactory in more accurately determining the material property values than the original procedure. The piecewise linear case illustrated that improved accuracy could be achieved, even when the correct parametrisation is unknown. It does however come at an increased computational cost.

Using the MTS model to describe the rate and temperature dependent plastic deformation in cemented Tungsten Carbide, industrial processes where this material is used can be studied and improved. Much like the example in Section 4.3, the effect

of different boundary conditions, anvil and high pressure cell design can be studied in the industrial HPHT process for example.

The Mechanical Threshold Stress model used in this and the previous chapter is a dislocation density based model where the choice of state variable is a stress-like quantity. In the following chapter, an alternative state variable choice is introduced and other dislocation density based extensions to the model foundation are discussed and implemented.

Chapter 5

Dislocation Density Based Modelling Extensions

The plastic response considering temperature and rate effects for the metallic materials in Chapters 3 and 4 are well represented using the Mechanical Threshold Stress model. This model does not however describe phenomena such as the Bauchinger effect or recrystallisation. State variable based model extensions that capture or mimic the material response in the presence of large strains, thermal recovery, cyclic loading and recrystallisation are therefore investigated and discussed in this chapter.

In Chapter 3, the development and implementation of the Mechanical Threshold Stress model was discussed with a phenomenological description on the work hardening of the evolving thermally activated stress component. The work hardening followed the original or a modified Voce-like functional form. In this chapter, the model framework is expanded by first introducing the dislocation density ratio as an alternative internal state variable choice following the modelling approach described by Estrin (1996). Thermal recovery of statistically stored dislocations and the effect of geometrically necessary dislocations in the case of small grain sizes or in the stage IV hardening regime are used to supplement the original Kocks-Mecking work hardening theory within the dislocation density based model framework.

The state variable based constitutive model framework is also extended in the case of cyclic deformation by introducing additional state variables to represent the equivalent back stress as well as a statistical wall dislocation density ratio. The latter

dislocations are modelled to inject back into the bulk statistically necessary dislocation density state variable once load reversal occurs.

A continuum based model for material response in the case of multiple waves of static and dynamic recrystallisation is introduced at the end of this chapter. This is presented as an extension to the isotropic plasticity state variable based constitutive model framework similar to the work by Brown and Bammann (2012). The driving forces, grain boundary mobility and interfacial subgrain surface area between unrecrystallised and recrystallised subgrains are used to model and predict the material response during recrystallisation.

5.1 Dislocation density based model variation

In the Mechanical Threshold Stress (MTS) model implementation of Chapter 3, an evolving threshold stress value $\hat{\sigma} = \frac{1}{2}M\mu b\sqrt{\rho}$ was chosen as the internal state variable. Recalling Section 3.2, the temperature and rate dependent evolution of the internal stress value in the presence of additional equivalent plastic strain according to the Kocks-Mecking work hardening theory can take the form

$$\frac{d\hat{\sigma}}{d\alpha} = \frac{M\mu b}{4\sqrt{\rho}}\frac{d\rho}{d\alpha} \quad \text{where} \quad \frac{d\rho}{d\alpha} = Mk_1\sqrt{\rho} - Mk_2(\dot{\alpha}, T)\,\rho. \tag{5.1}$$

Introducing the initial work hardening θ_0 as well as the temperature and rate dependent saturation stress $\hat{\sigma}_s(\dot{\alpha}, T)$ in Equations (3.16) leads to the Voce law in Equation (3.17). This means that the evolution of the threshold stress value could be expressed as a function of itself. An alternative choice on internal state variable could also be considered following the dislocation density based modelling approach of Estrin (1996). While the initial value of the true dislocation density values ($\rho_0 = \rho|_{\varepsilon_\mathrm{p}=0}$) make the choice of dislocation density itself a difficult choice for an internal state variable, a stress like constant $\sigma_0 = \frac{1}{2}M\mu b\sqrt{\rho_0}$ can be introduced so that the threshold stress value is now determined from

$$\hat{\sigma}_\varepsilon = \sigma_0\sqrt{\varrho}. \tag{5.2}$$

This modification introduces the dislocation density ratio variable $\varrho = \frac{\rho}{\rho_0}$, a new internal state variable with typical initial value $\varrho|_{\varepsilon_\mathrm{p}=0} = 1$. The constitutive formulation

may now be completed by using the theory on dislocation density based modelling to evolve the dislocation density ratio in the process of plastic deformation instead of the threshold stress directly. By introducing $C_1 = Mk_1/\sqrt{\rho_0}$ and $C_2\left(\dot{\alpha}, T\right) = Mk_2\left(\dot{\alpha}, T\right)$, evolution of the threshold stress value from Equation (5.1) may now take the form

$$\frac{d\hat{\sigma}_\varepsilon}{d\alpha} = \frac{\sigma_0}{2\sqrt{\varrho}}\frac{d\varrho}{d\alpha} \quad \text{where} \quad \frac{d\varrho}{d\alpha} = C_1\sqrt{\varrho} - C_2(\dot{\alpha}, T)\ \varrho. \tag{5.3}$$

In the description of the dislocation density based model used by Estrin (1996), a kinetic equation of the form in Equation (3.1) is used while we will stay with the form in Equation (3.3) used to construct the MTS model scaling functions in Equation (3.22). Assuming that the non-evolving thermal portion of the yield stress is negligible ($\hat{\sigma}_i = 0$) along with the introduction of Equation (5.2), the temperature and rate dependent flow stress for the model takes the form

$$\sigma_{\mathrm{Y}} = \hat{\sigma}_a + S_\varepsilon(\dot{\alpha}, T)\frac{\mu}{\mu_r}\sigma_0\sqrt{\varrho}. \tag{5.4}$$

The yield stress here is now a function of the dislocation density ratio internal state variable ϱ. The evolution of the dislocation density ratio in Equation (5.3) is equivalent to the evolution equation constructed by combining the accumulation and annihilation contributions from Equations (3.8) and (3.9) with the introduction of C_1 and C_2. While C_1 is a constant, a formulation for the annihilation function $C_2\left(\dot{\alpha}, T\right)$ is still needed to complete the model description. Estrin (1996) uses an annihilation function

$$C_2\left(\dot{\alpha}, T\right) = C_{20}\left(\frac{\dot{\alpha}}{\dot{\varepsilon}_{02}}\right)^{1/n}, \tag{5.5}$$

where C_{20} and $\dot{\varepsilon}_{02}$ are material constants while n may take different values for different temperatures. An alternative formulation may be constructed by considering Equations (3.16) and (3.26) so that the annihilation function is equivalent to the work by Chen and Gray (1996) and the MTS model of Follansbee and Kocks (1998). Using these equations:

$$C_2\left(\dot{\alpha},T\right)=\frac{2\theta_0}{\hat{\sigma}_s\left(\dot{\alpha},T\right)}\quad\text{and}\quad\hat{\sigma}_s\left(\dot{\alpha},T\right)=\hat{\sigma}_{0s}\exp\left[\frac{k_{\mathrm{B}}T}{g_{0s}b^3\mu}\ln\left(\frac{\dot{\alpha}}{\dot{\varepsilon}_{0s}}\right)\right],\tag{5.6}$$

so that the dynamic recovery is rather modelled by the annihilation function

$$C_2(\dot{\alpha},T)=C_{20}\exp\left[-\frac{T}{a_{02}\mu}\ln\left(\frac{\dot{\alpha}}{\dot{\varepsilon}_{02}}\right)\right].\tag{5.7}$$

In this function $C_{20}=2\theta_0/\hat{\sigma}_{0s}$ is a constant while $\dot{\varepsilon}_{02}\equiv\dot{\varepsilon}_{0s}$ for subscript consistency. The parameter a_{02} is again the convenient grouping of constants and parameters $a_{02}=g_{0s}b^3/k_{\mathrm{B}}$ much like Equation (3.48) with g_{0s} the normalised activation energy, b the magnitude of the Burgers' vector length and $k_{\mathrm{B}}=1.38064852\times10^{-23}\mathrm{m^2kgs^{-2}K^{-1}}$ the Boltzmann constant.

To illustrate the response of the alternative dislocation density based formulation compared to that of the MTS model, the temperature and rate dependence of the two model cases are illustrated here with arbitrary material parameter values. In both cases, the temperature dependent shear modulus is modelled using Equation (3.21) with $\mu_r=100\mathrm{GPa}$, $D_r=10\mathrm{GPa}$ and $T_r=200\mathrm{K}$ and a Poisson's ratio of 0.3. The athermal flow stress component is $\hat{\sigma}_a=10\mathrm{MPa}$ while the threshold stress scaling function is modelled using a reference strain rate value $\dot{\varepsilon}_0=10^7s^{-1}$. The scaled activation energy parameter $a_{0\varepsilon}=2\mathrm{K/MPa}$ and statistical constant values of $p_\varepsilon=\frac{1}{2}$ and $q_\varepsilon=\frac{3}{2}$ are assumed. In equation form, this means that for both models

$$\mu(T)=10^5-\frac{10^4}{\exp\left({}^{200}/_{T}\right)-1}\quad\text{and}\quad\sigma_{\mathrm{Y}}=10+\frac{\mu}{10^5}\left[1-\left(\frac{T}{2\mu}\ln\frac{10^7}{\dot{\alpha}}\right)^{2/3}\right]^2\hat{\sigma}.\tag{5.8}$$

In the MTS model, Voce hardening is modelled using an initial hardening rate $\theta_0=5\mathrm{GPa}$ while the temperature and rate dependent saturation stress parameters are $\hat{\sigma}_{0\varepsilon s}=1000\mathrm{GPa}$, $\dot{\varepsilon}_{0\varepsilon s}=10^{10}\mathrm{s^{-1}}$ and $a_{0\varepsilon s}=0.2\mathrm{Kms^2kg^{-1}}$. The initial state variable value is set to $\hat{\sigma}|_0=0\mathrm{MPa}$.

In the alternative formulation, a reference stress value $\sigma_0=100\mathrm{MPa}$ is used so that $\hat{\sigma}=100\sqrt{\varrho}$. From Equation (3.16) along with the definitions of $\sigma_0=\frac{1}{2}M\mu b\sqrt{\rho_0}$ and $C_1=Mk_1/\sqrt{\rho_0}$, an accumulation constant $C_1=2\theta_0/\sigma_0=100$ is chosen. The annihila-

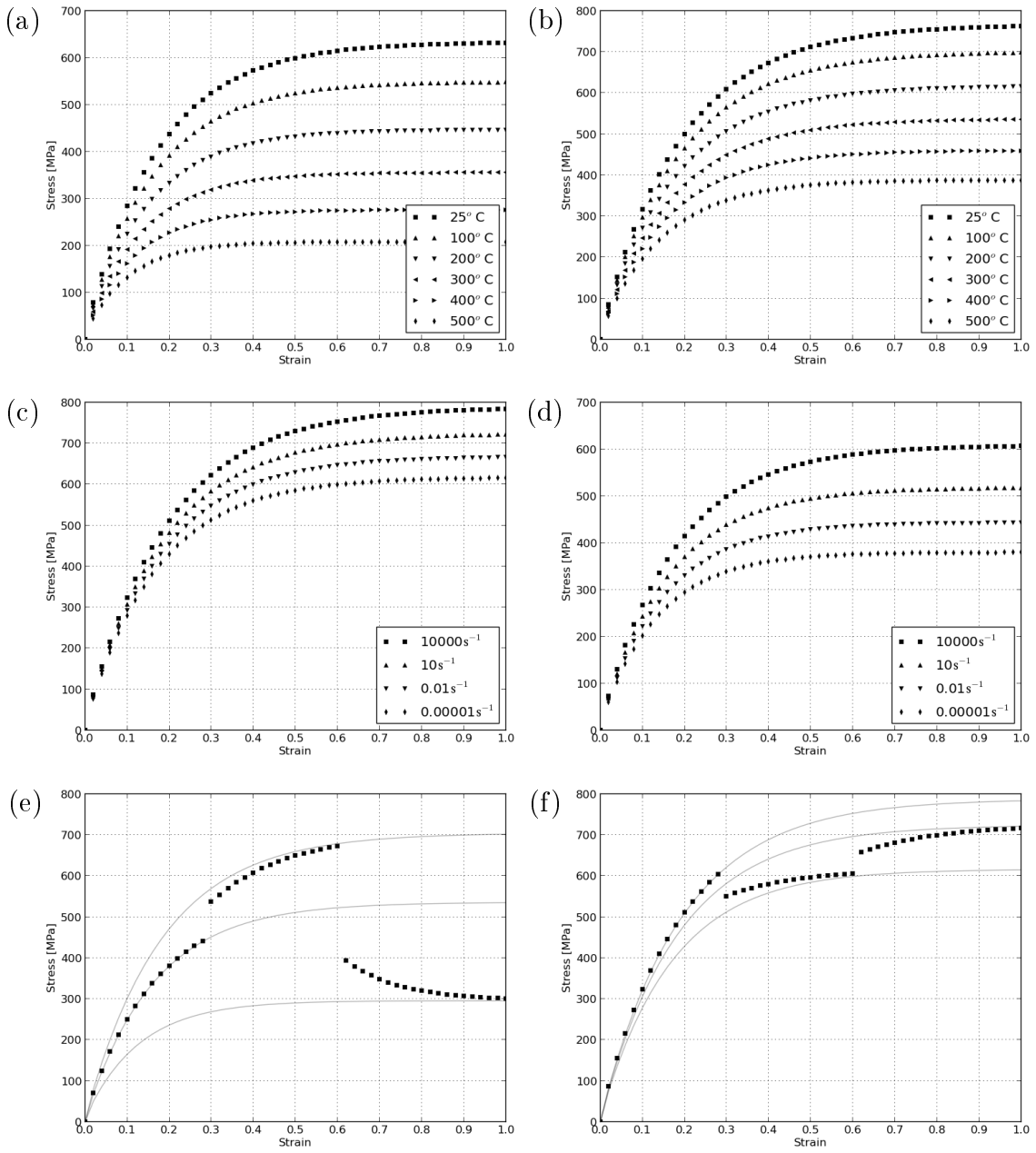

Figure 5.1: Temperature and rate dependence of the Mechanical Threshold Stress material model. Temperature dependence is illustrated for various temperatures at (a) $\dot{\varepsilon} = 0.0001\text{s}^{-1}$ and (b) $\dot{\varepsilon} = 1000\text{s}^{-1}$. Rate dependence is illustrated for different strain rates at (c) 25°C and (d) 250°C. (e) Deformation at $\dot{\varepsilon} = 1\text{s}^{-1}$ for temperatures starting at 200°C for the first 0.3 strain, 25°C up to 0.6 strain followed by 500°C up to completion. (f) Deformation at 25°C with rates changing from 10000s^{-1} to 0.00001s^{-1} followed by 10s^{-1} up to completion.

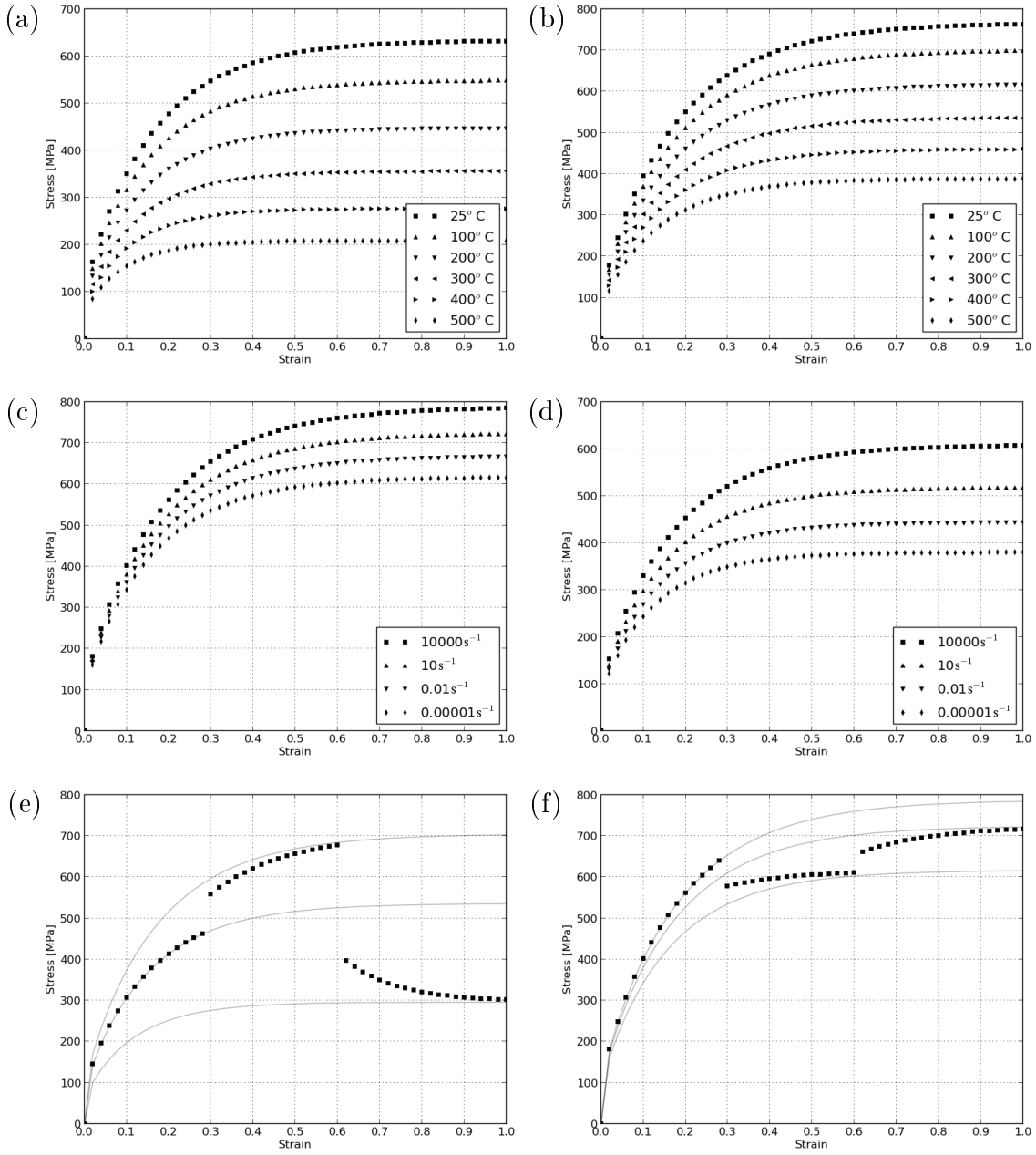

Figure 5.2: Temperature and rate dependence of the dislocation density based model. Temperature dependence is illustrated for various temperatures at (a) $\dot{\varepsilon} = 0.0001\text{s}^{-1}$ and (b) $\dot{\varepsilon} = 1000\text{s}^{-1}$. Rate dependence is illustrated for different strain rates at (c) 25°C and (d) 250°C. (e) Deformation at $\dot{\varepsilon} = 1\text{s}^{-1}$ for temperatures starting at 200°C for the first 0.3 strain, 25°C up to 0.6 strain followed by 500°C up to completion. (f) Deformation at 25°C with rates changing from 10000s^{-1} to 0.00001s^{-1} followed by 10s^{-1} up to completion.

tion function in Equation (5.7) is modelled using parameter values $C_{20} = 2\theta_0/\hat{\sigma}_{0s} = 10$, $a_{02} = 0.2\text{Kms}^2\text{k}g^{-1}$ and $\dot{\varepsilon}_{02} = 10^{10}\text{s}^{-1}$. The temperature and rate dependence of the two different models using the material parameter values stated are presented in Figures 5.1 and 5.2. In Figure 5.1(a) the MTS material model response at a constant strain rate of 10^{-4}s^{-1} is given for 25°C, 100°C, 200°C, 300°C, 400°C and 500°C while (b) shows the response at 10^{3}s^{-1}. The rate dependence is illustrated at (c) 25°C and (d) 250°C for strain rates 10^{4}s^{-1}, 10s^{-1}, 10^{-2}s^{-1} and 10^{-5}s^{-1} while (e) and (f) shows what happens if the temperatures and strain rates vary during the straining process. In Figure 5.2, the alternative dislocation density model response is given for the same temperature and strain rates for comparison.

By design, the two different choices of internal state variable based model formulation produce similar responses in terms of temperature and rate dependence as well as the initial work hardening and saturation stress values. The initial value of the reference threshold stress is zero in the Mechanical Threshold Stress formulation while the choice of $\sigma_0 = 100\text{MPa}$ and $\varrho_0 = 1$ means that the reference threshold stress is $\hat{\sigma} = 100\text{MPa}$ in the alternative dislocation density ratio based formulation. The result of this is visible at the onset of plasticity with a similar initial yield stress value in each of the MTS responses while there is a distinct temperature and rate dependent distribution of the initial yield stress values in the alternative formulation.

A benefit of the dislocation density ratio based constitutive equations lies in the ease with which it can be extended to model additional physical phenomena as discussed in the subsections to follow.

5.2 Geometrically necessary dislocations and stage IV hardening

Grain size effects are modelled in the limit where the density of geometric obstacles is much larger than that of the obstacles caused by other dislocations in the population (Estrin, 1996). The modelling of geometric effects are necessary to model materials with small grain sizes, many precipitates or in the case of large plastic strains. In this case a second mean free path L_g is identified which is related to the spacing between

geometric obstacles or grain boundaries. If a direct effect of the geometric obstacles on the flow stress is disregarded, the only effect these obstacles have will be on the rate of dislocation density evolution. The storage term associated with these geometrically necessary dislocations can be expressed as an extension to the incremental change in dislocation density in Equation (3.6) by:

$$d\rho^{(+)} = \frac{M}{bL_g}\, d\alpha. \tag{5.9}$$

In the dislocation density ratio based model used by Estrin (1996), the geometric mean free path is taken as the spacing between grain boundaries or other geometric obstacles with a stabilised obstacle structure. Considering the form of the dislocation density ratio evolution in Equation (5.3), this model introduces the constant $C = M\left(\rho_0 b L_g\right)^{-1}$. The alternative model formulation in Section 5.1 is therefore expanded in the case of stable small grain sizes or closely spaced geometrical obstacles through the addition of this constant to the dislocation density ratio evolution equation

$$\frac{d\varrho}{d\alpha} = C + C_1\sqrt{\varrho} - C_2(\dot{\alpha}, T)\ \varrho. \tag{5.10}$$

A further modification is necessary in the more general case where the geometric substructure does not remain constant as in the case with stage IV hardening during excessive straining. While the statistically determined mean free path relates to the total dislocation density through $L_s \propto 1/\sqrt{\rho}$, the geometrically determined mean free path L_g may be related to the average slip plane lattice incompatibility $\bar{\lambda}$ following the work by Acharya and Beaudoin (2000) and Kok et al. (2002). The relationship between the geometrically determined mean free path and average lattice incompatibility can be modelled in the same way as the statistical mean free path by $L_g \propto 1/\sqrt{\bar{\lambda}}$. Considering the nett dislocations are arranged in a linear fashion on the other hand, Acharya and Beaudoin (2000) used the relationship $L_g \propto 1/\bar{\lambda}$, leading more generally to the empirical statement by Kok et al. (2002):

$$L_g \propto \left(\frac{1}{\bar{\lambda}}\right)^{r_g} \tag{5.11}$$

where the parameter $1/2 \leq r_g \leq 1$ is introduced.

A stress like variable related to the slip plane lattice incompatibility has been used by Kok et al. (2002) as well as Brown and Bammann (2012). The latter work also used it in conjunction with recrystallisation. The numerical model considered here however can make use of the inverse geometrically determined mean free path or the average lattice slip plane incompatibility as an internal state variable within the dislocation density ratio framework. The storage term associated with geometrically necessary dislocation in Equation (5.9) can take the form

$$d\rho^{(+)} = \frac{M}{b}\bar{\lambda}^{r_g}\, d\alpha. \tag{5.12}$$

Instead of Equation (5.10), a more general form of the dislocation density ratio evolution equation is now given by

$$\frac{d\varrho}{d\alpha} = C_g\bar{\lambda}^{r_g} + C_1\sqrt{\varrho} - C_2(\dot{\alpha}, T)\ \varrho \tag{5.13}$$

where $C_g = M/\left(\rho_0 b\right)$. Further, Kok et al. (2002) observed that the evolution of the average slip plane lattice incompatibility is inversely proportional to the grain size d_{x}. Using the proportionality constant C_λ, an evolution equation for this parameter is

$$\frac{d\bar{\lambda}}{d\alpha} = \frac{C_\lambda}{d_{\mathrm{x}}}. \tag{5.14}$$

The addition of the large strain model extension is illustrated in Figure 5.3 using the same temperature and strain histories as used in the results of Section 5.1. The same material property values giving the material response illustrated in Figure 5.2 is used but this time including the additional average slip plane lattice incompatibility internal state variable with evolution Equation (5.14) and $C_\lambda/d_{\mathrm{x}} = 1$. The dislocation density ratio evolution equation is described by Equation (5.13) instead of Equation (5.3) with $C_g = 1000$ and $r_g = 1$.

In the figures, the effect of the geometrically necessary dislocation extension is visible. Instead of saturating as in the response visible in Figure 5.2, the response rather approaches a constant strain hardening state. In the original MTS model a similar effect is achieved by modifying the Voce hardening law as in Equation (3.25).

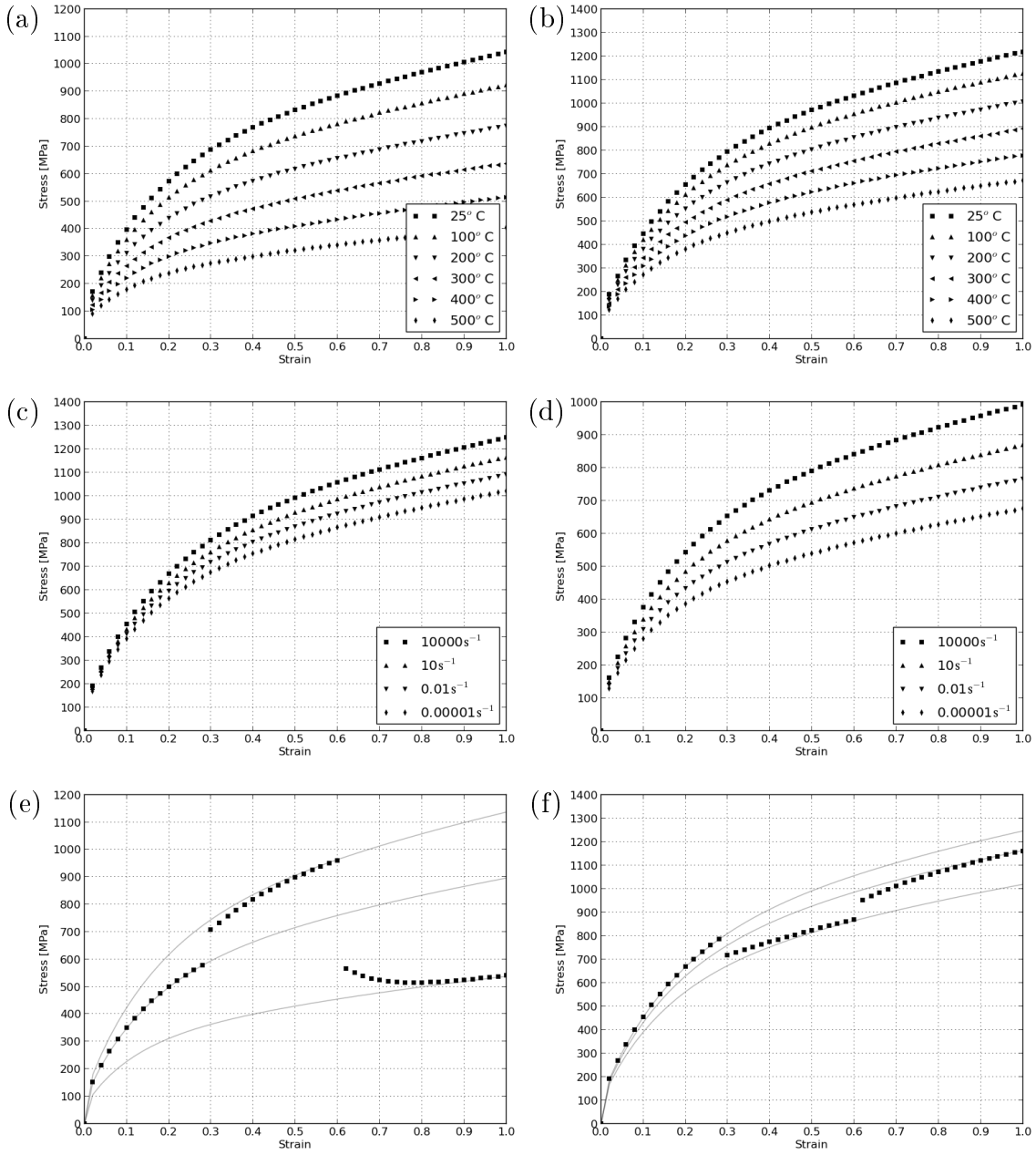

Figure 5.3: Temperature and rate dependence of the model including geometrically necessary dislocations. Temperature dependence is illustrated for various temperatures at (a) $\dot{\varepsilon} = 0.0001\text{s}^{-1}$ and (b) $\dot{\varepsilon} = 1000\text{s}^{-1}$. Rate dependence is illustrated for different strain rates at (c) 25°C and (d) 250°C. (e) Deformation at $\dot{\varepsilon} = 1\text{s}^{-1}$ for temperatures starting at 200°C for the first 0.3 strain, 25°C up to 0.6 strain followed by 500°C up to completion. (f) Deformation at 25°C with rates changing from 10000s^{-1} to 0.00001s^{-1} followed by 10s^{-1} up to completion.

Formal inclusion of the geometrically necessary dislocations however now have greater physical meaning and significance.

5.3 Thermal recovery

Inclusion of thermal recovery terms in the dislocation density ratio evolution equation are also possible. The thermal annihilation of dislocations depend on the dislocation density and temperature. Applied incrementally, the change in dislocation density is time dependent. An additional annihilation term in Equation (3.6) can take the general from

$$d\rho^{(-)} = r_{\mathrm{s}}(\sqrt{\rho}, T)\ dt. \tag{5.15}$$

From the work by Estrin (1996), a possible phenomenological expression for the thermal recovery coefficient r_s may be expressed as

$$r_{\mathrm{s}} = r_0 \exp\left(-\frac{U_0}{k_{\mathrm{B}}T}\right) \sinh\left(\frac{\beta\sqrt{\rho}}{k_{\mathrm{B}}T}\right). \tag{5.16}$$

In this expression, the static or thermal recovery is driven by the stress determined by the square root of the current dislocation density while U_0, β and r_0 are constants. In his explanation, Estrin (1996) only mentions the possible formulation in Equation (5.16) as a reasonable ansatz but it is not demonstrated. Various other choices are also possible for the form of the thermal recovery component of the dislocation density evolution equation. An alternative approximation used by Song and McDowell (2012) within a dislocation density framework reads

$$d\rho^{(-)} = k_3(T)\rho^{r_3}\ dt, \tag{5.17}$$

where r_3 is a constant and k_3 is temperature dependent. The subscripts here are added for consistency regarding this term as the next component in Equation (3.10). An Arrhenius form for k_3 is assumed with

$$k_3 = k_{30} \exp\left(\frac{-Q_{\mathrm{self}}}{RT}\right), \tag{5.18}$$

where k_{30} is a constant and Q_{self} is the activation energy associated with self diffusion. Using the formulation by Song and McDowell (2012) as a further extension to the dislocation density ratio evolution equation, the rate form of Equation (5.13) is now

$$\dot{\varrho} = \dot{\alpha}\left(C_g \bar{\lambda}^{r_g} + C_1\sqrt{\varrho} - C_2(\dot{\alpha}, T)\ \varrho\right) - C_3(T)\varrho^{r_3}. \tag{5.19}$$

The constant $C_{30} = k_{30}\rho_0^{r_3-1}$ is introduced here while $a_{03} = Q_{\text{self}}/R$ is associated with the scaled activation energy for self diffusion. The static or thermal recovery term is therefore modelled using

$$C_3(T) = C_{30}\exp\left(\frac{-a_{03}}{T}\right). \tag{5.20}$$

The thermal recovery extension in Equation (5.19) is illustrated in Figure 5.4 again using some of the temperature and strain histories as used in the results of Section 5.1. The same material property values giving the material response illustrated in Figure 5.2 is again used without the large strain effects that resulted in Figure 5.3, i.e. $C_g = 0$ in this case. The thermal recovery constants used are $C_{30} = 10\text{s}^{-1}$, $a_{03} = 5000\text{K}$ and $r_3 = 1$.

In Figure 5.4, the effect of thermal recovery is visible in the higher temperature and lower strain rate cases as expected. The thermal recovery effect is time dependent and therefore illustrated in the case where there is variable holding times at higher temperatures before continued straining. Three cases are illustrated in Figure 5.5. The model is displayed for a case where the material is strained to 50% at $\dot{\varepsilon} = 10^{-4}\text{s}^{-1}$, $T = 25°\text{C}$ and then an additional 50% at $\dot{\varepsilon} = 10^{-4}\text{s}^{-1}$, $T = 250°\text{C}$ after three different hold times of 1 minute, 20 minutes and a full day at 250°C.

The constitutive model formulated and demonstrated up to this point considers the isotropic case where the von Mises yield surface radius changes due to an incremental plastic strain increment or as a function of time. This model can be implemented into an isotropic hardening subroutine as in the Mechanical Threshold Stress case presented in Appendix C. Before expanding on the numerical implementation of the formulated model however, the purely isotropic model is instead seen as a special case or model variant where the full model also includes kinematic hardening effects. In the following section, the inclusion of cyclic effects are considered and motivated again using the work done by Estrin (1996).

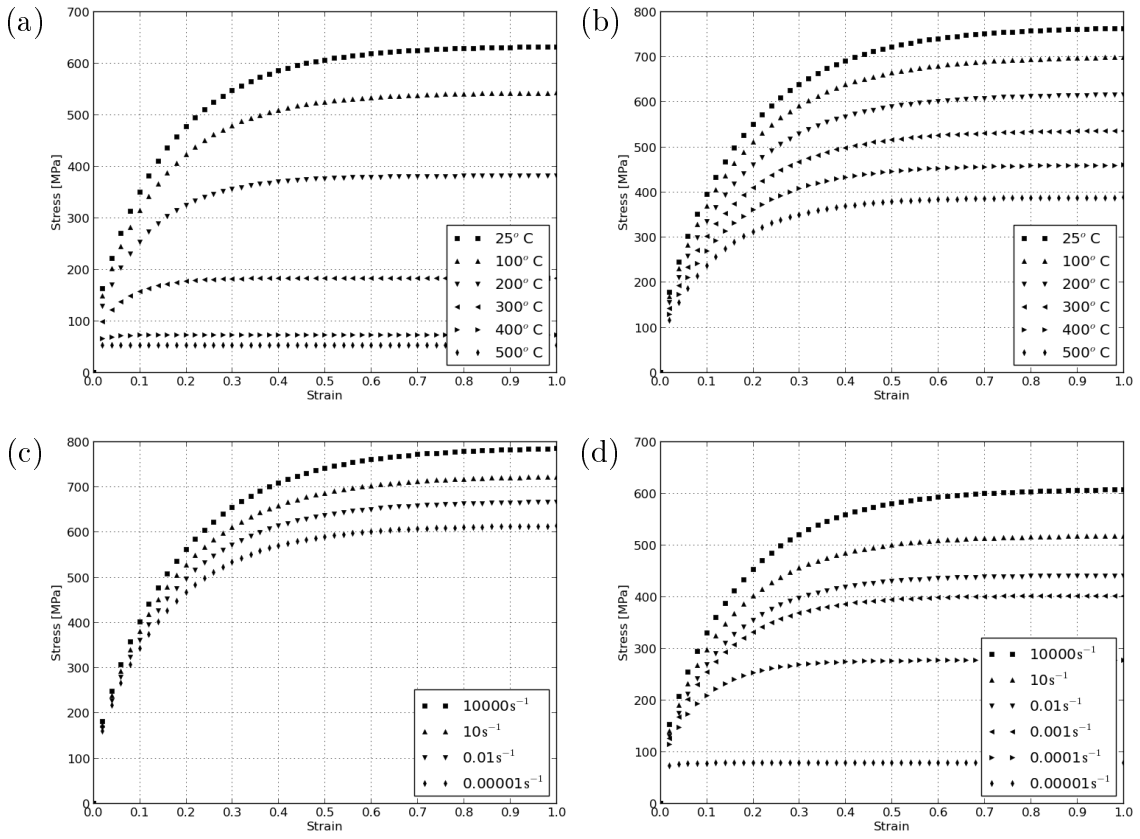

Figure 5.4: Temperature and rate dependence of the thermal recovery extended dislocation density ratio model. Temperature dependence is illustrated for various temperatures at (a) $\dot{\varepsilon} = 0.0001\text{s}^{-1}$ and (b) $\dot{\varepsilon} = 1000\text{s}^{-1}$. Rate dependence is illustrated for different strain rates at (c) 25°C and (d) 250°C.

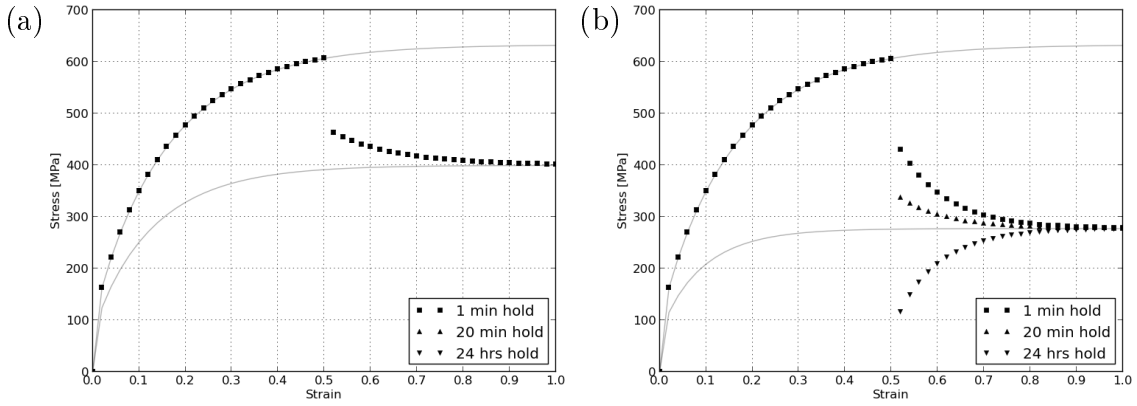

Figure 5.5: The effect of waiting time between additional straining at a higher temperature for the (a) original and (b) thermal recovery extended dislocation density ratio model. The model is first strained to 50% at 25°C and 0.0001s^{-1}. It is then left at 250°C for 1min, 20min or 24 hours before further straining at 250°C and 0.0001s^{-1}.

5.4 Cyclic effects

The constitutive equations developed for monotonic deformation are not fully equipped to produce the macroscopic mechanical response observed in cyclic deformation. From a microstructure-based standpoint, Estrin (1996) attributes some of the characteristic responses observed in cyclic deformation to what he calls a channel-like dislocation structure that forms under cyclic loading. The dislocation structure is viewed as a system of channels or regions of low dislocation density, separated by parallel narrow walls with a high density of segmented edge dislocations. Adjoining walls are linked by mobile screw dislocation segments or loops within the channels. The screw segments drag along the edge segments of the loop, changing the edge density. When an applied stress presses the edge segments against the walls, the wall dislocation density increases. Should the stress be reversed, the increased edge density increment can be recovered. This happens in the motion of the screw segments in the opposite direction if not woven into the dislocation structure of the walls or irreversibly trapped due to thermally activated jog formation.

With part of the dislocations recoverable in the event of load reversal, it is necessary to distinguish between truly immobilised and recoverable stored dislocation den-

sity. When the applied stress drops below the internal stress acting in the walls, the immobilised edge dislocations bulge out between the pinning points and inject mobile screw dislocations into the lower dislocation density regions. The generation of mobile screw dislocations is another process that can be taken into account. Following Estrin (1996), the dislocation dynamics considered in the channel-like structure may be cast into the constitutive equations of the isotropic model discussed in previous sections.

The edge dislocation density immobilised in the walls are identified with the dislocation density ratio internal state variable of the isotropic model formulation ϱ. The evolution of this dislocation density ratio therefore follows Equation (5.19). The density of dislocations trapped in the walls but partially recoverable upon stress reversal is included with the introduction of an additional dislocation variable ρ_r. As with the dislocation density ratio internal state variable $\varrho = \rho/\rho_0$, the non-dimensional form of the partially recoverable part of the dislocation density ratio is given by the internal state variable $\varpi = \rho_r/\rho_0$. Since ρ_r is a subset of ρ, the internal state variable ϖ is a subset of the total dislocation density ratio internal state variable ϱ. If the average channel width scales with $1/\sqrt{\varrho}$, the inversely proportional storage rate of ϖ is given by (Estrin, 1996):

$$\dot{\varpi} = \dot{\alpha}\left(C_4\sqrt{\varrho} - C_2(\dot{\varepsilon}_\mathrm{p}, T)\varpi\right) - C_5(T)\varpi. \tag{5.21}$$

Apart from the aforementioned storage rate, this rate equation includes a dynamic recovery term $C_2(\dot{\varepsilon}_\mathrm{p}, T)\varpi$ while $C_5(T)\varpi$ represents the recoverable edge density loss rate due to thermally activated jog formation. The last term is time rather than strain dependent and can take the form of the Arrhenius expression involving the activation energy for jog formation. If $a_{05} = Q_\mathrm{jog}/R$ is used as a parameter representing the scaled activation energy associated with jog formation:

$$C_5(T) = C_{50}\exp\left(\frac{-a_{05}}{T}\right). \tag{5.22}$$

Given that the dislocation density variable ϖ is recovered upon each stress reversal, an internal state variable update in the case of this event is needed that satisfies the condition

$$\varrho := \varrho - \varpi \qquad \text{and} \qquad \varpi := 0. \tag{5.23}$$

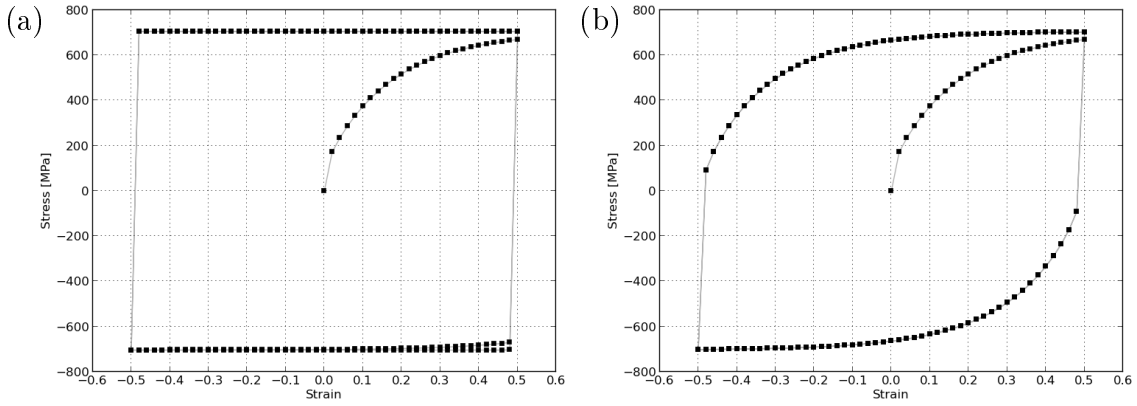

Figure 5.6: Cyclic behaviour of the dislocation density ratio based model at 25°C and 1s^{-1} (a) without and (b) with partially recoverable wall dislocation density upon load reversal. The

In Figure 5.6(a) the cyclic response of the model with parameter values given in Section 5.1 is illustrated at 25°C. The response starts at $\varepsilon = 0$ and is cycled with a strain amplitude of 50% at 1s^{-1}. The recoverable dislocation density ratio internal state variable is then added and evolved using Equation (5.21) with $C_4 = 100$ and $C_5 = 0\text{s}^{-1}$ resulting in the reset of $\varrho = 1$ at each load reversal. The cyclic response in the case where the dislocation density ratio is reset is given in Figure 5.6(b).

To account for the curvature of the mobile dislocation segments in the channels, Estrin (1996) introduces a back stress σ_B into his chosen one dimensional kinetic equation. The evolution of the one dimensional back stress is considered to obey the equation

$$\frac{d\sigma_\text{B}}{d\alpha} = C_6\sqrt{\varrho} - C_7\sigma_\text{B}, \tag{5.24}$$

introducing the two new parameters C_6 and C_7. The model response given the back stress extension is visible in Figure 5.7. In Figure 5.7(a) the cyclic response using $C_6 = 50\text{MPa}$, $C_4 = C_7 = 0$ and $C_5 = 0\text{s}^{-1}$ is demonstrated while the recoverable dislocation density ratio is activated for Figure 5.7(b) using $C_4 = 100$, $C_6 = 50\text{MPa}$, $C_5 = 0\text{s}^{-1}$ and $C_7 = 0$.

The numerical implementation makes use of the constitutive model described by Equations (5.4), (5.19), (5.21) and (5.24). This model is implemented as an `FCOMBINED`

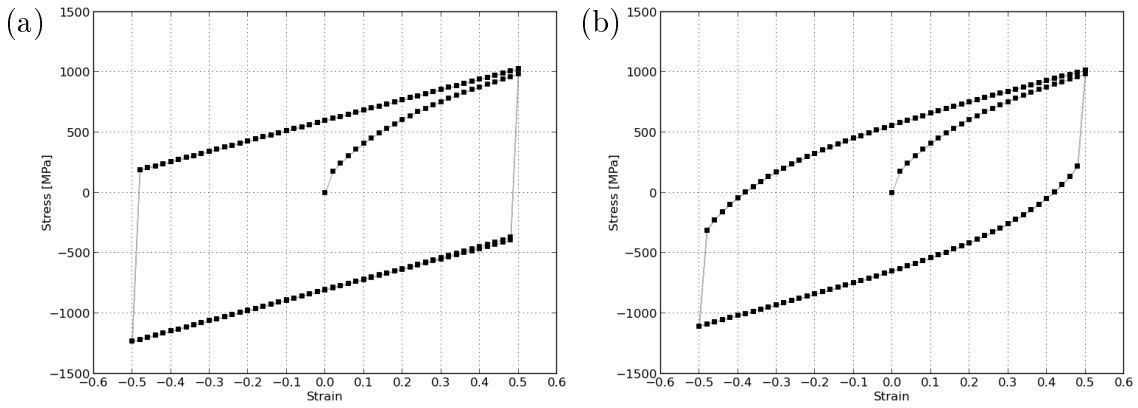

Figure 5.7: Behaviour of the dislocation density ratio based model with back stress evolution at $\dot{\varepsilon} = 1\text{s}^{-1}$ and 25°C. The cyclic behaviour (a) without and (b) with partially recoverable wall dislocation density upon load reversal is illusrated.

hardening subroutine that can replace the linear combined work hardening model verified in Section 2.4. Appendix E contains the Fortran code for the implementation discussed in the following section.

5.5 Numerical Implementation

Using the combined hardening user material framework in Appendix B, the dislocation density ratio based constitutive model is implemented numerically into Fortran subroutines given in Appendix E.

As with the MTS model implementation, the temperature dependent shear modulus following Equation (3.21) is again used in conjunction with dislocation density ratio based model. The shear modulus is therefore again returned by calling the `SHEARMOD` subroutine presented in Appendix C.1. The elastic properties μ_r, D_r and T_r in Equation (3.21) as well as Poisson's ratio ν are still passed to the material subroutine using the first four entries in the `PROPS` array of user defined material properties. The subroutine returns the shear modulus at the current temperature along with Poisson's ratio to evaluate the trial elastic state.

The dislocation density ratio based combined hardening model is implemented into a combined hardening subroutine `FCOMBINED` that is called by the Abaqus user material

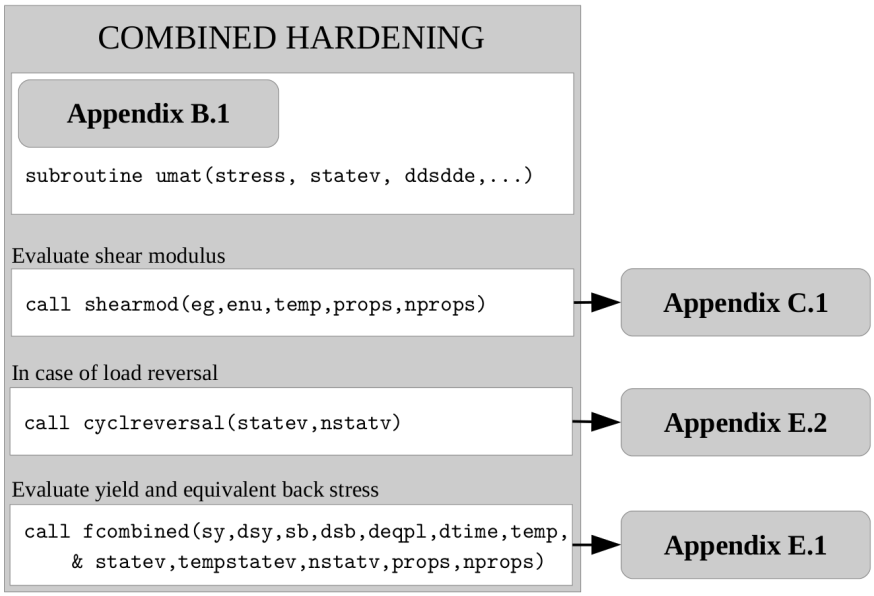

Figure 5.8: The dislocation density based combined hardening user material.

subroutine. This function replaces the linear combined hardening version of Chapter 2. The yield and back stress function `FCOMBINED` for the implemented model is attached in Appendix E.1 while E.2 is a subroutine called in the case of load reversal. The load reversal subroutine alters the internal state variables to satisfy Equation (5.23). Figure 5.8 shows the layout of the appended subroutines called by Appendix B.1 in this implementation.

The combined hardening subroutine uses four internal state variables (ISVs) namely:

- the average slip plane lattice incompatibility $\bar{\lambda}$,
- the main contributing dislocation density ratio ϱ,
- the partly recoverable wall dislocation density ratio ϖ,
- the equivalent back stress variable σ_{B}, since it is a function of itself according to Equation (5.24).

Given that the numerical combined elasto-plastic framework in Appendix B makes use of the `STATEV` array to store the $4 \leq$ `NTENS` ≤ 6 components of the shift tensor, the

four ISVs used by the `FCOMBINED` subroutine are stored in the seventh to tenth entry of the `STATEV` array

$$\left\{\bar{\lambda};\ \varrho;\ \varpi;\ \sigma_{\mathrm{B}}\right\} = \left\{\texttt{STATEV}(I) \text{ for } I \in [7,8,9,10]\right\}. \tag{5.25}$$

As in the linear hardening and MTS cases, the trial elastic state is evaluated by assuming that there is no additional equivalent plastic strain in the current increment $\delta\alpha = 0$. Given the incremental equivalent plastic strain and time step used as inputs to the `FCOMBINED` subroutine, the strain rate used in the calculations where needed is again determined using the rationale explained with the aid of Equation (3.29). The subroutine is given an estimate of the incremental plastic strain $\delta\alpha$, strain rate using Equation (3.29), temperature at the end of the increment and ISV values at the start of the current increment. The candidate ISV values at the end of the increment, yield stress $\sigma_{\mathrm{Y}}|_{t+\delta t}$, back stress $\sigma_{\mathrm{B}}|_{t+\delta t}$, and sensitivities resulting in $\mathcal{K} = d\sigma_{\mathrm{Y}}/d\alpha$ and $\mathcal{H} = d\sigma_{\mathrm{B}}/d\alpha$ are then solved. These values are returned in order to solve the equivalent incremental plastic strain using Newton's method on Equation (2.84).

5.5.1 Determining the average slip plane lattice incompatibility

The incremental change in average slip plane lattice incompatibility is determined from Equation (5.14). The updated value at time $t + \delta t$ is simply

$$\bar{\lambda}\big|_{t+\delta t} = \bar{\lambda}\big|_{t} + \delta\alpha\frac{C_{\lambda}}{d_{\mathrm{x}}}. \tag{5.26}$$

5.5.2 Calculating the evolving dislocation density ratio values

Backward Euler implicit integration is used taking the incremental plastic strain $\delta\alpha$, plastic strain rate $\dot{\alpha}$, duration of the time increment δt and temperature T into account. Using the rate of evolution from Equation (5.19), an incremental change in the main evolving dislocation density ratio ISV (ϱ) is determined so that the value at time $t+\delta t$

is given by

$$\begin{aligned} \varrho|_{t+\delta t} &= \varrho|_t + \delta\alpha \left(C_g \, \bar{\lambda}^{r_g}\big|_{t+\delta t} + C_1 \sqrt{\varrho|_{t+\delta t}} - C_2(\dot{\alpha}, T) \;\; \varrho|_{t+\delta t} \right) - \delta t C_3(T) \; \varrho^{r_3}|_{t+\delta t} \\ &= \varrho|_t + \delta\theta_\varrho|_{t+\delta t} \, . \end{aligned} \tag{5.27}$$

Here, $\delta\theta_\varrho|_{t+\delta t} = \delta\theta_\varrho \left(\bar{\lambda}\big|_{t+\delta t} \, , \, \varrho|_{t+\delta t} \, , \delta\alpha, \delta t, \dot{\alpha}, T \right)$ is a function of mainly the dislocation density ratio at the end of the increment $\varrho|_{t+\delta t}$ since the other values are treated as constants in the solution loop.

The implicit integration is done using Newton-Raphson given an initial guess $\varrho|_{t+\delta t} = \varrho|_t$ and a residual equation $\mathcal{R}_\varrho = \varrho|_{t+\delta t} - \varrho|_t - \delta\theta_\varrho|_{t+\delta t}$ based on Equation (5.27). The sensitivity

$$\mathcal{D}\mathcal{R}_\varrho = 1 - \delta\alpha \left(C_1 \; \varrho^{-1}\big|_{t+\delta t} - C_2(\dot{\alpha}, T) \right) + \delta t C_3(T) r_3 \; \varrho^{r_3 - 1}\big|_{t+\delta t} \tag{5.28}$$

is used to solve for the unknown value of the dislocation density ratio internal state variable. Upon solving for $\varrho|_{t+\delta t}$, the partially recoverable wall dislocation density ratio is updated. Using Equation (5.21) for the incremental change, implicit integration of this ISV results in

$$\varpi|_{t+\delta t} = \varpi|_t + \delta\alpha \left(C_4 \sqrt{\varrho|_{t+\delta t}} - C_2(\dot{\varepsilon}_\mathrm{p}, T) \; \varpi|_{t+\delta t} \right) - \delta t C_5(T) \; \varpi|_{t+\delta t} \, . \tag{5.29}$$

The value of the recoverable dislocation density ratio is given by reworking the update equation to

$$\varpi|_{t+\delta t} = \frac{\varpi|_t + \delta\alpha C_4 \sqrt{\varrho|_{t+\delta t}}}{1 + \delta\alpha C_2(\dot{\varepsilon}_\mathrm{p}, T) + \delta t C_5(T)} . \tag{5.30}$$

5.5.3 Updating the yield and equivalent back stress

In the numerical implementation of Appendix E, the yield stress is calculated using Equation (5.4). This means that once the value of the evolving dislocation density ratio at the end of the time step is solved, the resulting yield stress value is

$$\sigma_\mathrm{Y}|_{t+\delta t} = \hat{\sigma}_a + \frac{\mu\,(T)}{\mu_r} \sigma_0 \; S_\varepsilon|_{t+\delta t} \sqrt{\varrho|_{t+\delta t}} . \tag{5.31}$$

Using Equation (5.24) for the incremental change, the equivalent back stress is determined from

$$\sigma_{\mathrm{B}}|_{t+\delta t} = \sigma_{\mathrm{B}}|_t + \delta\alpha \left(C_6 \sqrt{\varrho|_{t+\delta t}} - C_7 \, \sigma_{\mathrm{B}}|_{t+\delta t} \right). \tag{5.32}$$

The back stress value at the end of the increment is thus calculated using

$$\sigma_{\mathrm{B}}|_{t+\delta t} = \frac{\sigma_{\mathrm{B}}|_t + \delta\alpha C_6 \sqrt{\varrho|_{t+\delta t}}}{1 + \delta\alpha C_7}. \tag{5.33}$$

The shift tensor $\boldsymbol{q}$ in the combined hardening numerical framework implemented in Appendix B is set to evolve incrementally as in Equation (2.79) with $\delta\sigma_{\mathrm{B}}\boldsymbol{n}$. Upon load reversal the incremental change in the equivalent back stress is also reversed. In this numerical implementation, the one dimensional equivalent back stress variable is therefore reversed when the subroutine in Appendix E.2 is called in order to facilitate a possible reduction or sign change in the incremental shift tensor calculation using Equation (5.33)

5.5.4 Sensitivities

The Newton-Raphson scheme is used to solve the absolute slip rate or consistency parameter and so the incremental equivalent plastic strain increment $\delta\alpha$ from the residual in Equation (2.84). The method requires the isotropic and kinematic stress component sensitivities $\mathcal{K} = d\sigma_{\mathrm{Y}}/d\delta\alpha$ and $\mathcal{H} = d\sigma_{\mathrm{B}}/d\delta\alpha$. The sensitivity of the calculated yield stress using Equation (5.31) and equivalent back stress using Equation (5.33) given a different equivalent plastic strain increment as input is therefore determined in this subsection.

The derivative of the yield stress with respect to the equivalent plastic strain increment can be determined using the chain rule. For notational brevity the time specification at the end of the increment is dropped on the relevant variables so that $\sigma_{\mathrm{Y}} \equiv \sigma_{\mathrm{Y}}|_{t+\delta t}$ for example. The sensitivity is given by

$$\frac{d\sigma_{\mathrm{Y}}}{d\delta\alpha} = \frac{\mu}{\mu_r}\left[\frac{\partial S_\varepsilon}{\partial\dot{\alpha}}\frac{d\dot{\alpha}}{d\delta\alpha}\hat{\sigma}_\varepsilon + S_\varepsilon\frac{d\hat{\sigma}_\varepsilon}{d\delta\alpha}\right] = \frac{\mu}{\mu_r}\sigma_0\left[\frac{\partial S_\varepsilon}{\partial\dot{\alpha}}\frac{\sqrt{\varrho}}{\delta t} + S_\varepsilon\frac{1}{2\sqrt{\varrho}}\frac{d\varrho}{d\delta\alpha}\right], \tag{5.34}$$

where $d\dot{\alpha}/d\delta\alpha = 1/\delta t$ when $\delta\alpha > 0$ following Equation (3.29) and $d\hat{\sigma}_{\varepsilon}/d\delta\alpha$ is determined from Equation (5.3). Still using the Arrhenius expression for the scaling function in Equation (3.22), the partial derivative of the scaling function with respect to the equivalent plastic strain rate is again determined from Equation (3.36).

The back stress sensitivity with respect to the equivalent plastic strain increment using Equation (5.33) is

$$\frac{d\sigma_{\mathrm{B}}}{d\delta\alpha} = \frac{\partial\sigma_{\mathrm{B}}}{\partial\delta\alpha} + \frac{\partial\sigma_{\mathrm{B}}}{\partial\varrho}\frac{d\varrho}{d\delta\alpha}. \tag{5.35}$$

The first partial derivative with respect to the incremental plastic strain is now calculated using

$$\frac{\partial\sigma_{\mathrm{B}}}{\partial\delta\alpha} = C_6\sqrt{\varrho}\,(1+\delta\alpha C_7)^{-1} - C_7\,(\sigma_{\mathrm{B}}|_t + \delta\alpha C_6\sqrt{\varrho})\,(1+\delta\alpha C_7)^{-2}. \tag{5.36}$$

Only the time value of $\sigma_{\mathrm{B}}|_t$ is specified since all other variables of interest are taken at the end of the increment. The second component of Equation (5.35) is given by

$$\frac{\partial\sigma_{\mathrm{B}}}{\partial\varrho}\frac{d\varrho}{d\delta\alpha} = \frac{\delta\alpha C_6}{2\sqrt{\varrho}(1+\delta\alpha C_7)}\frac{d\varrho}{d\delta\alpha}. \tag{5.37}$$

Both Equations (5.34) and (5.35) further only require the sensitivity of the main dislocation density ratio ISV with respect to the incremental plastic strain to complete the calculation. Given the implicit definition of the evolving dislocation density ratio internal state variable with $\delta\theta_{\varrho} \equiv \delta\theta_{\varrho}|_{t+\delta t}$ at the end of the increment in Equation (5.27), the derivative with respect to the incremental equivalent plastic strain is

$$\frac{d\varrho}{d\delta\alpha} = \frac{\partial\delta\theta_{\varrho}}{\partial\delta\alpha} + \frac{\partial\delta\theta_{\varrho}}{\partial\dot{\alpha}}\frac{d\dot{\alpha}}{d\delta\alpha} + \frac{\partial\delta\theta_{\varrho}}{\partial\varrho}\frac{d\varrho}{d\delta\alpha} + \frac{\partial\delta\theta_{\varrho}}{\partial\bar{\lambda}}\frac{d\bar{\lambda}}{d\delta\alpha}. \tag{5.38}$$

Inspecting the individual components, the partial derivative of the incremental update $\delta\theta_{\varrho}$ with respect to the equivalent plastic strain is

$$\frac{\partial\delta\theta_{\varrho}}{\partial\delta\alpha} = C_g\bar{\lambda}^{r_g} + C_1\sqrt{\varrho} - C_2(\dot{\alpha},T)\varrho. \tag{5.39}$$

Taking the dynamic recovery function in Equation (5.7) as the only rate dependent

part of the incremental update gives

$$\frac{d}{d\dot{\alpha}}C_2(\dot{\alpha},T) = -\frac{C_{20}T}{\dot{\alpha}a_{02}\mu}\exp\left[-\frac{T}{a_{02}\mu}\ln\left(\frac{\dot{\alpha}}{\dot{\varepsilon}_{02}}\right)\right]. \tag{5.40}$$

The second component of Equation (5.38) is therefore

$$\begin{aligned}\frac{\partial\delta\theta_{\varrho}}{\partial\dot{\alpha}}\frac{d\dot{\alpha}}{d\delta\alpha} &= -\frac{\delta\alpha}{\delta t}\varrho\frac{d}{d\dot{\alpha}}C_2(\dot{\alpha},T)\\ &= \frac{C_{20}T\varrho}{a_{02}\mu}\exp\left[-\frac{T}{a_{02}\mu}\ln\left(\frac{\dot{\alpha}}{\dot{\varepsilon}_{02}}\right)\right].\end{aligned} \tag{5.41}$$

The last component of Equation (5.38) is determined by inspecting Equations (5.26) and (5.27) so that

$$\frac{\partial\delta\theta_{\varrho}}{\partial\bar{\lambda}}\frac{d\bar{\lambda}}{d\delta\alpha} = \delta\alpha r_g C_g\bar{\lambda}^{r_g-1}\frac{C_{\lambda}}{d_{\mathrm{x}}}. \tag{5.42}$$

The third component of Equation (5.38) has the same quantity $d\varrho/d\delta\alpha$ as we are interested in. Rearranging the equation with this component on the left means that the left hand side of the equation is changed to

$$\frac{d\varrho}{d\delta\alpha} - \frac{\partial\delta\theta_{\varrho}}{\partial\varrho}\frac{d\varrho}{d\delta\alpha} = \left(1-\frac{\partial\delta\theta_{\varrho}}{\partial\varrho}\right)\frac{d\varrho}{d\delta\alpha} = \mathcal{DR}_{\varrho}\frac{d\varrho}{d\delta\alpha} \tag{5.43}$$

with $\mathcal{DR}_{\varrho}$ already calculated in Equation (5.28). The dislocation density ratio sensitivity with respect to the incremental equivalent plastic strain is finally calculated from

$$\begin{aligned}\frac{d\varrho}{d\delta\alpha} = \Bigg(&C_g\bar{\lambda}^{r_g} + C_1\sqrt{\varrho} - C_2(\dot{\alpha},T)\varrho + \frac{C_{20}T\varrho}{a_{02}\mu}\exp\left[-\frac{T}{a_{02}\mu}\ln\left(\frac{\dot{\alpha}}{\dot{\varepsilon}_{02}}\right)\right]\\ &+\delta\alpha r_g C_g\bar{\lambda}^{r_g-1}\frac{C_{\lambda}}{d_{\mathrm{x}}}\Bigg)/\mathcal{DR}_{\varrho}.\end{aligned} \tag{5.44}$$

The gradients and numerical implementation of the combined hardening model in Appendix E are now tested. This is done using an arbitrary set of material parameters and a single call to a one dimensional version of the user material framework that also uses the subroutine in Appendix E. The value of the residual equation, analytical

gradients as well as the estimated equivalent plastic strain increment are reported for each iteration. A forward finite difference estimate of the isotropic and kinematic sensitivities is also calculated within the one-dimensional test environment by perturbing the estimated plastic strain by 10^{-8}.

For this test, the virtual material parameters used are:

- The elastic property values of $\mu_r = 100\text{GPa}$, $D_r = 0\text{MPa}$ and $T_r = 200\text{K}$ in Equation (3.21) and a Poisson's ratio of $\nu = 0.3$ are used.
- The stress values in Equation (5.4) are chosen as $\hat{\sigma}_a = 0\text{MPa}$ and $\sigma_0 = 1000\text{MPa}$.
- The scaling function values in Equation (3.22) are chosen as $a_{0\varepsilon} = k_\text{B}/g_{0\varepsilon}b^3 = 0.2\text{K/MPa}$, $p_\varepsilon = q_\varepsilon = 1$ and $\dot{\varepsilon}_{0\varepsilon} = 10^6\text{s}^{-1}$.
- The average slip plane lattice incompatibility evolves following Equation (5.26) with $C_\lambda/d_\text{x} = 1$, while $C_g = 100$ and $r_g = 0.5$ in Equation (5.27).
- Dislocation accumulation is taken into account with $C_1 = 100$ in Equation (5.27).
- Dynamic recovery parameter values in Equation (5.7) are $C_{20} = 10$, $\dot{\varepsilon}_{02} = 10^6\text{s}^{-1}$ and a_{02}=2K/MPa.
- Back stress evolution according to Equation (5.24) is modelled using $C_6 = 10^5\text{MPa}$ and $C_7 = 500$.
- No thermal recovery or recoverable dislocation density is included meaning $C_{30} = 0\text{s}^{-1}$ in Equation (5.20), $C_{40} = 0$ in Equation (5.21) and $C_{50} = 0\text{s}^{-1}$ in Equation (5.22).

Assuming a time increment $\delta t = 1\text{s}$, temperature of $T = 500\text{K}$ and one dimensional incremental strain $\delta\varepsilon = 0.1$, the residual value, equivalent plastic strain and sensitivities for each iteration in the solution loop are given in Table 5.1. The function call results in a resolved von Mises yield stress of $\sigma_\text{Y} = 3135.67\text{MPa}$ of which the back stress contribution is $\sigma_\text{B} = 776.79\text{MPa}$

Out of the 0.1 total strain increment, the plastic strain increment is $\delta\alpha = 0.0874$ as seen in Table 5.1. According to the convergence of the residual and by comparison

Iteration	Residual	Plastic increment	Isotropic		Kinematic	
			Analytical	Finite Difference	Analytical	Finite Difference
1	25805.902	0	2437768.8	2436598.9	99067.947	99067.499
2	25628.511	1.0331E-5	28240.801	28240.800	12002.086	12002.083
3	22617.137	9.1737E-3	16902.784	16902.784	5391.4768	5391.4767
4	825.56331	8.4503E-2	16605.431	16605.431	5286.0136	5286.0135
5	0.5917212	8.7427E-2	16605.220	16605.220	5285.9391	5285.9389
6	2.99298E-7	8.7430E-2	16605.221	16605.220	5285.9391	5285.9389
7	2.8422E-12	8.7430E-2	16605.221	16605.219	5285.9391	5285.9389

Table 5.1: Test on the convergence of the dislocation density based combined hardening model material subroutine in Appendix E.

of the analytical sensitivity to the finite difference approximation in Table 5.1, the gradients are derived and implemented correctly.

With confidence in the implementation, the model implemented in Appendix E is now calibrated on experimental data in the following section using a one dimensional combined material framework.

5.6 Model calibration on cyclic data:

The combined hardening dislocation density ratio model is applied here to describe the cyclic deformation data for Alloy 800H and Inconel 738LC. The material data is digitised from the chapter in *"Unified Constitutive Laws of Plastic Deformation"* written by Estrin (1996).

Two cycles on the Alloy 800H is digitised and fit using the model. The deformation is modelled at 1123K and a strain rate of $2 \times 10^{-3}\text{s}^{-1}$. The model response fit to the digitised data is presented in Figure 5.9. The elastic parameter values of $\mu_r = 60\text{GPa}$, $\nu = 0.3$ and $D_r = 0\text{GPa}$ so that $\mu = \mu_r$ are used. The athermal stress component $\hat{\sigma}_a = 0\text{MPa}$ is used while the reference stress parameter $\sigma_0 = 734.41\text{MPa}$. Scaling factor parameter values are $a_{0\varepsilon} = 0.7424\text{K/MPa}$, $p_\varepsilon = 0.5$, $q_\varepsilon = 1.5$ and $\dot{\varepsilon}_{0\varepsilon} = 10^7\text{s}^{-1}$. The other material parameter values are $C_g = 0$ $C_{30} = 0\text{s}^{-1}$, $C_1 = 43.302$, $C_{20} = 32.469$, $a_{02} = 4.497\text{K/MPa}$, $\dot{\varepsilon}_{02} = 10^7\text{s}^{-1}$, $C_4 = 10.589$, $C_5 = 1.34 \times 10^{-8}\text{s}^{-1}$

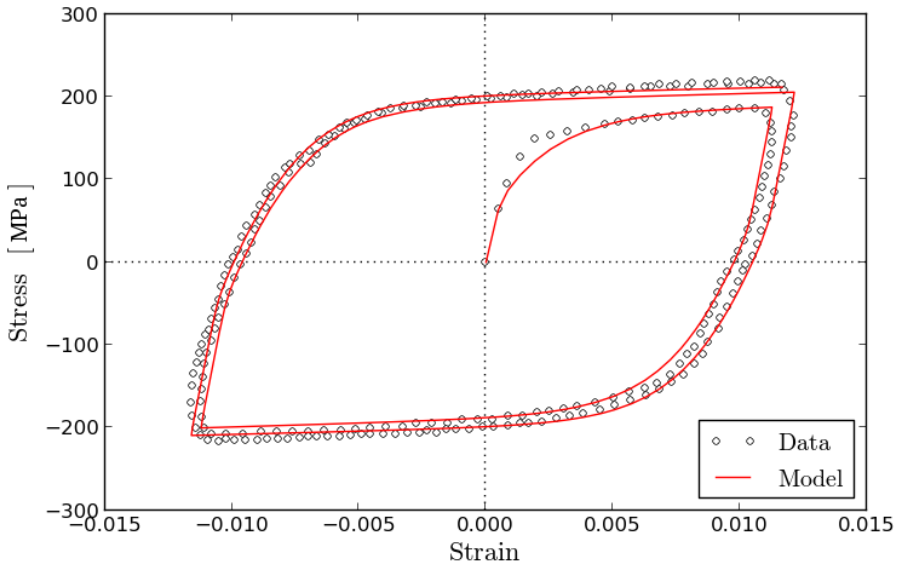

Figure 5.9: Cyclic data for Alloy 800H (Estrin, 1996) versus the implemented model prediction.

with the parameters associated with the back stress evolution $C_6 = 64897.42$MPa and $C_7 = 628.34$. The exact thermal properties, such as a_{05} for example, are not taken into account given only a single temperature is used during the characterisation. This means that any combination of C_{50} and a_{05} resulting in $C_5 = C_{50} \times \exp(-a_{05}/1123) = 1.34 \times 10^{-8}\text{s}^{-1}$ would result in the same response.

There is a good fit despite setting $C_g = 0\mu$m and therefore ignoring the effect of $\bar{\lambda}$ on the dislocation density accumulation. This is because the alloys have very low carbon content. The small volume fraction of carbides that form nucleate exclusively as films on the grain boundaries and therefore do not partake in most deformation processes apart from intergranular fracture. If more data is available at different rates and temperatures during the model characterisation, the parameter values could have other values. This example only used a single curve during the parameter characterisation however and therefore can not take these effects into account.

Variable strain rate monotonic data at 1123K as well as an experimental cyclic response at $\dot{\varepsilon} = 10^{-3}\text{s}^{-1}$ and 1123K for the Inconel 738LC material are digitised and therefore available during the characterisation in the second example. In Figure 5.10,

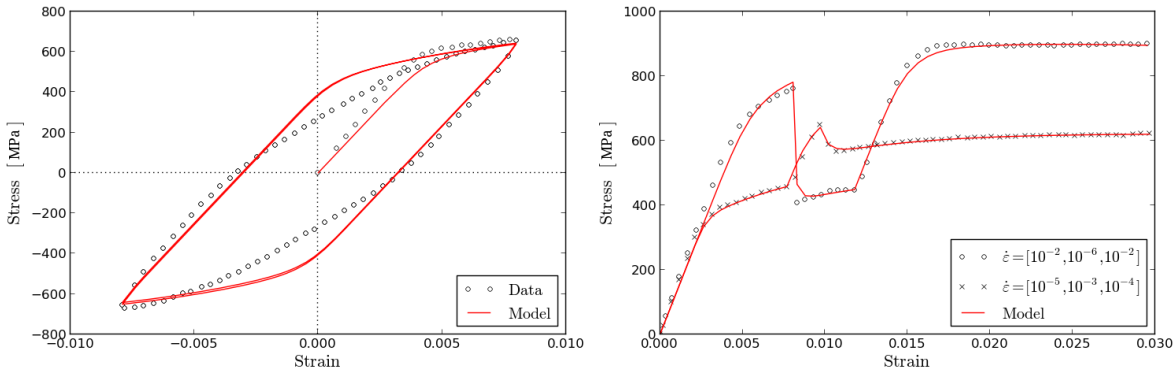

Figure 5.10: (a) Cyclic and (b) monotonic variable strain rate data for Inconel 738LC Estrin (1996) versus model prediction using the monotonic data for material parameter characterisation.

μ_r	50GPa	σ_0	4410.47MPa	C_g	0μm	C_{30}	0s^{-1}
ν	0.3	$a_{0\varepsilon}$	0.9392K/MPa	C_1	22.23	C_4	0.0039
D_r	0GPa	p_ε	0.2551	C_{20}	75.67	C_5	2.197$\times$10^{-7}s^{-1}
T_r	200K	q_ε	0.755	a_{02}	0.478K/MPa	C_6	30329.65MPa
$\hat{\sigma}_a$	277.184MPa	$\dot{\varepsilon}_{0\varepsilon}$	10^7s^{-1}	$\dot{\varepsilon}_{02}$	10^7s^{-1}	C_7	180.11

Table 5.2: Material parameter values for Inconel 738LC resulting in the model response in Figure 5.10.

the model prediction is presented along with the data. This is done for a case where the parameter characterisation is performed using mainly the monotonic variable rate data visible in Figure 5.10(b). For this reason the results in Figure 5.10(b) are in good agreement with the data. The material parameter values that result in the responses in Figure 5.10 are presented in Table 5.2.

The calibrated material parameter values are then used as initial condition in another calibration exercise where all of the cyclic data points are used. Only some of the cyclic data points are digitised from the relevant figure in Estrin (1996). In his figure there are three cycles seemingly identical to the first. In the characterisation, three cycles are modelled and compared to the data points of the digitised cyclic data. These data points are effectively given three times the weight of the remaining data points used during the characterisation process. The alternative material parameter values

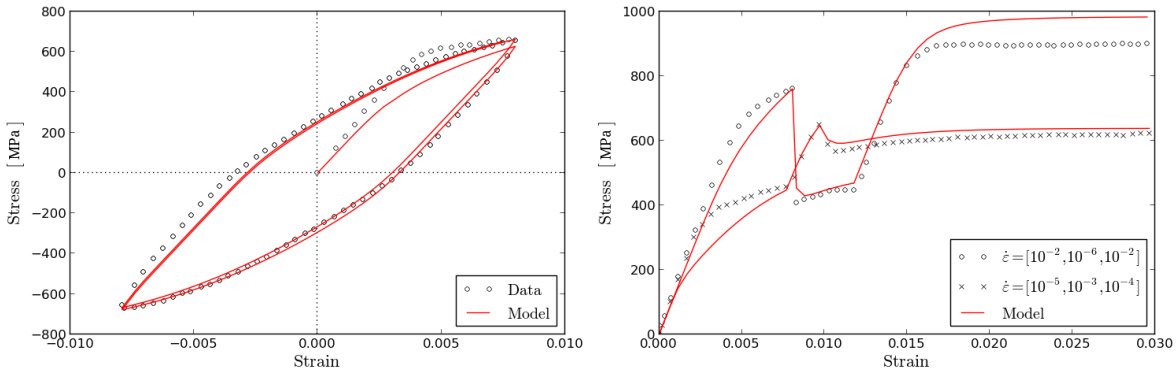

Figure 5.11: (a) Cyclic and (b) monotonic variable strain rate data for Inconel 738LC Estrin (1996) versus model prediction using all of the data points.

μ_r	50GPa	σ_0	1685.59MPa	C_g	0μm	C_{30}	0s^{-1}
ν	0.3	$a_{0\varepsilon}$	0.9169K/MPa	C_1	6.697	C_4	0
D_r	0GPa	p_ε	0.1106	C_{20}	7.217	C_5	$2.23\times10^{-9}\text{s}^{-1}$
T_r	200K	q_ε	0.3271	a_{02}	7.817K/MPa	C_6	123238.78MPa
$\hat{\sigma}_a$	116.08MPa	$\dot{\varepsilon}_{0\varepsilon}$	10^7s^{-1}	$\dot{\varepsilon}_{02}$	10^7s^{-1}	C_7	336.34

Table 5.3: Material parameter values for Inconel 738LC resulting in the model response in Figure 5.11.

obtained upon inclusion of the cyclic data in the comparison are now in Table 5.3.

The response using these material parameter values are given in Figure 5.11. The monotonic responses no longer fit the data as well as in Figure 5.10(b), but remain within reasonable accuracy while the modelled cyclic response is in better agreement with the data.

The back stress and yield stress values over the cycle modelled in Figure 5.11(a) are presented in Figure 5.12. The difference between the equivalent back stress variable in red and shift value (black stars) using a one dimensional model framework are illustrated. The equivalent back stress applied incrementally using Equation (5.24) while taking the flow direction into account is also illustrated. In this one dimensional example, reversing the equivalent back stress internal state variable upon load reversal in the numerical implementation produces an equivalent response in the shift tensor as if the plastic strain increment would have a directional component. This happens due

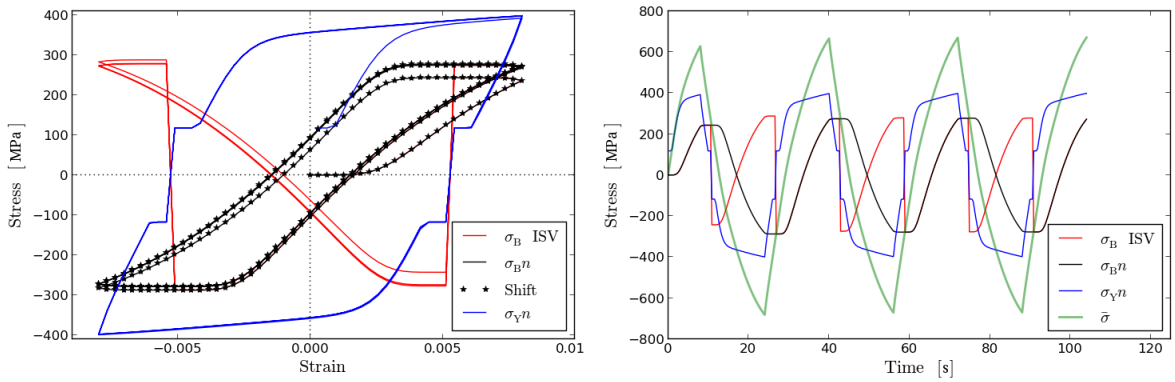

(a) (b)

Figure 5.12: The equivalent back stress internal state variable, shift variable and yield surface radius corresponding to the cyclic deformation in Figure 5.11 plotted as a function of (a) strain and (b) time. The equivalent stress is also plotted as a function of time in green.

to the fact that the shift is incrementally applied following $\delta \boldsymbol{q} = \delta \sigma_B \boldsymbol{n}$, as explained in Section 2.3.7.

The directional yield stress value $\sigma_Y \boldsymbol{n}$ is shown in blue with the effective stress also displayed in Figure 5.12(b) over the time period using a green line. If there is no incremental plastic strain during a deformation increment it is visible that the yield stress value is simply equal to the athermal stress value $\sigma_Y = \hat{\sigma}_a = 116.08$MPa.

The model does not capture the response of the Inconel 738LC as well as that of the Alloy 800H. Alloy 800H is a solid solution hardened Ni-Cr-Al-Ti alloy while Inconel 738LC is a super alloy that is both hardened by solid solution and gamma prime precipitate γ' Ni_3Al (Guzman et al., 2012). The latter therefore has more complex deformation mechanisms not built into the model presented. The extended dislocation density ratio based model built on the MTS framework is only well equipped to model and predict the cyclic responses of materials in cases where the implemented deformation mechanisms dominate. In the following section, an isotropic version of this dislocation density based modelling approach is extended to also include recrystallisation.

5.7 Recrystallisation

During recrystallisation, new grains nucleate and grow to replace the worked microstructure of a strained material (Haessner, 1978; Humphreys and Hatherly, 1995). At elevated temperatures, subgrains expand at the expense of neighbouring subgrains with a higher level of stored energy. As grain and subgrain boundaries move, the dislocation structure associated with the higher energy is swept away, effectively leaving behind recrystallised material with a lower dislocation density (Doherty, 2005).

Early fundamental work in modelling recrystallisation was done by Johnson and Mehl (1939), Avrami (1939) and Kolmogorov (1937), commonly referred to as the Johnson-Mehl-Avrami-Kolmogorov or simply JMAK model. This model is based on the assumptions that recrystallised nuclei form randomly within the pre-existing microstructure and that these nuclei grow at a constant, isotropic rate. Using the Avrami form, the evolution of the fraction of recrystallised material f_{x} can be modelled over time using

$$f_{\mathrm{x}}(t) = 1 - \exp\left(-Bt^n\right). \tag{5.45}$$

In this model, B is a function that takes into account the shape of the subgrains as well as the constant nucleation rate and constant growth rate while n is a constant.

Nucleation distribution tends to rather occur nonrandomly. It usually happens at preferred sites such as prior grain boundaries, edges, corners and other inhomogeneities. The growth rate also varies, meaning the ideal JMAK behaviour is rarely exhibited by real materials (Humphreys and Hatherly, 1995; Chen et al., 2002). Further work on the JMAK model was done by Cahn (1956) for example, to take the saturation of grain boundary nucleation into account as well as the effect of the grain boundary surface area per unit volume. Roberts et al. (1979) replaced the time dependence in Equation (5.45) by a strain dependence representing the instantaneous time taken for the dynamic recrystallisation process.

Many models capable of both static and dynamic recrystallisation further have kinetics or some form of critical recrystallisation criteria that depends explicitly on strain or strain rate (Pietrzyk, 2002; Roucoules et al., 2003; Svyetlichnyy, 2007). Considering finite element analyses where transient loading conditions are modelled with the possibility of nonuniform and variable strain rate, such models are usually not sufficiently

general.

The criteria used to determine the onset of recrystallisation is sometimes a value associated with critical strain or critical stored energy. Assuming the stored energy is only a function of dislocation density, a critical value of dislocation density may be used for the onset of recrystallisation as done by Bailey and Hirsch (1962). An alternative could be the critical size of subgrain dimensions associated with a stable nucleus (Sandström and Lagneborg, 1975; Roberts and Ahlblom, 1978).

A recrystallisation model similar to the one validated by Brown and Bammann (2012) is implemented. The model has the ability to simulate multiple waves of recrystallisation. Various recrystallised and unrecrystallised volume fractions can exist simultaneously. This model differs from the JMAK form and no critical value is associated with the onset of recrystallisation. The recrystallisation is instead based on the mobility of grain and subgrain boundaries. The driving force behind the recrystallisation is provided by the stored energy in the dislocation structure.

The recrystallisation is implemented as an extension to the isotropic dislocation density ratio based model formulation. The model combines the Kocks-Mecking work hardening theory implemented using a dislocation density ratio internal state variable that evolves following Equation (5.19), with the theory accompanying the recrystallised volume fraction growth rate formulation used by Brown and Bammann (2012).

In the following subsection the theory used to develop the multiple cycle recrystallisation model is covered. The numerical implementation of the theory into a material subroutine useful for finite element analysis is then discussed. The numerical discussion includes the management of state variables, how multiple recrystallisation cycles may be tracked as well as the analytical sensitivities required. The model parameters are fit to Cobalt data between 600°C and 900°C as well as a large range of strain rate and temperature data from monotonic compression tests on oxygen free high conductivity Copper.

5.7.1 Modelling theory

The process of recrystallisation is typically broken up into three sections. Nucleation mainly occurs during an incubation time before recrystallisation is really detected.

This is followed by an increasing rate of recrystallisation up to a point where growing subgrains impinge on the potential growth of one another. The recrystallisation process over time during isothermal annealing is commonly represented by a plot of the total volume fraction of recrystallised material ($0 \leq f_{\mathrm{x}} \leq 1$) as a logarithmic function of time. The process has a sigmoidal form as is usually the case with a diffusive interface description formulation in the kinetics of phase transformations (Humphreys and Hatherly, 1995).

Instead of a JMAK type model using Equation (5.45), the more general evolution of the recrystallised volume fraction is solved. From the work by Cahn and Hagel (1962), the recrystallised volume fraction growth rate is

$$\dot{f}_{\mathrm{x}} = A_{\mathrm{x}} v_{\mathrm{x}}. \tag{5.46}$$

In this growth rate equation, A_{x} is the interfacial area between recrystallised and unrecrystallised regions. This is multiplied by the average boundary velocity of the interface sweeping through the unrecrystallised region, v_{x}.

The rate of interface migration can be expressed by the driving pressure P for boundaries with a specific energy and mobility M (Furu et al., 1995; Doherty et al., 1997; Huang and Humphreys, 1999). Average grain boundary velocity is simply calculated using

$$v_{\mathrm{x}} = MP. \tag{5.47}$$

As the material deforms, the average misorientation angle $\bar{\theta}$ across the geometrically necessary subgrain boundaries increase, which in turn increases the mobility of the boundaries. Chen et al. (2002) use the empirical form

$$\bar{M} = M_0 \exp\left(-\frac{Q_M}{RT}\right)\left[1 - \exp\left(-C_M\left(\frac{\bar{\theta}}{\theta_m}\right)^{r_M}\right)\right] \tag{5.48}$$

to express the average subgrain boundary mobility $\bar{M}$ in terms of the average misorientation angle. In this expression, M_0, C_M and the exponent r_M are constants. θ_m is the misorientation angle associated with a high angle boundary while R is the universal gas constant and Q_M the activation energy for grain boundary mobility.

Brown and Bammann (2012) replaced the misorientation angle ratio with a stress like variable related to the mean free path of geometrically necessary dislocations. This stress like variable is used as internal state variable in their model to capture geometric effects. In the dislocation density ratio based model implementation used here, the internal state variable equivalent is the average slip plane lattice misorientation $\bar{\lambda}$ introduced in Equation (5.12).

Chen et al. (2002) observed the relationship between the effective subgrain diameter $\bar{d}_{\mathrm{x}}$, misorientation $\bar{\theta}$ and Burger's vector length b

$$\bar{d}_{\mathrm{x}}\bar{\theta} \propto b. \tag{5.49}$$

We now assume that the average distance between geometrically necessary dislocations is mainly as a result of subgrain boundaries. Under this assumption, the mean free path of geometrically necessary dislocations is proportional to the mean subgrain boundary diameter $L_g \propto \bar{d}_{\mathrm{x}}$. Using Equation (5.11), the relationship between the average misorientation angle and the average slip plane lattice misorientation is

$$\bar{\theta} \propto \left(\bar{\lambda}\right)^{r_g}. \tag{5.50}$$

The misorientation angle ratio of Equation (5.48) is now replaced in the current context by the internal state variable associated with the average lattice slip plane incompatibility. This results in the approximation for the average subgrain boundary mobility

$$\bar{M} = M_0 \exp\left(-\frac{Q_M}{RT}\right)\left[1 - \exp\left(-C_{M\theta}\bar{\lambda}^{r_{M\theta}}\right)\right]. \tag{5.51}$$

The constant $C_{M\theta}$ and exponent $r_{M\theta}$ values now differ from the original formulation to accommodate the various proportionalities. The driving force for the motion of the geometrically necessary boundaries is the stored energy in the dislocation structure. The expression of the stored energy in the average assembly as used by Chen et al. (2002) is considered. According to Humphreys and Hatherly (1995), the pressure driving the subgrain boundary growth can in it's simplest form be expressed as $P = \mu b^2\rho/2$. This assumes that the boundary energy effects on the driving force are negligible. Considering the dislocation density ratio used as evolving internal state variable in the current

framework, the pressure is calculated by

$$P = \frac{1}{2}\mu b^2 \rho_0 \varrho. \tag{5.52}$$

The evolution rate of the recrystallised volume fraction can now be modelled in the current setting with ϱ and $\bar{\lambda}$ as internal state variables. Including the above mentioned theory into a single expression, the rate of recrystallisation is rewritten by introducing new functions and constants

$$\dot{f}_{\mathrm{x}} = A_{\mathrm{x}} \varrho C_{\mathrm{Rx0}} C_{\mathrm{Rx}T}(T) C_{\mathrm{Rx}\lambda}\left(\bar{\lambda}\right). \tag{5.53}$$

The function is rewritten so that C_{Rx0} effectively contains all the pre-exponential constants. Similarly $C_{\mathrm{Rx}T}(T)$ contains the temperature dependence in a single function

$$C_{\mathrm{Rx}T}(T) = \mu\left(T\right) \exp\left(-\frac{a_{0\mathrm{Rx}}}{T}\right). \tag{5.54}$$

Here, $a_{0\mathrm{Rx}}$ is again the convenient grouping of the activation energy and universal gas constant as done in Equation (5.20). The function $C_{\mathrm{Rx}\lambda}\left(\bar{\lambda}\right)$ contains the geometric effects in the rewritten function

$$C_{\mathrm{Rx}\lambda}\left(\bar{\lambda}\right) = 1 - \exp\left(-C_{\mathrm{Rx}\lambda 0} \bar{\lambda}^{r_{\mathrm{Rx}\lambda}}\right), \tag{5.55}$$

where $C_{\mathrm{Rx}\lambda 0}$, and $r_{\mathrm{Rx}\lambda}$ replaces the constant $C_{M\theta}$ and exponent $r_{M\theta}$ in Equation (5.51) for subscript consistency.

For the grain boundary interfacial area between the recrystallised and unrecrystallised volume fractions, Speich and Fisher (1966) proposed the empirical relation $A_{\mathrm{x}} \propto f_{\mathrm{x}}(1 - f_{\mathrm{x}})$ based on their extensive experiments on nickel. Brown and Bammann (2012) then assumed the altered form $A_{\mathrm{x}} \propto f_{\mathrm{x}}^{a}(1 - f_{\mathrm{x}})^{b}$, with the exponents a and b.

During static recrystallisation, the dislocation density in the unrecrystallised phase of the material may decrease due to static or thermal recovery as per Equation (5.17). The volume fraction associated with the recrystallised phase of the material could also increase. This is effectively visible as softening of the bulk material. Dynamic recrystallisation is more complex as both the unrecrystallised and recrystallised material volume fractions continue to harden in the presence of added plastic strain. The ma-

terial can also recrystallise numerous times and contain multiple cycles or waves of recrystallisation simultaneously (Luton and Sellars, 1969; Sandström and Lagneborg, 1975; McQueen and Jonas, 1975). Considering multiple cycles of recrystallisation, a volume fraction f_{x_i} now represents the material volume fraction that has undergone i cycles of recrystallisation.

As in the model by Brown and Bammann (2012), $f_{\mathrm{x}_i} - f_{\mathrm{x}_{i+1}}$ represents the total volume fraction of material that has been recrystallised $i+1$ times. The original unrecrystallised material has a volume fraction $f_{\mathrm{x}_0} = 1$ and each volume fraction now has it's own set of internal state variables. The variables ϱ_{x_i} and $\bar{\lambda}_{\mathrm{x}_i}$ here represent the internal state variables associated with the material volume fraction $f_{\mathrm{x}_i} - f_{\mathrm{x}_{i+1}}$.

The altered form of the grain boundary interfacial area $A_{\mathrm{x}} \propto f_{\mathrm{x}}^a(1-f_{\mathrm{x}})^b$ is used in Equation (5.53). If $C_{\mathrm{Rx}0}$ is different from the original value, it still contains all of the pre-exponential constants while resolving the proportionality in the grain boundary interfacial area formulation. The evolution of the first recrystallisation cycle volume fraction is now determined from the rate equation

$$\dot{f}_{\mathrm{x}_1} = \varrho_{\mathrm{x}_0} C_{\mathrm{Rx}0} C_{\mathrm{Rx}T}(T) C_{\mathrm{Rx}\lambda}\left(\bar{\lambda}_{\mathrm{x}_0}\right) f_{\mathrm{x}_1}^{r_{\mathrm{Rx}a}} (1-f_{\mathrm{x}_1})^{r_{\mathrm{Rx}b}}. \tag{5.56}$$

The internal state variables associated with the original unrecrystallised material volume fraction are ϱ_{x_0} and $\bar{\lambda}_{\mathrm{x}_0}$. $r_{\mathrm{Rx}a}$ and $r_{\mathrm{Rx}b}$ are the exponents used in the empirical relation of the interfacial grain boundary area again renamed for consistency. For additional recrystallisation cycles, the fraction of f_{x_1}undergoing a second cycle of recrystallisation for example is $f_{\mathrm{x}_2}/f_{\mathrm{x}_1}$ while the volume fraction $(f_{\mathrm{x}_1} - f_{\mathrm{x}_2})/f_{\mathrm{x}_1}$ has only recrystallised once. Following Brown and Bammann (2012), the interfacial area per total material volume is therefore proportional to

$$A_{\mathrm{x}_2} \propto f_{\mathrm{x}_1}\left(\frac{f_{\mathrm{x}_2}}{f_{\mathrm{x}_1}}\right)^{r_{\mathrm{Rx}a}}\left(1-\frac{f_{\mathrm{x}_2}}{f_{\mathrm{x}_1}}\right)^{r_{\mathrm{Rx}b}}. \tag{5.57}$$

Some regions within the recrystallised volume fraction $f_{\mathrm{x}_1} - f_{\mathrm{x}_2}$ would have newly recrystallised due to the dislocation structure contained in $f_{\mathrm{x}_0} - f_{\mathrm{x}_1}$. Earlier recrystallised regions on the other hand have already hardened to motivate the additional recrystallisation cycle. A model simply using the relation in Equation (5.57) would

therefore under predict the volume fraction evolution rate if homogenised values of ϱ_{x_1} and $\bar{\lambda}_{\mathrm{x}_1}$ are used. Once the first recrystallisation cycle has completed, $f_{\mathrm{x}_1} \approx 1$. In this case no new dislocation free zones are added to the volume fraction region $f_{\mathrm{x}_1} - f_{\mathrm{x}_2}$. It would only then become more homogeneous with continued deformation. Brown and Bammann (2012) accounted for this observation with the introduction of a scaling function $1 + c(1 - f_{\mathrm{x}_1})$ that decreases to one as $f_{\mathrm{x}_1} \approx 1$. Using this scaling function correction, the recrystallised volume fraction growth rate is generalised in the current context as

$$\dot{f}_{\mathrm{x}_{i+1}} = \varrho_{\mathrm{x}_i} C_{\mathrm{Rx}0} C_{\mathrm{Rx}T}(T) C_{\mathrm{Rx}\lambda}\left(\bar{\lambda}_{\mathrm{x}_i}\right) g(f_{\mathrm{x}_i}, f_{\mathrm{x}_{i+1}}) \tag{5.58}$$

where

$$g(f_{\mathrm{x}_i}, f_{\mathrm{x}_{i+1}}) = f_{\mathrm{x}_i}\left(\frac{f_{\mathrm{x}_{i+1}}}{f_{\mathrm{x}_i}}\right)^{r_{\mathrm{Rx}a}}\left(1 - \frac{f_{\mathrm{x}_{i+1}}}{f_{\mathrm{x}_i}}\right)^{r_{\mathrm{Rx}b}}\left(1 + C_{\mathrm{Rx}c}\left(1 - f_{\mathrm{x}_i}\right)\right). \tag{5.59}$$

Given a time increment δt, the first (f_{x_1}) and second (f_{x_2}) volume fractions can both progress, meaning region $f_{\mathrm{x}_1} - f_{\mathrm{x}_2}$ will increase by δf_{x_1} and decrease by δf_{x_2}. Assuming recrystallisation removes the dislocation structure, the dislocation density ratio within a newly recrystallised portion δf_{x_1} should be reset. If the region $f_{\mathrm{x}_1}(t) - f_{\mathrm{x}_2}(t) - \delta f_{\mathrm{x}_2}$ hardens or recovers as if no recrystallisation occurs, the dislocation density ratio at $t + \delta t$ is given using rate Equation (5.19):

$$\begin{aligned}\left\{\varrho_{\mathrm{x}_1}\right\}^{t+\delta t}_{f_{\mathrm{x}_1}(t)-f_{\mathrm{x}_2}(t)-\delta f_{\mathrm{x}_2}} \approx &\left\{\varrho_{\mathrm{x}_1}\right\}^{t}_{f_{\mathrm{x}_1}(t)-f_{\mathrm{x}_2}(t)} + \\ &\left(\dot{\alpha}\left(C_g \bar{\lambda}^{r_g}_{\mathrm{x}_1} + C_1\sqrt{\varrho_{\mathrm{x}_1}} - C_2(\dot{\alpha}, T)\,\varrho_{\mathrm{x}_1}\right) - C_3(T)\varrho^{r_3}_{\mathrm{x}_1}\right)\delta t.\end{aligned} \tag{5.60}$$

Now using the rule of mixtures:

$$\left\{\varrho_{\mathrm{x}_1}\right\}^{t+\delta t}_{f_{\mathrm{x}_1}(t+\delta t)-f_{\mathrm{x}_2}(t+\delta t)} = \frac{f_{\mathrm{x}_1}(t) - f_{\mathrm{x}_2}(t) - \delta f_{\mathrm{x}_2}}{f_{\mathrm{x}_1}(t) - f_{\mathrm{x}_2}(t) + \delta f_{\mathrm{x}_1} - \delta f_{\mathrm{x}_2}}\left\{\varrho_{\mathrm{x}_1}\right\}^{t+\delta t}_{f_{\mathrm{x}_1}(t)-f_{\mathrm{x}_2}(t)-\delta f_{\mathrm{x}_2}}. \tag{5.61}$$

Substituting Equation (5.60) into Equation (5.61), the general form of the dislocation density ratio evolution can be rewritten by taking the limit $\delta t \to 0$ and substituting $i = 1$ in the same way as Brown and Bammann (2012):

$$\dot{\varrho}_{\mathrm{x}_i} = \dot{\alpha}\left(C_g \bar{\lambda}^{r_g}_{\mathrm{x}_i} + C_1\sqrt{\varrho_{\mathrm{x}_i}} - C_2(\dot{\alpha}, T)\,\varrho_{\mathrm{x}_i}\right) - C_3(T)\varrho^{r_3}_{\mathrm{x}_i} - \frac{\dot{f}_{\mathrm{x}_i}}{f_{\mathrm{x}_i} - f_{\mathrm{x}_{i+1}}}\varrho_{\mathrm{x}_i}. \tag{5.62}$$

Doing the same for the internal state variable associated with the average slip plane lattice incompatibility:

$$\dot{\bar{\lambda}}_{\mathrm{x}_i} = \dot{\alpha} C_{\lambda \mathrm{x}} - \frac{\dot{f}_{\mathrm{x}_i}}{f_{\mathrm{x}_i} - f_{\mathrm{x}_{i+1}}} \bar{\lambda}_{\mathrm{x}_i}, \tag{5.63}$$

where $C_{\lambda \mathrm{x}}$ is a constant related to $C_\lambda / d_{\mathrm{x}}$ in Equation (5.14) for a specific grain size. In the presence of recrystallisation, the equivalent threshold stress of Equation (5.2) is calculated using the average dislocation density ratio

$$\bar{\varrho} = \sum_{i=0}^{n_{\mathrm{x}}-1} \varrho_{\mathrm{x}_i} \left(f_{\mathrm{x}_i} - f_{\mathrm{x}_{i+1}} \right), \tag{5.64}$$

where n_{x} is the total number of recrystallisation cycles.

5.8 Numerical Implementation

The MTS model was implemented in Appendix C as an extension to the isotropic hardening user material framework in Appendix A. Similarly, the dislocation density ratio based constitutive model with recrystallisation is implemented numerically into Fortran subroutines given in Appendix F. The temperature dependent shear modulus following Equation (3.21) is still used and returned by calling the `SHEARMOD` subroutine presented in Appendix C.1.

The model is implemented into an isotropic hardening subroutine `FISOTROPIC` called by the Abaqus user material framework. A residual subroutine `RGET` is used to determine the recrystallised volume fraction and internal state variable values per volume fraction. The yield stress function `FISOTROPIC` for the implemented model is attached in Appendix F.1 while F.2 is the subroutine called to solve the internal state variables per volume fraction. Figure 5.13 shows the layout of the appended subroutines called by Appendix A.1 in this implementation.

The internal state variables are solved using fully implicit Backward Euler integration. The model integrates the various values incrementally with previous converged ISV values stored in the `STATEV` vector and updated at the end of the increment. Other values that are useful in an analysis apart from the internal state variables needed in the recrystallisation and density ratio based evolution include the accumulated volume

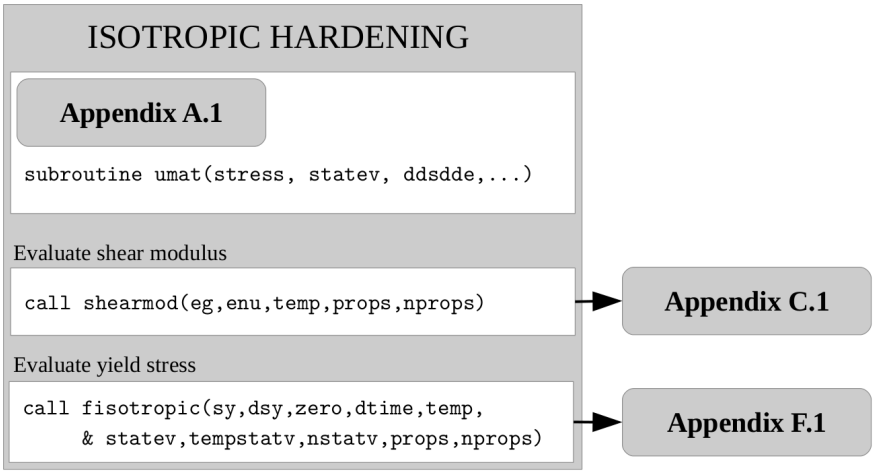

Figure 5.13: The dislocation density based isotropic hardening user material with recrystallisation.

fraction averaged equivalent plastic strain. An internal state variable for the equivalent plastic strain is also assigned per recrystallisation volume fraction α_{x_i}. This is done to keep track of the equivalent plastic strain that accumulates and is reset by each wave of recrystallisation. If a specific recrystallisation volume fraction f_{x_i} is active, the plastic strain increment $\delta\alpha$ is added to the internal state variable

$$\alpha_{\mathrm{x}_i}|_{t+\triangle t} = \alpha_{\mathrm{x}_i}|_t + \delta\alpha. \tag{5.65}$$

The values of the volume fraction averaged plastic strain and misorientation can be calculated as in Equation (5.64) by

$$\bar{\alpha} = \sum_{i=0}^{n_{\mathrm{x}}-1} \alpha_{\mathrm{x}_i} \left(f_{\mathrm{x}_i} - f_{\mathrm{x}_{i+1}}\right) \quad \text{and} \quad \bar{\bar{\lambda}} = \sum_{i=0}^{n_{\mathrm{x}}-1} \bar{\lambda}_{\mathrm{x}_i} \left(f_{\mathrm{x}_i} - f_{\mathrm{x}_{i+1}}\right). \tag{5.66}$$

The total length of the state variable array (`NSTATV`) is set in the Abaqus input file with the `*DEPVAR` card. In this implementation, the volume fraction averaged equivalent plastic strain, dislocation density ratio and average slip plane lattice misorientation are stored in the first three entries of the state variable array `STATEV(1:3)`. Tracking the evolution of the equivalent plastic strain, dislocation density ratio, average slip

plane lattice misorientation as well as volume fraction for each recrystallisation cycle means four entries in the STATEV array need to be allocated per volume fraction. This means that given the maximum number of possible recrystallising volume fractions (NRRX$= n_{\mathrm{x}}$), the total length of the STATEV array (NSTATV) as given by the material definition in the Abaqus input file should be at least DEPVAR=4*NRRX+3 so that enough memory is allocated to the problem. The previous converged values of the volume fraction averaged quantities as well as the ISV values at the end of the previous increment are stored in the state variable array sent as input and then returned at the end of the current increment as

$$\mathtt{STATEV}(1:4*\mathtt{NRRX}+3) = \left\{\bar{\alpha}, \bar{\varrho}, \bar{\bar{\lambda}}, \alpha_{\mathrm{x}_0}, \varrho_{\mathrm{x}_0}, \bar{\lambda}_{\mathrm{x}_0}, f_{\mathrm{x}_1}, ..., \alpha_{\mathrm{x}_{n_{\mathrm{x}}-1}}, \varrho_{\mathrm{x}_{n_{\mathrm{x}}-1}}, \bar{\lambda}_{\mathrm{x}_{n_{\mathrm{x}}-1}}, f_{\mathrm{x}_{n_{\mathrm{x}}}}\right\}. \tag{5.67}$$

Following Brown and Bammann (2012), it makes no sense evolving and updating the ISV values for the original volume fraction ϱ_{x_0} and $\bar{\lambda}_{\mathrm{x}_0}$ once it has been fully recrystallised. This happens when the first recrystallised volume fraction in the state variable array defined above approaches unity $f_{\mathrm{x}_1} \approx 1$. If this is the case, the state variable values associated with the first recrystallised volume fraction is shifted so that it is now associated with the new default volume fraction. If this is the case, the previous converged values in the state variable array may alternatively be considered as

$$\mathtt{STATEV}(7:4*\mathtt{NRRX}+3) = \left\{f_{\mathrm{x}_0} \approx 1, \alpha_{\mathrm{x}_0}, \varrho_{\mathrm{x}_0}, \bar{\lambda}_{\mathrm{x}_0}, f_{\mathrm{x}_1}, ..., \alpha_{\mathrm{x}_{n_{\mathrm{x}}-2}}, \varrho_{\mathrm{x}_{n_{\mathrm{x}}-2}}, \bar{\lambda}_{\mathrm{x}_{n_{\mathrm{x}}-2}}, f_{\mathrm{x}_{n_{\mathrm{x}}-1}}\right\}. \tag{5.68}$$

To reduce the amount of allocated memory required, an internal state variable shift applied to the STATEV array would result in a new state variable array where

$$\mathtt{STATEV}(4:4*\mathtt{NRRX}+3) = \{\mathtt{OLD\_STATEV}(8:4*\mathtt{NRRX}+3), 0, 0, 0, 0\}. \tag{5.69}$$

In this implementation, the potential state variable array shift happens before calculating the stresses associated with the current time increment and additional evolution of the ISV's.

5.8.1 Plasticity and internal state evolution

Considering the temperature at the end of a specific time increment solved, the shear modulus and kinetic equation scale function are first evaluated as given in Equations (3.21) and (3.22). To determine the yield stress from Equation (5.4), the threshold stress value and therefore average dislocation density ratio at the end of the current increment is required as in Equation (5.64). The numerical implementation needs to cycle through each of the recrystallised volume fractions, evolving the associated internal state variables and then adding the contribution to the the average dislocation density ratio.

The maximum number of volume fractions to track is set with $n_{\mathrm{x}} =$`(NSTATV-3)/4`. The value of `NSTATV` is set using the `*DEPVAR` card in the Abaqus input file, used to allocate the memory required. The volume fractions are effectively fully recrystallised and internal state variables shifted once $f_{\mathrm{x}_1} > 0.999$ in the implementation presented. Internal state variable updates also only cycle through each of the following volume fractions as long as the conditions $f_{\mathrm{x}_{i+1}} > 0.001$ and $i+1 \leq n_{\mathrm{x}}$ are met to save on computational time. This is different from the implementation by Brown and Bammann (2012) in that they evolve all volume fraction state variables, even before it contributes to the overall material response.

Given that the implementation cycles through the volume fractions, a single variable is used for values of the volume fractions, rates and internal state variables needed within the specific cycle evaluated. The values are stored to the temporary state variable array before continuing to the next cycle. In the next cycle, the same variables now effectively just point to alternate entries of the state variable array. Here, we use the subscripts xc and xn to represent the variables associated with the current $c = i$ and next $n = i + 1$ volume fractions.

To start the flow rule evaluation, the values associated with the default volume fraction $i = 0$ are set from the known conditions $f_{\mathrm{x}_0} = 1$ and $\dot{f}_{\mathrm{x}_0} = 0$, meaning $f_{\mathrm{x}c} = 1$ and $\dot{f}_{\mathrm{x}c} = 0$. The volume fraction averaged quantities are also initialised with $\bar{\alpha} = 0$, $\bar{\varrho} = 0$ and $\bar{\bar{\lambda}} = 0$. A vector $\mathbf{x} = \left\{\varrho_{\mathrm{x}_i}, \bar{\lambda}_{\mathrm{x}_i}\right\}_{t+\delta t}$ represents an estimate of the internal state variable values associated with the current volume fraction. The construction of the various residuals and solutions necessary to solve the internal state variable evolution is constructed next.

Considering that from Equation (5.48) the misorientation fractional value $\bar{\theta}/\theta_M$ should be below unity, Equation (5.55) is evaluated so that

$$C_{\mathrm{Rx}\lambda} = 1 - \exp\left(-C_{\mathrm{Rx}\lambda 0} \min\left([x_2, 1]\right)^{r_{\mathrm{Rx}\lambda}}\right). \tag{5.70}$$

The recrystallised volume fraction growth associated with the next volume fraction $f_{\mathrm{x}n}$ is calculated by first setting the estimated variable value equal to the previous converged value $f_{\mathrm{x}n} = \left\{f_{\mathrm{x}_{i+1}}\right\}_t = \texttt{STATEV}(4 * \texttt{i} + 7)$. The minimum value $f_{\mathrm{x}n} \geq 10^{-4}$ is introduced in the presented implementation in order to avoid a zero interface surface area when using Equation (5.59). This condition assumes that nucleation has already happened. $f_{\mathrm{x}n}$ is now the current estimate of $\left\{f_{\mathrm{x}_{i+1}}\right\}_{t+\delta t}$, and the validity of this estimate is determined by evaluating the residual:

$$f_{R_{\mathrm{x}}} = f_{\mathrm{x}n} - \left\{f_{\mathrm{x}_{i+1}}\right\}_t - \delta t \dot{f}_{\mathrm{x}n}, \tag{5.71}$$

where the rate using Equation (5.58) is determined by

$$\dot{f}_{\mathrm{x}n} = x_1 C_{\mathrm{Rx}0} C_{\mathrm{Rx}T}(T) C_{\mathrm{Rx}\lambda}\left(x_2\right) g_{\mathrm{x}}(f_{\mathrm{x}c}, f_{\mathrm{x}n}). \tag{5.72}$$

Should the residual equation be violated, the updated estimate on the following volume fraction is solved using Newton's method:

$$\left\{f_{\mathrm{x}n}\right\}^{k+1} = \left\{f_{\mathrm{x}n}\right\}^{k} - \left(1 - x_1 C_{\mathrm{Rx}0} C_{\mathrm{Rx}T}(T) C_{\mathrm{Rx}\lambda}\left(x_2\right) \left\{\frac{dg_{\mathrm{x}}}{df_{\mathrm{x}n}}\right\}^{k}\right)^{-1} \left\{f_{R_{\mathrm{x}}}\right\}^{k} \tag{5.73}$$

with

$$\begin{aligned} \frac{dg_{\mathrm{x}}}{df_{\mathrm{x}n}} =& r_{\mathrm{Rx}a}\left(\frac{f_{\mathrm{x}n}}{f_{\mathrm{x}c}}\right)^{r_{\mathrm{Rx}a}-1}\left(1 - \frac{f_{\mathrm{x}n}}{f_{\mathrm{x}c}}\right)^{r_{\mathrm{Rx}b}}\left(1 + C_{\mathrm{Rx}c}\left(1 - f_{\mathrm{x}c}\right)\right) \\ & - r_{\mathrm{Rx}b}\left(\frac{f_{\mathrm{x}n}}{f_{\mathrm{x}c}}\right)^{r_{\mathrm{Rx}a}}\left(1 - \frac{f_{\mathrm{x}n}}{f_{\mathrm{x}c}}\right)^{r_{\mathrm{Rx}b}-1}\left(1 + C_{\mathrm{Rx}c}\left(1 - f_{\mathrm{x}c}\right)\right). \end{aligned} \tag{5.74}$$

Once the value of the next volume fraction is solved, the residuals on the two ISV estimates can be determined using the evolution rates of Equations (5.62) and (5.63),

resulting in the residual equations

$$f_{R_1}(x_1,x_2) = x_1 - \varrho_{\mathrm{x}_i}|_t - \delta\alpha\left(C_0 x_2^{r_g} + C_1\sqrt{x_1} - C_2(\dot{\alpha},T)x_1\right) + \delta t C_3(T)x_1^{r_3} + \delta t\frac{\dot{f}_{\mathrm{xc}}}{f_{\mathrm{xc}} - f_{\mathrm{xn}}(x_1,x_2)}x_1 = 0 \tag{5.75}$$

and

$$f_{R_2}(x_1,x_2) = x_2 - \lambda|_t - \delta\alpha C_\lambda + \delta t\frac{\dot{f}_{\mathrm{xc}}}{f_{\mathrm{xc}} - f_{\mathrm{xn}}(x_1,x_2)}x_2 = 0. \tag{5.76}$$

The internal state variable updates are solved by using the initial guess $\mathbf{x} = \left\{\varrho_{\mathrm{x}_i}, \bar{\lambda}_{\mathrm{x}_i}\right\}_t = \{\texttt{STATEV}(4*\texttt{i}+5, 4*\texttt{i}+6)\}$, sent in to the `RGET` subroutine in Appendix F.2. The residual values and sensitivities are returned to the `FISOTROPIC` subroutine. The values are updated using the Newton-Raphson scheme

$$\{\mathbf{x}\}^{k+1} = \{\mathbf{x}\}^k - \left[\{\mathbf{F}'_R\}^k\right]^{-1}\{\mathbf{f}_R\}^k \tag{5.77}$$

where $F'_{R\,ij} = \partial f_{R_i}/\partial x_j$ are the components of the Jacobian matrix. Considering the numerical implementation, the inverse of matrix $\mathbf{F}'_R$ is constructed directly using

$$[\mathbf{F}'_R]^{-1} = \frac{1}{\det(\mathbf{F}'_R)}\begin{bmatrix} F'_{R\,2,2} & -F'_{R\,1,2} \\ -F'_{R\,2,1} & F'_{R\,1,1} \end{bmatrix} \tag{5.78}$$

with $\det(\mathbf{F}'_R) = F'_{R\,1,1}F'_{R\,2,2} - F'_{R\,1,2}F'_{R\,2,1}$. The partial derivatives of the residual equations that make up the components of the Jacobian matrix are:

$$\begin{aligned}
\frac{\partial f_{R_1}}{\partial x_1} &= 1 - \delta\alpha\left(\frac{1}{2}C_1 x_1^{-1/2} - C_2\right) + \delta t r_3 C_3 x_1^{r_3-1} + \delta t\frac{\dot{f}_{\mathrm{xc}}}{f_{\mathrm{xc}} - f_{\mathrm{xn}}} + \delta t x_1\frac{\dot{f}_{\mathrm{xc}}}{(f_{\mathrm{xc}} - f_{\mathrm{xn}})^2}\frac{df_{\mathrm{xn}}}{dx_1}, \\
\frac{\partial f_{R_1}}{\partial x_2} &= -\delta\alpha r_g C_g x_2^{r_g-1} + \delta t x_1\frac{\dot{f}_{\mathrm{xc}}}{(f_{\mathrm{xc}} - f_{\mathrm{xn}})^2}\frac{df_{\mathrm{xn}}}{dx_2}, \\
\frac{\partial f_{R_2}}{\partial x_1} &= \delta t x_2\frac{\dot{f}_{\mathrm{xc}}}{(f_{\mathrm{xc}} - f_{\mathrm{xn}})^2}\frac{df_{\mathrm{xn}}}{dx_1}, \\
\frac{\partial f_{R_2}}{\partial x_2} &= 1 + \delta t\frac{\dot{f}_{\mathrm{xc}}}{f_{\mathrm{xc}} - f_{\mathrm{xn}}} + \delta t x_2\frac{\dot{f}_{\mathrm{xc}}}{(f_{\mathrm{xc}} - f_{\mathrm{xn}})^2}\frac{df_{\mathrm{xn}}}{dx_2}.
\end{aligned} \tag{5.79}$$

The derivatives of the next volume fraction with respect to the current internal state variable estimates are determined from the residual in Equation (5.71) as:

$$\begin{aligned}\frac{df_{\mathrm{x}c}}{dx_1} =& \delta t C_{\mathrm{Rx}0} C_{\mathrm{Rx}T}(T) C_{\mathrm{Rx}\lambda}\left(x_2\right) g_{\mathrm{x}}(f_{\mathrm{x}c}, f_{\mathrm{x}n}) \left(1 - \delta t x_1 C_{\mathrm{Rx}0} C_{\mathrm{Rx}T}(T) C_{\mathrm{Rx}\lambda}\left(x_2\right) \frac{dg_{\mathrm{x}}}{df_{\mathrm{x}n}}\right)^{-1} \\ \frac{df_{\mathrm{x}c}}{dx_2} =& \delta t x_1 C_{\mathrm{Rx}0} C_{\mathrm{Rx}T}(T)(f_{\mathrm{x}c}, f_{\mathrm{x}n}) \frac{dC_{\mathrm{Rx}\lambda}}{dx_2} \left(1 - \delta t x_1 C_{\mathrm{Rx}0} C_{\mathrm{Rx}T}(T) C_{\mathrm{Rx}\lambda}\left(x_2\right) \frac{dg_{\mathrm{x}}}{df_{\mathrm{x}n}}\right)^{-1}\end{aligned} \tag{5.80}$$

and

$$\frac{dC_{\mathrm{Rx}\lambda}}{dx_2} = \begin{cases} r_{\mathrm{Rx}\lambda} C_{\mathrm{Rx}\lambda 0} x_2^{r_{\mathrm{Rx}\lambda}-1} \left[1 - \exp\left(-C_{\mathrm{Rx}\lambda 0} x_2^{r_{\mathrm{Rx}\lambda}}\right)\right] & \text{if } \; x_2 \leq 1, \\ 0 & \text{otherwise.} \end{cases} \tag{5.81}$$

Before possibly moving to the next volume fraction, the current volume fraction contribution to the equivalent dislocation density is needed. This is updated along with the contribution to the yield stress sensitivity required to resolve the flow rule residual and solve the equivalent plastic strain increment. The contribution to the average dislocation density ratio is calculated as in Equation (5.64) by updating the value of the equivalent dislocation density ratio variable

$$\bar{\varrho} = \bar{\varrho} + x_1 \left(f_{\mathrm{x}c} - f_{\mathrm{x}n}\right). \tag{5.82}$$

The sensitivity of the yield stress with respect to the equivalent plastic strain increment is determined by

$$\frac{d\sigma_{\mathrm{Y}}}{d\delta\alpha} = \frac{\mu}{\mu_r} \left[\frac{\sigma_0 \sqrt{\bar{\varrho}}}{\delta t} \frac{dS_\varepsilon}{d\dot{\alpha}} + \frac{S_\varepsilon \sigma_0}{2\sqrt{\bar{\varrho}}} \frac{d\bar{\varrho}}{d\delta\alpha}\right]. \tag{5.83}$$

The definition of the scaling factor in Equation (3.22) still leads to:

$$\frac{dS_\varepsilon}{d\dot{\alpha}} = \frac{T}{\dot{\alpha} p_\varepsilon q_\varepsilon a_{0\varepsilon} \mu} \left(\frac{T}{a_{0\varepsilon}\mu} \ln\left(\frac{\dot{\varepsilon}_{0\varepsilon}}{\dot{\alpha}}\right)\right)^{1/q_\varepsilon - 1} \left[1 - \left(\frac{T}{a_{0\varepsilon}\mu} \ln\left(\frac{\dot{\varepsilon}_{0\varepsilon}}{\dot{\alpha}}\right)\right)^{1/q_\varepsilon}\right]^{1/p_\varepsilon - 1}. \tag{5.84}$$

In Appendix F.2, the contribution of the scaling factor to the yield stress sensitivity is calculated at the end of the recrystallisation cycle evaluations. The equivalent

dislocation density ratio sensitivity is determined upon inspection of Equation (5.64) by

$$\frac{d\bar{\varrho}}{d\delta\alpha} = \sum_{i=0}^{n_{\mathrm{x}}-1} \left[\frac{d\varrho_{\mathrm{x}_i}}{d\delta\alpha} \left(f_{\mathrm{x}_i} - f_{\mathrm{x}_{i+1}} \right) + \varrho_{\mathrm{x}_i} \left(\frac{df_{\mathrm{x}_i}}{d\delta\alpha} - \frac{df_{\mathrm{x}_{i+1}}}{d\delta\alpha} \right) \right]. \tag{5.85}$$

From the first volume fraction condition with $f_{\mathrm{x}_0} = 1$, it is evident that $df_{\mathrm{x}_0}/d\delta\alpha = 0$. The incremental contribution to the average dislocation density ratio sensitivity added at each cycle means that given the initialised variable value $d\bar{\varrho}/d\delta\alpha = 0$, the sensitivity is updated within each cycle evaluation in the same way as in Equation (5.82) by

$$\frac{d\bar{\varrho}}{d\delta\alpha} = \frac{d\bar{\varrho}}{d\delta\alpha} + \frac{dx_1}{d\delta\alpha} \left(f_{\mathrm{xc}} - f_{\mathrm{x}n} \right) + x_1 \left(\frac{df_{\mathrm{xc}}}{d\delta\alpha} - \frac{df_{\mathrm{x}n}}{d\delta\alpha} \right) \tag{5.86}$$

where $df_{\mathrm{xc}}/d\delta\alpha = 0$ for the first volume fraction. Given the residual Equation (5.71) with $\dot{f}_{\mathrm{x}n}$ now a function of $\mathbf{x}$ according to Equation (5.72):

$$\frac{df_{\mathrm{x}n}}{d\delta\alpha} = \frac{\partial f_{\mathrm{x}n}}{\partial x_1} \frac{dx_1}{d\delta\alpha} + \frac{\partial f_{\mathrm{x}n}}{\partial x_2} \frac{dx_2}{d\delta\alpha} + \frac{\partial f_{\mathrm{x}n}}{\partial f_{\mathrm{xc}}} \frac{df_{\mathrm{xc}}}{d\delta\alpha}. \tag{5.87}$$

The sensitivities of x_1 and x_2 with respect to equivalent plastic strain increment are approximated in the presented implementation by again using the residual equations for the evolution of the internal state variables in Equations (5.75) and (5.76).

Following the example in Equation (5.27), the updated internal state variable associated with the dislocation density ratio evolution in Equation (5.75) is given by

$$x_1 = \varrho_{\mathrm{x}_i}|_t + \delta\theta_{x_1}|_{t+\delta t}\,, \tag{5.88}$$

where $\delta\theta_{x_1}|_{t+\delta t} = \delta\theta_{x_1}\left(\delta\alpha, \delta t, \dot{\alpha}, T, x_1, x_2\right)$ is a function effectively solved using the residual subroutine `RGET`. During a call to the `RGET` subroutine, $\delta\theta_{x_1}|_{t+\delta t}$ is mainly seen as a function of the x_1 and x_2 values at the end of the increment since the other values are effectively constant during a specific solution loop.

Further sensitivities are however required so that the equivalent plastic strain can be determined from within the user material framework. The total derivative of x_1 with respect to the equivalent plastic strain using Equation (5.88) is determined from

the chain rule

$$\frac{dx_1}{d\delta\alpha} = \frac{\partial\delta\theta_{x_1}}{\partial\delta\alpha} + \frac{\partial\delta\theta_{x_1}}{\partial\dot{\alpha}}\frac{d\dot{\alpha}}{d\delta\alpha} + \frac{\partial\delta\theta_{x_1}}{\partial f_{\mathrm{xc}}}\frac{df_{\mathrm{xc}}}{d\delta\alpha} + \frac{\partial\delta\theta_{x_1}}{\partial x_1}\frac{dx_1}{d\delta\alpha} + \frac{\partial\delta\theta_{x_1}}{\partial x_2}\frac{dx_2}{d\delta\alpha}. \tag{5.89}$$

The derivative of the equivalent strain rate with respect to incremental plastic strain is $d\dot{\alpha}/d\delta\alpha = 1/\delta t$. The value of $df_{\mathrm{xc}}/d\delta\alpha$ is equal to zero in the first volume fraction due to $f_{\mathrm{xc}} = f_{\mathrm{x}_0} = 1$. If not in the first volume fraction it is carried over from the preceding volume fraction calculation. The equivalent plastic strain increment sensitivity in this case is taken as the sensitivity of the next volume fraction as determined in the previous solution loop, i.e. $df_{\mathrm{xc}}/d\delta\alpha|_{f_{\mathrm{x}_{i+1}}} = df_{\mathrm{xn}}/d\delta\alpha|_{f_{\mathrm{x}_i}}$.

Rearranging Equation (5.89) and noting that $(1 - \partial\delta\theta_{x_1}/\partial x_1) \equiv \partial f_{R_1}/\partial x_1$ and $-\partial\delta\theta_{x_1}/\partial x_2 \equiv \partial f_{R_1}/\partial x_2$ in Equations (5.79) implies

$$\frac{\partial f_{R_1}}{\partial x_1}\frac{dx_1}{d\delta\alpha} + \frac{\partial f_{R_1}}{\partial x_2}\frac{dx_2}{d\delta\alpha} = \Gamma_{x_1} \tag{5.90}$$

where Γ_{x_1} contains all of the sensitivity components in Equation (5.89) not associated with x_1 and x_2:

$$\Gamma_{x_1} = \frac{\partial\delta\theta_{x_1}}{\partial\delta\alpha} + \frac{\partial\delta\theta_{x_1}}{\partial\dot{\alpha}}\frac{d\dot{\alpha}}{d\delta\alpha} + \frac{\partial\delta\theta_{x_1}}{\partial f_{\mathrm{xc}}}\frac{df_{\mathrm{xc}}}{d\delta\alpha}. \tag{5.91}$$

Doing the same as in Equation (5.90) for $dx_2/d\delta\alpha$ leads more generally to the system of equations

$$\frac{\partial f_{R_i}}{\partial x_1}\frac{dx_1}{d\delta\alpha} + \frac{\partial f_{R_i}}{\partial x_2}\frac{dx_2}{d\delta\alpha} = \Gamma_{x_i}. \tag{5.92}$$

For the first residual equation ($i = 1$) the right hand side of Equation (5.92) is

$$\begin{aligned}\Gamma_{x_1} &\equiv -\frac{\partial f_{R_1}}{\partial\delta\alpha} - \frac{\partial f_{R_1}}{\partial\dot{\alpha}}\frac{d\dot{\alpha}}{d\delta\alpha} - \frac{\partial f_{R_1}}{\partial df_{\mathrm{xc}}}\frac{df_{\mathrm{xc}}}{d\delta\alpha} \\ &= C_0 x_2^{r_g} + C_1\sqrt{x_1} - C_2 x_1 - \dot{\alpha}\frac{dC_2}{d\dot{\alpha}} + x_1\left[\delta t\frac{\dot{f}_{\mathrm{xc}}}{(f_{\mathrm{xc}} - f_{\mathrm{xn}})^2} - \frac{1}{f_{\mathrm{xc}} - f_{\mathrm{xn}}}\right]\frac{df_{\mathrm{xc}}}{d\delta\alpha},\end{aligned} \tag{5.93}$$

with $dC_2/d\dot{\alpha}$ in Equation (5.40).

The second residual has no equivalent plastic strain rate dependence. The approx-

imate derivative of this residual equation with respect to plastic strain gives

$$\Gamma_{x_2} \equiv -\frac{\partial f_{R_2}}{\partial \delta\alpha} - \frac{\partial f_{R_2}}{\partial df_{\text{xc}}}\frac{df_{\text{xc}}}{d\delta\alpha} = C_\lambda + x_2\left[\delta t \frac{\dot{f}_{\text{xc}}}{\left(f_{\text{xc}} - f_{\text{xn}}\right)^2} - \frac{1}{f_{\text{xc}} - f_{\text{xn}}}\right]\frac{df_{\text{xc}}}{d\delta\alpha}. \tag{5.94}$$

The values of $\partial f_{R_i}/\partial x_j$ in Equation (5.92) are the same components used to construct the matrix needed in Equation (5.77). The relevant derivatives of the current volume fraction internal state variables with respect to equivalent plastic strain are then given by

$$\frac{dx_1}{d\delta\alpha} = \frac{1}{\det(\mathbf{F}'_R)}\left(F'_{R\,2,2}\Gamma_{x_1} - F'_{R\,1,2}\Gamma_{x_2}\right) \tag{5.95}$$

and

$$\frac{dx_2}{d\delta\alpha} = \frac{1}{\det(\mathbf{F}'_R)}\left(F'_{R\,1,1}\Gamma_{x_2} - F'_{R\,2,1}\Gamma_{x_1}\right). \tag{5.96}$$

These equations are used to approximate the current volume fraction contribution to the average dislocation density ratio sensitivity with respect to equivalent plastic strain.

The equivalent plastic strain for the current volume fraction is $\alpha_{\text{xc}} = \texttt{STATEV}(4*\texttt{i}+4) + \delta\alpha$. The volume averaged equivalent plastic strain and average slip plane lattice misorientation are updated in the same way as the equivalent dislocation density in Equation (5.82):

$$\begin{aligned}\bar{\alpha} =& \bar{\alpha} + \alpha_{\text{xc}}\left(f_{\text{xc}} - f_{\text{xn}}\right),\\ \bar{\bar{\lambda}} =& \bar{\bar{\lambda}} + x_2\left(f_{\text{xc}} - f_{\text{xn}}\right).\end{aligned} \tag{5.97}$$

Once all of the current volume fraction contributions are accounted for, the current volume fraction values are stored in the associated temporary state variable locations

$$\begin{aligned}\texttt{TEMPSTATEV}(4*\texttt{i}+4) =& \alpha_{\text{xc}}\\ \texttt{TEMPSTATEV}(4*\texttt{i}+5) =& x_1\\ \texttt{TEMPSTATEV}(4*\texttt{i}+6) =& x_2\\ \texttt{TEMPSTATEV}(4*\texttt{i}+7) =& f_{\text{xn}}.\end{aligned} \tag{5.98}$$

A check is performed to see whether additional volume fractions are considered by evaluating $i \leq \texttt{NRRX} - 1$. In the implementation here, different from the implementation by Brown and Bammann (2012), $f_{\text{xn}} \geq 0.001$ is also evaluated since it makes no

sense to spend computational power to evaluate the next volume fraction if it does not contribute to the global response. If both these conditions are met, the variables are updated for the next volume fraction evaluation with $f_{\text{xc}} = f_{xn}$, $\dot{f}_{\text{xc}} = \dot{f}_{xn}$, $df_{\text{xc}}/d\delta\alpha = df_{xn}/d\delta\alpha$ and $i = i+1$. Setting the initial guess $\mathbf{x} = \{\texttt{STATEV}(4 * \texttt{i} + 5, 4 * \texttt{i} + 6)\}$ subject to $x_1 \geq 1$ and $x_2 \geq 10^{-4}$, the evaluation of the next volume fraction is considered by again starting at Equation (5.70).

To test the gradients and numerical implementation of the isotropic hardening model with recrystallisation in Appendix F, a single increment is now modelled and analysed using an arbitrary set of material parameters. This is done using a simple one dimensional version of the user material framework that also uses the subroutine in Appendix F.

The value of the residual equation, analytical gradients as well as the estimated equivalent plastic strain increment are reported for each iteration. Components and sensitivities on the various nested solution loops are also reported for the final iteration. A forward finite difference estimate of various sensitivities are also calculated within the one dimensional test environment by perturbing the estimated plastic strains or relevant values by 10^{-8}.

Material parameters of an arbitrary virtual material used to test the implementation is:

- The elastic property values of $\mu_r = 50\text{GPa}$, $D_r = 0\text{MPa}$ and $T_r = 200\text{K}$ in Equation (3.21) and a Poisson's ratio of $\nu = 0.3$ are used.

- The temperature and rate dependent scaling function in Equation (3.22) is modelled with $a_{0\varepsilon} = 0.5\text{K/MPa}$, $p_\varepsilon = 1$, $q_\varepsilon = 1$ and $\dot{\varepsilon}_{0\varepsilon} = 10^7\text{s}^{-1}$.

- The athermal yield stress component and reference stress values using Equation (5.4) are $\hat{\sigma}_a = 0\text{MPa}$ and $\sigma_0 = 1000\text{MPa}$.

- The evolution of $\bar{\lambda}$ according to Equation (5.63) is modelled using $C_{\lambda\text{x}} = 1$.

- The parameters associated with the evolution of the dislocation density ratio in Equation (5.62) are $C_g = 100$, $r_g = 1$, $C_1 = 100$, $C_{20} = 10$, $a_{02} = 2\text{K/MPa}$, $\dot{\varepsilon}_{02} = 10^{10}\text{s}^{-1}$and $C_{30} = 0\text{s}^{-1}$

Iteration	Residual	Approximate Sensitivity	Finite Difference	Plastic Increment	Variation from final
1	13000.0	9.455E9	-	0.	8.511E-2
2	12875.5	7.021E5	6.992E5	1.342E-6	8.511E-2
3	12392.6	16975.49	16975.26	1.503E-2	7.008E-2
4	9861.02	7260.04	7255.09	8.212E-2	2.989E-3
5	409.91	7048.15	7042.58	8.511E-2	2.439E-6
6	0.3342	7047.98	7042.41	8.511E-2	9.99E-11
7	1.37E-5	7047.98	7042.41	8.511E-2	4.02E-15
8	5.52E-10	7047.98	7042.41	8.511E-2	-

Table 5.4: Test on the convergence of the equivalent plastic strain increment using the dislocation density based model with recrystallisation in Appendix F.

- The pre-exponential constant in Equation (5.53) is $C_{\mathrm{Rx0}} = 1\mathrm{s}^{-1}$. From Equation (5.54), $a_{0\mathrm{Rx}} = 10000\mathrm{K}$ while $C_{\mathrm{Rx}\lambda 0} = 1$ and $r_{\mathrm{Rx}\lambda} = 2$ in Equation (5.55).

- Equation (5.59) is modelled using $r_{\mathrm{Rx}a} = 0.2$, $r_{\mathrm{Rx}b} = 1.2$ and $C_{\mathrm{Rx}c} = 10$.

A single call to the one dimensional user material is made using a total strain increment $\delta\varepsilon = 0.1$, temperature of $T = 800\mathrm{K}$ and time increment of $\delta t = 1\mathrm{s}$. To investigate various aspects of the recrystallisation implemented, a second volume is activated assuming $f_{\mathrm{x}_1} = 0.1$. The internal state variables associated with the unrecrystallised volume fraction are assigned initial values $\varrho_{\mathrm{x}_0} = 10$ and $\bar{\lambda}_{\mathrm{x}_0} = 0.2$ while the internal state variables associated with the first volume fraction recrystallised are initialised using $\varrho_{\mathrm{x}_1} = 1$ and $\bar{\lambda}_{\mathrm{x}_1} = 10^{-4}$.

The solution is obtained to within a tolerance of 10^{-8} in eight iterations as illustrated in Table 5.4. The equivalent plastic strain increment converges to a solution of $\delta\alpha$ =0.08511. Three volume fractions are active at the end of the increment with f_{x_1} increasing from 0.1 at the start to 0.3083 at the end of the increment while f_{x_2}=0.0066 is activated during the increment. The internal state variable values at the end of the increment are $\varrho_{\mathrm{x}_0} = 28.196$ and $\bar{\lambda}_{\mathrm{x}_0} = 0.285$ for the unrecrystallised volume fraction while $\varrho_{\mathrm{x}_1} = 10.711$ and $\bar{\lambda}_{\mathrm{x}_1} = 0.050$ as well as $\varrho_{\mathrm{x}_2} = 8.578$ and $\bar{\lambda}_{\mathrm{x}_2} = 0.042$. The function call results in a yield stress of 1934.89MPa attributed to the volume fraction averaged dislocation density ratio $\bar{\varrho} = 22.791$.

(a)

Volume Fraction		$\partial\delta\theta_{x_1}/\partial\delta\alpha + \partial\delta\theta_{x_1}/\partial\dot{\alpha} \times 1/\delta t$	$\partial\delta\theta_{x_2}/\partial\delta\alpha$	$dx_1/d\delta\alpha$	$dx_2/d\delta\alpha$	$df_{xn}/d\delta\alpha$
f_{x_0}	**AN**	216.541	1.000	181.174	1.000	2.235
	FD	216.541	1.000	181.174	1.000	2.235
f_{x_1}	**AN**	202.088	1.000	140.489	0.576	0.253
	FD	202.088	1.000	140.489	0.576	0.253
f_{x_2}	**AN**	192.896	1.000	119.087	0.483	6.54E-3
	FD	192.896	1.000	119.087	0.483	6.54E-3

(b)

Volume Fraction	$dx_1/d\delta\alpha$		$df_{xn}/d\delta\alpha$		**Equation (5.86)**		
	AN	**FD**	**AN**	**FD**	**AN**	**FD**	**% Difference**
f_{x_0}	181.174	181.174	2.235	2.235	62.299	62.299	-
f_{x_1}	123.311	122.962	0.225	0.228	58.900	58.762	0.234
f_{x_2}	122.609	119.496	6.28E-3	6.46E-3	2.511	2.547	1.423
TOTAL					123.710	123.607	0.083

Table 5.5: Comparison between analytically approximated (AN) and finite difference (FD) sensitivity components for the dislocation density based model with recrystallisation. (a) Individual components and solution to the system of equations in Equation (5.92) internally using $df_{xc}/d\delta\alpha = 0$. (b) Components of the equivalent dislocation density sensitivity used in Equation (5.86).

There is an approximate 0.079% difference between the sensitivity using Equation (5.83) and the finite difference approximation according to Table 5.4. If the sensitivities are determined and implemented correctly, this slight variation could be partially attributed to the various conditional statements implemented to avoid zero value denominators and only evolve state variables of volume fractions between 0.001 and 0.999. The difference may also be partially explained by the multiplicative accumulation of variations as a result of the nested solution loops.

Table 5.5 contains values of analytical and finite difference sensitivity components for comparison. These values are reported at the end of the evaluation. Table 5.5(a) shows a breakdown of individual components as well as the solution to the system of equations in Equation (5.92). Equation (5.92) is investigated here within each volume fraction loop in the code by calls to the `RGET` subroutine meaning the finite difference component of $df_{xc}/d\delta\alpha$ can't be compared. Because of this reason Table 5.5(a) illustrates the sensitivity comparisons for a case where $df_{xc}/d\delta\alpha = 0$ removes the last term

in Equation (5.91). The values tabulated include the solutions to $dx_1/d\delta\alpha$ in Equation (5.95) and $dx_2/d\delta\alpha$ in Equation (5.96) as well as the effective value of $df_{xn}/d\delta\alpha$ in Equation (5.87) for all the active volume fractions considered at the end of the increment under the test condition $df_{xc}/d\delta\alpha = 0$. Partial derivatives of the internal state variables x_1 and x_2 with respect to the incremental plastic strain using Equation (5.93) and Equation (5.94) with $C_\lambda = 1$ are also compared.

The contribution of various components to the equivalent dislocation density sensitivity in Equation (5.86) is given in Table 5.5(b). Here the origin of the slight difference between the analytical and finite difference sensitivity in Table 5.4 is again visible for a case where $df_{xc}/d\delta\alpha = 0$ is not enforced. The finite difference contributions to $dx_1/d\delta\alpha$ and $df_{xn}/d\delta\alpha$ in Table 5.5(b) now differs from the values in Table 5.5(a) because of the inclusion of these other sensitivities. The f_{x_1} finite difference value of $dx_1/d\delta\alpha$ is now 122.962 instead of 140.489 when $df_{xc}/d\delta\alpha$ was ignored while the f_{x_0} values are the same in the two tables since $df_{xc}/d\delta\alpha = 0$ is true for this case with $f_{xc} \equiv f_{x_0} = 1$. While the analytical and finite difference sensitivities for the first and second volume fractions are closely similar, the difference gets larger for each next volume fraction contribution calculated. As illustrated in Table 5.5(b) the origin of the 0.079% difference in Table 5.4 is found due to the 0.083% difference between the finite difference and approximated sensitivity of the second term of Equation (5.83). There is possibly an additional sensitivity not taken into account for the volume fractions further down the line or a small numerical error gets compounded by each subsequent volume fraction contribution. Fortuitously, the contribution is small enough that a sufficiently accurate sensitivity is used resulting in a satisfactory rate of convergence.

In Table 5.6, the convergence of the solution to x_1, x_2 and f_{xn} using the RGET subroutine in Appendix F is illustrated. This is done to find the solution of the internal state variables associated with f_{x_1}, i.e. $x_1 \equiv \varrho_{x_1}$, $x_2 \equiv \bar{\lambda}_{x_1}$ and $f_{xn} \equiv f_{x_2}$ using the final strain increment value $\delta\alpha$ =0.08511.

Convergence of the recrystallised volume fractions f_{x_1} and f_{x_2} are finally reported in Table 5.7. The iterations indicate the convergence of f_{x_1} using $\delta\alpha$ =0.08511 as well as $\varrho_{x_0} = 28.196$ and $\bar{\lambda}_{x_0} = 0.285$ while f_{x_2} is solved using $\varrho_{x_1} = 10.711$ and $\bar{\lambda}_{x_1} = 0.050$. Comparison of the finite difference and analytical sensitivities indicate that the solution is correctly implemented following Equations (5.73) and (5.74).

Iteration	Residual		Solution		Sensitivity	Analytical	Difference
1	f_{R_1}	-6.78984	x_1	1.00000	$\partial f_{R_1}/\partial x_1$	-1.53418	-1.53417
	f_{R_2}	-8.511E-2	x_2	1.00E-4	$\partial f_{R_1}/\partial x_2$	-8.51132	-8.51132
	$\|\boldsymbol{f}_R\|$	6.79037	f_{xn}	1.00E-3	$\partial f_{R_2}/\partial x_1$	0.00000	0.00000
					$\partial f_{R_2}/\partial x_2$	1.67783	1.67783
2	f_{R_1}	-7.71686	x_1	3.70714	$\partial f_{R_1}/\partial x_1$	0.51907	0.51907
	f_{R_2}	1.864E-4	x_2	5.073E-2	$\partial f_{R_1}/\partial x_2$	-7.89961	-7.89963
	$\|\boldsymbol{f}_R\|$	7.71686	f_{xn}	2.657E-3	$\partial f_{R_2}/\partial x_1$	5.735E-5	5.732E-5
					$\partial f_{R_2}/\partial x_2$	1.68987	1.68987
3	f_{R_1}	12.8683	x_1	18.5645	$\partial f_{R_1}/\partial x_1$	1.78652	1.78657
	f_{R_2}	1.681E-4	x_2	5.011E-2	$\partial f_{R_1}/\partial x_2$	12.8093	12.8094
	$\|\boldsymbol{f}_R\|$	12.8683	f_{xn}	1.148E-2	$\partial f_{R_2}/\partial x_1$	7.778E-5	7.779E-5
					$\partial f_{R_2}/\partial x_2$	1.75931	1.75931
4	f_{R_1}	0.95271	x_1	11.3599	$\partial f_{R_1}/\partial x_1$	1.48829	1.48825
	f_{R_2}	1.790E-5	x_2	5.033E-2	$\partial f_{R_1}/\partial x_2$	-1.28178	-1.28179
	$\|\boldsymbol{f}_R\|$	0.95271	f_{xn}	6.960E-3	$\partial f_{R_2}/\partial x_1$	7.106E-5	7.112E-5
					$\partial f_{R_2}/\partial x_2$	1.72327	1.72327
5	f_{R_1}	1.234E-2	x_1	10.71978	$\partial f_{R_1}/\partial x_1$	1.44916	1.44910
	f_{R_2}	2.374E-6	x_2	5.035E-2	$\partial f_{R_1}/\partial x_2$	-2.15244	-2.15251
	$\|\boldsymbol{f}_R\|$	1.234E-2	f_{xn}	6.572E-3	$\partial f_{R_2}/\partial x_1$	7.024E-5	7.015E-5
					$\partial f_{R_2}/\partial x_2$	1.72021	1.72021
6	f_{R_1}	2.310E-6	x_1	10.7113	$\partial f_{R_1}/\partial x_1$	1.44862	1.44863
	f_{R_2}	4.38E-11	x_2	5.035E-2	$\partial f_{R_1}/\partial x_2$	-2.16361	-2.16365
	$\|\boldsymbol{f}_R\|$	2.310E-6	f_{xn}	6.567E-3	$\partial f_{R_2}/\partial x_1$	7.023E-5	7.022E-5
					$\partial f_{R_2}/\partial x_2$	1.72017	1.72017
					$df_{R_1}/d\delta\alpha$	201.969	202.026
7	f_{R_1}	7.55E-14	x_1	10.7113	$\partial f_{R_1}/\partial x_1$	1.44862	1.44861
	f_{R_2}	2.08E-17	x_2	5.035E-2	$\partial f_{R_1}/\partial x_2$	-2.16362	-2.16365
	$\|\boldsymbol{f}_R\|$	7.55E-14	f_{xn}	6.567E-3	$\partial f_{R_2}/\partial x_1$	7.023E-5	7.022E-5
					$\partial f_{R_2}/\partial x_2$	1.72017	1.72017

Table 5.6: `RGET` residuals and convergence for internal state variables associated with f_{x_1} using $\delta\alpha$ =0.08511.

Volume Fraction	Iteration	Residual	Fraction Value	Sensitivity	
				Analytical	Difference
f_{x_1}	1	-0.22806	0.10000	0.84796	0.84796
	2	7.557E-2	0.36896	1.26292	1.26292
	3	1.020E-3	0.30912	1.22681	1.22681
	4	2.464E-7	0.30829	1.22622	1.22622
	5	1.44E-14	0.30829	1.22622	1.22622
f_{x_2}	1	-3.905E-3	1.000E-3	0.23417	0.234167
	2	1.019E-2	1.768E-2	0.95339	0.95339
	3	3.620E-4	6.989E-3	0.86139	0.86139
	4	1.804E-6	6.569E-3	0.85264	0.85264
	5	4.92E-11	6.567E-3	0.85260	0.85260

Table 5.7: Convergence of the recrystallised volume fractions f_{x_1} and f_{x_2}.

From the various convergence histories and sensitivity comparisons tabulated, the subroutines implemented in Appendix F are considered sufficiently accurate. The model is now characterised on experimental data for Cobalt and Copper.

5.9 Model calibration on recrystallisation data

The model outlined and implemented into an isotropic numerical framework is now characterised to data where dynamic recrystallisation is prevalent.

The first data set is digitised from a paper on aspects of dynamic recrystallisation in Cobalt at high temperatures by Kapoor et al. (2009). The true stress as a function of true plastic strain for Cobalt at 600°C, 700°C, 750°C, 800°C, 900°C and 950°C is extracted from the paper for strain rates of 10^0, 10^{-1} and 10^{-2}.

The material parameter values that result in the fit displayed in Figure 5.14 are as follow:

- The elastic properties using the shear model relationship in Equation (3.21) are $\mu_r = 81815$MPa, $D_r = 6519$MPa, $T_r = 200$K and a Poisson's ratio of $\nu = 0.31$.
- The temperature and rate dependent scaling function in Equation (3.22) is modelled with $a_{0\varepsilon} = 1.924$K/MPa, $p_\varepsilon = 2/3$, $q_\varepsilon = 3/2$ and $\dot{\varepsilon}_{0\varepsilon} = 10^7 \text{s}^{-1}$.

- The athermal yield stress component and reference stress values using Equation (5.4) are $\hat{\sigma}_a = 0$MPa and $\sigma_0 = 83.7$MPa.
- The average slip plane lattice incompatibility is affected by a constant that can be calibrated in both Equations (5.55) and (5.62) where it plays a role and so the evolution of $\bar{\lambda}$ according to Equation (5.63) is simply modelled using $C_{\lambda \mathrm{x}} = 1$.
- The parameters associated with the evolution of the dislocation density ratio in Equation (5.62) are $C_g = 584.64$, $r_g = 1$, $C_1 = 156.61$, $C_{20} = 7.566$, $a_{02} = 0.496$K/MPa, $\dot{\varepsilon}_{02} = 10^{10}\mathrm{s}^{-1}$, $C_{30} = 12121.95\mathrm{s}^{-1}$, $a_{03} = 39274.9$K and $r_3 = 7.346$.
- The recrystallisation parameters are finally $C_{\mathrm{Rx}0} = 1562.08\mathrm{s}^{-1}$ for the pre-exponential constant in Equation (5.53), $a_{0\mathrm{Rx}} = 21049.20$K in Equation (5.54) with $C_{\mathrm{Rx}\lambda 0} = 8.442$ and $r_{\mathrm{Rx}\lambda} = 2.321$ in Equation (5.55).
- The equivalent interfacial subgrain boundary area function in Equation (5.59) is modelled using $r_{\mathrm{Rx}a} = 0.0797$, $r_{\mathrm{Rx}b} = 1.339$ and $C_{\mathrm{Rx}c} = 19.415$.

These material parameter values are found using numerical optimisation and may not be exactly those of Cobalt found in literature. The parameter values are selected automatically to fit the data curves during a characterisation procedure similar to the one outlined at the end of Section 3.5.

An illustration of the form of the recrystallised volume fraction and calculated equivalent dislocation density is presented in Figure 5.15. Multiple recrystallised volume fractions are visible in Figure 5.15(a) as well as an internal state variable shift at two occasions. These shifts happen once the first volume fraction f_{x_1} is bigger than 0.999 as explained in the second paragraph of §5.8.1.

The contribution of each recrystallised volume fraction dislocation density ratio ϱ_{x_i} to the equivalent dislocation density ratio $\bar{\varrho}$ according to Equation (5.64) is demonstrated in Figure 5.15(b). In this specific example, the equivalent dislocation density ratio and therefore the equivalent stress has a multiple peak response that approaches a steady state solution. This type of response is also visible in some of the digitised experimental data.

In Chapter 3, the MTS model is described and calibrated to Oxygen free high conductivity Copper data digitised from a Ph.D. thesis by Tanner (1998). Some of

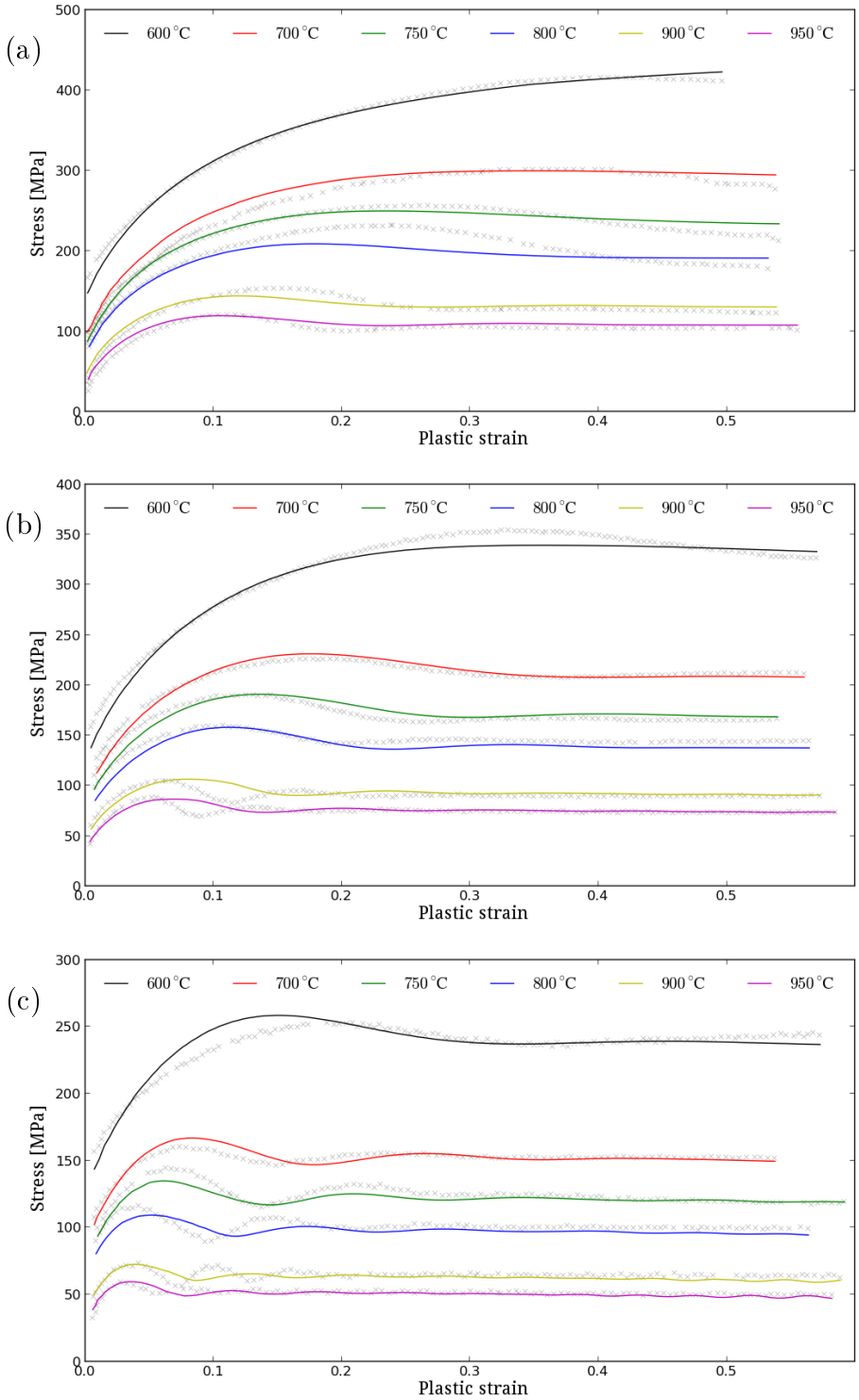

Figure 5.14: Numerical model (solid line) calibrated to the true stress vs. true plastic strain data for Co at different temperatures and strain rates of (a) $1s^{-1}$, (b) $0.1s^{-1}$and (c) $0.001s^{-1}$ from Kapoor et al. (2009).

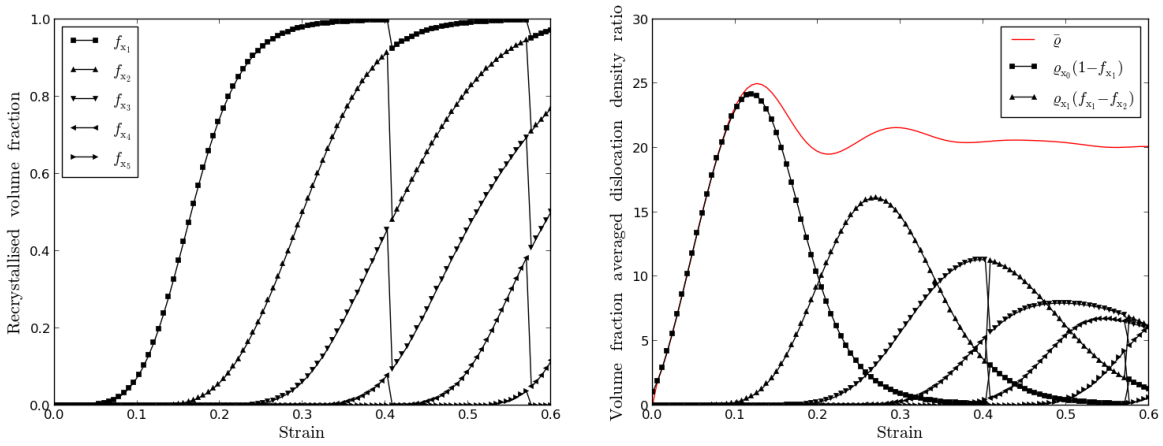

(a) (b)

Figure 5.15: (a) Recrystallised volume fractions and (b) volume fraction averaged dislocation density ratio using the recrystallisation model calibrated to the cobalt dynamic recrystallisation data when modelled at 800°C and a strain rate of 0.1s^{-1}.

the data digitised from this document is given in Figure 3.1 for room temperature at various strain rates, 134°C and 202°C at a strain rate of 0.0004s^{-1} as well as three different strain rates at 269°C.

Other data also digitised from the experimental work done by Tanner is not used during the characterisation exercise in Section 3.5 since the material undergoes softening and recrystallisation. Given the dislocation density based model with the extension to include recrystallisation, the bigger set of copper data is now characterised.

The material parameters resulting in the fit to the Copper data in Figure 5.16 are:

- $\mu_r = 43.8\text{GPa}$, $D_r = 4.7\text{GPa}$, $T_r = 252\text{K}$ and $\nu = 1/3$ for the elastic properties using the shear model relationship in Equation (3.21).
- $a_{0\varepsilon}$ =2.1037K/MPa, $p_\varepsilon = 1$, $q_\varepsilon = 2$, and $\dot{\varepsilon}_{0\varepsilon}$ =10^6s^{-1} for the temperature and rate dependent scaling function in Equation (3.22).
- The athermal yield stress component is $\hat{\sigma}_a$ =12.519MPa and reference stress is $\sigma_0 = 17.295\text{MPa}$ using Equation (5.4).
- $C_{\lambda\text{x}} = 1$ is used for the evolution of $\bar{\lambda}$ according to Equation (5.63).

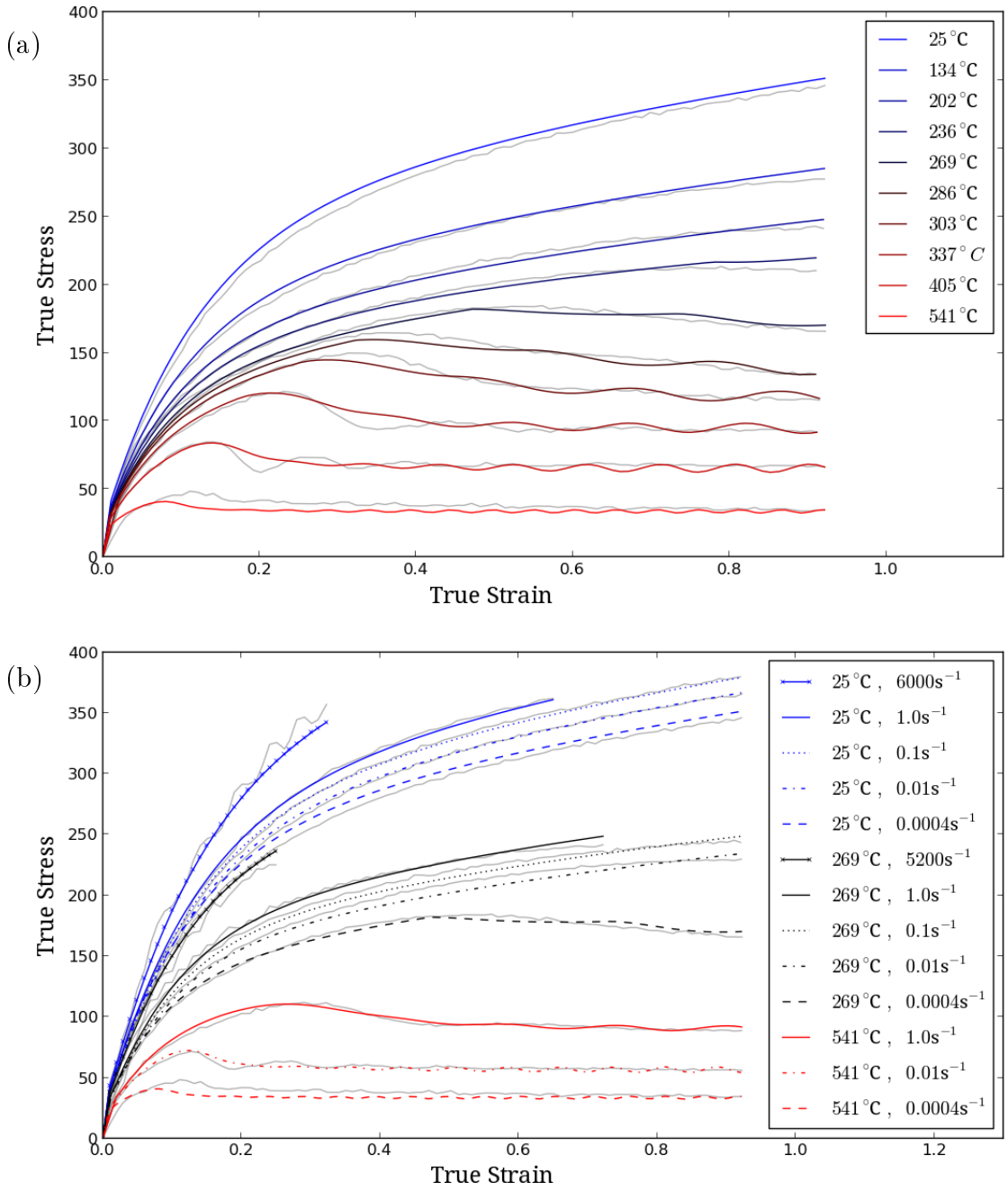

Figure 5.16: Numerical model (colored lines) calibrated to Tanner and McDowell's OFHC copper data (1999) for different strain rates and temperatures. (a) Different temperature responses at $\dot{\varepsilon} = 0.0004\text{s}^{-1}$. (b) Modelled rate dependence at 25°C, 269°C and 541°C.

- $C_g = 6378.74$, $r_g = 0.769$, $C_1 = 278.87$, $C_{20} = 11.773$, $a_{02} = 0.904$K/MPa, $\dot{\varepsilon}_{02} = 4.0112 \times 10^{12}$, $C_{30} = 83.07\text{s}^{-1}$, $a_{03} = 6370.675$K and $r_3 = 0.8079$ for the dislocation density ratio evolution in Equation (5.62).

- $C_{\text{Rx0}} = 9346.62\text{s}^{-1}$ in Equation (5.53), $a_{0\text{Rx}} = 17633.796$K in Equation (5.54) while $C_{\text{Rx}\lambda 0} = 47.247$ and $r_{\text{Rx}\lambda} = 3.87$ in Equation (5.55). $r_{\text{Rx}a} = 0.1424$, $r_{\text{Rx}b} = 1.7677$ and $C_{\text{Rx}c} = 393.44$ in Equation (5.59).

These simulations confirm the ability of the extended model to capture the complex material response due to recrystallisation.

Chapter 6

Roughing of a Steel Alloy.

Austenite grain growth is an important factor that determines the final microstructure and mechanical properties of the product. The dislocation density based model with recrystallisation is used in this chapter to investigate the through thickness microstructural variation due to different roll reduction schedules. The behaviour of a high strength low alloy (HSLA) steel is modelled during hot rolling or roughing.

The model is first characterised on experimental test data for compressive tests performed on cylindrical test specimens. The test data has various amounts of straining with various interpass times between each additional compression. In the times between reduction the material undergoes static recrystallisation.

The data and material are discussed in the first subsection of this chapter. The material is a C-Mn-Nb-Ti-V microalloyed steel. Extensive data is available on mainly the hardening, recovery and static recrystallisation of the alloy in the austenite (γ-Fe) phase. The material model presented in Section 5.7 is characterised to this available steel data. The recrystallisation model parameters are identified that best represent the static recrystallisation observed in the experimental material response using a material point based simulation. In Section 6.3 one of the compression experiments is modelled in more detail using an axi-symmetric finite element analysis in Abaqus. The global stress - strain results from the finite element simulation compares well to the experimental data.

A single roll pass is also modelled in Abaqus for different amounts of reduction. The microstructural variation through the thickness of a steel slab is of interest when

modelling the hot rolling process. There is however no grain size data available for the alloy under investigation. Nevertheless, a normal grain growth model is introduced in Section 6.5 and calibrated to grain growth data on similar HSLA steels. Should experimental grain size data on the alloy of interest become available at a later stage, this will allow calibrating the developed grain growth model for the alloy under investigation.

Finally, different roll reduction schedules are simulated in Abaqus. The microstructural variation using the stress and strain states as well as the grain growth model is compared and investigated as a result of these different schedules.

6.1 Data and Problem description

The influence of the strain sequence during hot slab rolling or roughing was investigated by Maubane et al. (2014) for a plain carbon, C-Mn-V and C-Mn-Nb-Ti-V microalloyed steel. The data was made available for the work done in this chapter. The alloy chemistry considered is given in Table 6.1.

The reheating and roughing experiments were conducted in a Bähr deformation dilatometer. They used a constant austenising temperature, constant soaking time, various heating rates and roughing strain sequences. Information on six different roughing sequences or reduction schedules for which experimental tests were done is given in Table 6.2. Each of the reductions were performed at a slightly higher strain rate compared to one before. The cylindrical specimens tested were approximately 10mm high with a diameter of 5mm.

In Table 6.2, the six different schedules are indicated with upper case roman numerals I to VI. The first schedule consists of 14 reductions of 7% each. The reduction rates start at 0.3s^{-1} for the first 7% and then increases with 0.2s^{-1} each next reduction to end at a rate of 2.9s^{-1} for the fourteenth pass. During the sequence, the temperature slowly decreases to represent the cooling down of the metal slab. Schedule II consists of 10 reductions of 10% each while schedule III consists of $6\times15\%$ reductions. Additional schedules tested experimentally repeated the 7%, 10% and 15% reduction sequences op to a point followed by one final reduction of 40%.

Some of the schedules were performed multiple times with different waiting or interpass times between additional straining. Three different data sets are available

% **C**	% **Mn**	% **Si**	% **Nb**	% **Ti**	% **V**	% **Al**	**N** [*ppm*]	**S** [*ppm*]
0.134	1.5	0.38	0.04	0.025	0.028	0.049	55	41

Table 6.1: C-Mn-Nb-Ti-V microalloyed steel chemistry

			Schedule					
Reduction	$\dot{\varepsilon}[\mathrm{s}^{-1}]$	$T[^{\circ}\mathrm{C}]$	*I*	*II*	*III*	*IV*	*V*	*VI*
R1	0.3	1150	0.07	0.10	0.15	0.07	0.10	0.15
R2	0.5	1145	0.07	0.10	0.15	0.07	0.10	0.15
R3	0.7	1140	0.07	0.10	0.15	0.07	0.10	0.15
R4	0.9	1135	0.07	0.10	0.15	0.07	0.10	0.15
R5	1.1	1130	0.07	0.10	0.15	0.07	0.10	0.40
R6	1.3	1125	0.07	0.10	0.15	0.07	0.10	
R7	1.5	1120	0.07	0.10		0.07	0.40	
R8	1.7	1115	0.07	0.10		0.07		
R9	1.9	1110	0.07	0.10		0.40		
R10	2.1	1105	0.07	0.10				
R11	2.3	1100	0.07					
R12	2.5	1095	0.07					
R13	2.7	1090	0.07					
R14	2.9	1085	0.07					

Table 6.2: Nominal engineering strain roughing sequences for which experimental data is available

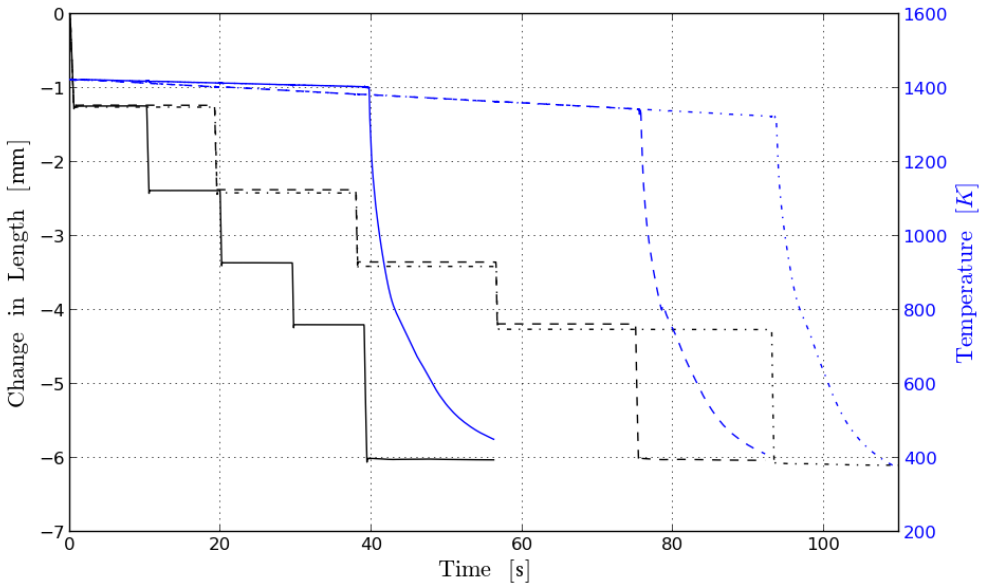

Figure 6.1: The change in length and temperature once 1150°C was reached for three different Schedule VI experiments with varying interpass time. Run 1 - solid line; Run 2 - dashed line; Run 3 - dash-dot line.

for schedule VI for example. After the starting temperature of 1150°C is reached, the tests were done with different interpass times. In the one case the interpass time between each subsequent compression was approximately 9 to 10 seconds. Another test had an interpass period of approximately 20 seconds between each compression while another waited 40 seconds between the fourth and fifth compression step. The change in length and change in temperature from the initial compression for the three different experiments for schedule VI are visible in Figure 6.1. A constant decrease in temperature of about 0.5Ks^{-1} is visible throughout the experiment before the specimen is quenched.

The true stress - true strain data for the same three schedule VI tests during compression is displayed in Figure 6.2. This figure indicates to some degree the temperature dependence of the material response. It also indicates the potential variability in the material response as seen in the first compression steps, all measured for the same strain rate and temperature. For run 1 to 3 in Figure 6.1 the displacements up to about -1.3929mm in the same approximate time step is associated with the first

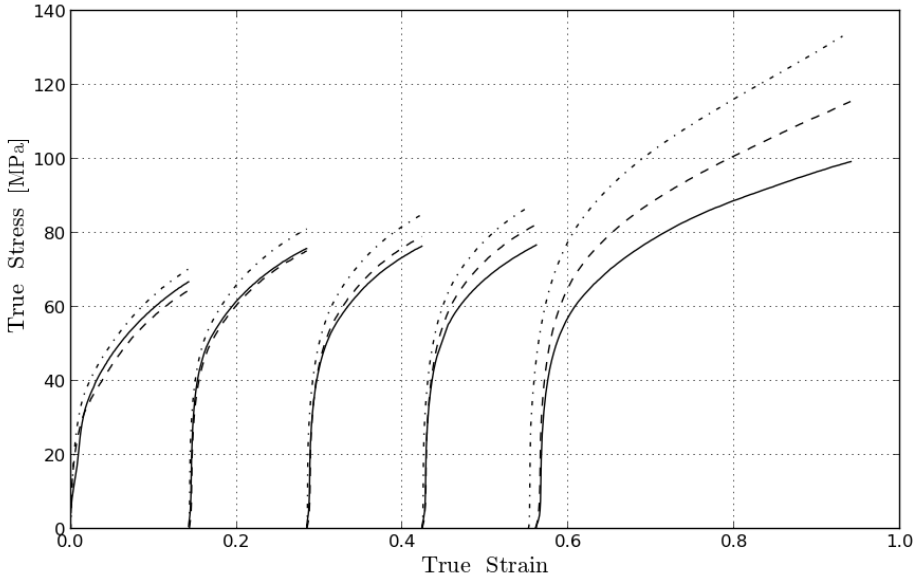

Figure 6.2: The true stress - true strain curves for the loading part of the three different Schedule VI experiments with varying interpass time. Run 1 - solid line; Run 2 - dashed line; Run 3 - dash-dot line.

$\ln(-1.3929/10+1)$ =15% strain interval in Figure 6.2. At the end of this first compression step, the true stress values in Figure 6.2 for the three different experiments are 67.26MPa, 64.84MPa and 70.54MPa with an average value of 67.55MPa. This translates to a possible variation in material response of $(70.54-64.84)/67.55 \approx 8.44\%$ when the same material is subjected to different temperature and strain histories as a result of the different interpass times.

The potential variability continues to be visible in the first four compression steps of the experiments with 20 second wait between compression. These experimental results are visible as the dashed and dash-dot lines in Figures 6.1 and 6.2 respectively. The first four reductions resulted in different responses in Figure 6.2 despite being subjected to similar temperatures and strains according to Figure 6.1.

The roughing sequence data for schedule VI with approximately 10 second interpass time between additional straining is used as illustration in this chapter. The strain histories for this case are visible in Figure 6.3 and Table 6.3. Here it is visible that the experimentally achieved strain increments and strain rates are slightly lower than

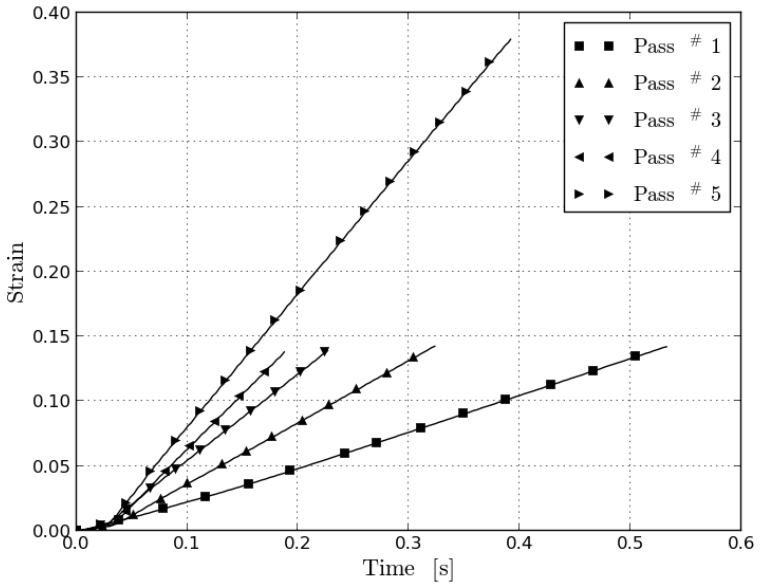

Figure 6.3: The strain history of the schedule VI experiment with approximately 10 second interpass time.

those intended in Table 6.2. These values are reported here mainly as they will be used to define the steps and displacement boundary conditions of the finite element analysis in Section 6.3.

6.2 Fitting the data

In general, the data is fit above a strain value of 0.01 or additional 0.01 strain for each subsequent compression curve. For a given set of material parameter values, here just referred to as the vector $\mathbf{x}$, the model is evaluated for the same temperatures and strain rates as the experimental data. The stress values at each of the N valid data points are then compared to the predicted stress value to construct an objective function.

The objective function is assembled by comparing the model predicted stress value σ_i^{model} to the associated stress value of the i^{th} valid data point σ_i^{data}. The objective function used for the parameter identification is

Total Time [s]	**Time Increment** [s]	**Strain Increment**	**Effective Strain Rate**
11562.6703	-	-	-
11563.2181	0.5478	0.1458	0.2662
11572.8431	9.6250	-	-
11573.1752	0.3321	0.1449	0.4363
11582.5775	9.4023	-	-
11582.8129	0.2354	0.1429	0.6072
11592.1566	9.3437	-	-
11592.3539	0.1973	0.1419	0.7192
11601.6693	9.3154	-	-
11602.0697	0.4004	0.3854	0.9624

Table 6.3: Total times from the initial compression at 1150°C with the actual strain increments per compression step and effective strain increments for schedule VI with approximately 10 second interpass times as observed in the experimental data.

$$f_{\text{obj}}(\mathbf{x}) = \sum_{i=1}^{N} \left(\frac{\sigma_i^{\text{model}}(\mathbf{x}) - \sigma_i^{\text{data}}}{\sigma_i^{\text{data}}} \right)^2 . \tag{6.1}$$

Initial material parameter values are chosen and then improved by minimising this objective function. Material parameter value constraints are also assigned. This is done to ensure $1 < q_\varepsilon < 2$ for example. The parameter identification is performed using the the downhill simplex method. If a constraint is violated, the objective function is penalised.

Not all of the data is used in the characterisation. A single data set for each roughing schedule is modelled and compared. The model outputs and experimental data for all the different data sets on schedules I to VI are illustrated in Figure 6.4. In Figure 6.4, the green curves represent the material model response used to evaluate the objective function on a subset of the data. The red curves in Figure 6.4 are predicted responses using the material model. In this figure the benefit of this physically developed state variable based model is visible in its ability to not only model but also predict material response.

The material parameter values resulting in the fit given in Figure 6.4 are :

- The elastic properties using the shear model relationship in Equation (3.21) are

$\mu_r = 85908$MPa, $D_r = 6758.8$MPa, $T_r = 180$K and a Poisson's ratio of $\nu = 0.29$.

- The temperature and rate dependent scaling function in Equation (3.22) is modelled with $a_{0\varepsilon} = 1.4343$K/MPa, $p_\varepsilon = 0.5914$, $q_\varepsilon = 1.0973$, and $\dot{\varepsilon}_{0\varepsilon} = 10^7 \text{s}^{-1}$.

- The athermal yield stress component and reference stress values using Equation (5.4) are $\hat{\sigma}_a = 11.175$MPa and $\sigma_0 = 82.126$MPa.

- The evolution of $\bar{\lambda}$ according to Equation (5.63) is again modelled using $C_{\lambda \text{x}} = 1$.

- The parameters associated with the evolution of the dislocation density ratio in Equation (5.62) are $C_g = 4369.3$, $r_g = 0.5701$, $C_1 = 146.63$, $C_{20} = 41.47$, $a_{02} = 0.5413$K/MPa, $\dot{\varepsilon}_{02} = 10^3 \text{s}^{-1}$, $C_{30} = 1.6078 \times 10^9 \text{s}^{-1}$, $a_{03} = 36257$K and $r_3 = 2$.

- The recrystallisation parameters are $C_{\text{Rx}0} = 4352.8 \text{s}^{-1}$ for the constant in Equation (5.53), $a_{0\text{Rx}} = 33092$K in (5.54) with $C_{\text{Rx}\lambda 0} = 549.21$ and $r_{\text{Rx}\lambda} = 2.519$ in Equation (5.55). The equivalent interfacial subgrain boundary area function in Equation (5.59) is modelled using $r_{\text{Rx}a} = 0.2874$, $r_{\text{Rx}b} = 1.0001$ and $C_{\text{Rx}c} = 17.935$.

The material parameter values used to model the different schedules do a satisfactory job of reproducing the data given the expected material variability of about 8.44% observed in Section 6.1. In some cases an accurate representation of the strain hardening, static recrystallisation and thermal dependence is captured by the model.

The internal state variable evolution using the calibrated material model for the schedule VI strain roughing sequence with approximately 10 second interpass time is given again in Figure 6.5. The recrystallised volume fractions for the multiple waves of recycling are given in (a) over the time history and in (b) over the strain history.

The first wave of static recrystallisation results in an approximately 58% recrystallised material after the first 9.625 second interpass time. After the second reduction and subsequent 9.4023 second interpass time, the material model indicates that the original material is replaced by more that 90% recrystallised material. Approximately 70% of the material has also undergone a second wave of recrystallisation. After about 39 seconds into the experiment, the model indicates that the original material has been

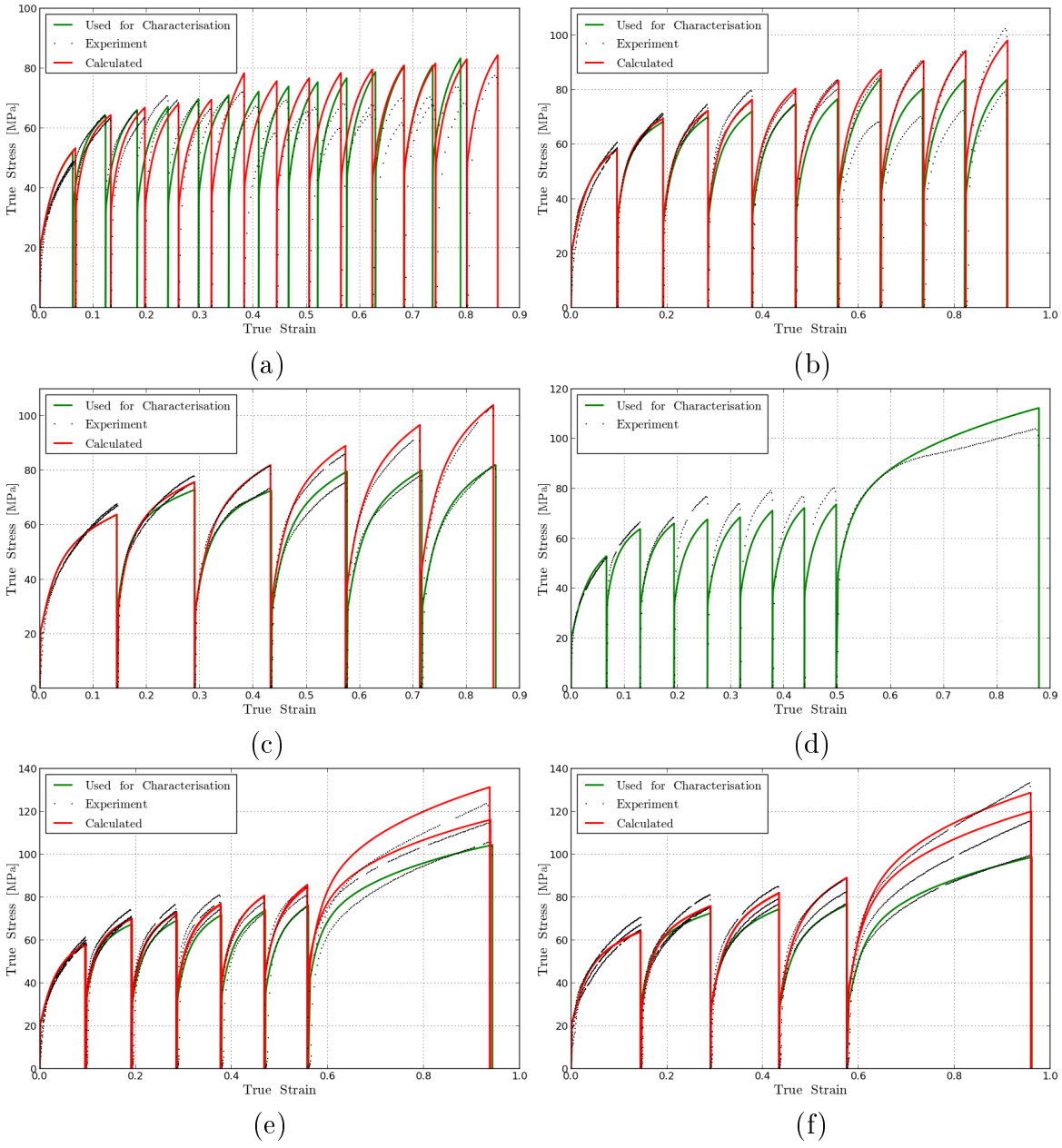

Figure 6.4: Model response compared to the experimental data for schedule (a) I (b) II (c) III (d) IV (e) V (f) VI

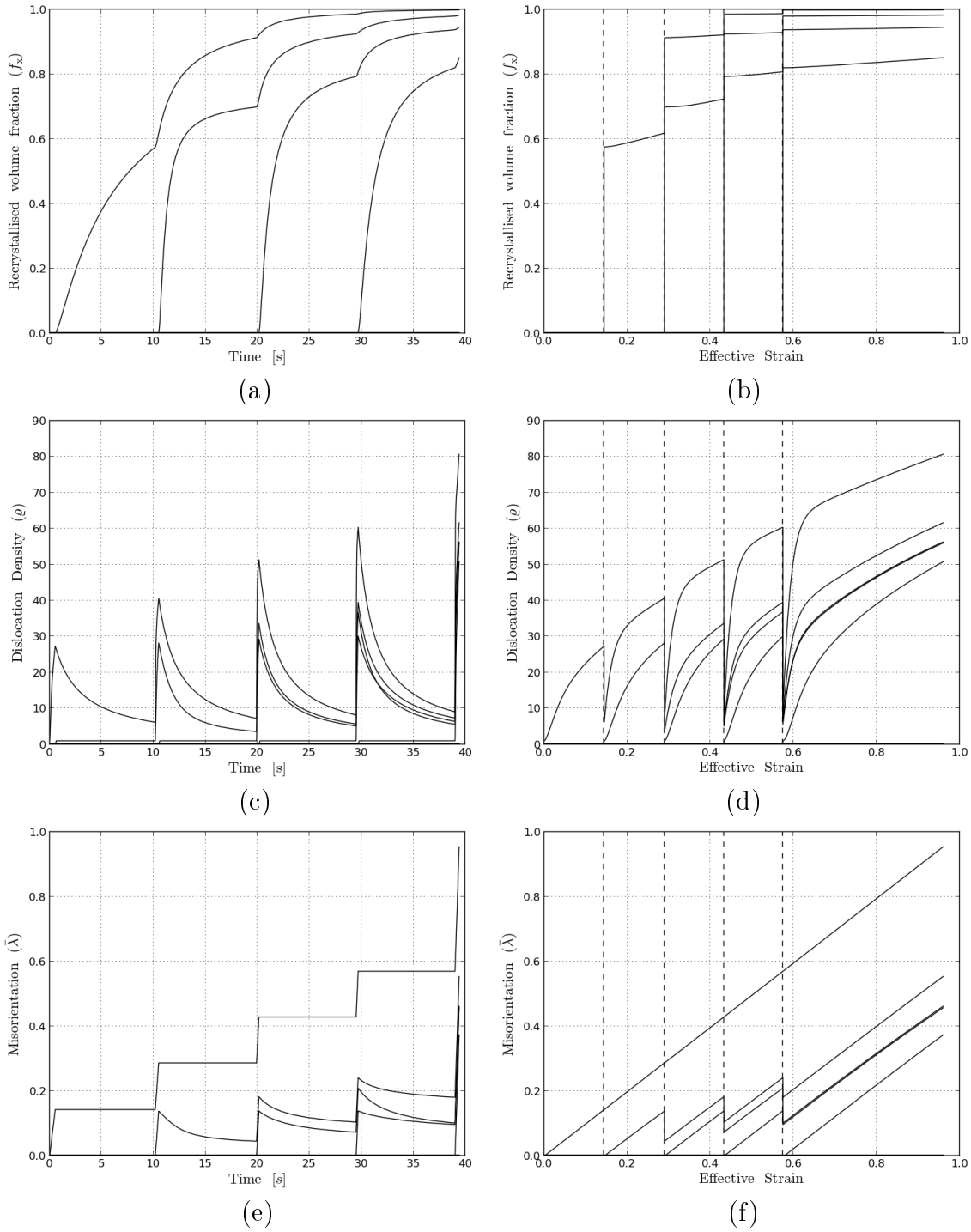

Figure 6.5: Internal state variable evolution for the the schedule VI data with an approximate 10 second interpass time between each reduction. (a,b) Recrystallised volume fraction; (c,d) dislocation density ratio and (e,f) average slip plane lattice misorientation over time and strain histories.

virtually replaced with a new microstructure where more than 80% of the material has seen four waves of recrystallisation.

Figures 6.5(c) and (d) indicate the dislocation density ratio state variables per recrystallised volume fraction over the time and strain history respectively. Apart from the static recrystallisation, there is also a significant amount of thermal recovery in the predicted material response. In Figure 6.5(c) the dislocation density self diffusion over time is visible while Figure 6.5(d) indicates the dislocation density evolution per volume fraction. In Figures 6.5(e) and (f) the average slip plane lattice misorientation over the time and strain histories are presented. This internal state variable evolves as in Equation (5.63) with $C_{\lambda \mathrm{x}} = 1$. This means that in the absence of recrystallisation $\dot{\bar{\lambda}} = \dot{\alpha}$, as seen in the straight line in Figure 6.5(f) for $\bar{\lambda}_{\mathrm{x}_0}$. The reduction in this ISV as a function of time is an indication of the effect of the static recrystallisation on the average slip plane lattice misorientation of the recrystallised material using the rule of mixtures.

Up to the present point in this chapter, all of the results are material point simulator based. Next, the schedule VI strain roughing sequence with approximately 10 second interpass time is modelled in detail using Abaqus. This is done using Table 6.3 to create different steps and boundary conditions. The material parameter values in this subsection are used with the recrystallisation extended material model in Appendix F called by the isotropic user material subroutine in Appendix A.

6.3 Axi-symmetric compression

The experimental test data was extracted by tests done on cylindrical specimens 10mm high with a diameter of 5mm. The finite element analysis is therefore done using an axi-symmetric model with contact, similar to the models used in Sections 2.1.2 and 2.2. A quarter axi-symmetric model 5mm high with a 2.5mm radius is modelled. From the temperature history in Figure 6.1, a linear change in temperature is modelled starting at 1423K and ending with 1400K at a total time of 40 seconds.

The experimental data values in Table 6.3 is used to set up different modelling steps and boundary conditions. Five compression steps and four interpass steps are set up.

Step	Purpose	Total Reduction	Step Time	Total Time	Die Displacement
0	Initial	0	0	0	0
1	Reduce	15%	0.5478	0.5478	-0.6785
2	Remove	15%	0.01	0.5578	-0.6685
3	Interpass	15%	9.615	10.1728	-0.6685
4	Reduce	30%	0.3321	10.5049	-1.2614
5	Remove	30%	0.01	10.5149	-1.2514
6	Interpass	30%	9.3923	19.9072	-1.2514
7	Reduce	45%	0.2354	20.1426	-1.7594
8	Remove	45%	0.01	20.1526	-1.7494
9	Interpass	45%	9.3337	29.4863	-1.7494
10	Reduce	60%	0.1973	29.6836	-2.1881
11	Remove	60%	0.01	29.6936	-2.1781
12	Interpass	60%	9.3054	38.999	-2.1781
13	Reduce	100%	0.4004	39.3994	-3.0873

Table 6.4: The modelled die displacement boundary condition over the simulation time

The contact surface is initially in contact with the top surface of the axi-symmetric test specimen model. A friction coefficient of $\mu_{\text{frict}} = 0.3$ is further assumed for a reasonably lubricated contact surface.

In a compression step the displacement of the rigid contact surface is prescribed to represent the total strain applied. In an interpass time step, the surface is first displaced 0.01mm in a 0.01s interval so that it is no longer in contact with the material. After waiting the required amount of time, the next compression step is modelled. The step times, total simulation time, equivalent and prescribed die displacement is given in Table 6.4.

The von Mises stresses, equivalent plastic strains, dislocation density ratio, average slip plane lattice misorientation and volume fraction recrystallised are displayed in Appendix G at the end of each compression and inter pass step modelled. The contours of the internal state variables for the axi-symmetric simulation indicate the evolution and distribution of these values throughout the simulated experiment. For the sake of

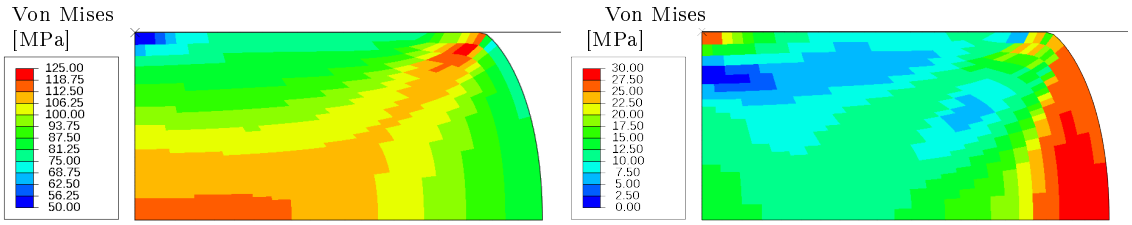

(a) (b)

Figure 6.6: Von Mises stress contours on the compressed axi-symmetric billet at (a) 39.3994s and (b) 10 seconds afterwards.

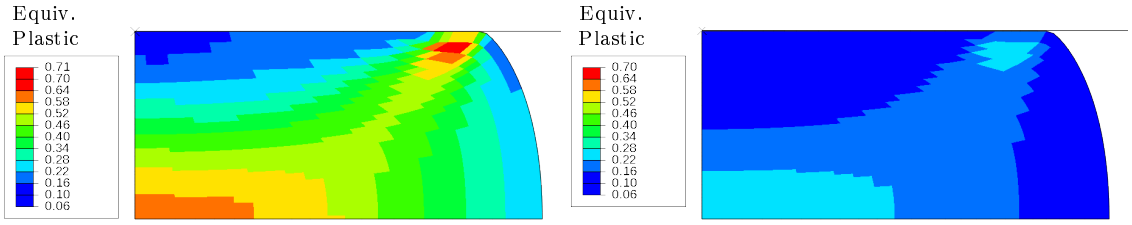

(a) (b)

Figure 6.7: Equivalent plastic strain contours on the compressed axi-symmetric at (a) 39.3994s and (b) 10 seconds afterwards.

brevity, only selected figures are included in the main text.

In Figure 6.6, the equivalent von Mises stress distribution is displayed at the end of the compression (39.3994s) as well as 10 seconds afterwards. The same is done for the equivalent plastic strains and dislocation density ratio in Figures 6.7 and 6.8.

The stresses are displayed between 50MPa and 125MPa in Figure 6.6(a) while Figure 6.6(b) shows residual stress values between 0MPa and 30MPa. The equivalent plastic strain contours in Figures 6.7(a) and (b) are displayed for the same range between 0.06 and 0.7 while the dislocation density ratio contours in Figures 6.8(a) and (b) are displayed for the same range between 10 and 50.

Comparing Figure 6.7(a) to Figure 6.7(b) the amount of strain recovered if an additional 10 seconds are allowed for recrystallisation is illustrated while the dislocation structure is reset due to both thermal recovery and recrystallisation.

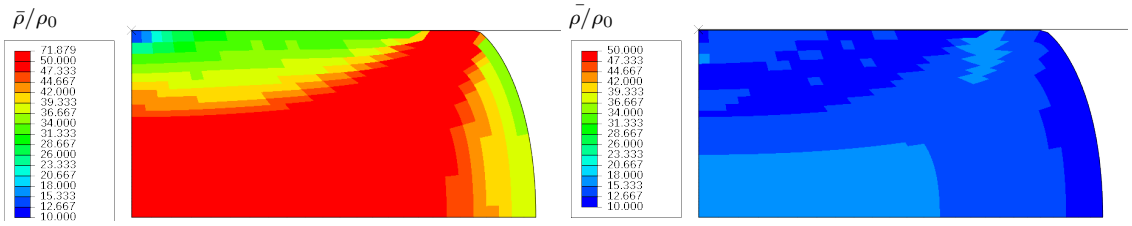

(a) (b)

Figure 6.8: Dislocation density contours on the compressed axi-symmetric at (a) 39.3994s and (b) 10 seconds afterwards.

In Figure 6.9, the internal state variables associated with the active recrystallised volume fractions are displayed 10 seconds after the final reduction.

The discontinuous contours especially visible in 6.9(c), (d) and (e) are as a result of an internal state variable shift once the original material f_{x_0} has fully recrystallised in that region ($f_{x_1} \geq 0.999$). This means that while 6.9(c) represents the contours of the internal state variable associated with f_{x_3} for example, contours in the centre of the billet in 6.9(c) is associated with the fourth recrystallisation cycle.

The total reaction force at the lower nodes are extracted at each point in the simulation time. The values at these mid plane nodes are extracted due to the possibility of roll over at the contact interface. The reaction forces and total displacement from the finite element simulation are used to approximate the true stress over true strain curves. The experimental data, material model response and finite element result are compared in Figure 6.10.

The finite element results yield slightly larger stress values than those predicted by the material point simulation, but are still reasonably accurate in replicating the experimental results. A single roll pass for different amounts of reduction are modelled in the next section, again using the same material model and parameters.

6.4 Roll pass reduction

A roll pass reduction is modelled given a double roll setup. The slab is pulled through by two rolls at either side. In this section, a single roll pass is modelled in Abaqus

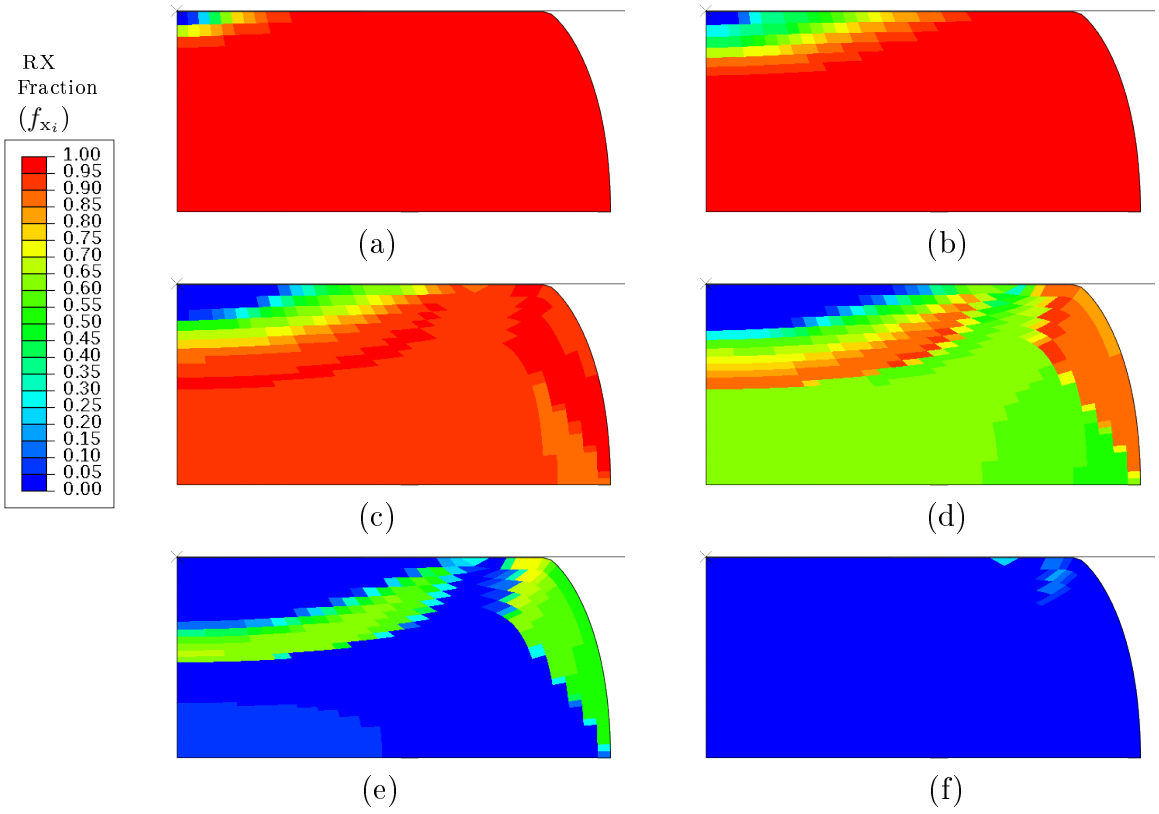

Figure 6.9: Recrystallised volume fractions (a) f_{x_1}, (b) f_{x_2}, (c) f_{x_3}, (d) f_{x_4}, (e) f_{x_5} and (f) f_{x_6} 10 seconds after the simulation.

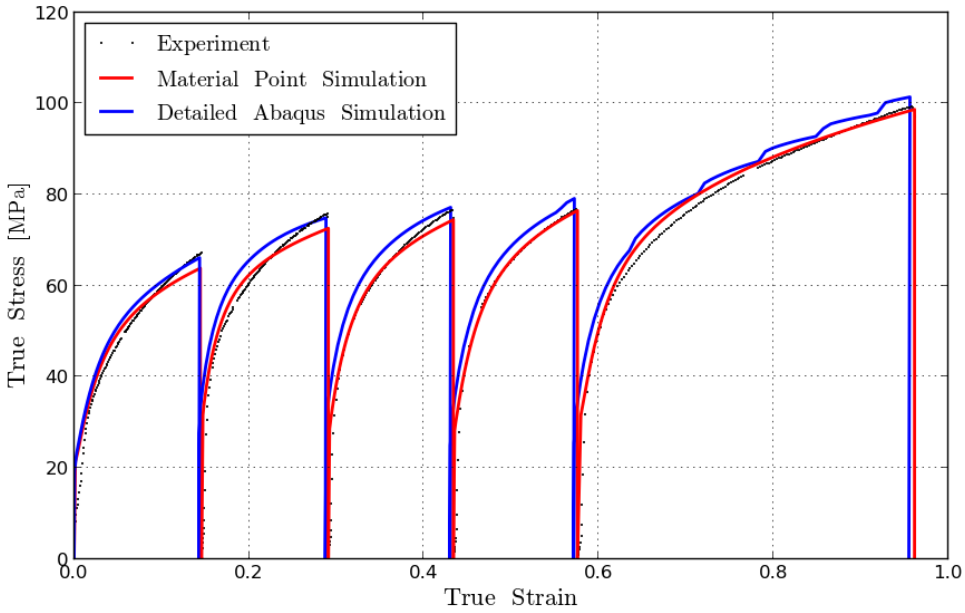

Figure 6.10: Comparison of the material point integration and the axi-symmetric Abaqus simulation true stress vs. true strain results to the experimental data on the schedule VI data with an approximate 10 second interpass time between each reduction.

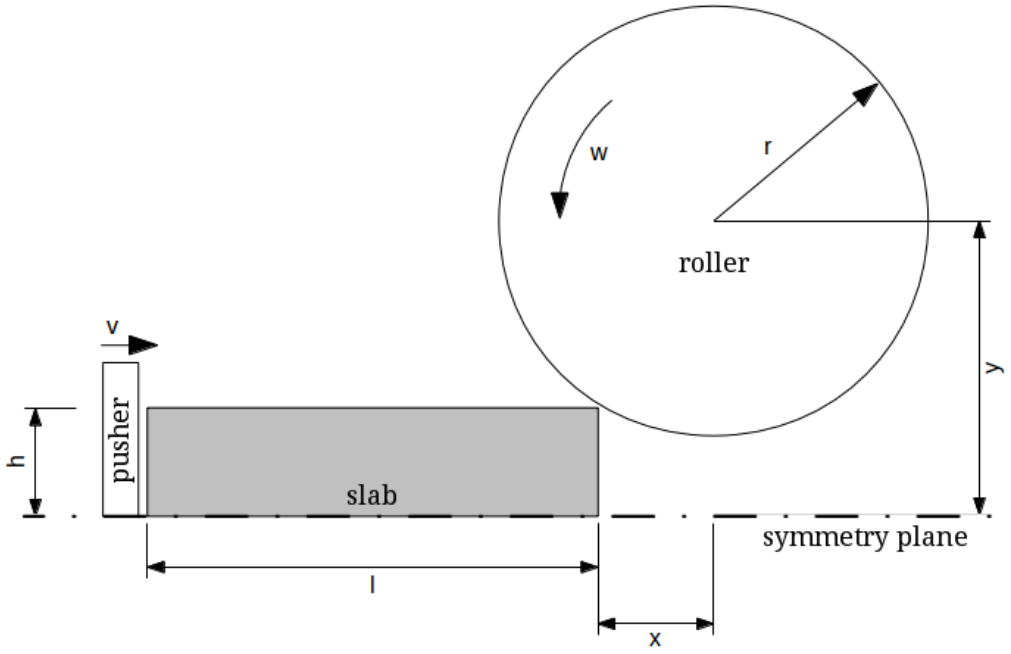

Figure 6.11: Single roll pass reduction setup

to investigate the effect roll speed and percentage reduction has on the effective strain rate and strain penetration.

The model is set up similar to the work done by Muntin and Zinyagin (2014). In their work, they performed a single roll pass simulation using a pusher to bring the slab into initial contact with the roller. No roll flattening is taken into account meaning the roller itself is simply modelled as an analytical rigid surface with prescribed roll radius. The prescribed pusher velocity is selected to be sufficiently slower than the roll peripheral velocity. The roller pulls the slab through once there is an adequate amount of friction due to the contact interface between the upper surface of the metal slab and the roller. Due to the higher roll peripheral velocity, the pusher, still moving at the same prescribed velocity, simply gets left behind. The model setup taking symmetry, the various dimensions and the pusher into account is given in Figure 6.11.

A half slab height of 120mm and section length of 500mm is modelled using a mesh of 100×24 CPE4 elements in Abaqus. CPE4 is a four node linear plane strain element using full integration. A roll diameter of 475mm is modelled and assumed to rotate

at a roll peripheral speed of 1.5ms^{-1}. The radial velocity of 6.3158s^{-1} is applied as a boundary condition. A friction coefficient of $\mu_{\text{frict}} = 0.4$ is modelled between the roller and the slab contact surfaces. The pusher is in contact with the material slab at the start of the simulation. A prescribed velocity of 0.5ms^{-1} is assigned to the rigid surface used to represent the roller. This velocity is lower than the average steady state slab velocity. This results in the pusher being left behind once the friction between the slab and roller starts to pull the slab though. The pusher therefore does not further influence the solution.

The x and y values in Figure 6.11 vary based on the percentage reduction modelled. The y value determines the reduction amount while x merely determines the time taken before contact takes place. The slab is further assumed to have a constant temperature of 1100°C. The single roll pass is modelled in Abaqus for a 7%, 10%, 15%, 20% and 40% reduction although single passes of 20% and higher in slab rolling are generally not achievable due to a maximum bite limitation $\triangle h = \mu_{\text{frict}}^2 R$ where R is the roll radius. Figure 6.12 shows the von Mises stress contours for the different amounts of reduction. Similarly, Figure 6.13 show the equivalent plastic strains and Figure 6.14 the instantaneous plastic strain rates.

From the single roll pass reduction it seems that a sufficient amount of the original metal slab has to be passed through the roll to be safe that the edge effects do not play a part in the through thickness values reported. Maximum localised strain rates could be above of 15s^{-1} for a roll peripheral speed of 1.5ms^{-1} given the current model and dimensions as seen in Figure 6.14. The minimum strain rate experienced through the thickness of the slab is at least 1.5s^{-1} in the 7% reduction case up to at least 7.5s^{-1} in the 40% reduction case.

In order to investigate the through thickness microstructure as a result of different roughing sequences, the current model could need an additional extension to also include an approximation on the grain size. For this study, a normal grain growth model is introduced in the following section. The grain growth model provides a size estimate that is then linked to the material model used in the simulation of the full roughing schedule.

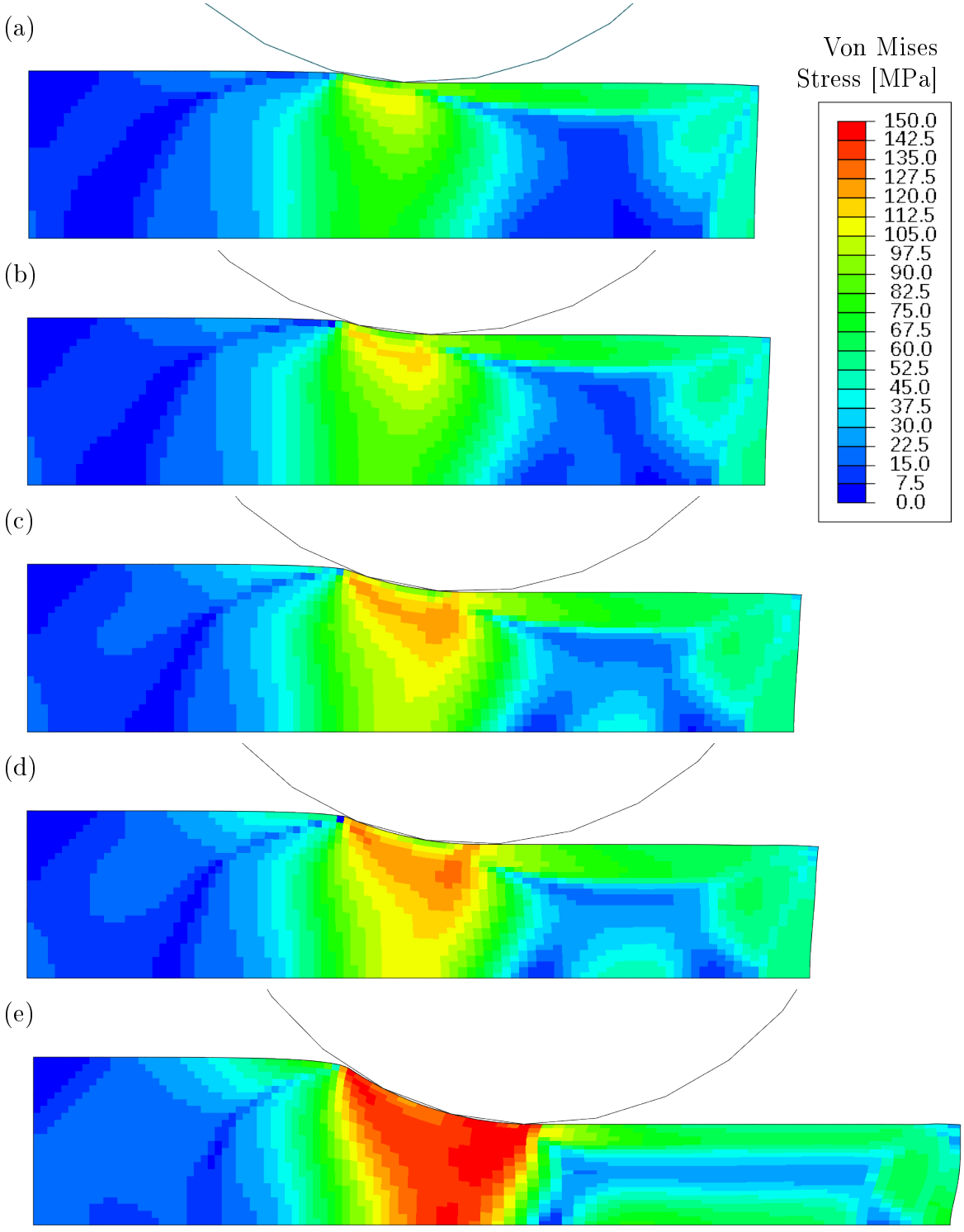

Figure 6.12: Von Mises Stress contours for (a) 7%, (b) 10%, (c) 15%, (d) 20% and (e) 40% reduction.

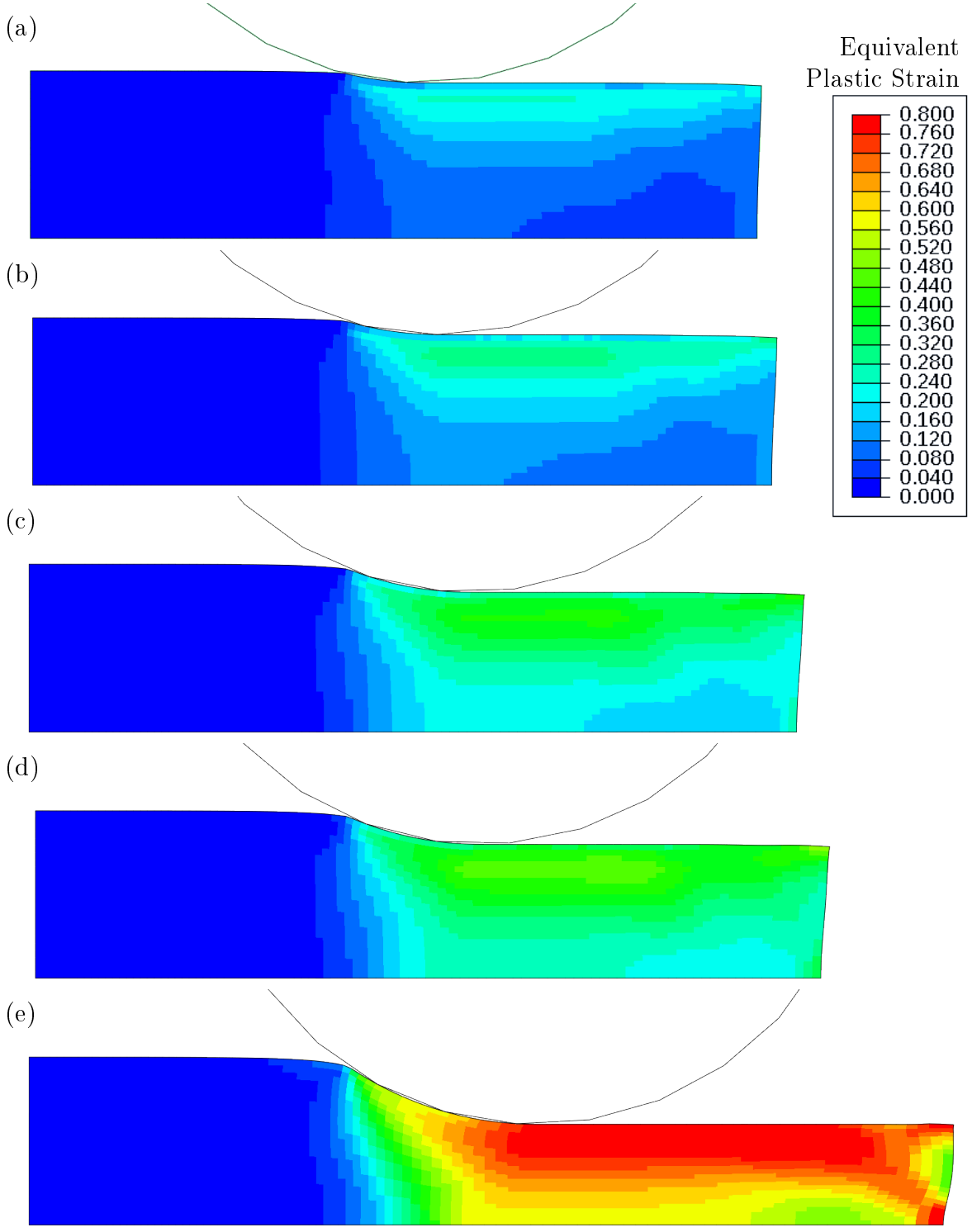

Figure 6.13: Equivalent plastic strain for (a) 7%, (b) 10%, (c) 15%, (d) 20% and (e) 40% reduction.

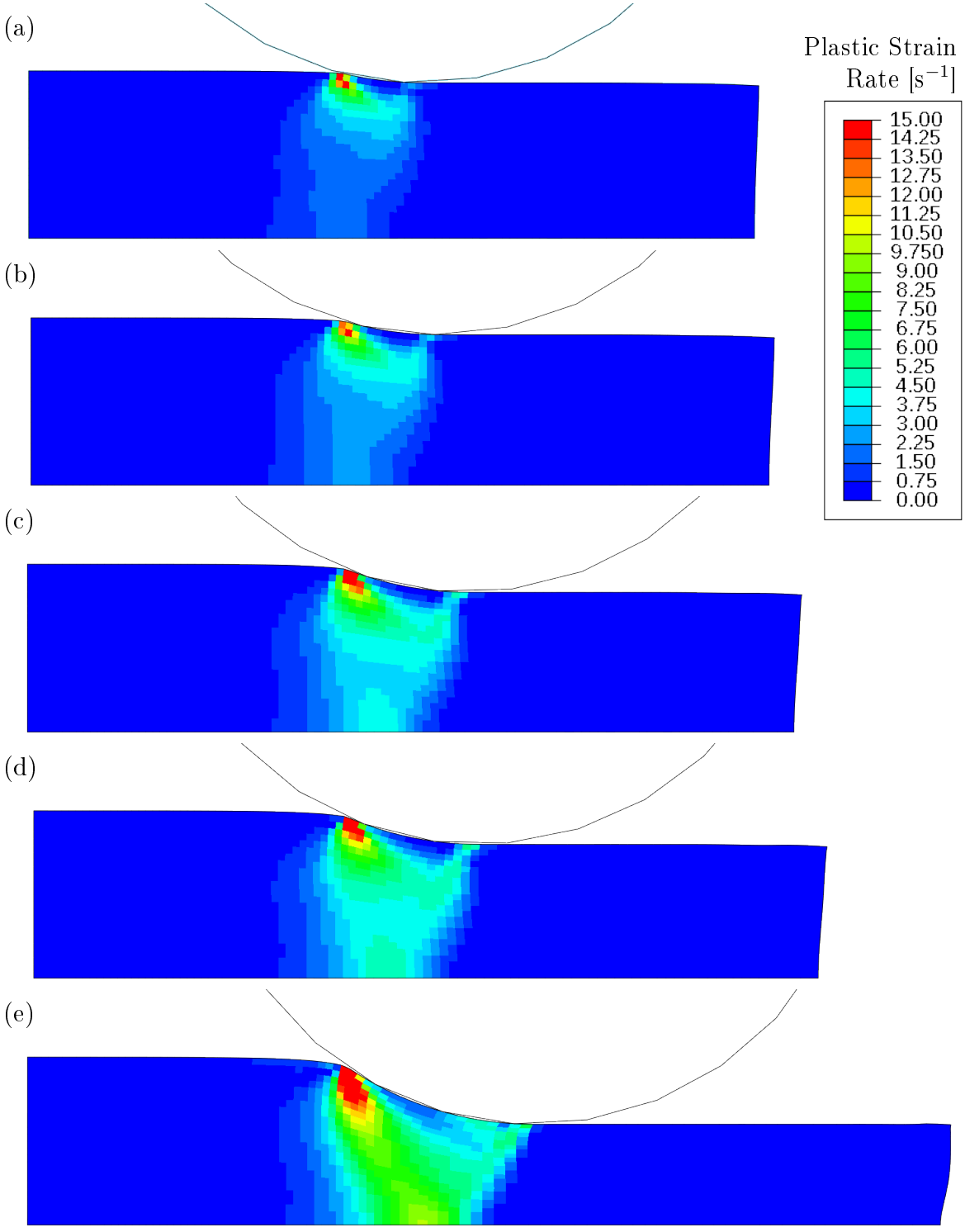

Figure 6.14: Instantaneous equivalent plastic strain rate for (a) 7%, (b) 10%, (c) 15%, (d) 20% and (e) 40% reduction.

6.5 Grain size estimate

In the hot rolling of metal alloys, the austenite grain growth is an important factor that determines the final microstructure and mechanical properties of the product. Quantifying the microstructural variation through the thickness of a steel slab is therefore of interest when modelling the hot rolling process. Using the finite element method, this requires a material model that allows the investigation of microstructure development as a result of multiple roll passes.

Although the grain size is not explicitly coupled to the numerically implemented dislocation density ratio based material model including recrystallisation in Section 5.8, its effects on the geometrically necessary dislocation density accumulation can be added following Equation (5.14). The numerical implementation followed that of Brown and Bammann (2012) where the grain size dependent evolution of the average slip plane lattice misorientation is not included and the value of C_λ/d_x in Equation (5.14) is replaced by the constant $C_{\lambda\mathrm{x}}$ in Equation (5.63). Given the reasonable fit between the model and the experimental data in Figure 6.4, and the fact that no grain size or grain growth data is available for the C-Mn-Nb-Ti-V steel alloy of interest, the effect of grain size on the mean flow stress and response of the material is not formally included. One option is to approximate the microstructure evolution and through thickness variation based on the internal state variables already at our disposal.

The variation of internal variables and material state including residual stress and equivalent plastic strain upon completion of a single roll pass was illustrated in the previous section, following a model setup similar to that of Muntin and Zinyagin (2014). Pereda et al. (2015) modelled two reduction passes. Two rolls placed one after the other resulted in either a 37% reduction followed by 31% or 31% followed by 37%. Following a finite element analysis of their setup, they illustrate the through-thickness plastic strain values after a single reduction of either 31% or 37% as well as the accumulated plastic deformation for the two choices on the order of reduction. Once the different strain penetrations are available, they use software developed by Uranga et al. (2004) to investigate the impact of the calculated strain gradients on the through-thickness microstructural evolution after the fact. In their work, a more uniform through-thickness microstructure was observed in the 31% reduction followed by 37% reduction case due

mainly to better strain penetration.

Using the material model implemented in Section 5.8, various ISV distributions through the thickness of the metal slab can be extracted. Volume fraction averaged equivalent plastic strain according to Equation (5.66) as well as residual stresses and other internal state variable quantities can give a reasonable account of the microstructural evolution as a result of a specific reduction schedule. Higher strain penetration or ISV homogeneity through the thickness of the slab could be a reasonable indication of finer austenite microstructures as well as a higher degree of homogenisation. It would also be possible to post process the already available values indicating material state to a representative microstructure following for example the work of Pereda et al. (2015).

To further extend the investigation, grain size prediction is discussed and implemented to work within the existing model. This method uses a normal grain growth model to approximate the grain size evolution per volume fraction and an equivalent volume fraction averaged grain size. Considering various active recrystallised volume fractions, the equivalent grain size estimate can be calculated by combining the values determined per volume fraction as is the case with the other equivalent internal state values. The equivalent grain size is given by

$$\bar{d}_{\mathrm{x}} = \left[\sum_{i=0}^{n_{\mathrm{x}}-1} \frac{1}{d_{\mathrm{x}_i}} \left(f_{\mathrm{x}_i} - f_{\mathrm{x}_{i+1}} \right) \right]^{-1} . \tag{6.2}$$

6.5.1 Normal grain growth

To approximate the grain size and through-thickness microstructure, a normal austenite grain growth model is solved in isolation. Yue et al. (2010) name various authors that start off using a simple empirical equation

$$d_{\mathrm{x}} = K_t t^{r_t} \tag{6.3}$$

to represent the normal grain growth in metals and alloys where d_{x} is the average grain size at holding time t. The time exponent r_t and parameter K_t are temperature dependent parameters. The influence of the initial grain size $d_{\mathrm{x}0}$ on the grain growth behaviour is considered in cases where the growth started before reaching the isothermal

annealing temperature. It also plays a role when the initial to "current" grain size value is comparable. The initial grain size is included in Equation (6.3) leading to

$$d_{\mathrm{x}} - d_{\mathrm{x0}} = K_t t^{r_t}. \tag{6.4}$$

Taking the logarithm of both sides, the relationship $\ln(d_{\mathrm{x}} - d_{\mathrm{x0}}) = \ln K_t + r_t \ln t$ can be used to determine the temperature dependent time exponent and K_t parameter. An alternative form of Equation (6.3) makes use of a grain growth exponent so that $d_{\mathrm{x}}^{r_d} = K_d t$. More generally Beck (1948) or Burke and Turnbull (1952) give the equation

$$d_{\mathrm{x}}^{r_d} - d_{\mathrm{x0}}^{r_d} = K_d t \tag{6.5}$$

when d_{x0} is comparable in size to d_{x}. From the theory on grain growth, the proportionality of the growth rate to the interfacial free energy per unit volume or inverse proportionality of the rate of boundary migration to curvature predicts a grain growth exponent $r_d = 2$ according to Xun and Lavernia (2004). Various authors (see Li and Xia, 2002; Xun and Lavernia, 2004 and Rong et al., 2008 for example) showed that $r_d > 2$ in most cases better fit experimental data, with grain growth exponent values ranging between 2 and 5 depending on various metallic systems and temperature ranges. The value of $r_d = 2$ is typically valid for a system that has no defects or precipitates, with grain growth controlled by the grain boundary curvature mechanism. Sellars and Davies (1979) found that the temperature dependent value of K_d in Equation (6.5) can be expressed as an Arrhenius type equation. If Q_d is the activation energy for grain growth and K_{d0} is the pre-exponential term, the equation takes the form

$$d_{\mathrm{x}}^{r_d} - d_{\mathrm{x0}}^{r_d} = K_{d0} \exp\left(\frac{-Q_d}{RT}\right) t. \tag{6.6}$$

Equation (6.6) is used in recent publications such as the work by Némethová et al. (2009), Liu et al. (2013), Huo et al. (2014) and Pietrzyk et al. (1995).

Lee and Lee (2008) and Zhang et al. (2011) use the formulation in Equation (6.3) with K_t also modelled as an Arrhenius type expression. Liu et al. (2013) observed that the initial grain size varies with isothermal temperature. This is also consistent

observations by Xu et al. (2012). Typically the initial grain size may be ignored if $d_{\mathrm{x}} > 3d_{\mathrm{x0}}$ according to Uhm et al. (2004).

In the finite element formulation model, a differential equation on grain growth is desired instead of an empirical formulation. By differentiating a form similar to Equation (6.6) with time on both sides it is possible to obtain a grain growth rate model. An ordinary differential equation of grain growth used by Huo et al. (2014), is given by:

$$\frac{d}{dt}d_{\mathrm{x}} = K_{D0}\exp\left(\frac{-Q_d}{RT}\right)d_{\mathrm{x}}^{-r_D}. \tag{6.7}$$

The model parameters K_{D0} and r_D as well as the activation energy have to be determined. If we use this model to estimate the grain growth per volume fraction, an approximate set of parameters are needed in the absence of grain growth data on the actual C-Mn-Nb-Ti-V alloy of interest. Austenite grain growth data for various different alloys are digitised from a few publications to get a sense of the approximate grain growth of similar alloys. The grain growth data digitised for the various alloys selected is given in Figure 6.15. Grain growth data for seven different steel alloys were digitised at various temperatures between 900°C and 1250°C. The chemical compositions of these seven alloys may be compared to that of the C-Mn-Nb-Ti-V alloy in Table 6.5. Although these alloys differ from the chemical composition of the alloy considered, the grain sizes are not explicitly linked to material response and merely considered for investigation in this section.

The model parameters for Equation (6.7) are determined again using the downhill simplex method. The model parameters K_{D0} and r_D are determined as well as the initial grain sizes in each case. The activation energy over gas constant value $Q_d/R = 40000$ was selected manually. Values of $K_{D0} = 3.79 \times 10^{13}$ and $r_D = 1.241$ resulted in the fit between the model and data points given in Figure 6.16. There is a satisfactory degree of accuracy between the model predicted grain growth and the data digitised from the work by Némethová et al. (2009). These values result in an approximate estimated grain growth when used with the associated grain growth model in Equation (6.7).

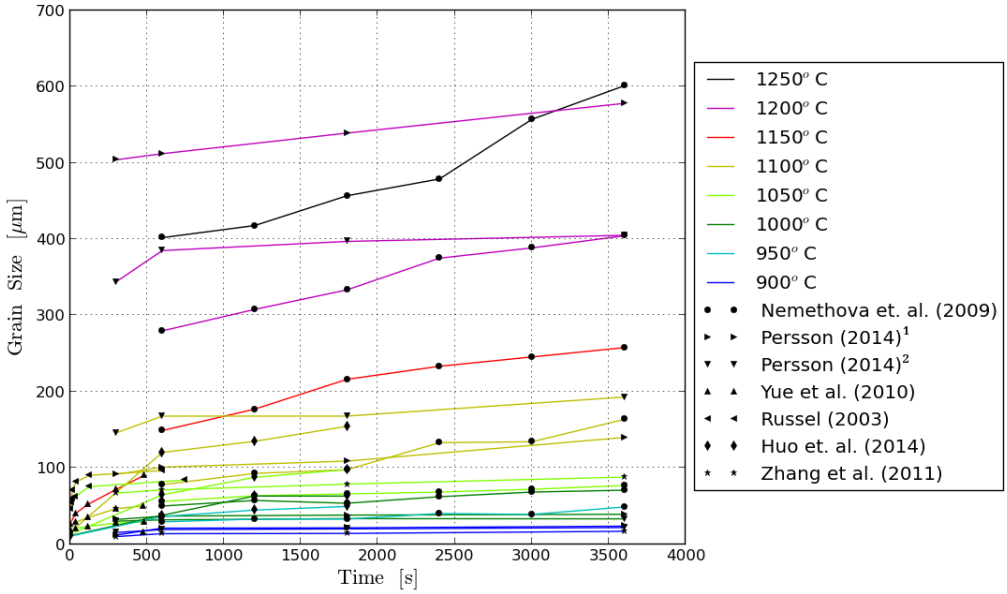

Figure 6.15: Grain growth data as digitised from various sources.

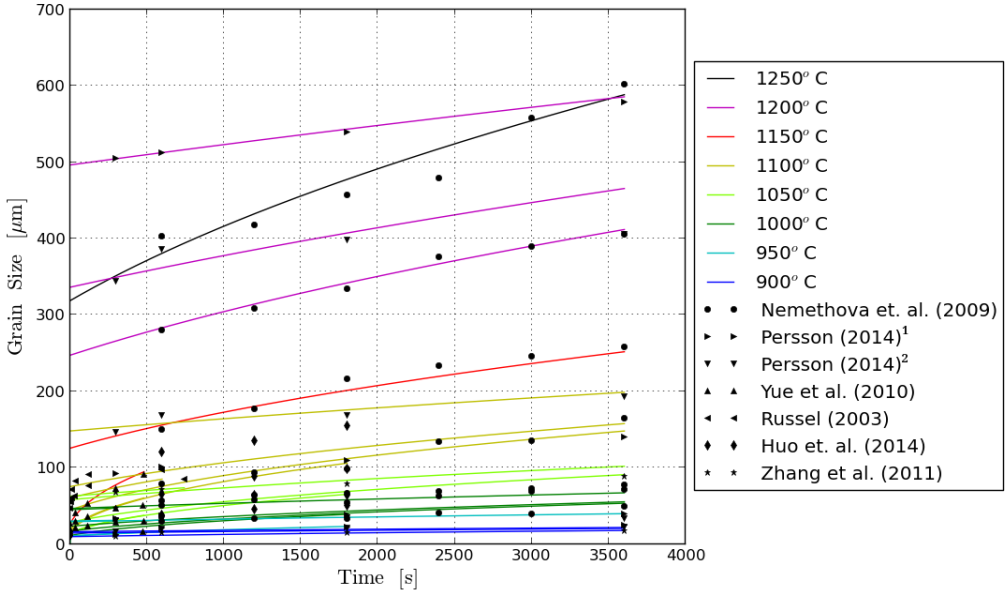

Figure 6.16: Fit between the grain growth model and the austenite grain growth model.

Alloying element	Current	Némethová et al. (2009)	Persson (2014)[1]	Persson (2014)[2]	Yue et al. (2010)	Russell (2003)	Huo et al. (2014)	Zhang et al. (2011)
C	0.134	0.12	0.95	0.98	0.99	0.17	0.28	0.39
Mn	1.5	1.54	0.31	0.93	0.31	0.74	0.77	0.69
Si	0.38	0.12	0.22	0.46	0.24	0.012	0.34	1.61
Nb	0.04	0.48	-	-	-	-	-	-
Ti	0.025	0.01	14*	60*	-	-	-	-
V	0.028	0.18	-	-	-	-	0.02	0.07
Al	0.049	0.015	0.033	0.028	-	0.04	-	-
N	55*	42*	-	-	-	47*	-	-
S	41*	10*	20*	40*	30*	80*	40*	12*
P	-	40*	0.012	0.016	0.01	90*	0.01	89*
B	-	5*	-	-	-	-	-	-
O	-	15*	10*	15*	-	-	14*	-
H	-	1.3*	-	-	-	-	1.6*	-
Cr	-	-	1.46	1.99	1.44	0.019	1.16	0.91
Ni	-	-	0.03	0.16	0.05	0.01	0.07	1.82
Mo	-	-	0.013	0.54	0.02	-	0.23	0.42
Cu	-	-	0.03	0.18	0.12	0.016	0.12	0.06
As	-	-	20*	70*	-	-	-	-
Sn	-	-	20*	0.01	-	-	-	-
Sb	-	-	20*	0.068	-	-	-	-
Pb	-	-	8*	20*	-	-	-	-
Ca	-	-	4*	5*	-	-	-	-

Table 6.5: Chemical composition of the alloy characterised as well as others for which grain growth data is digitised from the sources indicated. The alloying element content is shown in weight percentage or parts per million (*).

6.5.2 Grain size internal state evolution for the rolling schedules

The tuned grain growth model is used to estimate the grain growth and microstructural variation of the C-Mn-Nb-Ti-V microalloyed steel if different strain roughing sequences are performed. The average grain size of the material specimens tested were $80\mu m$ before the tests.

The isolated grain growth model is assumed to evolve following Equation (6.7). The value of $Q_d/R = 40000$, $K_{D0} = 3.79 \times 10^{13}$ and $r_D = 1.241$ is used from the fit to the grain growth data in Figure 6.16. This means that the grain sizes following this model are updated incrementally using

$$d_{\mathrm{x}_i}|_{t+\delta t} = d_{\mathrm{x}_i}|_t + 3.79 \times 10^{13} \exp\left(\frac{-40000}{T}\right) \left(d_{\mathrm{x}_i}|_{t+\delta t}\right)^{-1.241} \delta t. \tag{6.8}$$

for each i^{th} volume fraction. The volume fraction averaged equivalent using this approach is then determined following Equation (6.2).

Once a new recrystallised volume fraction is activated, an initial grain size of $d_{\mathrm{x}_{i+1}}|_{f_{\mathrm{x}_{i+1}} \approx 0,\ \dot{f}_{\mathrm{x}_{i+1}} \neq 0} = 1\mu\mathrm{m}$ is assigned. This is done to prevent numerical issues arising from $d_{\mathrm{x}_{i+1}} = 0$ in the denominator. The result of this model on the estimated grain size per volume fraction as well as volume fraction averaged grain size is presented in Figure 6.17 for the schedule VI strain roughing sequence. This figure illustrates the internal state variables for the same model and histories given in Figure 6.5.

Using the chosen grain growth model, the form of the grain size as a function of time for each volume fraction is illustrated by the black lines in Figure 6.17 while the red lines indicate the volume fraction averaged grain size using Equation (6.2). At the end of the material point simulation, the final volume fraction averaged grain size is estimated at around 15μm.

The model is added to the Abaqus user material subroutine used in Section 6.4. A grain size estimate per volume fraction and an equivalent means there are now four equivalent ISV values instead of three. There are also six ISVs per volume fraction instead of the original four given in the implementation of Appendix F.

The maximum number of recrystallised volume fractions now modelled based on the length of the state variable array as assigned using `*DEPVAR` in the Abaqus input

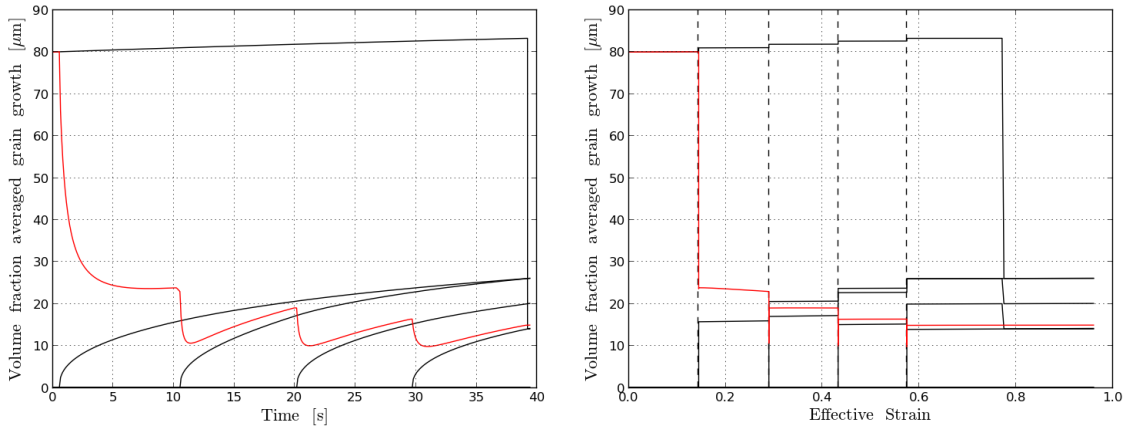

(a) (b)

Figure 6.17: Grain size evolution over (a) time and (b) strain histories. These histories correspond to those in Figure 6.5. The black lines indicate the grain size per volume fraction while the red lines indicate the equivalent volume fraction averaged grain size using Equation (6.2).

file is therefore now n_x =`(NSTATV-4)/6`.

The grain size approximation and the material parameters used in this section are now used during the simulation of multiple reduction rolls. This is done to simulate and investigate the effect of different reduction schedules on the final through thickness microstructure of the rolled plate.

6.6 Multiple Roll Pass Simulations

The same material parameter values identified on the C-Mn-Nb-Ti-V alloy in Section 6.2 are used to model multiple roll pass simulations for different rolling schedules. Symmetry is again taken into account so that only half of the metal slab and a single roller is modelled. The slab is modelled using 20 quadratic plane strain elements through the half thickness of the slab. The metal slab has an initial length of 750mm and half height of 120mm. The roller is modelled as a rigid analytical surface with a diameter of 950mm. In these simulation again no roll flattening is taken into account.

In this simulation setup, the metal slab is pulled through the rolls from side to

side. Instead of the pusher setup illustrated in Figure 6.11, the roller is modelled in contact with the slab at the onset of the simulation. Using the dimensions labelled in Figure 6.11 with $l = 750$mm, $h = 120$mm and $r = 475$mm, the initial location of the roller is at $x = 0$mm and $y = r + h = 595$mm. Contact between the roller and slab is modelled using hard normal contact with a friction coefficient $\mu_{\text{frict}} = 0.4$ as in Section 6.4.

The roll height and radial velocity are prescribed boundary conditions. The simulation of multiple roll passes associated with schedule VI in Table 6.2 is broken up into 15 different steps. In the first step, the roller is displaced to its proper height associated with a 15% true reduction. This means that the roller is displaced $120\text{mm} \times (\exp(-0.15) - 1) = -16.715$mm downward. The reduction is performed by pressing the roller into the metal slab using a prescribed zero radial velocity boundary condition. Once the roller is at the correct height, a roll simulation is performed in step 2.

The different roll steps are performed to simulate different metal slab exit velocities for each roll pass. The first roll is done at 0.3ms^{-1} with each subsequent roll velocity increasing by 0.2ms^{-1}. These velocities are associated with the increased strain rate for each subsequent reduction presented in Table 6.2. At the end of the roll pass simulation, step 3 models a 9s interpass step before again reducing the roll height to a 30% total reduction in step 4. The reduction is again done over a 1s interval. Apart from the localised deformation in the vicinity of the roller, the bulk slab section is effectively left for 10s before another roll is simulated in step 5.

The roll process in step 5 is performed assuming a slab velocity 0.2ms^{-1} faster than the previous one in the opposite direction, effectively rolling the metal slab from side to side. Because of the different velocities, the roll steps are simulated over different times. Assuming no slip between the roller and slab, each roll pass is modelled over a 750mm section. A slab velocity of 0.3ms^{-1} in step 2 means the roll step is simulated over $0.75\text{m}/0.3\text{ms}^{-1} = 2.5$s. The prescribed radial velocity in step 2 is $\omega = v/r = 0.3\text{ms}^{-1}/0.475\text{m} = 0.6316\text{s}^{-1}$. In step 5, a roll simulation performed 0.2ms^{-1} faster in the opposite direction means a roller radial velocity of $-0.5\text{mms}^{-1}/0.475\text{m} = -1.0526\text{s}^{-1}$ is simulated in a step time of $0.75\text{m}/0.5\text{ms}^{-1} = 1.5$s. A breakdown of the step information, times and boundary conditions for all 15 steps

Step	Purpose	Total Reduction	Step time	Total time	Slab velocity	Radial velocity	Roller displ	Roller height
0	Initial	0	0.	0.	0.	0.	0	595
1	Reduce	15%	1.	1.	0.	0.	-16.715	578.285
2	Roll	15%	2.5	3.5	0.3	0.6316	-16.715	578.285
3	interpass	15%	9	12.5	0.	0.	-16.715	578.285
4	Reduce	30%	1.	13.5	0.	0.	-31.102	563.898
5	Roll	30%	1.5	15	-0.5	-1.0526	-31.102	563.898
6	interpass	30%	9	24	0.	0.	-31.102	563.898
7	Reduce	45%	1	25	0.	0.	-43.485	551.515
8	Roll	45%	1.0714	26.0714	0.7	1.4737	-43.485	551.515
9	interpass	45%	9	35.0714	0.	0.	-43.485	551.515
10	Reduce	60%	1	36.0714	0.	0.	-54.142	540.857
11	Roll	60%	0.8333	36.9047	-0.9	-1.8947	-54.142	540.857
12	interpass	60%	9	45.9047	0.	0.	-54.142	540.857
13	Reduce	100%	1	46.9047	0.	0.	-75.854	519.146
14	Roll	100%	0.6818	47.5865	1.1	2.3158	-75.854	519.146
15	interpass	100%	10	57.5865	0.	0.	-75.854	519.146

Table 6.6: Step information and boundary conditions of the multiple roll pass simulation associated with Schedule VI. Radial velocities are instantaneous and constant throughout a specific step modelled while displacement of the roller height is defined as a piecewise linear function of total time.

modelled for roll schedule IV is presented in Table 6.6

As in Section 6.3, where the experimental setup for schedule IV is modelled, the entire metal slab section is prescribed a uniform temperature of 1423K at the start of the simulation. The temperature is assumed to decrease at 0.5Ks^{-1} over the course of the simulation. Contours of the von Mises stresses, equivalent plastic strains and other internal state variables are attached in Appendix H for various times throughout the multiple roll pass simulation representing Schedule VI.

6.6.1 Through thickness variation

In Appendix H, the von Mises stresses and internal state variable contours are displayed at the end of each roll pass and inter pass time. To facilitate the comparison and get acquainted with how the stresses and values develop and change throughout the

simulation, the through thickness values can also be extracted and plotted. For the sake of brevity, mainly figures of the extracted values plotted as a function of the distance from the centre is used in this section.

The through thickness von Mises stress values are extracted 350mm away from the roller. These values are displayed in Figure 6.18(a) at the end of each roll pass step simulated and in Figure 6.18(b) 10 seconds later. The residual stress is plotted over the distance from the centre of the metal slab to the surface.

The through thickness residual stress values extracted are also compared as a variation from the average value in each case in Figures 6.18(c) and (d). The standardised values are given in Figures 6.18(e) and (f). Standardising the values so that the average is zero and standard deviation equal to one allows a better depiction of the form of the variation. In these figures, the values are displayed as a function of the normalised distance from the centre of the slab to the surface. According to Figures 6.18(c) and (e), the residual stress distribution has a consistent form for each 15% reduction while the last 40% reduction sees an increased residual stress closer to the surface.

By comparing Figure 6.18(a) after the reduction roll to Figure 6.18(b) 10 seconds later, the amount of thermal recovery and recrystallisation is in each interpass step is visible. The residual stress at the centre of the slab drops by about 40% from what it was at the end of the first two roll passes (R1 and R2), 50% in the third (R3), 57% in the fourth (R4) and 68% upon completion of the final reduction (R5).

Taking the residual stress variation in the fourth reduction (R4), an approximate 15MPa variation drops to about 0.6MPa variation when comparing the highest and lowest residual stress values for R4 in Figure 6.18(b). Consulting Figure 6.18(b), this translates to about 4% variation through the thickness before the final reduction. In the same way, the von Mises stress variation after the final roll pass of about 43MPa upon completion of the roll reduction simulation drops to about 12MPa after a 10 second interpass time. This is a variation of about 60% according to the plot for R5 in Figure 6.18(b).

In Figure 6.19 the through thickness equivalent plastic strain variation 350mm away from the roller is displayed. Figure 6.19(a) are plots of the equivalent plastic strains at the end of each roll pass step simulated while Figure 6.19(b) again shows the plastic strains 10 seconds later. In these figures, the values extracted from the finite element

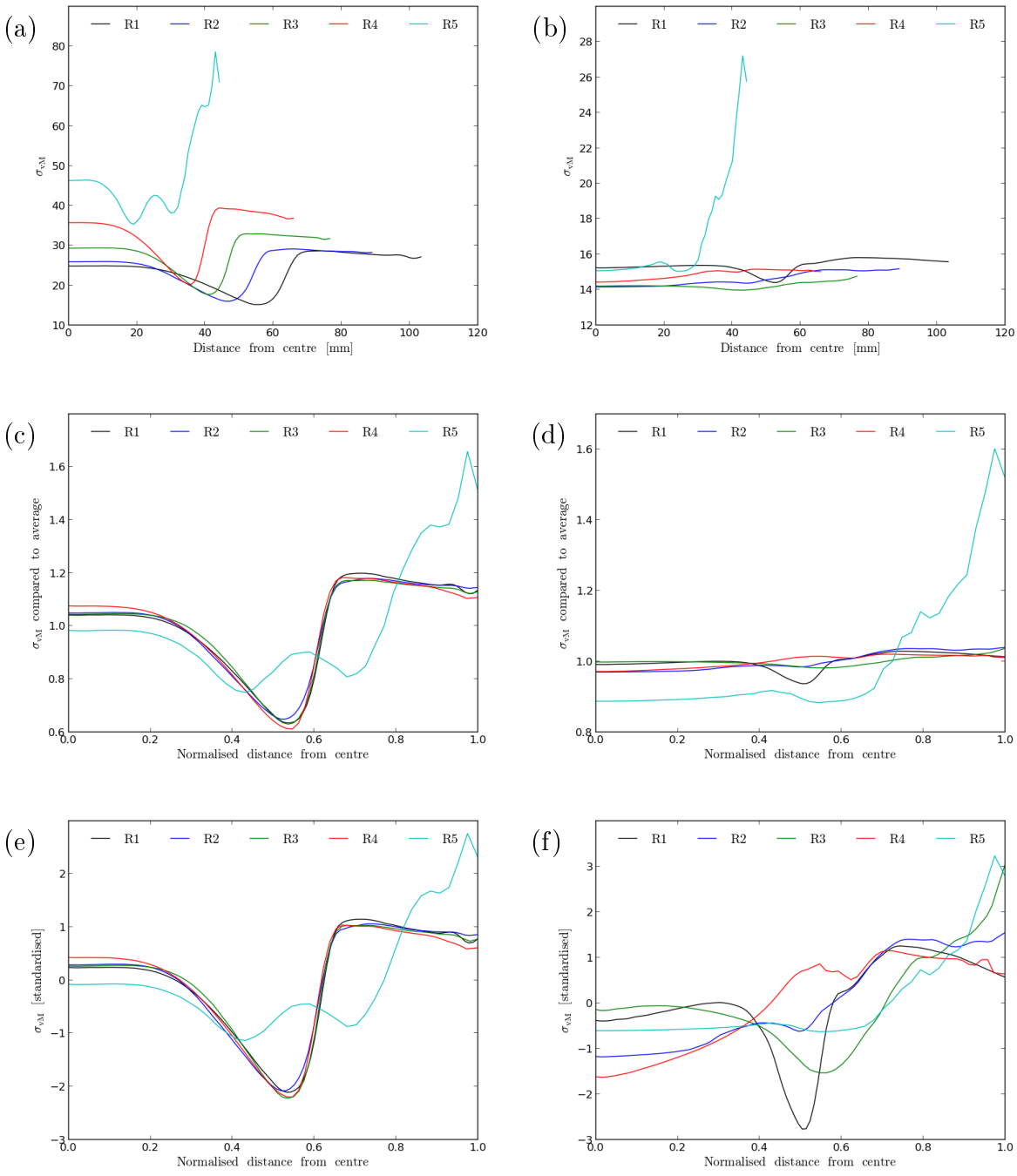

Figure 6.18: Residual von Mises stress values (left) after reduction and (right) after a static recrystallisation interpass period. (a,b) The values as extracted. (c,d) Compared to the average value in each case. (e,f) Standardised.

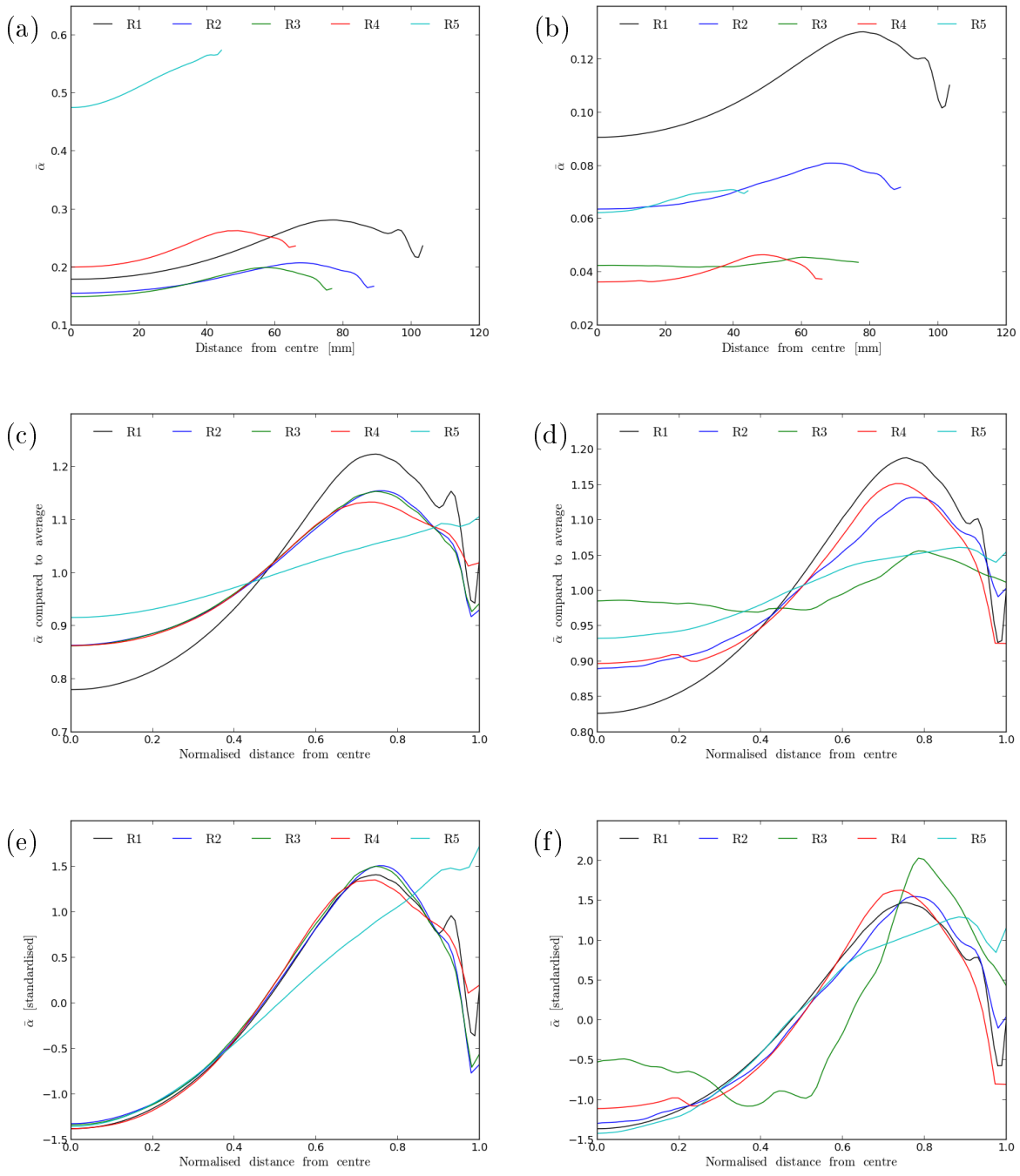

Figure 6.19: Volume fraction averaged equivalent plastic strain values (left) after reduction and (right) after a static recrystallisation interpass period. (a,b) The values as extracted. (c,d) Compared to the average value in each case. (e,f) Standardised.

simulation are again plotted as a function of the distance from the centre of the metal slab to the surface.

Figures 6.19(c) and (d) show the variation from the average value as a function of the normalised distance from the centre while Figures 6.19(e) and (f) again show the standardised through thickness variation.

For the first reduction (R1), the equivalent plastic strains in Figure 6.19(a) are between 0.18 and 0.284 compared to 0.09 and 0.13 after static recrystallisation in Figure 6.19(b). This is a reduction of between 50% in the centre and 54% below the surface of the metal slab.

Similarly, the strains between 0.156 and 0.208 after the second roll pass (R2) drops to 0.064 (59%) and 0.081 (61%) after static recrystallisation for example. If the same is done for all of the curves, the third roll pass sees a reduction in equivalent plastic strain between 71% and 77% thanks to static recrystallisation, roll pass 4 approximately 82% reduction and roll pass 5 between 87% and 89% reduction.

The strain variation according to Figure 6.19(d) is 36% for the first roll pass, 24% after roll pass 2 and 9% after roll pass 3. Roll pass 4 sees an increase in the through thickness equivalent plastic strain variation again with the variation after 10 seconds in Figure 6.19(d) around 26%. At the end of the simulation the equivalent plastic strains vary by about 13% according to the curve for R5 in Figure 6.19(d).

The distributed equivalent plastic strain during the fifth reduction roll pass is illustrated in Figure 6.20(a). Using the characterised normal grain growth model in Equation (6.8), the approximated volume fraction averaged estimated grain sizes at the same time (here 0.4791 seconds into roll pass 5) is displayed in Figure 6.20(b). The colour bar is scaled for values between 13.5μm and 14.4μm which is in approximately the same range as the end of the material point simulation in Figure 6.17.

The through thickness approximated volume fraction averaged grain size is extracted as in the residual stress and equivalent plastic strain case 350mm away from the roller. In Figure 6.21(a) the average grain sizes 10 seconds after each reduction is displayed. According to these results the average grain size is decreased following each subsequent 15% reduction followed by an increased grain size and distribution after the final 40% reduction. After the first roll pass (R1) the average grain size is around 24μm with about 9% variation through the thickness of the slab according to Figure 6.21(b).

(a)

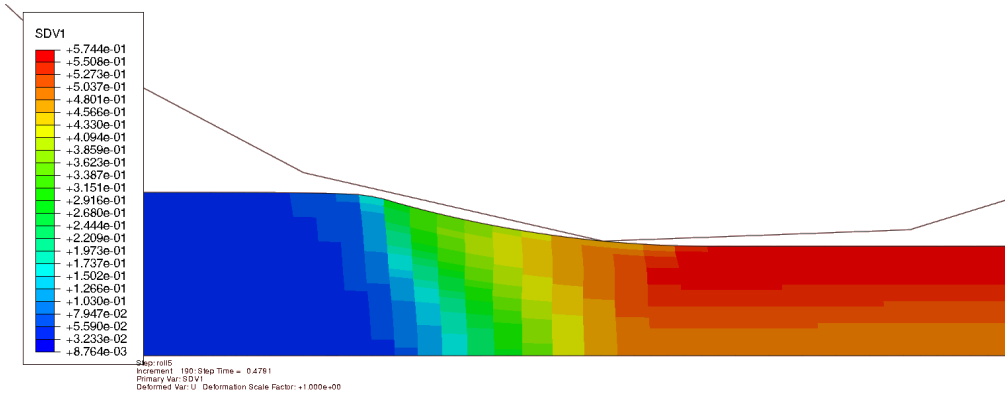

(b)

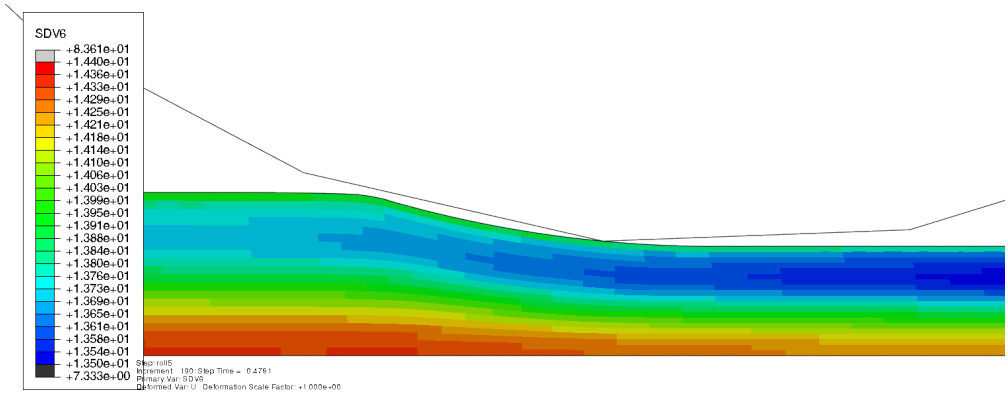

Figure 6.20: (a) Equivalent strain and (b) equivalent grain size estimate for the final roll of schedule IV.

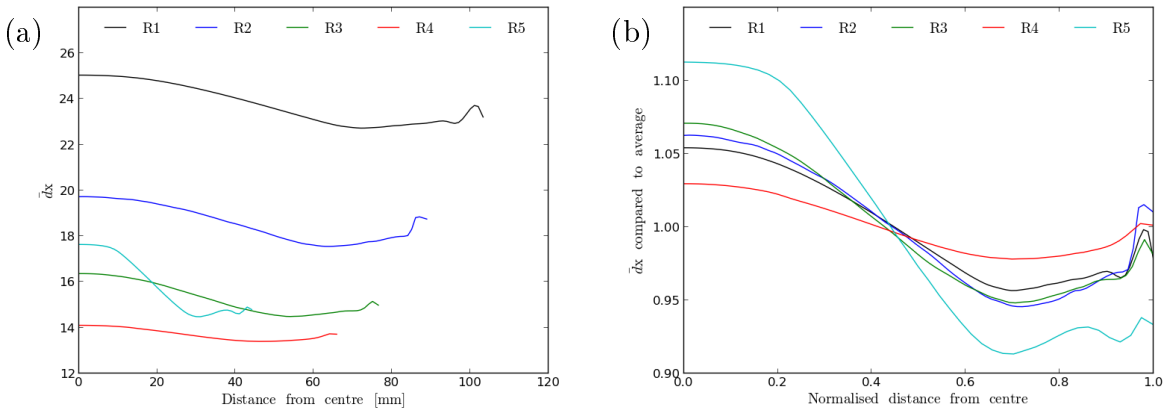

Figure 6.21: Grain size estimates after each interpass period. (a) The values as extracted, (b) compared to the average value.

After the second roll pass (R2) the average grain size is around 18.5μm followed by around 15μm for R3 and 14μm for R4. The final slab has an average through thickness grain size of around 16μm, 17.5μm in the centre of the slab and around 14.5μm at the surface.

Different schedules can also be modelled as for a comparison on the resulting through thickness state and microstructure. Considering the different roll schedules in Table 6.2, four different schedules are now modelled for comparison. The different roughing schedules consist of 14×7%, 10×10%, 6×15% and 5×20% reductions. The schedules are modelled using the same material parameters and normal grain growth is again assumed using Equation (6.8).

The resulting through thickness values extracted after each reduction and 10 seconds afterwards, 350mm away from the roller, are presented in Appendix I. In Figure 6.22, the through thickness values at the very end of the different simulations are plotted on the same axes.

Figure 6.22(a) shows the through thickness equivalent plastic strains for the four different schedules 10 seconds after the final reduction roll pass modelled. Out of all four schedules, the 6×15% schedule has on average the least residual strain while the 14×7% schedule has on average the most. The 10×10% roughing schedule has the most homogeneous strain distribution according to the comparison in Figure 6.22(a).

The residual stresses are compared in Figure 6.22(b). Here, the 10×10% reduction roll passes are seen to also result in the most uniform residual stress distribution. In Figure 6.22(c), the most uniform grain size distribution is as a result of the 5×20% roughing schedule. The volume fraction averaged grain sizes in this case are around 15μm. The 14×7% reduction roll passes have the least homogeneous through thickness grain sizes ranging from around 42μm in the centre to around 20μm at the surface.

The grain sizes in this example are only estimates based on the lack of data. If grain size data is available, additional effects on the equivalent grain size can be modelled and validated against the experimental observations.

6.7 Conclusions

In this chapter, the dislocation density based model with recrystallisation is seen to accurately model and predict the hardening, recovery and static recrystallisation of a C-Mn-Nb-Ti-V microalloyed steel in the austenite phase. The model was calibrated on material data without access to grain size data. The grain sizes were approximated by solving a normal grain growth model per material volume fraction and estimating the average grain size per integration point as a volume fraction averaged quantity. This, along with the other quantities available to inspect material state, is then used to compare the through thickness variation of the material subjected to different roughing schedules. Unfortunately, the grain sizes in this example are only estimates due to the lack of data. If grain size data is available, additional effects on the equivalent grain size can be modelled and validated against the experimental observations. Only then can the effect of grain size on the mechanical response of the material also be included in the material model implementation.

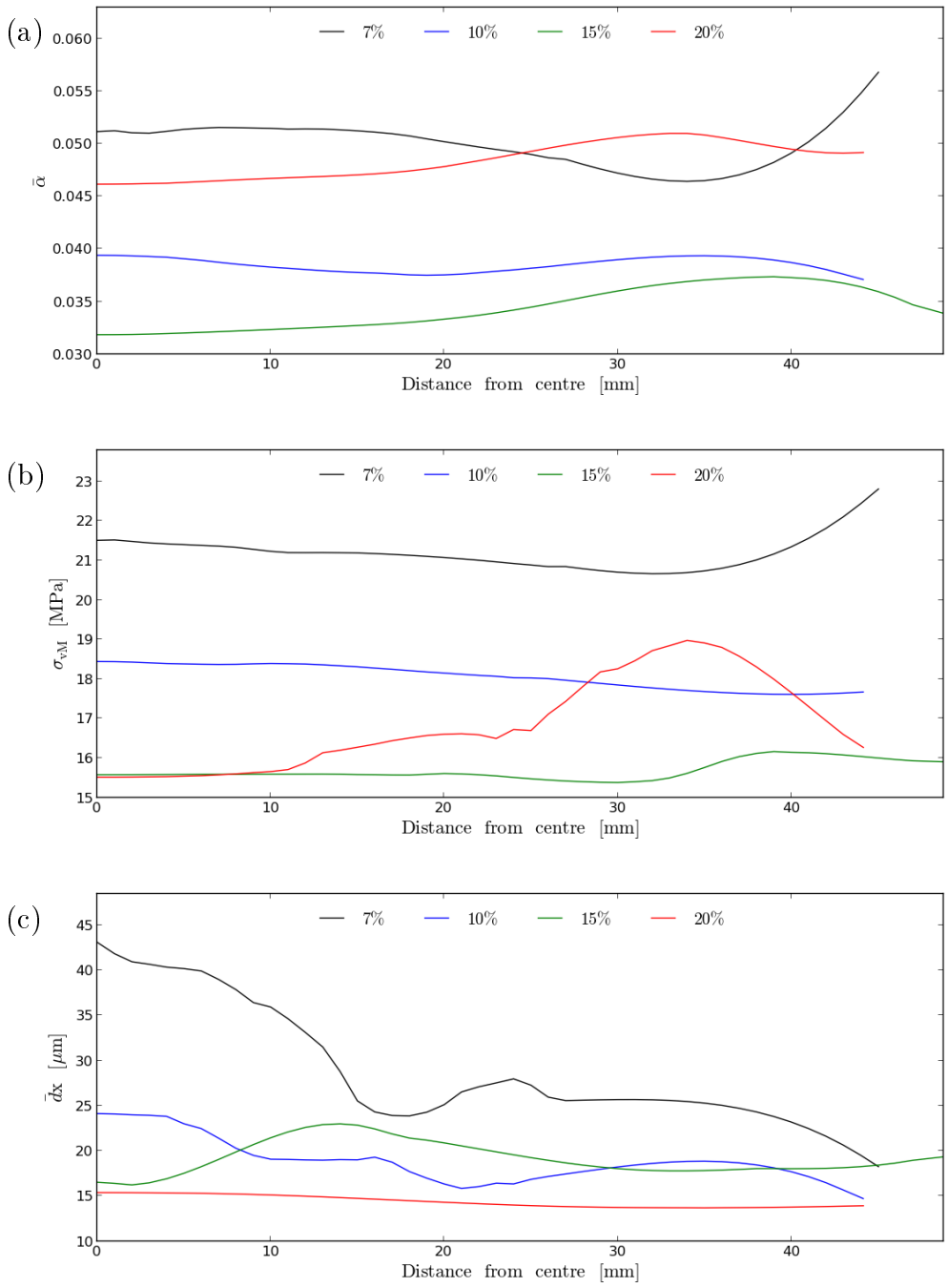

Figure 6.22: Comparison of (a) equivalent plastic strain, (b) residual stress and (c) volume fraction averaged grain size for four different roughing schedules.

Chapter 7

Conclusions

In this thesis, different material models were successfully implemented, characterised and used within a Finite Element Analysis (FEA) environment. In Chapter 2, the effect of different strain formulations on the behaviour of the same linear strain hardening plasticity formulation was investigated. In this study the correct choice of strain formulation became more important depending on the degree of deformation in the problem modelled. Different FEA software packages were also compared.

Section 2.2 illustrated the software comparison by solving the same boundary value problem in Abaqus, CalculiX and Code_Aster. Slightly different solutions were obtained most likely due to varied strain formulations and contact algorithms. This comparison illustrated an acceptable average inter-package variation between 0.68% and 1.17%. The comparison also served as a cross product verification. Using this verification, a generic user material framework for computational plasticity was developed based on the corotational hypo-elastoplastic strain formulation. The framework in the purely isotropic and combined hardening cases were verified against the internal implementation in Abaqus using linear strain hardening models. A check was also done in rotated axes to verify that both material frameworks are objective implementations of the underlying formulation.

Given the objective implementation of von Mises plasticity in the isotropic and combined hardening cases, more sophisticated model formulations were implemented and used in the remainder of the thesis. These models come into play through different scalar equation formulations based on particular choices of kinetic equation, internal

state variables and state variable evolution equations. The first such model implemented following a different scalar formulation was the Mechanical Threshold Stress (MTS) model in Chapter 3. The kinetic equation leading to the form of the MTS scaling functions as well as the development of the microstructure evolution equation in the form of the Voce-law and other popular choices were discussed. Numerical implementation of the MTS model including analytical sensitivities required for proper convergence within the isotropic user material framework were derived. The implementation was shown to be correct using a simple numerical study to check the convergence rate of the residual and compare analytical and finite difference approximated gradient values. The MTS model was characterised on Copper data using a material point simulation and compared favourably to detailed finite element analyses in Abaqus.

In Chapter 4, the MTS model was characterised to cemented Tungsten Carbide data. Imperfect compression, possibly due to test frame compliance or load eccentricity, is taken into account by performing an FEA during the parameter identification stage. Given unknown experimental boundary values, material parameter identification is still possible by including boundary value parameters as unknowns in the detailed modelling of the imperfect compression experiments. This was illustrated using a virtual experiment. Piecewise linear boundary parametrisation demonstrated the ability to accurately capture the material response despite inexact parametrisation of a transient boundary value. Using the MTS model to describe the rate and temperature dependent plastic deformation in cemented Tungsten Carbide, industrial processes where this material is used can be studied and improved. The effect of different operating conditions, anvil and high pressure cell design can be studied in the industrial HPHT process for example. An FEA on a setup used for the synthesis of diamond using a cubic anvil high pressure apparatus was simulated in Section 4.3 as illustration.

An alternative choice on internal state variable, the dislocation density ratio, was chosen to replace the evolving internal stress like variable of the original mechanical threshold stress model in Chapter 5. Within the alternative modelling environment, various extensions were discussed and implemented to include further physical phenomena present during metal forming. The inclusion of geometrically necessary dislocations and stage IV hardening was achieved by including an additional internal state

variable to represent the average slip plane lattice incompatibility. Modification of the microstructural evolution equation to include thermal or static recovery of statistical dislocations was also included. Cyclic effects were finally motivated by viewing the microstructure as a system of channels or regions of low dislocation density, separated by parallel narrow walls with a high density of segmented edge dislocations. The numerical implementation using all of the extensions for a combined hardening dislocation density based model was presented and tested in Section 5.5.

The characterisation of the combined hardening dislocation density based model was successfully illustrated on digitised experimental data for two different metal alloys. From the fit to experimental data, this extended dislocation density ratio based model is well equipped to model and predict the cyclic responses of the materials investigated.

An extension on the isotropic dislocation density ratio model is also covered Chapter 5 to include recrystallisation. Some of the foundation theory on recrystallisation modelling was first discussed as well as the assumptions made in the implemented modelling approach. The model describes multiple waves of recrystallisation. Each recrystallised or unrecrystallised volume fraction has its own set of internal state variables. The numerical implementation as well as choices made to keep track of, initialise or shift internal state variables as needed at the onset or completion of a specific wave of recrystallisation were also discussed. The recrystallisation model was shown to reproduce the general material response and steady state stresses of Cobalt and Copper undergoing dynamic recrystallisation. The recrystallisation model was also used to model the stress-strain response of a microalloyed C-Mn-Nb-Ti-V steel in Chapter 6. Numerical optimisation was used to estimate material parameters by comparing material response using candidate parameter values to experimental stress-strain data.

Stress-strain data obtained from different cylindrical test specimens, subjected to different roughing schedules were used in the material parameter identification. The model was calibrated using a fraction of the experimental data while data not used validated the ability of the model to also predict material response. The through thickness microstructural variation was estimated by linking a normal grain growth model to the mechanical response. The model was calibrated on material data without access to grain size data. The grain sizes were approximated by solving a normal grain growth model per material volume fraction and estimating the average grain size per

integration point as a volume fraction averaged quantity. This, along with the other quantities available to inspect material state, were then used to compare the through thickness variation of the material subjected to different roughing schedules.

7.1 Suggestions and possible future work

This thesis demonstrated the benefit of using state variable based plasticity formulations to model complex material behaviour. If new deformation mechanisms are required, the physically based plasticity models considered in this thesis can be extended to accomplish this goal.

The grain size estimate in Chapter 6 is currently independent of material behaviour despite a strongly grain size dependent evolution of the average slip plane lattice incompatibility reported by Kok et al. (2002). The grain size dependence in this parameter is effectively switched off in the model implemented for recrystallisation to avoid a high evolution rate following Equation (5.63) with $C_{\lambda \mathrm{x}}{=}C_{\lambda}/d_{\mathrm{x}}$ in the case of small grain sizes instead of a constant value of $C_{\lambda \mathrm{x}}$ following the model by Brown and Bammann (2012).

Should the effect of grain size on material response be one of the first model extensions considered, a Hall-Petch (Hall, 1951; Petch, 1953) type grain size effect could be included using an additional stress value in the yield function or a modified version of the scaling function in Equation (3.22). If grain sizes are explicitly linked to the material response it could also be necessary to investigate a grain size evolution equation that address additional grain growth, shape, pinning and refinement mechanisms.

Most of the material developments covered address deformation mechanisms valid for pure metals using a von Mises yield surface. Model extensions to address the anisotropy and other imperfections of real metals and alloys are a possible area of future interest. Stacking, polycrystalline material structure, grain boundary sliding and other mechanisms during super plastic forming could be included or considered as an extension to the material models. Work focused on the modelling of alloys could also require implementation of specific mechanisms to address solid solution strengthening, solute drag or effects of precipitates on multiple phase materials or grain boundary pinning for example.

Further investigation into easier material parameter estimation is another avenue of future research. Currently, the high dimensionality and varied sensitivity of the material parameters in especially the recrystallisation model require a lot of parameter space exploration. In many cases multiple initial guesses were considered during the numerical characterisation and successful termination at different locations suggested a highly multimodal objective function. Future work could investigate the benefit associated with the use of other inverse analysis techniques, optimisation or machine learning procedures during the objective material parameter characterisation.

Bibliography

Abaqus 6.11, 2011a. Abaqus Theory Manual. Dassault Systémes, Ch. 4.3 Metal, pp. 757–818.

Abaqus 6.11, 2011b. Abaqus/Standard - Abaqus/Explicit version 6.11. URL http://www.3ds.com/products-services/simulia/products/abaqus/

Acharya, A., Beaudoin, A. J., 2000. Grain-size effect in viscoplastic polycrystals at moderate strains. Journal of the Mechanics and Physics of Solids 48 (10), 2213–2230.

Auricchio, F., Beirao da Veiga, L., Lovadina, C., Reali, A., 2005. An Analysis of some Mixed-Enhanced Finite Element for Plane Linear Elasticity. Computer Methods in Applied Mechanics and Engineering 194, 2947–2968.

Avrami, M., 1939. Kinetics of phase change. I: General theory. The Journal of chemical physics 7 (12), 1103–1112.

AZO Materials, 2002. Properties: Tungsten Carbide - An Overview. URL http://www.azom.com/properties.aspx?ArticleID=1203

Bailey, J. E., Hirsch, P. B., 1962. The recrystallization process in some polycrystalline metals. Proc.Roy.Soc. A267, 11–30.

Banerjee, B., 2007. The Mechanical Threshold Stress model for various tempers of AISI 4340 steel. International Journal of Solids and Structures 44 (3-4), 834–859.

Banerjee, B., Bhawalkar, A., 2008. An extended mechanical threshold stress plasticity model: modeling 6061-T6 aluminum alloy. Journal of Mechanics of Materials and Structures 3 (3), 391–424.

Beck, P., 1948. Effect of Recrystallized Grain Size on Grain Growth. Journal of Applied Physics 19, 507–509.

Brown, A. A., Bammann, D. J., 2012. Validation of a model for static and dynamic recrystallization in metals. International Journal of Plasticity 32-33, 17–35.

Burke, J. E., Turnbull, D., 1952. Recrystallization and Grain Growth. Progress in Metal Physics 3, 220 – 292.

Cahn, J. W., 1956. The Kinetics of Grain Boundary Nucleated Reactions. Acta Metallurgica 4, 449–459.

Cahn, J. W., Hagel, W. C., 1962. Theory of the pearlite reaction. Decomposition of Austenite by Diffusional Processes, 131–196.

Chaboche, J. L., 2008. A review of some plasticity and viscoplasticity constitutive theories. International Journal of Plasticity 24 (10), 1642–1693.

Chen, S. P., Zwaag, S., Todd, I., 2002. Modeling the kinetics of grain-boundary-nucleated recrystallization processes after cold deformation. Metallurgical and Materials Transactions A 33 (3), 529–537.

Chen, S. R., Gray, G. T., 1996. Constitutive behavior of tantalum and tantalum-tungsten alloys. Metallurgical and Materials Transactions A 27A, 2994–3006.

Cook, R. D., 1974. Improved two-dimensional finite element. ASCE Journal of Structural Division ST9, 1851–1863.

Dhondt, G., Wittig, K., 1998. CalculiX:A Free Software Three-Dimensional Structural Finite Element Program.
URL `http://www.dhondt.de/`

Doherty, R. D., 2005. Primary recrystallization. Encyclopedia of Materials: Science and Technology, 7847–7850.

Doherty, R. D., Hughes, D. A., Humphreys, F. J., Jonas, J. J., Juul Jensen, D., Kassner, M. E., King, W. E., McNelley, T. R., McQueen, H. J., Rollett, A. D., 1997. Current issues in recrystallization: A review. Materials Science and Engineering A 238 (2), 219–274.

Dunlay, W. A., Tracy, C., Perrone, P., 1989. A Proposed Uniaxial Compression Test for High Strength Ceramics. Tech. rep., U.S. Army Materials Technology Laboratory.

Électricité de France, 2012. Code_Aster 11.3.0.
URL `www.code-aster.org/`

Elguedj, T., Bazilevs, Y., Calo, V. M., Hughes, T. J. R., 2008. B and F Projection Methods for Nearly Incompressible Linear and Non-linear Elasticity and Plasticity using Higher-order NURBS Elements. Computer Methods in Applied Mechanics and Engineering 197, 2732–2762.

Engauge, 2007. Digitizer 4.1.
URL `http://digitizer.sourceforge.net/`

Estrin, Y., 1996. Dislocation-density-related constitutive modeling. In: Krausz, A., Krausz, K. (Eds.), Unified constitutive laws of plastic deformation. Academic Press, San Diego, Ch. 2, pp. 69 – 106.

Estrin, Y., Mecking, H., 1984. A unified phenomenological description of work hardening and creep based on one-parameter models. Acta Metallurgica 32 (1), 57–70.

Follansbee, P. S., Kocks, U. F., 1998. A constitutive description of copper based on the use of the mechanical threshold stress as an internal state variable. Acta Materialia 36 (1), 81–93.

Fontanari, V., Bellin, F., Visintainer, M., Ischia, G., 2006. Study of Pressure Sensitive Plastic Flow Behaviour of Gasket Materials. Experimental Mechanics 46, 313–323.

Furu, T., Ø rsund, R., Nes, E., 1995. Subgrain growth in heavily deformed aluminium-experimental investigation and modelling treatment. Acta Metallurgica Et Materialia 43 (6), 2209–2232.

Glaser, S., Armero, F., 1997. On the Formulation of Enhanced Strain Finite Elements in Finite Deformation. Engineering with Computers 14, 759–791.

Goto, D. M., Garrett, R. K., Bingert, J. F., Chen, S. R., Gray, G. T., 2000. The mechanical threshold stress constitutive-strength model description of HY-100 steel. Metallurgical and Materials Transactions A 31 (8), 1985–1996.

Guzman, I., Granda, E., Mendez, R., Lopez, G., Acevendo, J., Gonzalez, D., 2012. Particle Size of Gamma Prime as a Result of Vacuum Heat Treatment of INCONEL 738 Super Alloy. Journal of Materials Science and Performance 22 (4), 1143–1148.

Haessner, F., 1978. Recrystallization of Metallic Materials.

Hall, E., 1951. The deformation and ageing of mild steel: III discussion of results. Proceedings of the Physical Society of London Section B 64, 747–753.

Han, Q.-G., Jia, X.-P., Qin, J.-M., Li, R., Zhang, C., Li, Z.-C., Tian, Y., Ma, H., 2009. Finite-element analysis on performance and shear stress of cemented tungsten carbide anvils used in the China-type cubic-anvil high-pressure apparatus. High Pressure Research 29 (3), 457–465.

Holzapfel, G., 2000. Nonlinear Solid Mechanics: A Continuum Approach for Engineering. Wiley.

Huang, Y., Humphreys, F. J., 1999. Measurements of grain boundary mobility during recrystallization of a single-phase aluminium alloy. Acta Materialia 47 (7), 2259–2268.

Hughes, T. J. R., Winget, J., 1980. Finite rotation effects in numer- ical integration of rate constitutive equations arising in large- deformation analysis. International Journal for Numerical Methods in Engineering 15, 1862–1867.

Humphreys, F. J., Hatherly, M., 1995. Recrystallization and Related Annealing Phenomena, 2nd Edition. Elsevier.

Huo, Y., Wang, B., Lin, J., Jiang, Y., Zhou, J., 2014. Modeling of austenitic grain growth of 25CrMo4 steel for the high-speed railway axle during hot working. Indian Journal of Engineering & Materials Sciences 21 (August), 371–378.

Johnson, W. A., Mehl, R. F., 1939. Reaction kinetics in processes of nucleation and growth. Trans.AIME 135, 416–458.

Jones, E., Oliphant, E., Peterson, P., 2001. SciPy: Open Source Scientific Tools for Python.
URL `http://www.scipy.org/`

Kapoor, R., Paul, B., Raveendra, S., Samajdar, I., Chakravartty, J., 2009. Aspects of Dynamic Recrystallization in Cobalt at High Temperatures. Metallurgical and Materials Transactions A 40 (4), 818–827.

Kocks, U. F., 1976. Laws for work-hardening and low temperature creep. Journal of Engineering Materials and Technology 98, 76–85.

Kocks, U. F., 1987. Constitutive behaviour based on crystal plasticity. In: Miller, A. K. (Ed.), Unified constitutive equations for creep and plasticity. Elsevier, London, pp. 1–88.

Kocks, U. F., 2001. Realistic constitutive relations for metal plasticity. Materials Science and Engineering A 317 (1-2), 181–187.

Kocks, U. F., Argon, A. S., Ashby, M. F., 1975. Thermodynamics and Kinetics of Slip. In: Progress in Materials Science. Vol. 19. Pergamon, Oxford.

Kocks, U. F., Tomé, C., Wenk, H., 1998. Texture and Anisotropy. Cambridge University Press.

Kok, S., Beaudoin, A. J., Tortorelli, D. A., 2002. On the development of stage IV hardening using a model based on the mechanical threshold. Acta Materialia 50 (7), 1653–1667.

Kolmogorov, A. N., 1937. On the statistical theory of the crystallization of metals. Izv.Akad.Nauk SSSR, Ser.Mat. (3), 355–359.

Lee, S. J., Lee, Y. K., 2008. Prediction of austenite grain growth during austenitization of low alloy steels. Materials and Design 29 (9), 1840–1844.

Li, R., Ma, H. A., Han, Q. G., Liang, Z. Z., Yin, B. H., Liu, W. Q., Jia, X., 2007. Simulation of pressure distribution in a pyrophyllite high-pressure cell by finite-element analysis. High Pressure Research 27 (2), 249–257.

Li, W., Xia, K., 2002. Kinetics of the α Grain Growth in a Binary Ti-44Al Alloy and a Ternary Ti-44Al-0.15Gd Alloy. Materials Science and Engineering A 329 (331), 430–434.

Liu, F., Xu, G., Zhang, Y. L., Hu, H. J., Zhou, L. X., Xue, Z. L., 2013. In situ observations of austenite grain growth in Fe-C-Mn-Si super bainitic steel. International Journal of Minerals, Metallurgy and Materials 20 (11), 1060–1066.

Luton, M. J., Sellars, C. M., 1969. Dynamic recrystallization in nickel and nickel-iron alloys during high temperature deformation. Acta Metallurgica 17 (8), 1033–1043.

Mathisen, K. M., Okstad, K. M., Kvamsdal, T., Raknes, S. B., 2011. Isogeometric analysis of finite deformation nearly incompressible solids. Rakenteiden Mekaniikka 44 (3), 260–278.

Maubane, R., Banks, K., Stumpf, W., Siyasiya, C., Tuling, A., 2014. The Influence of Initial Grain Size and Strain Sequence of Slab Hot Rolling on the Austenite Evolution of Peritectic Microalloyed Plate Steels. Advanced Materials Research 1019, 339–346.

McQueen, H. J., Jonas, J. J., 1975. Recovery and Recrystallization During High Temperature Deformation. Plast Deform of Mater, 393–493.

Mecking, H., 1977. Description of hardening curves of fcc single- and polycrystals. In: Thompson, A. W. (Ed.), Work hardening in tension and fatigue. TMS-AIME, New York, p. 67.

Mecking, H., Kocks, U. F., 1981. . Acta Materialia 29, 1865–1877.

Miehe, C., Apel, N., Lamprecht, M., 2002. Anisotropic additive plasticity in the logarithmic strain space: modular kinematic formulation and implementation based on incremental minimization principles for standard materials. Computer Methods in Applied Mechanics and Engineering 191, 5383 – 5425.

Mourad, H. M., Bronkhorst, C. A., Addessio, F. L., Cady, C. M., Brown, D. W., Chen, S. R., Gray, G. T., 2013. Incrementally objective implicit integration of hypoelastic-viscoplastic constitutive equations based on the mechanical threshold strength model. Computational Mechanics 53 (5), 941–955.

Muntin, A., Zinyagin, A., 2014. FEM Modelling and Experimental Research of Through-Thickness Strain Distribution During Hot Plate Rolling. In: 23rd International Conference on Metallurgy and Materials, Brno, Czech Republic, 21 - 23 May 2014. pp. 377–382.

Nabarro, F. R. N., Basinski, Z. S., Holt, D. B., 1964. The plasticity of pure single crystals. Advances in Physics 13 (50), 193–323.

Némethová, L., Kvačkaj, T., Mišičko, R., Pokorný, I., Kovárová, I., 2009. Structural Changes of C-Mn-Nb-V Steel During Reheating. Acta Metallurgica Slovaca 15 (3), 173–179.

Pereda, B., Uranga, P., Stalheim, D., Barbosa, R., Rebellato, M. A., 2015. Through-Thickness Homogenization in Thin Slab Direct Rolling of NB Microalloyed Steels. In: TMS (Ed.), HSLA Steels 2015, Microalloying 2015 & Offshore Engineering Steels 2015: Conference Proceedings. John Wiley & Sons, Inc., Hoboken, NJ, USA, pp. 309–316.

Persson, E., 2014. Austenite grain growth in bearing steels.

Petch, N., 1953. The cleavage strength of polycrystals. Journal of the Iron and Steel Institute 174, 25.

Pietrzyk, M., 2002. Through-process modelling of microstructure evolution in hot forming of steels. Journal of Materials Processing Technology 125-126, 53–62.

Pietrzyk, M., Roucoules, C., Hodgson, P. D., 1995. Modelling the Thermomechanical and Microstructural Evolution during Rolling of a Nb HSLA Steel. ISIJ International 35 (5), 531–541.

Prager, W., 1956. A New Method of Analyzing Stress and Strains in Work-Hardening Plastic Solids. Journal of Applied Mechanics 23, 493–496.

Roberts, W., Ahlblom, B., 1978. A nucleation criterion for dynamic recrystallization during hot working. Acta Metallurgica 26 (5), 801–813.

Roberts, W., Boden, H., Ahlblom, B., 1979. Dynamic Recrystallization Kinetics. Metal Science (March-April), 195–205.

Rong, R., Yucheng, W., Wenming, T., Fengtao, W., Tugen, W., Zhixiang, Z., 2008. Synthesis and Grain Growth Kinetics of In Situ FeAl Matrix Nanocomposites (II). Transactions of Nonferrous Metals Society of China 18, 66–71.

Roucoules, C., Pietrzyk, M., Hodgson, P. D., 2003. Analysis of work hardening and recrystallization during the hot working of steel using a statistically based internal variable model. Materials Science and Engineering A 339 (1-2), 1–9.

Russell, K. C., 2003. Precipitate Coarsening and Grain Growth in Steels. The Iron & Steel Society (1), 437–456.

Sandström, R., Lagneborg, R., 1975. A model for hot working occurring by recrystallization. Acta Metallurgica 23 (3), 387–398.

Sano-Furukawa, A., Hattori, T., Arima, H., Yamada, A., Tabata, S., Kondo, M., Nakamura, A., Kagi, H., Yagi, T., 2014. Six-axis multi-anvil press for high-pressure, high-temperature neutron diffraction experiments. Review of Scientific Instruments 85 (11), 0–8.

Sellars, C. M., Davies, G., 1979. The physicals metallurgy of hot working. In: TMS (Ed.), Proceedings of the International Conference on the hot working and forming process. London, pp. 3–15.

Simo, J. C., Armero, F., 1992. Geometrically Non-linear Enhanced Strain Mixed Methods and the Method of Incompatible Modes. International Journal for Numerical Methods in Engineering 33, 1413–1449.

Simo, J. C., Hughes, T. J. R., 1997. Computational Inelasticity. Spriner.

Simo, J. C., Miehe, C., 1992. Associative coupled thermoplasticity at finite strains: Formulation, numerical analysis and implementation. Computer Methods in Applied Mechanics and Engineering 98 (1), 41–104.

Song, J. E., McDowell, D. L., 2012. Grain Scale Crystal Plasticity Model with Slip and Microtwinning for a Third Generation Ni-Base Disk Alloy. John Wiley & Sons, Hoboken, pp. 159–166.

Speich, G. R., Fisher, R. M., 1966. Recrystallization in rapidly heated 3 1/4silicon iron. Recrystallization, Grain Growth and Textures, 563–598.

Svyetlichnyy, D. S., 2007. A coupled model of flow stress and microstructure evolution. NUMIFORM'07, Mater.Proc.Design, 1307–1312.

Tanner, A. B., 1998. Ofhc Cu (June).

Tanner, A. B., McDowell, D. L., 1999. Deformation, temperature and strain rate sequence experiments on OFHC Cu. International Journal of Plasticity 15 (4), 375–399.

Tanner, A. B., McGinty, R. D., McDowell, D. L., 1999. Modeling temperature and strain rate history effects in OFHC Cu. International Journal of Plasticity 15 (6), 575–603.

Uhm, S., Moon, J., Lee, C., Yoon, J., Lee, B., 2004. Prediction Model for the Austenite Grain Size in the Coarse Grained Heat Affected Zone of Fe-C-Mn Steels: Considering the Effect of Initial Grain Size on Isothermal Growth Behavior. ISIJ International 44 (7), 1230–1237.

Uranga, P., Fernández, A. I., López, B., Rodriguez-Ibabe, J. M., 2004. Modeling of Austenite Grain Size Distribution in Nb Microalloyed Steels Processed by Thin Slab Casting and Direct Rolling (TSDR) Route. ISIJ International 44 (8), 1416–1425.

Varshni, Y. P., 1970. Temperature dependence of the elastic constants. Physical Review B 2 (10), 3952–3958.

Wang, H., He, D., Tan, N., Wang, W., Wang, J., Dong, H., Ma, H., Kou, Z., Peng, F., Liu, X., Li, S., 2010. Note: An anvil-preformed gasket system to extend the pressure range for large volume cubic presses. Review of Scientific Instruments 81 (11), 11–13.

Wang, H., He, D., Yan, X., Xu, C., Guan, J., Tan, N., Wang, W., 2011. Quantitative measurements of pressure gradients for the pyrophyllite and magnesium oxide

pressure-transmitting mediums to 8GPa in a large-volume cubic cell. High Pressure Research 31 (4), 581–591.

Xu, Y., Tang, D., Song, Y., Pan, X., 2012. Prediction model for the austenite grain growth in a hot rolled dual phase steel. Materials and Design 36, 275–278.

Xun, Y., Lavernia, E. J., 2004. Grain Growth in Nanocrystalline Zn-22% Al. Materials Science and Engineering A 371, 135–140.

Yue, C., Zhang, L., Liao, S., Gao, H., 2010. Kinetic analysis of the austenite grain growth in GCr15 steel. Journal of Materials Engineering and Performance 19 (1), 112–115.

Zhang, S. S., Li, M. Q., Liu, Y. G., Luo, J., Liu, T. Q., 2011. The growth behavior of austenite grain in the heating process of 300M steel. Materials Science and Engineering A 528 (15), 4967–4972.

Ziegler, H., 1959. A Modification of Prager's Hardening Rule. Quarterly of Applied Mathematics 17, 55–65.

Appendix A

Abaqus Isotropic User Material

The combined user material makes calls to two different subroutines that also need to be specified

- A subroutine `SHEARMOD` that takes the material property array and returns a shear modulus value as well as a Poisson's ratio.
- A strain hardening subroutine `FISOTROPIC` that returns the isotropic yield stress as well as the equivalent plastic strain sensitivity.

A.1 The Isotropic Elasto-plastic Framework

[parent-folder]/umat_iso.f

```
      subroutine umat(stress, statev, ddsdde, sse, spd, scd, rpl,
     & ddsddt, drplde, drpldt, stran, dstran, time, dtime, temp, dtemp,
     & predef, dpred, cmname, ndi, nshr, ntens, nstatv, props, nprops,
     & coords, drot, pnewdt, celent, df0, df1, noel, npt, layer,
     & kspt, kstep, kinc)
```

```
c
      implicit real*8(a-h,o-z)
      character*8 cmname
c
      dimension stress(ntens), statev(nstatv), ddsdde(ntens, ntens),
     & ddsddt(ntens), drplde(ntens), stran(ntens), dstran(ntens),
     & predef(1), dpred(1), props(nprops), coords(3), drot(3, 3),
     & df0(3, 3), df1(3, 3), flow(6), tempstatv(nstatv)
c
      parameter(zero=0.d0, one=1.d0, two=2.d0, three=3.d0, six=6.d0,
     & enumax=.4999d0, newton=10, toler=1.0d-6)
c
c assign temporary state variables
      do k1=1,nstatv
       tempstatv(k1)=statev(k1)
      enddo
c
c elastic properties
      call shearmod(eg,enu,temp,props,nprops)
      eg2=two*eg
      eg3=three*eg
      emod = eg2*(1.d0+enu)
      ebulk3=emod/(one-two*enu)
      elam=(ebulk3-eg2)/three
c
c elastic stiffness
      do k1=1, ndi
        do k2=1, ndi
          ddsdde(k2, k1)=elam
        end do
        ddsdde(k1, k1)=eg2+elam
      end do
```

```
      do k1=ndi+1, ntens
        ddsdde(k1, k1)=eg
      end do
c
c calculate predictor stress and elastic strain
      do k1=1, ntens
        do k2=1, ntens
          stress(k2)=stress(k2)+ddsdde(k2, k1)*dstran(k1)
        end do
      end do
c
c calculate equivalent von mises stress
      smises=(stress(1)-stress(2))**2+(stress(2)-stress(3))**2
     & +(stress(3)-stress(1))**2
      do k1=ndi+1,ntens
        smises=smises+six*stress(k1)**2
      end do
      smises=sqrt(smises/two)
c
      call fisotropic(sy,dsy,zero,dtime,temp,
     & statev,tempstatv,nstatv,props,nprops)
c
c determine if actively yielding
      if (smises.gt.(one+toler)*sy) then
c
c actively yielding
c separate the hydrostatic from the deviatoric stress
c calculate the flow direction
      shydro=(stress(1)+stress(2)+stress(3))/three
      do k1=1,ndi
        flow(k1)=(stress(k1)-shydro)/smises
      end do
```

```
      do k1=ndi+1, ntens
        flow(k1)=stress(k1)/smises
      end do
c
c solve for equivalent von mises stress
c and equivalent plastic strain increment using newton iteration
      deqpl=zero
      do kewton=1, newton
        rhs=smises-eg3*deqpl-sy
        deqpl=deqpl+rhs/(eg3+dsy)
call fisotropic(sy,dsy,deqpl,dtime,temp,
     & statev,tempstatv,nstatv,props,nprops)
        if(abs(rhs).lt.toler) goto 10
      end do
c
c write warning message to .msg file
      write(7,2) newton
 2    format(//,30x,'***warning - plasticity algorithm did not ',
     & 'converge after ',i3,' iterations')
 10   continue
c
c update stress, elastic and plastic strains and
c equivalent plastic strain
      do k1=1,ndi
        stress(k1)=flow(k1)*sy+shydro
      end do
      do k1=ndi+1,ntens
        stress(k1)=flow(k1)*sy
      end do
c
c formulate the jacobian (material tangent)
c first calculate effective moduli
```

```
      effg=eg*sy/smises
      effg2=two*effg
      effg3=three/two*effg2
      efflam=(ebulk3-effg2)/three
      effhrd=eg3*dsy/(eg3+dsy)-effg3
      do k1=1, ndi
        do k2=1, ndi
          ddsdde(k2, k1)=efflam
        end do
        ddsdde(k1, k1)=effg2+efflam
      end do
      do k1=ndi+1, ntens
        ddsdde(k1, k1)=effg
      end do
      do k1=1, ntens
        do k2=1, ntens
          ddsdde(k2, k1)=ddsdde(k2, k1)+effhrd*flow(k2)*flow(k1)
        end do
      end do
      endif
c
c update state variable array
      do k1=1,nstatv
       statev(k1)=tempstatv(k1)
      enddo
c
      return
      end
c
```

A.2 The Simple Shear Model

[parent-folder]/simpleshear.f

```
      subroutine shearmod(eg,enu,temp,props,nprops)
      implicit real*8(a-h,o-z)
      dimension props(nprops)
      eg = props(1)
      enu=min(dabs(props(2)),0.4999d0)
      return
      end
```

A.3 Linear Strain Hardening

[parent-folder]/linearharden.f

```
      subroutine fisotropic(sy,dsy,deqpl,dtime,temp,
     & statev,tempstatev,nstatv,props,nprops)
      implicit real*8(a-h,o-z)
      dimension statev(nstatv),tempstatev(nstatv),props(nprops)
      eqpl = statev(1)+deqpl
      sy = props(3)+props(4)*eqpl
      dsy = props(4)
      tempstatev(1) = eqpl
      return
      end
```

Appendix B

Abaqus Combined User Material

The combined user material makes a call to the Abaqus utility subroutine `ROTSIG` as well as calls to three different subroutined that also need to be specified

- A subroutine `SHEARMOD` that takes the material property array and returns a shear modulus value as well as a Poisson's ratio.
- A subroutine `CYCLREVERSAL` in the event of a load reversal.
- A strain hardening subroutine `FCOMBINED` that returns the isotropic and kinematic stresses as well as their sensitivities.

B.1 The Combined Elasto-plastic Framework

[parent-folder]/umat_comb.f

```
      subroutine umat(stress, statev, ddsdde, sse, spd, scd, rpl,
     & ddsddt, drplde, drpldt, stran, dstran, time, dtime, temp, dtemp,
     & predef, dpred, cmname, ndi, nshr, ntens, nstatv, props, nprops,
     & coords, drot, pnewdt, celent, df0, df1, noel, npt, layer,
```

```
     & kspt, kstep, kinc)
c
      implicit real*8(a-h,o-z)
c
      character*8 cmname
c
      dimension stress(ntens), statev(nstatv), ddsdde(ntens, ntens),
     & ddsddt(ntens), drplde(ntens), stran(ntens), dstran(ntens),
     & predef(1), dpred(1), props(nprops), coords(3), drot(3, 3),
     & df0(3, 3), df1(3, 3), tempstatev(nstatv), alpha(6), flow(6),
     &  xi(6), xiprev(6)
c
      parameter(zero=0.d0, one=1.d0, two=2.d0, three=3.d0, six=6.d0,
     & enumax=.4999d0, newton=10, toler=1.0d-6)
c
c elastic properties
      call shearmod(eg,enu,temp,props,nprops)
      eg2=two*eg
      eg3=three*eg
      elam=(ebulk3-eg2)/three
c
c elastic stiffness
      do k1=1, ndi
        do k2=1, ndi
          ddsdde(k2, k1)=elam
        end do
        ddsdde(k1, k1)=eg2+elam
      end do
      do k1=ndi+1, ntens
        ddsdde(k1, k1)=eg
      end do
c
```

```
c recover and rotate shift tensor
      call rotsig(statev(1), drot, alpha, 1, ndi, nshr)
c
c previous effective stress
      do k1=1,ntens
        xiprev(k1)=stress(k1)-alpha(k1)
      enddo
c
c current predictor stress
      do k1=1, ntens
        do k2=1, ntens
          stress(k2)=stress(k2)+ddsdde(k2, k1)*dstran(k1)
        end do
      end do
c
c get trial effective stress:
      xixiprev = zero
      do k1=1,ntens
        xi(k1)=stress(k1)-alpha(k1)
        xixiprev = xi(k1)*xiprev(k1)
      enddo
c
c if sign change, then call load reversal subroutine
      if(xixiprev.lt.toler)then
        call cyclreversal(statev,nstatv)
      endif
c
c assign temporary state variables
      do k1=1,nstatv
        tempstatev(k1)=statev(k1)
      enddo
c
```

```
c calculate equivalent von mises stress
      smises=(xi(1)-xi(2))**2+(xi(2)-xi(3))**2+(xi(3)-xi(1))**2
      do k1=ndi+1,ntens
        smises=smises+six*xi(k1)**2
      end do
      smises=sqrt(smises/two)
c
c check yield surface
      call fcombined(sy0,dsy,sb0,dsb,zero,dtime,temp,
     & statev,tempstatev,nstatv,props,nprops)
c
c determine if actively yielding
      if (smises.gt.(one+toler)*sy0) then
c
c actively yielding
c separate the hydrostatic from the deviatoric stress
c calculate the flow direction
      shydro=(stress(1)+stress(2)+stress(3))/three
      do k1=1,ndi
        flow(k1)=(stress(k1)-alpha(k1)-shydro)/smises
      end do
      do k1=ndi+1,ntens
      flow(k1)=(stress(k1)-alpha(k1))/smises
      end do
c
c solve for equivalent von mises stress
c and equivalent plastic strain increment using newton iteration
      sy=sy0
      sb=sb0
      deqpl=zero
      do kewton=1, newton
        rhs=smises-eg3*deqpl-sy-sb+sb0
```

```
        deqpl=dabs(deqpl+rhs/(eg3+dsy+dsb))
        call fcombined(sy,dsy,sb,dsb,deqpl,dtime,temp,
     & statev,tempstatev,nstatv,props,nprops)
        if(abs(rhs).lt.toler*sy0) goto 10
      end do
c
c write warning message to .msg file
      write(7,2) newton
 2    format(//,30x,'***warning - plasticity algorithm did not ',
     & 'converge after ',i3,' iterations')
 10   continue
c
c update stress
      do k1=1,ndi
        alpha(k1)=alpha(k1)+(sb-sb0)*flow(k1)
        stress(k1)=alpha(k1)+flow(k1)*sy+shydro
      end do
      do k1=ndi+1,ntens
        alpha(k1)=alpha(k1)+(sb-sb0)*flow(k1)
        stress(k1)=alpha(k1)+flow(k1)*sy
      end do
c
c formulate the jacobian (material tangent)
c first calculate effective moduli
      effg=eg*(sy+sb-sb0)/smises
      effg2=two*effg
      effg3=three/two*effg2
      efflam=(ebulk3-effg2)/three
      effhrd=eg3*(dsy+dsb)/(eg3+dsy+dsb)-effg3
      do k1=1, ndi
        do k2=1, ndi
          ddsdde(k2, k1)=efflam
```

```
        end do
        ddsdde(k1, k1)=effg2+efflam
      end do
      do k1=ndi+1, ntens
        ddsdde(k1, k1)=effg
      end do
      do k1=1, ntens
        do k2=1, ntens
          ddsdde(k2, k1)=ddsdde(k2, k1)+effhrd*flow(k2)*flow(k1)
        end do
      end do
      endif
c
c update state variable array
      do k1=1,ntens
        tempstatev(k1)=alpha(k1)
      enddo
      do k1=1,nstatv
        statev(k1)=tempstatev(k1)
      enddo
c
      return
      end
```

B.2 Load Reversal

[parent-folder]/simpleloadreversal.f

```
      subroutine cyclreversal(statev,nstatv)
```

```
      implicit real*8(a-h,o-z)
      dimension statev(nstatv)
      ! code here to act on state variables in the load reversal case
      return
      end
```

B.3 Combined Linear Strain Hardening

[parent-folder]/combinedlinear.f

```
      subroutine fcombined(sy,dsy,sb,dsb,deqpl,dtime,temp,
     & statev,tempstatev,nstatv,props,nprops)
      implicit real*8(a-h,o-z)
      dimension statev(nstatv),tempstatev(nstatv),props(nprops)
      eqpl = statev(7)+deqpl
      sy = props(3)+props(4)*eqpl
      dsy = props(4)
      sb = props(5)*eqpl
      dsb = props(5)
      tempstatev(7) = eqpl
      return
      end
```

Appendix C

Mechanical Threshold Stress Subroutine

C.1 The Mechanical Threshold Stress Shear Model

[parent-folder]/shear_varshni.f

```
subroutine shearmod(eg,enu,temp,props,nprops)
implicit real*8(a-h,o-z)
dimension props(nprops)
emu0=props(1)
ed0=props(2)
et0=props(3)
enu=min(dabs(props(4)),0.499d0)
if(temp.gt.et0) then
  eg = emu0 - ed0/(dexp(et0/temp)-1.d0)
else
  eg = emu0
```

```
      endif
      return
      end
```

C.2 The Mechanical Threshold Stress Model

[parent-folder]/mts_harden.f

```
      subroutine fisotropic(sy,dsy,deqpl,dtime,temp,
     & statev,tempstatev,nstatv,props,nprops)
      implicit real*8(a-h,o-z)
      dimension statev(nstatv),tempstatev(nstatv),props(nprops)
c
      character*8 cmname
      parameter(zero=0.d0,one=1.d0,two=2.d0,newtonmax=10,toler=1.0d-8,
     & ratemin=1.d-10)
c
c     material properties
      emu0=props(1)
      ed0=props(2)
      et0=props(3)
c     props(4) is used for poisson's ratio
      sa=props(5)
      se0s=props(6)
      si=props(7)
      a0e=props(8)
      a0es=props(9)
      a0i=props(10)
      hard0=props(11)
```

```
      rate0=props(12)
      rate0es=props(13)
      qe=props(14)
      pe=props(15)
      qi=props(16)
      pi=props(17)
      pow=props(18)
      cm=props(19)
c
      cmname = 'MTS_POWR'
      if(cm.gt.zero)then
        cmname = 'MTS_TANH'
      endif
c
c     check
      rate = deqpl/dtime
      if(rate.lt.ratemin)then
        rate = ratemin
      endif
c
c     harden in statev
      sep = statev(1)
      sec = sep
c
      emu = emu0 - ed0/(dexp(et0/temp)-one)
      emuSF = emu/emu0
c
      sfi0 = temp/(a0i*emu)
      sfli = dlog(rate0/rate)*sfi0
      sfi = (one-sfli**(one/qi))**(one/pi)
c
      sfe0 = temp/(a0e*emu)
```

```
      sfle = dlog(rate0/rate)*sfe0
      sfe = (one-sfle**(one/qe))**(one/pe)
c
      c0 = -temp/(emu*a0es)
      sat = se0s*(rate/rate0es)**c0
c
      if(cmname(5:8).eq.'TANH')then
        hard = hard0*(one-(dtanh(pow*sec/sat)/dtanh(pow)))
        dhard = deqpl*hard0*pow/
     &   (dtanh(pow)*sat*dcosh(pow*sec/sat)**two)
      else
        hard = hard0*(one-(sec/sat))**pow
        dhard = (deqpl*hard0*pow*(one-(sec/sat))**(pow-one))/sat
      endif
      f = sec - sep - deqpl*hard
c
      if(dabs(f).gt.toler)then
      kount=1
      do while((dabs(f).gt.toler).and.(kount.lt.newtonmax))
        kount=kount+1
        sec = sec - f/(one+dhard)
        if(cmname(5:8).eq.'TANH')then
          hard = hard0*(one-(dtanh(pow*sec/sat)/dtanh(pow)))
          dhard = deqpl*hard0*pow/
     &            (dtanh(pow)*sat*dcosh(pow*sec/sat)**two)
        else
          hard = hard0*(one-(sec/sat))**pow
          dhard = (deqpl*hard0*pow*(one-(sec/sat))**(pow-one))/sat
        endif
        f = sec - sep - deqpl*hard
      enddo
      endif
```

```
c
c     Yield stress
      sy = sa + emusf*(sfi*si+sfe*sec)
c
c     Partial gradient componenets
c     d(sec)/d(epl)
      dsecdeqpl = hard/(one+dhard)
c     d(sfi)/d(epl)
      dsfideqpl = sfi0*(one-sfli**(one/qi))**(one/pi-one)*
     &          sfli**(one/qi-one)/(pi*qi*rate)
c     d(sfe)/d(epl)
      dsfedeqpl = sfe0*(one-sfle**(one/qe))**(one/pe-one)*
     &          sfle**(one/qe-one)/(pe*qe*rate)
c     d(sec)/d(rate)
      dsecdrt = c0*dhard*se0s*sec*(rate/rate0es)**(c0-one)/
     &          ((dhard+one)*rate0es*sat)
c     Total
c     d(yield)/d(epl)
      dsy =  emuSF*(sfe*(dsecdeqpl+dsecdrt/dtime)+dsfedeqpl*sec/dtime+
     &       dsfideqpl*si/dtime)
c
      tempstatev(1) = sec
      return
      end
```

Appendix D

Point based inverse material parameter identification

Instead of using a finite element analysis where boundary conditions are constructed from various unknowns, a cheaper choice would be to determine material properties with the help of something like a single point integration procedure.

A Mechanical Threshold Stress routine is written in Python to perform the approximate parameter identification for this reason. This routine takes strain history as a function of time and determines the equivalent force. The force at each data point is determined by multiplying the yield stress with an appropriate area. Figure D.1 shows the effect of using the initial area, as well as the effect of a proper Poisson area compensation. A uniaxial Abaqus simulation is used as a reference. The force versus strain for the Abaqus simulation is given as the red lines of Figure D.1. The same MTS material parameters as used in the FEA simulation are then used in the single point integration method.

In the one case, the force is determined by

$$F(t) = \frac{1}{4}\pi D_o^2 \sigma_{\mathrm{Y}}(t), \tag{D.1}$$

with D_o the initial test section diameter of 7 mm. An area compensation, with a scale factor is seen to have the best fit to the reference curve. This scale factor is included and is motivated by the stress gradients seen in Figure 4.11(e). The chosen

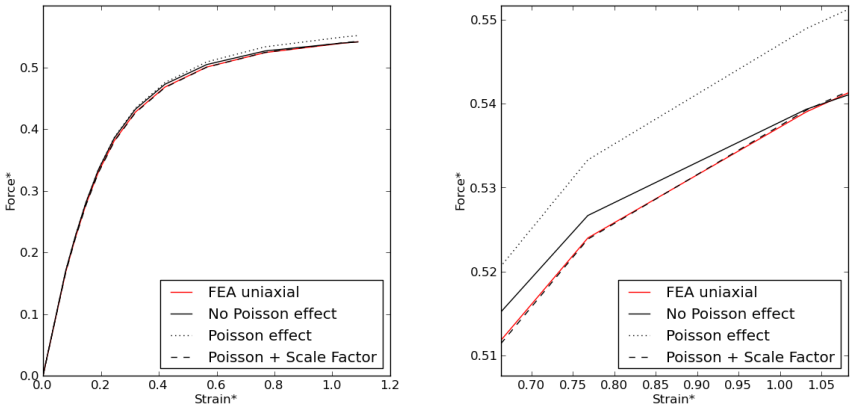

(a) (b)

Figure D.1: Normalised force versus strain curves. Uniaxial compression FEA curve compared to a single point integration curve where initial area is used, proper area compensation is applied and combined with a 0.99 scale factor. A full curve is visible in (a) with detail in (b).

compensation for area and resulting force calculation is determined from

$$F(t) = \frac{S_f}{4}\pi \left[D_o(1 + \nu\varepsilon_{\mathrm{e}}(t) + 0.5\varepsilon_{\mathrm{p}}(t))\right]^2 \sigma_{\mathrm{Y}}(t), \tag{D.2}$$

where $\varepsilon_{\mathrm{e}}(t)$ is the elastic strain component at a given time and $\varepsilon_{\mathrm{p}}(t)$ is the plastic strain component. The area compensation takes elastic and plastic strains into account, while a scale factor S_f of 0.99 was chosen. This slight area compensation scale factor is seen to produce a fairly good match to the finite element uniaxial simulation of Figure D.1.

One way of using the room temperature test to approximate the MTS material parameters, is by taking the average of the three strain gauge readings and assuming that this is the effective strain rate for a single element. Another approach involves the approximation of the room temperature test by three distinct cylindrical elements, each with one third the area of the actual specimen. In the latter approximation, the three strain gauge readings are used to construct a linear varying strain field. This is done by using the coordinates of the strain gauges in their original locations seen in

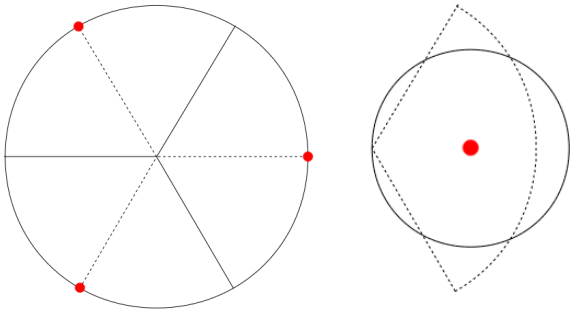

(a) (b)

Figure D.2: (a) The location of the three strain gauges equally spaced around the circumference of the central test section. During the three cylinder approximation, a 120° circular sector is modelled by a cylindrical element with the same area. (b) The effective cylindrical approximation to a 120° sector with the centroids coinciding.

Figure D.2 to construct a spatially varying strain field of the form

$$\varepsilon(x, y, t) = C_0(t) + C_1(t)x + C_2(t)y. \tag{D.3}$$

The time dependent equivalent strains at the centroids of the 120° sectors are then determined by inserting the centroid coordinates into Equation (D.3). The resulting strains as a function of time are used to determine each of the three cylindrical elements' contribution to the force in the same way as the single cylinder approximation, using only a third of the full specimen area. The single cylinder (average strain) procedure and three cylinder procedures are now compared and evaluated using virtual problems.

In the first virtual problem, a finite element analysis is run with a linear displacement field boundary condition similar to the one described in Equations (4.3) and (4.4) that resulted in the fit seen in Figure 4.12. The strains at the three locations around the central circumference and the reaction force is extracted from the finite element simulation and treated as if it were experimental data. A parameter identification is then performed where the seven MTS material parameters are determined using numerical optimisation. In the single cylinder procedure, the average of the three strain gauges as a function of time is used in to determine the forces for a given set of material parameters. In the three cylinder procedure, a linear interpolation of the strains is used

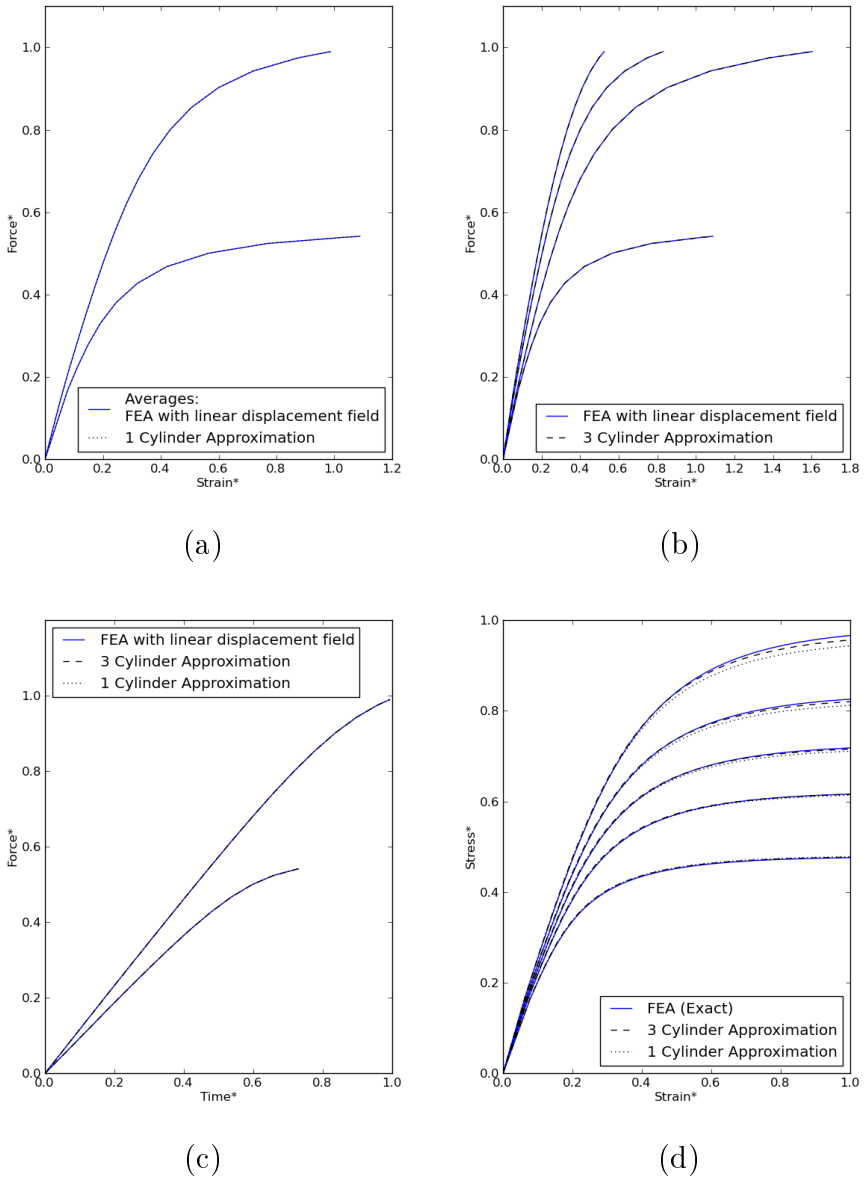

Figure D.3: Comparison of the single cylinder and three cylinder procedures to fit MTS material parameters for a linear displacement distribution. (a) Normalised force versus strain using a single cylinder and the average of the three strains in the room temperature comparison. (b) Normalised force versus strain using a three cylinder fit and the three finite element strains. (c) Normalised force as a function of time fitted using the single and three cylinder approximation. (d) The known true MTS material response versus that determined from the single and three cylinder procedures for a constant strain rate of $0.0001s^{-1}$.

Parameter	Exact value	Single cylinder	Three cylinder
${\hat{\sigma}_a}^*$	1.0000	1.00771882	1.00547183
${\hat{\sigma}_{0\varepsilon s}}^*$	1.0000	0.94674572	0.97238436
${k_{\mathrm{B}}}/{g_{0\varepsilon}b^3}^*$	1.0000	0.97057691	0.96244947
${k_{\mathrm{B}}}/{g_{0\varepsilon s}b^3}^*$	1.0000	1.62117934	1.36908000
${\theta_0}^*$	1.0000	1.02377007	1.04064404
${\mu_r}^*$	1.0000	1.00701314	1.00479798
${D_r}^*$	1.0000	1.00450078	0.99620249

Table D.1: The single cylinder and three cylinder approximation to the material parameters, given the first set of virtual experimental data.

at each sector centroid location and the smaller equivalent cylinder contribution to the total force is used to determine the force as a function of time. The squared difference between the approximated and virtual experiment forces for each time increment is used as the current function value. The optimisation is again performed using the `fmin` algorithm.

The converged normalised results are visible in Table D.1. The converged curve fit of the normalised forces as a function of time is visible in Figure D.3(c). The force over strain is also plotted in Figure D.3(a) using the average of the tree strains for the single cylinder approximation and Figure D.3(b) using the virtual experimental strains and three cylinder approximation.

The material response is determined given the converged MTS material parameters. The constant strain rate curves at a strain rate of $0.0001s^{-1}$ is plotted for $25°C$, $150°C$, $250°C$, $350°C$ and $500°C$. Comparing these curves to the response using the known virtual experiment parameters used in the FEA simulation, it appears that both procedures are able to approximate the actual material with reasonable accuracy. This should therefore also hold true for the experimental data if the experiment was subject to sufficiently small strains. Although neither procedure replicates the known response exactly, the three cylinder procedure performs the best.

A second virtual experiment is run with the exact same MTS material parameters. A more complex boundary condition is applied so that both the angle and magnitude of the displacement field reference point have a nonlinear time dependence. The force and three strains obtained from a finite element analysis is again used as virtual

Parameter	Exact value	Single cylinder	Three cylinder
$\hat{\sigma}_a{}^*$	1.0000	1.51329714	1.06111960
$\hat{\sigma}_{0\varepsilon s}{}^*$	1.0000	0.87864129	0.96890237
$k_B/g_{0\varepsilon}b^{3*}$	1.0000	1.10881247	1.22509147
$k_B/g_{0\varepsilon s}b^{3*}$	1.0000	0.71519620	0.62102419
$\theta_0{}^*$	1.0000	0.45646766	0.79337991
$\mu_r{}^*$	1.0000	1.01079021	1.03017389
$D_r{}^*$	1.0000	1.14494185	1.10360844

Table D.2: The single cylinder and three cylinder approximation to the material parameters, given the second set of virtual experimental data.

experimental data.

The converged single cylinder and three cylinder approximation results are visible in Table D.2 for the second virtual experiment. The associated curve fits are visible in Figure D.4. The material response using the converged parameters are compared to the actual material in Figure D.4(d). Since this problem has a more complex and higher strain, the single and three cylinder procedures do not approximate the true material response as well as in the first virtual experiment. In this example, the three cylinder approximation does noticeably better than the single cylinder equivalent, but it is evident that the three strains should be properly coupled as it would be in a finite element analysis.

If the real experimental tests are closer related to the first virtual problem with smaller strains, it is likely that the one and three cylinder procedures would be well suited to determine the material parameters which would closely approximate the actual material response. These two methods are now used on the actual experimental data.

D.1 Results on experimental data

The MTS material parameters of an experimentally tested material is now determined using the one and three cylinder procedures. This is again done on the material test of which the room temperature data is represented in Figure 4.1(a) and (d). The strain history and its associated time data is used the same way as mentioned in the virtual

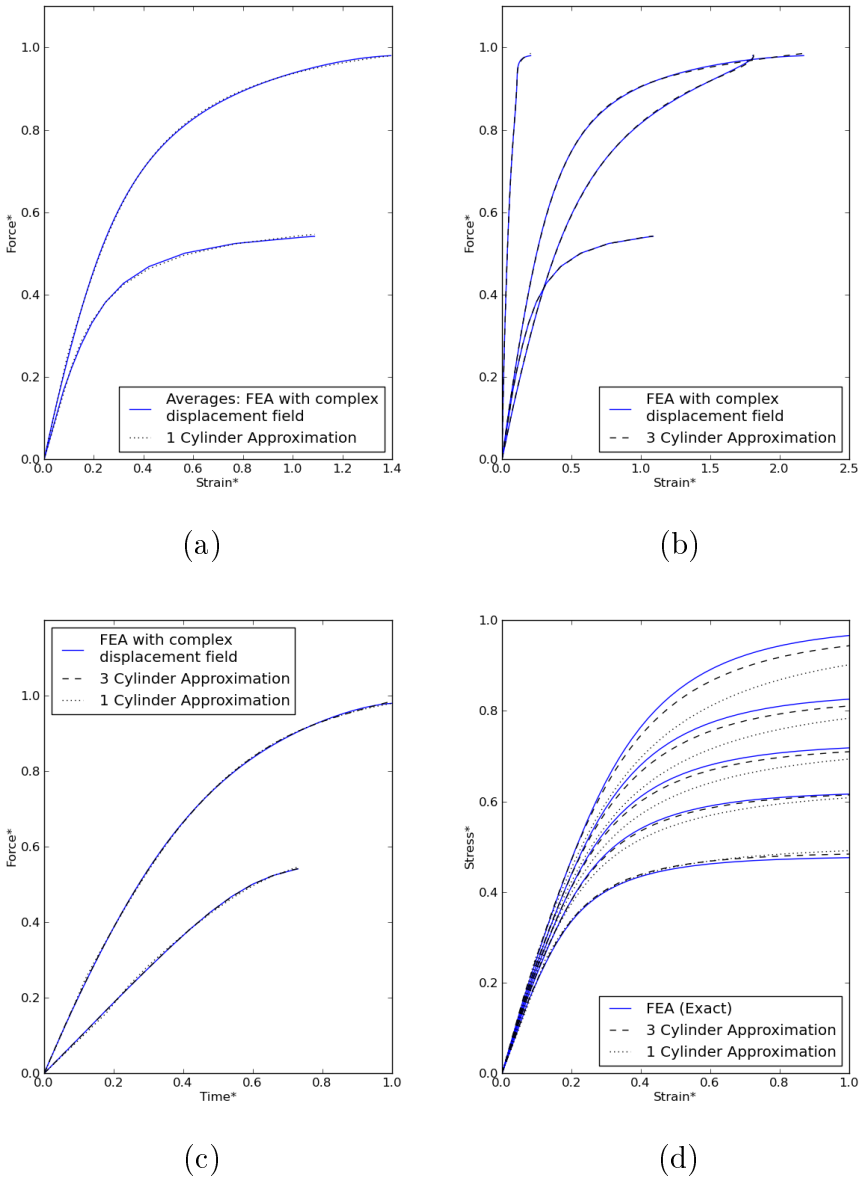

Figure D.4: Comparison of the single cylinder and three cylinder procedures to fit MTS material parameters for an arbitrary selected complex displacement distribution. (a) Normalised force versus strain using a single cylinder and the average of the three strains in the room temperature comparison. (b) Normalised force versus strain using a three cylinder fit and the three finite element strains. (c) Normalised force as a function of time fitted using the single and three cylinder approximation. (d) The known true MTS material response verus that determined from the single and three cylinder procedures for a constant strain rate of $0.0001s^{-1}$.

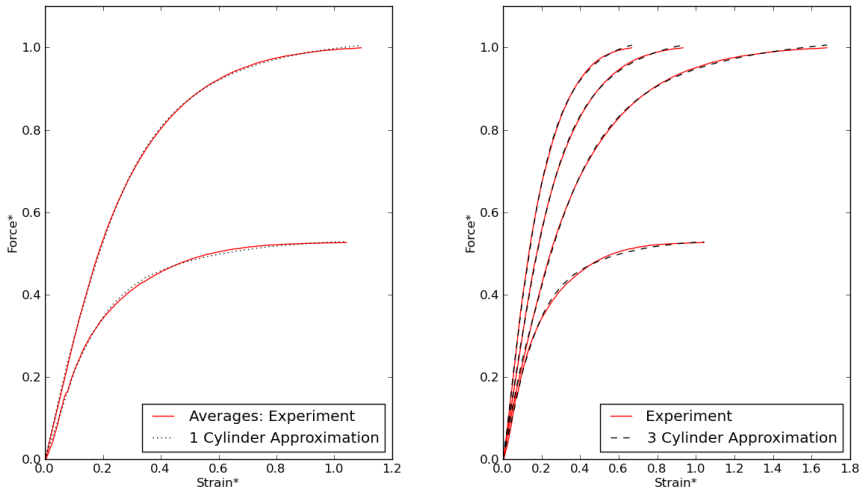

(a)

(b)

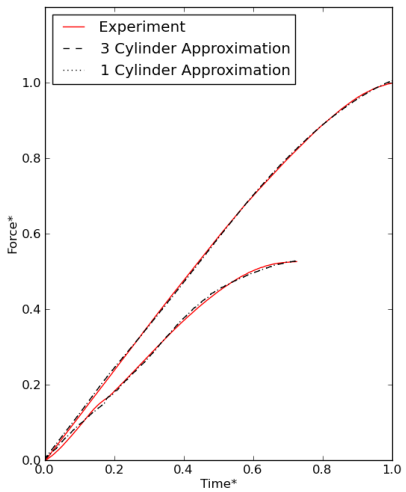

(c)

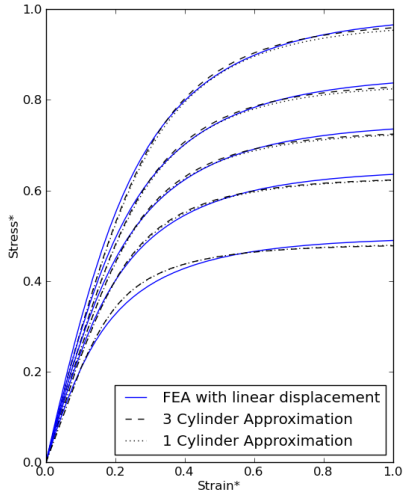

(d)

Figure D.5: Comparison of the single cylinder and three cylinder procedures to fit MTS material parameters on experimental data compared to the MTS material determined from the inverse finite element analysis. (a) Normalised force versus strain using a single cylinder and the average of the three strain gauges in the room temperature comparison. (b) Normalised force versus strain using a three cylinder fit and the three gauge strains. (c) Normalised force as a function of time fitted using the single and three cylinder approximation. (d) The inverse FEA determined MTS material response verus that determined from the single and three cylinder procedures for a constant strain rate of $0.0001s^{-1}$.

experiments to obtain the force curve as a function of time. The converged curve fit are displayed in Figure D.5.

In this case, both the single cylinder and three cylinder procedure returned material parameter values that result in similar material response. The materials determined by the single and three cylinder procedures also closely match the material response using the parameters determined by the finite element inverse analysis of which the results could be seen in Figure 4.12.

From Figure D.5(d), the exact material response is not clear but it is evident that all of the methods result in similar material response required to approximate the experimental results. Comparing the results of Figure D.3(d) and D.5(d), it is also possible that the one and three cylinder approximated materials could come close to the true material response.

Appendix E

Dislocation Density Ratio Based Combined Hardening Subroutine

E.1 Combined Hardening Subroutine

[parent-folder]/dens_combined.f

```
      subroutine fcombined(sy,dsy,sb,dsb,deqpl,dtime,temp,
     & statev,tempstatev,nstatv,props,nprops)
c
      implicit real*8(a-h,o-z)
      dimension statev(nstatv),tempstatev(nstatv),props(nprops)
c
      parameter(zero=0.d0,half=0.5d0,one=1.d0,two=2.d0,newtonmax=10,
     & toler=1.0d-8,ratemin=1.d-10)
c
c     material properties
      emu0=props(1)
```

```
      ed0=props(2)
      et0=props(3)
c     props(4) is used for poisson's ratio
c     stress values
      sa=props(5)
      s0=props(6)
c     scaling function
      a0e=props(7)
      pe=props(8)
      qe=props(9)
      rate0=props(10)
c     evolve misorient
      cld=props(11)
c     geometric disl
      cg=props(12)
      rg=props(13)
c     accumulation
      c1=props(14)
c     dynamic recovery
      c20=props(15)
      a02=props(16)
      rate02=props(17)
c     thermal recovery
      c30=props(18)
      a03=props(19)
      r3=props(20)
c     recoverable
      c4=props(21)
      c50=props(22)
      a05=props(23)
c     back stress
      c6=props(24)
```

```
      c7=props(25)
c
c     check
      rate = deqpl/dtime
      if(rate.lt.ratemin)then
        rate = ratemin
      endif
c
c     statevariables
      x1p=statev(1) !misorientation
      x2p=statev(2) !dislocation ratio
      x3p=statev(3) !recoverable disl.
c     previous back stress:
      sbp=statev(4)
c
      emu=emu0-ed0/(dexp(et0/temp)-one)
      emusf=emu/emu0
c
c     scaling function
      sfe0=temp/(a0e*emu)
      sfle=dlog(rate0/rate)*sfe0
      sfe=(one-sfle**(one/qe))**(one/pe)
c
c     dynamic recovery
      c2t=-temp/(emu*a02)
      c2=c20*dexp(c2t*dlog(rate/rate0))
      dc2drt=c2*c2t
c
c     thermal recovery
      c3=c30*dexp(-a03/temp)*dtime
      c5=c50*dexp(-a05/temp)*dtime
c
```

```
c     update lattice incompatibility
      x1=x1p+cld*deqpl
c     initial guess for dislocation dens.
      x2=x2p
      sqx2=dsqrt(x2)
c
      f=-deqpl*(cg*x1**rg+c1*sqx2-c2*x2)+c3*x2**r3
      ddf=one-deqpl*(half*c1/sqx2-c2)
      if(dabs(f).gt.toler)then
      kount=0
      do while((dabs(f).gt.toler).and.(kount.lt.newtonmax))
      kount=kount+1
      x2=dabs(x2-f/ddf)
      sqx2=dsqrt(x2)
      f=x2-x2p-deqpl*(cg*x1**rg+c1*sqx2-c2*x2)+c3*x2**r3
      ddf=one-deqpl*(half*c1/sqx2-c2)
      enddo
      endif
      x3=(x3p+deqpl*c4*sqx2)/(one+deqpl*c2+c5)
c
c     equivalent threshold and yield stress
      sec=s0*sqx2
      sy=sa+emusf*sfe*sec
c     back stress
      sbnum=sbp+deqpl*c6*sqx2
      sbden=one+deqpl*c7
      sb=sbnum/sbden
c
c     dislocation sensitivity (EQ. 5.44)
      dx2de=(cg*x1**rg+c1*sqx2-c2*x2-dc2drt*x2+
     & deqpl*rg*cg*cld*(x1**(rg-one)))/ddf
c     isotropic senistivity
```

```
      dsec=half*s0*dx2de/sqx2
      dsfe=sfe0*(one-sfle**(one/qe))**(one/pe-one)*
     & sfle**(one/qe-one)/(pe*qe*rate*dtime)
      dsy=emusf*(sfe*dsec+dsfe*sec)
c     back stress sensitivity
      dsb=(c6*sqx2 + half*deqpl*c6*dx2de/sqx2)/sbden-
     & c7*sbnum/(sbden**two)
c
c     update temporary state variable array
      tempstatev(1)=x1
      tempstatev(2)=x2
      tempstatev(3)=x3
      tempstatev(4)=sb
c
      return
      end
```

E.2 Load Reversal Subroutine

[parent-folder]/dens_reversal.f

```
      subroutine cyclreversal(statev,nstatv)
      implicit real*8(a-h,o-z)
      dimension statev(nstatv)
      ! density - recoverable
      statev(2) = statev(2)-statev(3)
      ! reset recoverable
      statev(3) = 0.d0
      ! swap backstress
```

```
      statev(4) = -statev(4)
      return
      end
```

Appendix F

Subroutine for the Dislocation Density Based Model With Static and Dynamic Recrystallisation

F.1 Isotropic Hardening Subroutine

[parent-folder]/rx_iso.f

```
      subroutine fisotropic(sy,dsy,depl,dtime,temp,
     & statev,tempstatev,nstatv,props,nprops)
c
      implicit real*8(a-h,o-z)
      logical checkrx
      dimension props(nprops),statev(nstatv),tempstatev(nstatv),
     & xi(2),xj(2),r(2),drdx(2,2),fxinfo(3),reps(2),dxdr(2,2),
     & fxnvec(5),xjupd(2)
```

```
      parameter(zero=0.d0,half=0.5d0,one=1.d0,two=2.d0,
     & toler=1.d-4,x10=one,x20=1.d-10,fxn0=1.d-4,ratelim=1.d-8)
c
c elastic properties:
      emu0 = props(1)
      ed0 = props(2)
      et0 = props(3)
      enu = props(4)
c reference stress values
      siga = props(5)
      sig0 = props(6)
c scaling function
      a0e = props(7)
      rate0 = props(8)
      qe = props(9)
      pe = props(10)
c
      rate = depl/dtime
      if(rate.lt.ratelim)then
      rate = ratelim
      endif
c
      if(temp.gt.et0)then
      emu = emu0 - ed0/(dexp(et0/temp)-one)
      sfe0 = temp/(a0e*emu)
      else
      emu = emu0
      sfe0 = one/a0e
      endif
      emusf = emu/emu0
c
      sfel = dlog(rate0/rate)*sfe0
```

```
      sfe = dabs(one-sfel**(one/qe))**(one/pe)
c isv shift
      nrrx = (nstatv-3)/4
      if(statev(7).gt.(0.999d0))then
      ixvf=0
      do while(ixvf.lt.nrrx)
      lstskip = 4*(ixvf)+3
      statev(lstskip+1)=statev(lstskip+5)
      statev(lstskip+2)=statev(lstskip+6)
      statev(lstskip+3)=statev(lstskip+7)
      statev(lstskip+4)=statev(lstskip+8)
      enddo
      statev(lstskip+5)=zero
      statev(lstskip+6)=zero
      statev(lstskip+7)=zero
      statev(lstskip+8)=zero
      endif
c
      fxc = one
      fxcp = one
      fxcr = zero
      dfxcde = zero
      x1eq = zero
      x2eq = zero
      dx1eqde = zero
      plastic = zero
c
      ixvf = 1
      checkrx = .true.
      do while((ixvf.lt.nrrx).and.(checkrx))
      lstskip = 4*(ixvf-1)+3
      xeplp = statev(lstskip+1)
```

```
 x1p = max(statev(lstskip+2),x10)
 x2p = max(statev(lstskip+3),x20)
 fxnp = max(statev(lstskip+4),fxn0)
 xi = (/x1p,x2p/)
 xj = (/x1p,x2p/)
 fxinfo = (/fxc,fxcr,fxnp/)
 call rget(r,drdx,fxnvec,reps,xj,xi,fxinfo,
&  depl,dtime,temp,props,nprops)
 fx = dsqrt(r(1)*r(1) + r(2)*r(2))
 fxd = drdx(1,1)*drdx(2,2)-drdx(2,1)*drdx(1,2)
 icount = 0
 newtmax=15
 if(xi(1).eq.(one))then
 newtmax = 50
 endif
 do while((icount.lt.newtmax).and.(dabs(fx).ge.toler))
 icount = icount+1
 if(dabs(fxd).gt.zero)then
 dxdr = reshape((/drdx(2,2),-drdx(2,1),
&      -drdx(1,2),drdx(1,1)/),(/2,2/))/fxd
 xjupd = reshape(matmul(dxdr,reshape(r,(/2,1/))),(/2/))
 xj=xj-xjupd
 xj = (/max(dabs(xj(1)),x10),max(dabs(xj(2)),x20)/)
 fxinfo = (/fxc,fxcr,fxnp/)
 call rget(r,drdx,fxnvec,reps,xj,xi,fxinfo,
&  depl,dtime,temp,props,nprops)
 fx = dsqrt(r(1)*r(1) + r(2)*r(2))
 fxd = drdx(1,1)*drdx(2,2)-drdx(2,1)*drdx(1,2)
 else
 xj = (/x1p,x2p/)
 fx = zero
 endif
```

```
      enddo
      x1 = max(xj(1),x10)
      x2 = max(xj(2),x20)
      fxn = min(dabs(fxnvec(1)),one)
c
c  add fxc contribution to Gamma
      rx0 = one/(fxc-fxn)
      dxdfxc0 = dfxcde*(dtime*fxcr*rx0*rx0-rx0)
      dx1dfxc = dxdfxc0*x1
      dx2dfxc = dxdfxc0*x2
      reps=reps+(/dx1dfxc,dx2dfxc/)
c
      if(fxn.le.(1.d-3))then
      checkrx = .false.
      endif
      fxnr = fxnvec(2)
      dfxndx1 = fxnvec(3)
      dfxndx2 = fxnvec(4)
      dfxndfxc = fxnvec(5)

      xepl = xeplp*fxcp/fxc+depl
c
      tempstatev(lstskip+1) = xepl
      tempstatev(lstskip+2) = x1
      tempstatev(lstskip+3) = x2
      tempstatev(lstskip+4) = fxn
c
      x1eq = x1eq + x1*(fxc-fxn)
      x2eq = x2eq + x2*(fxc-fxn)
      plastic = plastic + xepl*(fxc-fxn)
c
      if(dabs(fxd).gt.0)then
```

```
      dx1de = dxdr(1,1)*reps(1)+dxdr(1,2)*reps(2)
      dx2de = dxdr(2,1)*reps(1)+dxdr(2,2)*reps(2)
      dfxnde = dfxndx1*dx1de+dfxndx2*dx2de+dfxndfxc*dfxcde


      dx1eqde = dx1eqde + dx1de*(fxc-fxn) +
     &      x1*(dfxcde - dfxnde)
      dfxcde = dfxnde
      fxc = fxn
      fxcp = fxnp
      fxcr = fxnr
      endif
c      endif
      ixvf = ixvf+1
      end do
c
      tempstatev(1) = plastic
      tempstatev(2) = x1eq
      tempstatev(3) = x2eq
c
      sqx1 = dsqrt(x1eq)
      sec = sig0*sqx1
      sy = siga + emusf*sfe*sec
c partial derivatives
c     d(sec)/d(epl)
      dsecdepl = half*sig0*dx1eqde/sqx1
c     d(sfe)/d(epl)
      dsfedepl = (sfe0*(one-sfel**(one/qe))**(one/pe-one)*
     &     sfel**(one/qe-one)/(pe*qe*rate))/dtime
c     total
      dsy = emusf*(sfe*dsecdepl+dsfedepl*sec)
      return
```

```
      end
```

F.2 Recrystallisation Residual Subroutine

[parent-folder]/getr.f

```
      subroutine rget(r,drdxj,fxnvec,reps,xj,xi,fxinfo,
     &  depl,dtime,temp,props,nprops)
c
      implicit real*8(a-h,o-z)
      dimension props(nprops),r(2),drdxj(2,2),fxinfo(3),reps(2),
     &  xj(2),xi(2),fxnvec(5)
c
      parameter(zero=0.d0,half=0.5d0,one=1.d0,two=2.d0,
     & toler=1.d-10,ratelim=1.d-8)
c
c elastic properties:
      emu0 = props(1)
      ed0 = props(2)
      et0 = props(3)
      enu = props(4)
c reference stress values
      siga = props(5)
      sig0 = props(6)
c scaling function
      a0e = props(7)
      rate0 = props(8)
c evolution of misorient:
```

```
      cld = props(11)
c stage 4
      cg = props(12)
      rg = props(13)
c storage
      c1 = props(14)
c dynamic recovery:
      c20 = props(15)
      a02 = props(16)
      rate02 = props(17)
c thermal recovery
      c30 = props(18)
      r3 = props(19)
      a03 = props(20)
c recrystallisation
      cx0 = props(21)
      a0x = props(22)
      cxl = props(23)
      rxl = props(24)
      rxa = props(25)
      rxb = props(26)
      cxc = props(27)
c
c get info from previous values: contained in fxinfo:
      fxc = fxinfo(1)
      fxcr = dabs(fxinfo(2))
      fxnp = fxinfo(3)
c
      rate = depl/dtime
      if(rate.lt.ratelim)then
      rate = ratelim
      endif
```

```
c
      if(temp.gt.et0)then
      emu = emu0 - ed0/(dexp(et0/temp)-one)
      r2m = -temp/(emu*a02)
      r3c = c30*dexp(-a03/temp)*dtime
      r5c0 = cx0*dexp(-a0x/temp)*emu*dtime
      else
c use constants:
      emu = emu0
      r2m = -a02
      r3c = c30*dtime
      r5c0 = cx0*emu*dtime
      endif
c isv's at previous convergence and current guess:
      x1p = max(xi(1),one)
      x2p = max(xi(2),zero)
      x1 = max(xj(1),one)
      x2 = max(xj(2),zero)
c
c growth of next recrystallised volume:
      cldbar = min(x2,one)
      r5c1 = (one-dexp(-cxl*(cldbar)**rxl))
      r5c = r5c0*r5c1*(x1)
c interfacial area
      fxn = fxnp
      rxg = fxc*((fxn/fxc)**rxa)*((one-fxn/fxc)**rxb)*
     & (one+cxc*(one-fxc))
      drxg = rxa*((fxn/fxc)**(rxa-one))*
     & ((one-fxn/fxc)**rxb)*(one+cxc*(one-fxc)) -
     & rxb*((fxn/fxc)**rxa)*((one-fxn/fxc)**(rxb-one))*
     & (one+cxc*(one-fxc))
      fxnr = dabs(r5c*rxg)
```

```
      ffxn = fxn - fxnp - fxnr
c resolve residual
      icount = 0
      do while((icount.lt.15).and.(dabs(ffxn).gt.toler))
      icount = icount+1
      dffxn = one - half*r5c*drxg
      if(dabs(dffxn).lt.toler)then
      dffxn = toler
      endif
      fxn = min(dabs(fxn - ffxn/dffxn),fxc-toler)
      rxg = fxc*((fxn/fxc)**rxa)*((one-fxn/fxc)**rxb)*
     & (one+cxc*(one-fxc))
      drxg = rxa*((fxn/fxc)**(rxa-one))*
     & ((one-fxn/fxc)**rxb)*(one+cxc*(one-fxc)) -
     & rxb*((fxn/fxc)**rxa)*((one-fxn/fxc)**(rxb-one))*
     & (one+cxc*(one-fxc))
      fxnr = dabs(r5c*rxg)
      ffxn = fxn - fxnp - fxnr
      end do
c partial : change of fxn with respect to x1 and x2:
c partial gradients d(fxn)/d(x1)
      ddfxdr = (one-r5c*drxg)
      if(dabs(ddfxdr).lt.toler)then
      ddfxdr = toler
      endif
      dfxndx1 = (r5c0*r5c1*rxg)/ddfxdr
      dmdx2 = zero
      if(x2.lt.one)then
      dmdx2 = one
      endif
      dr5c1dm = rxl*cxl*dexp(-cxl*(cldbar)**rxl)*
     & (cldbar)**(rxl-one)
```

```
      dfxndm = (r5c0*dr5c1dm*x1*rxg)/ddfxdr
c partial gradients d(fxn)/d(x2)
      dfxndx2 = dfxndm*dmdx2
c partial d(fxn)/d(fxc)
      drxgdfxc = ((fxn/fxc)**rxa)*((one-fxn/fxc)**rxb)*
     & (one+cxc*(one-fxc))
     & - rxa*((fxn/fxc)**rxa)*((one-fxn/fxc)**rxb)*
     & (one+cxc*(one-fxc))
     & + rxb*((fxn/fxc)**(rxa+one))*((one-fxn/fxc)**(rxb-one))*
     & (one+cxc*(one-fxc))
     & - cxc*fxc*((fxn/fxc)**rxa)*((one-fxn/fxc)**rxb)
      dfxndfxc = r5c*drxgdfxc
c residual equations on the isv values:
      c2 = c20*(rate/rate02)**r2m
      dc2de = c20*r2m*((rate/rate02)**(r2m-one))/
     & (dtime*rate02)
      sqx1p = dsqrt(x1p)
      sqx1 = dsqrt(x1)
      hx2 = cld
      hx1temp = -r3c*(x1**r3+x1p**r3)
      hx1 = (cg)*(x2)**rg+c1*sqx1-c2*x1
      if(fxn.ge.fxc)then
      rx0 = zero
      else
      rx0 = one/(fxc - fxn)
      endif
      rfxc = fxcr*rx0
      drx = rfxc*rx0
      r1 = x1-x1p-hx1*depl-hx1temp+x1*rfxc
      r2 = x2-x2p-hx2*depl+x2*rfxc
      r = (/ r1 , r2 /)
c partial : change in residual with respect to x1 and x2:
```

```
      dhrdrtemp=-r3*r3c*x1**(r3-one)
      dhrdr=half*c1/sqx1-c2
c partial gradients d(fr1)/d(x1)
      dr1dr0=one-dhrdr*depl-dhrdrtemp+rfxc
      dr1dx1=dr1dr0+x1*drx*dfxndx1
c partial gradients d(fr1)/d(x2)
      dr1dx2=-depl*rg*(cg)*(x2)**(rg-one)+
     & x1*drx*dfxndx2
c partial gradients d(f2)/d(x1)
      dr2dx1 = x2*drx*dfxndx1
c partial gradients d(f2)/d(x2)
      dr2dl0= one + rfxc
      dr2dx2 = dr2dl0 + x2*drx*dfxndx2
      drdxj=reshape((/dr1dx1,dr2dx1,dr1dx2,dr2dx2/),(/2,2/))
c
      dr1de = hx1 - depl*dc2de*x1
      dr2de = hx2
      reps = (/dr1de,dr2de/)
c exchange new supplementary info using fxinfo:
      fxnvec(1) = fxn
      fxnvec(2) = fxnr
      fxnvec(3) = dfxndx1
      fxnvec(4) = dfxndx2
      fxnvec(5) = dfxndfxc
c
      return
      end
```

Appendix G

Internal State Contours for Recrystallisation during Axi-symmetric Compression

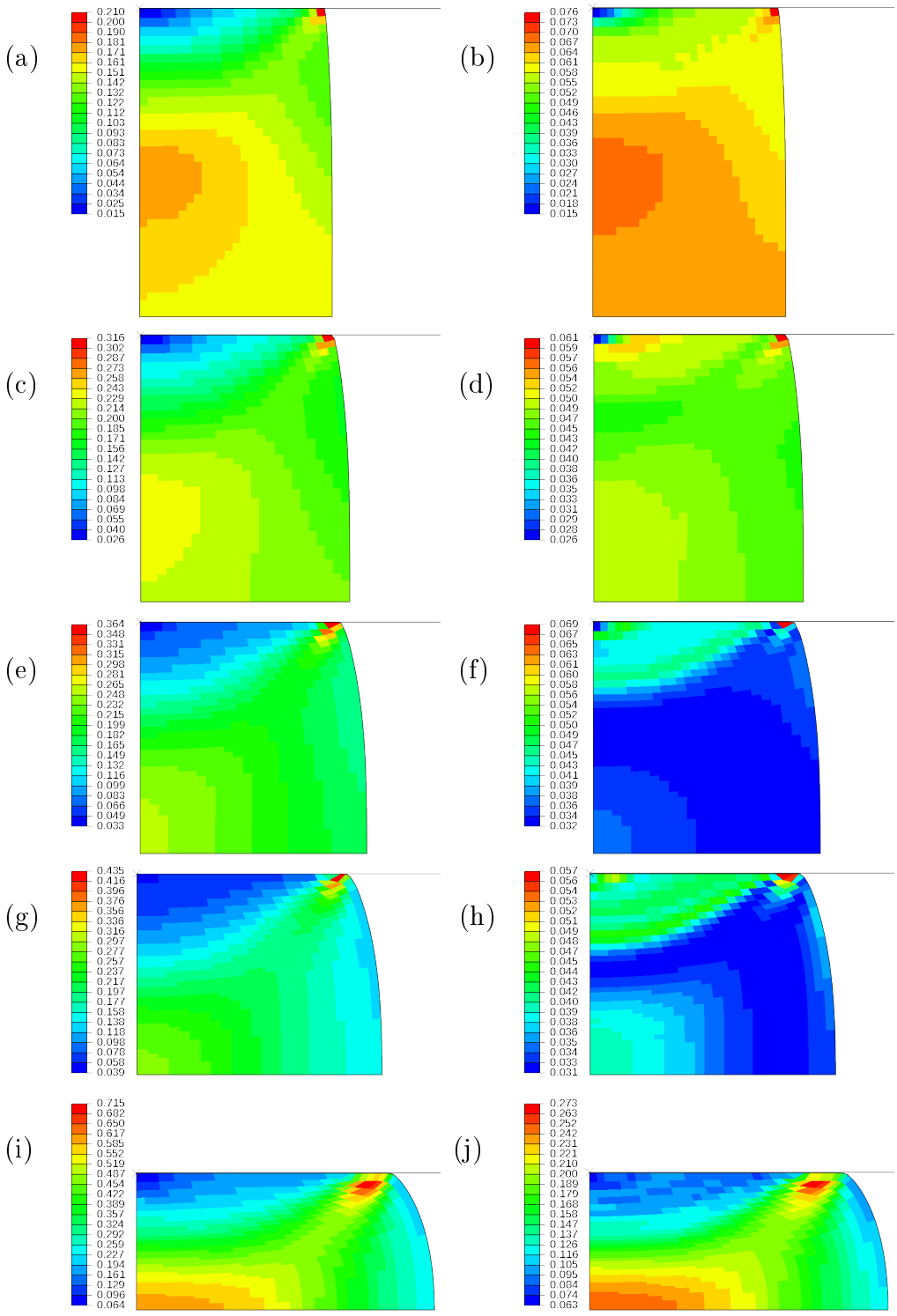

Figure G.1: Equivalent plastic strain distributions in the axi-symmetric billet at (a) 0.5478s, (b) 10.1728s, (c) 10.5049s, (d) 19.9072s, (e) 20.1426s, (f) 29.4863s, (g) 29.6836s, (h) 38.999s, (i) 39.3994s and (j) 10 seconds after the final reduction.

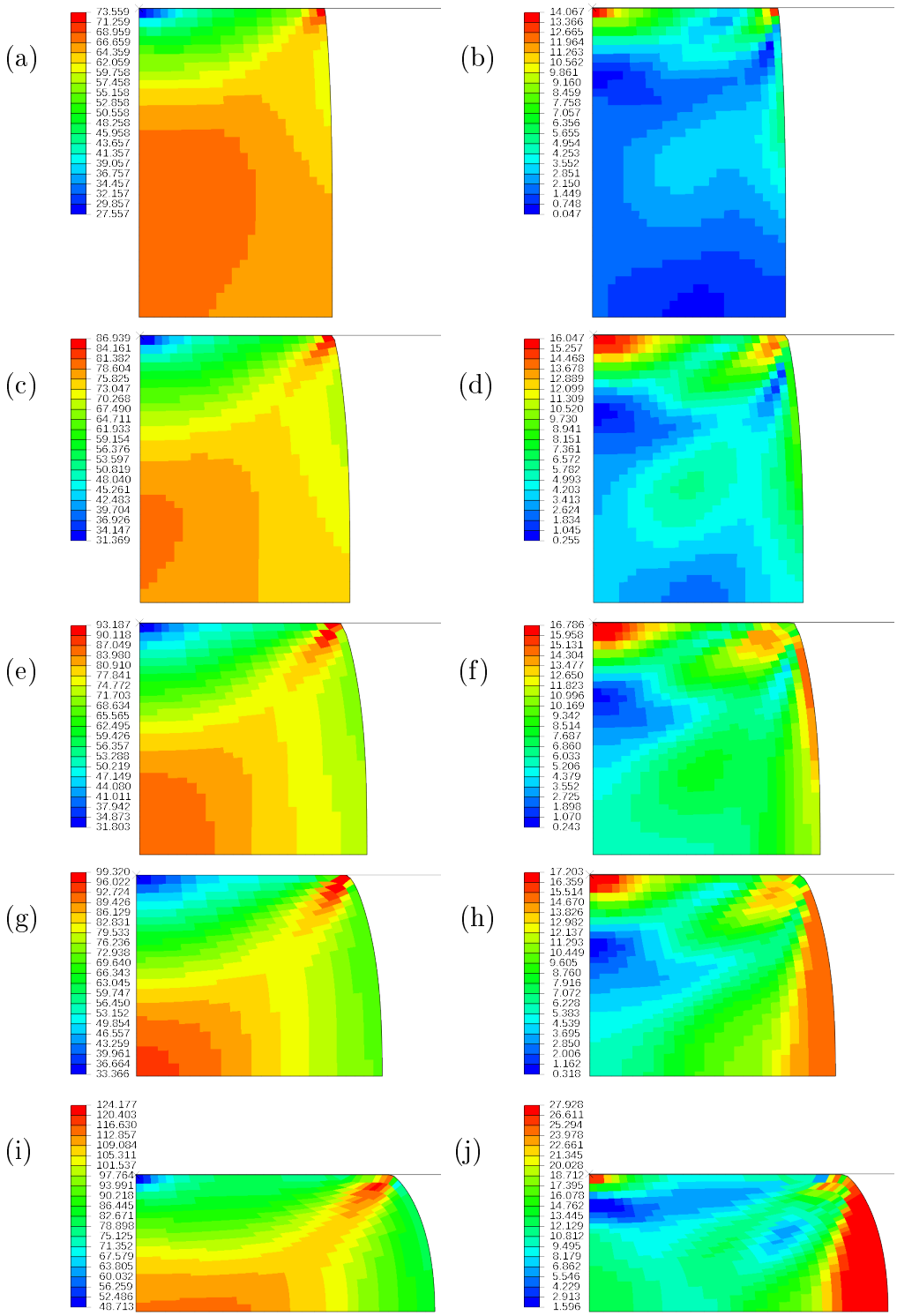

Figure G.2: Von Mises stress distributions in the axi-symmetric billet at (a) 0.5478s, (b) 10.1728s, (c) 10.5049s, (d) 19.9072s, (e) 20.1426s, (f) 29.4863s, (g) 29.6836s, (h) 38.999s, (i) 39.3994s and (j) 10 seconds after the final reduction.

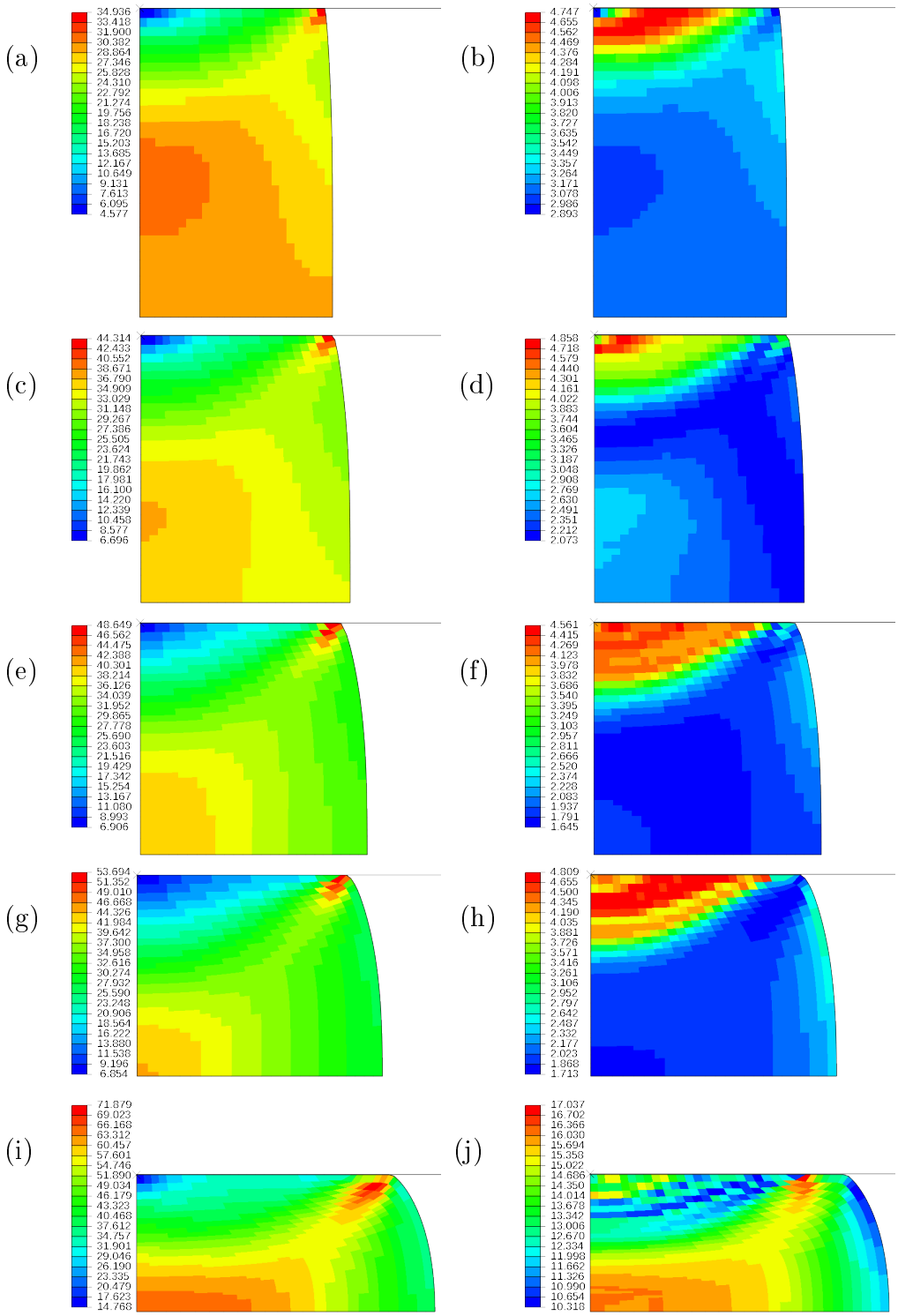

Figure G.3: Dislocation density ratio distributions in the axi-symmetric billet at (a) 0.5478s, (b) 10.1728s, (c) 10.5049s, (d) 19.9072s, (e) 20.1426s, (f) 29.4863s, (g) 29.6836s, (h) 38.999s, (i) 39.3994s and (j) 10 seconds after the final reduction.

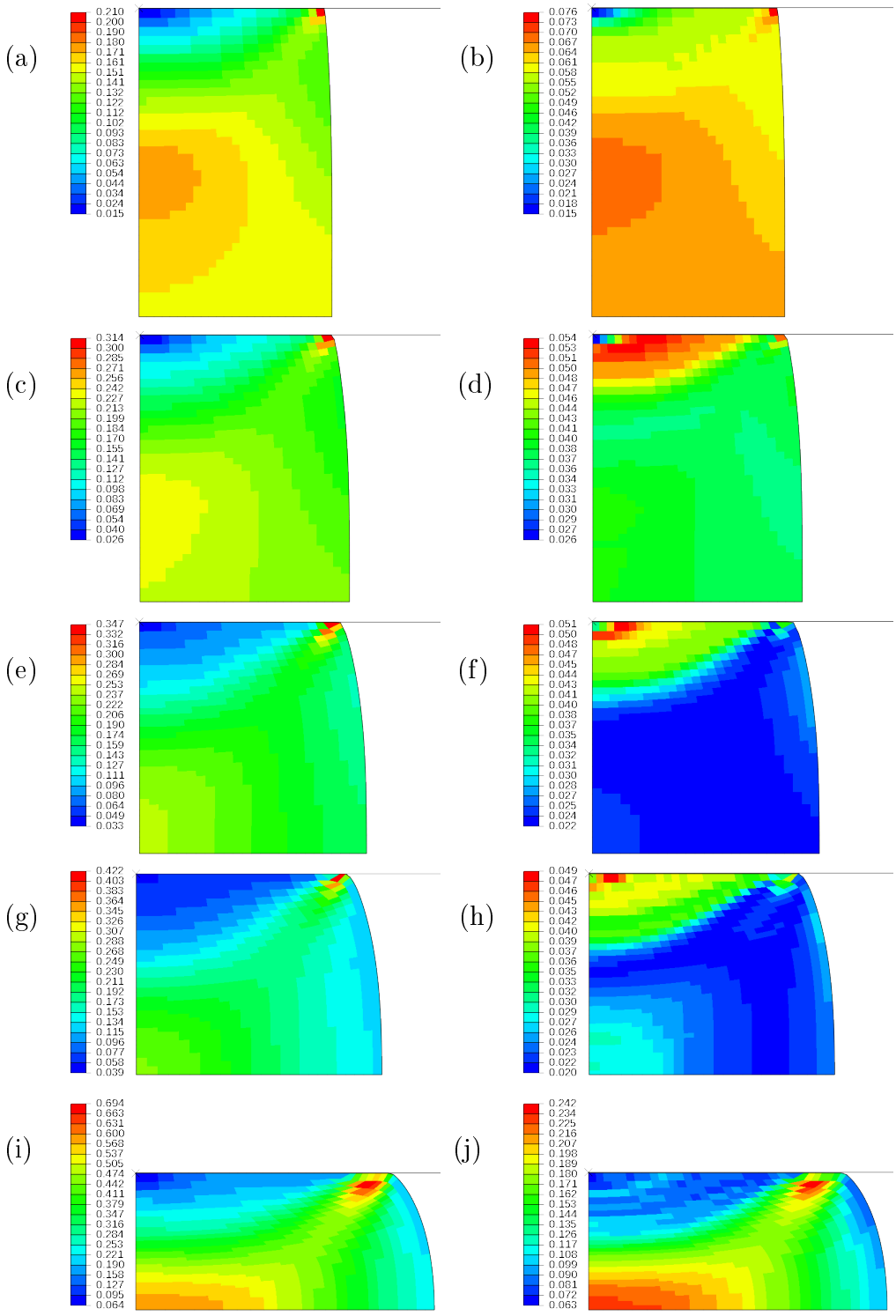

Figure G.4: Average slip plane lattice misorientation distributions in the axi-symmetric billet at (a) 0.5478s, (b) 10.1728s, (c) 10.5049s, (d) 19.9072s, (e) 20.1426s, (f) 29.4863s, (g) 29.6836s, (h) 38.999s, (i) 39.3994s and (j) 10 seconds after the final reduction.

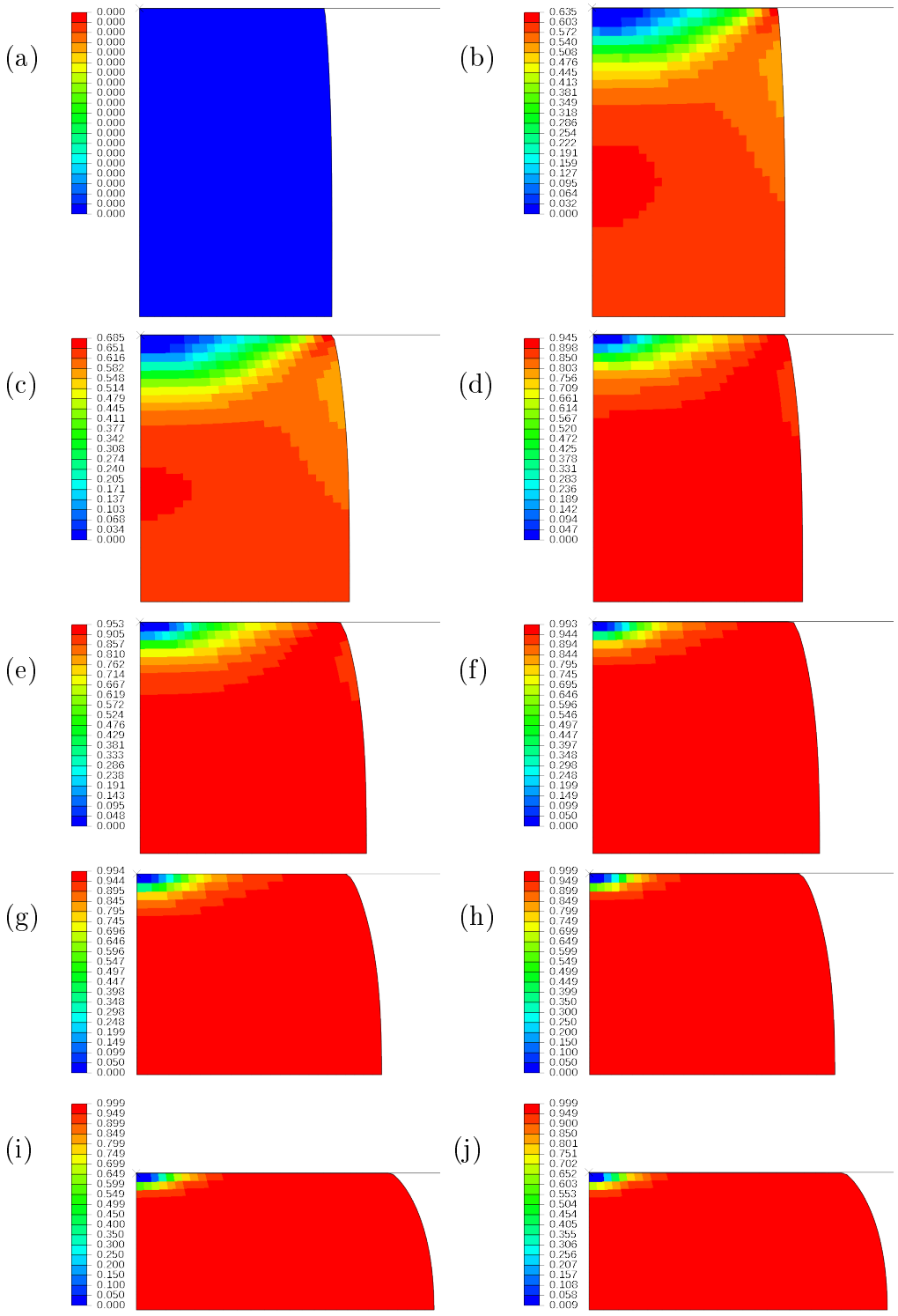

Figure G.5: Volume fraction recrystallised at least once (f_{x_1}) in the axi-symmetric billet at (a) 0.5478s, (b) 10.1728s, (c) 10.5049s, (d) 19.9072s, (e) 20.1426s, (f) 29.4863s, (g) 29.6836s, (h) 38.999s, (i) 39.3994s and (j) 10 seconds after the final reduction.

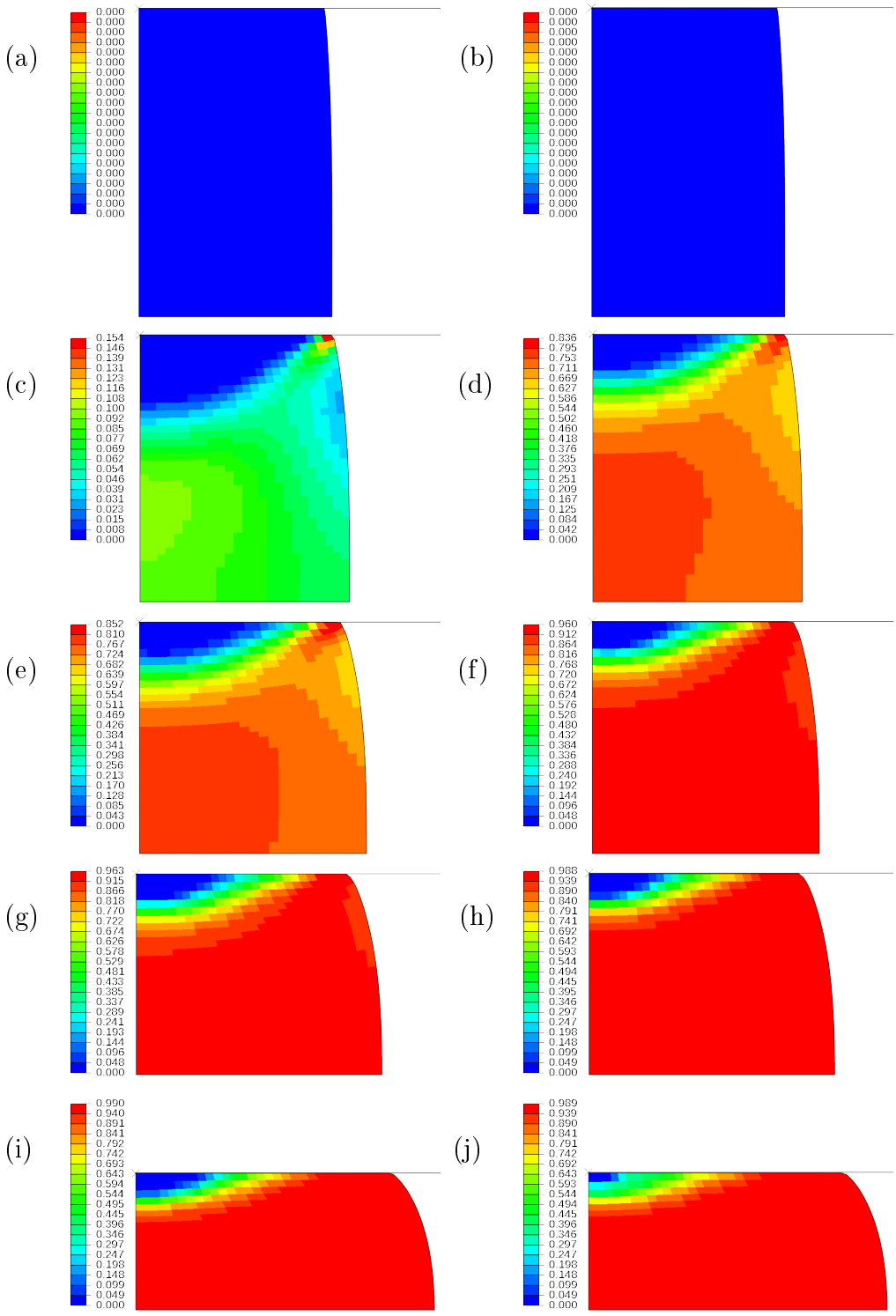

Figure G.6: Volume fraction recrystallised at least twice ($f_{\mathrm{x_2}}$) in the axi-symmetric billet at (a) 0.5478s, (b) 10.1728s, (c) 10.5049s, (d) 19.9072s, (e) 20.1426s, (f) 29.4863s, (g) 29.6836s, (h) 38.999s, (i) 39.3994s and (j) 10 seconds after the final reduction.

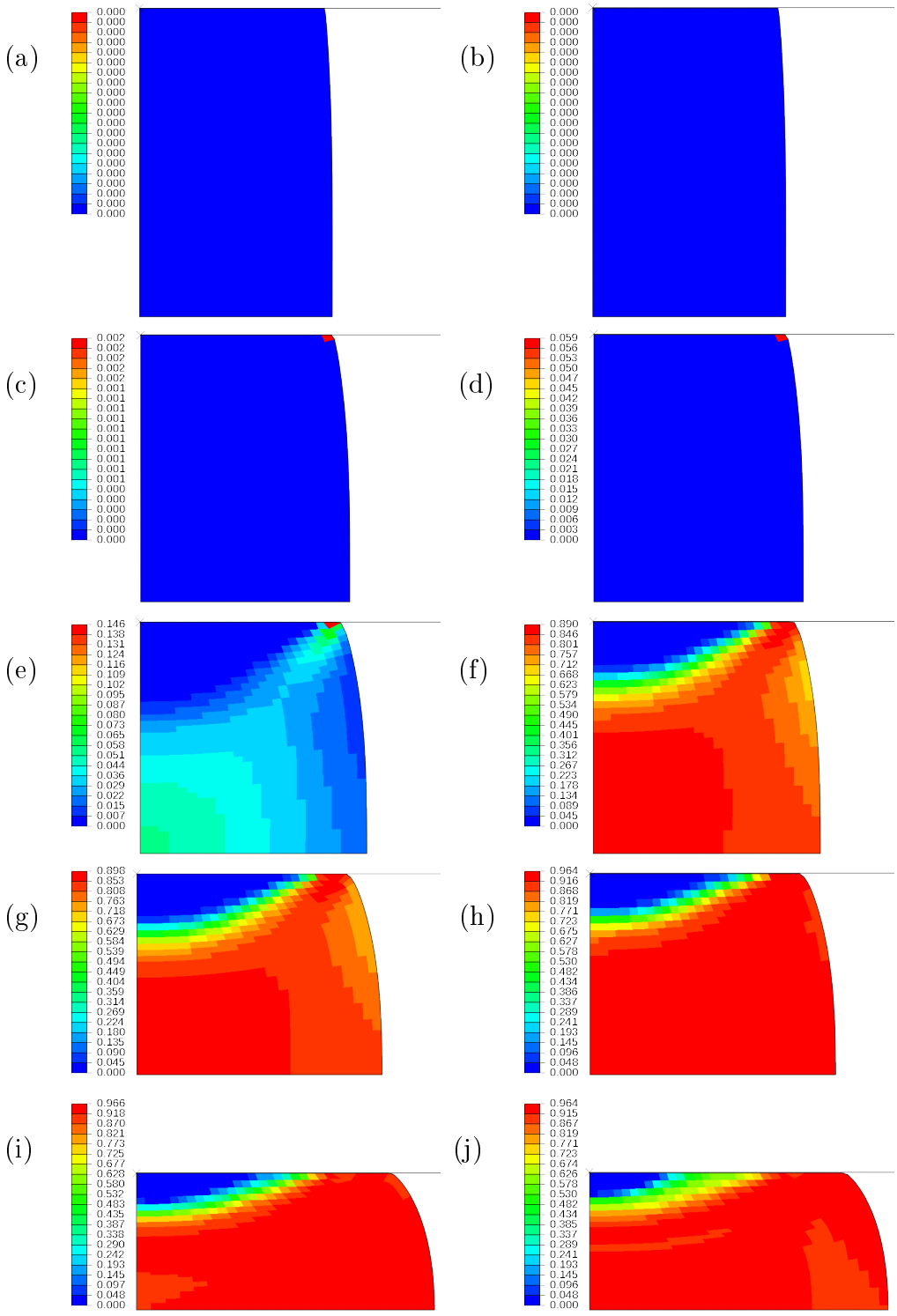

Figure G.7: Volume fraction recrystallised at least three times (f_{x_3}) in the axi-symmetric billet at (a) 0.5478s, (b) 10.1728s, (c) 10.5049s, (d) 19.9072s, (e) 20.1426s, (f) 29.4863s, (g) 29.6836s, (h) 38.999s, (i) 39.3994s and (j) 10 seconds after the final reduction.

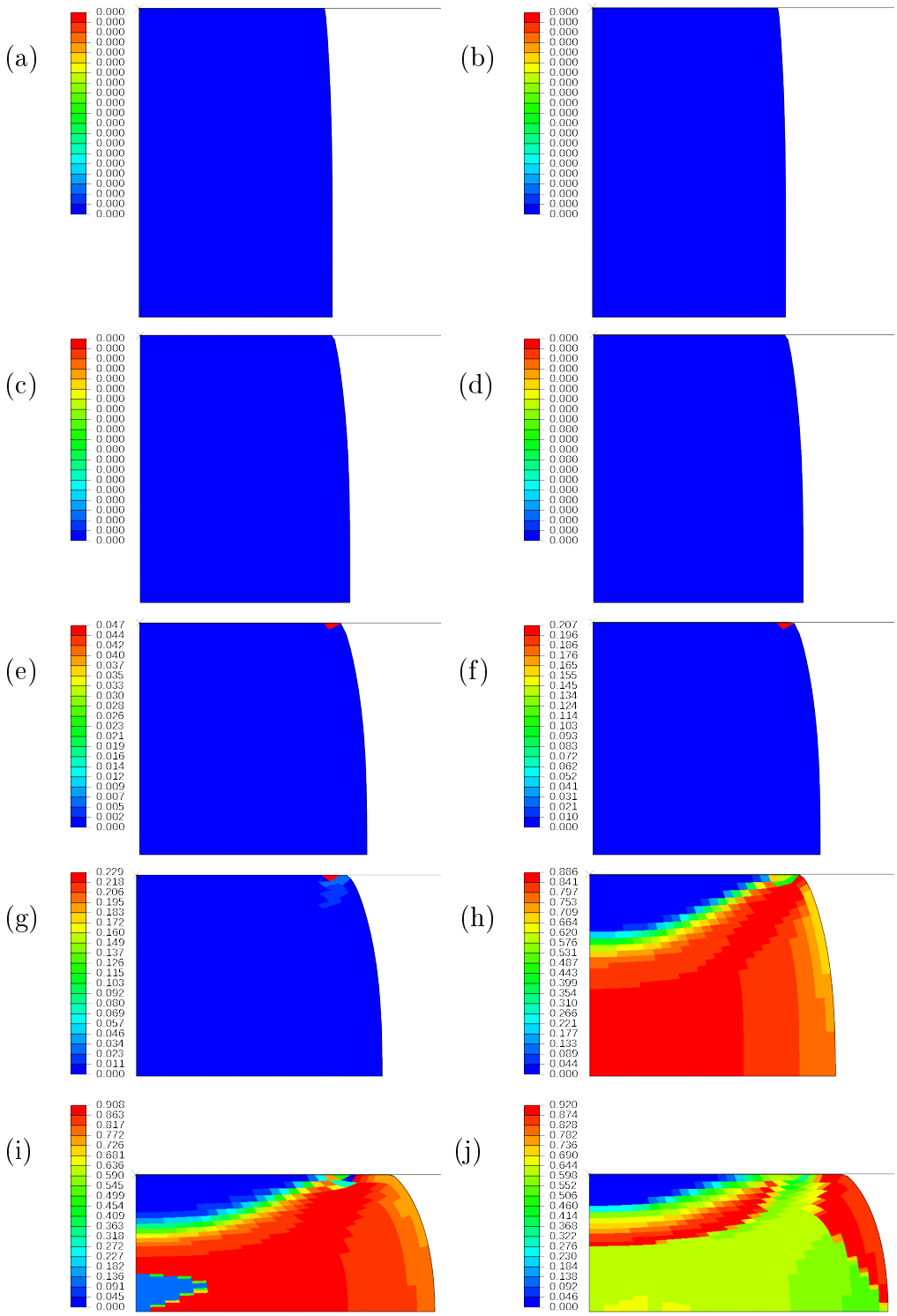

Figure G.8: Volume fraction recrystallised at least four times (f_{x_4}) in the axi-symmetric billet at (a) 0.5478s, (b) 10.1728s, (c) 10.5049s, (d) 19.9072s, (e) 20.1426s, (f) 29.4863s, (g) 29.6836s, (h) 38.999s, (i) 39.3994s and (j) 10 seconds after the final reduction. The discontinuous contours in (i) and (j) are as a result of a state variable shift once the original material f_{x_0}has fully recrystallised ($f_{\mathrm{x}_1} \geq 0.999$).

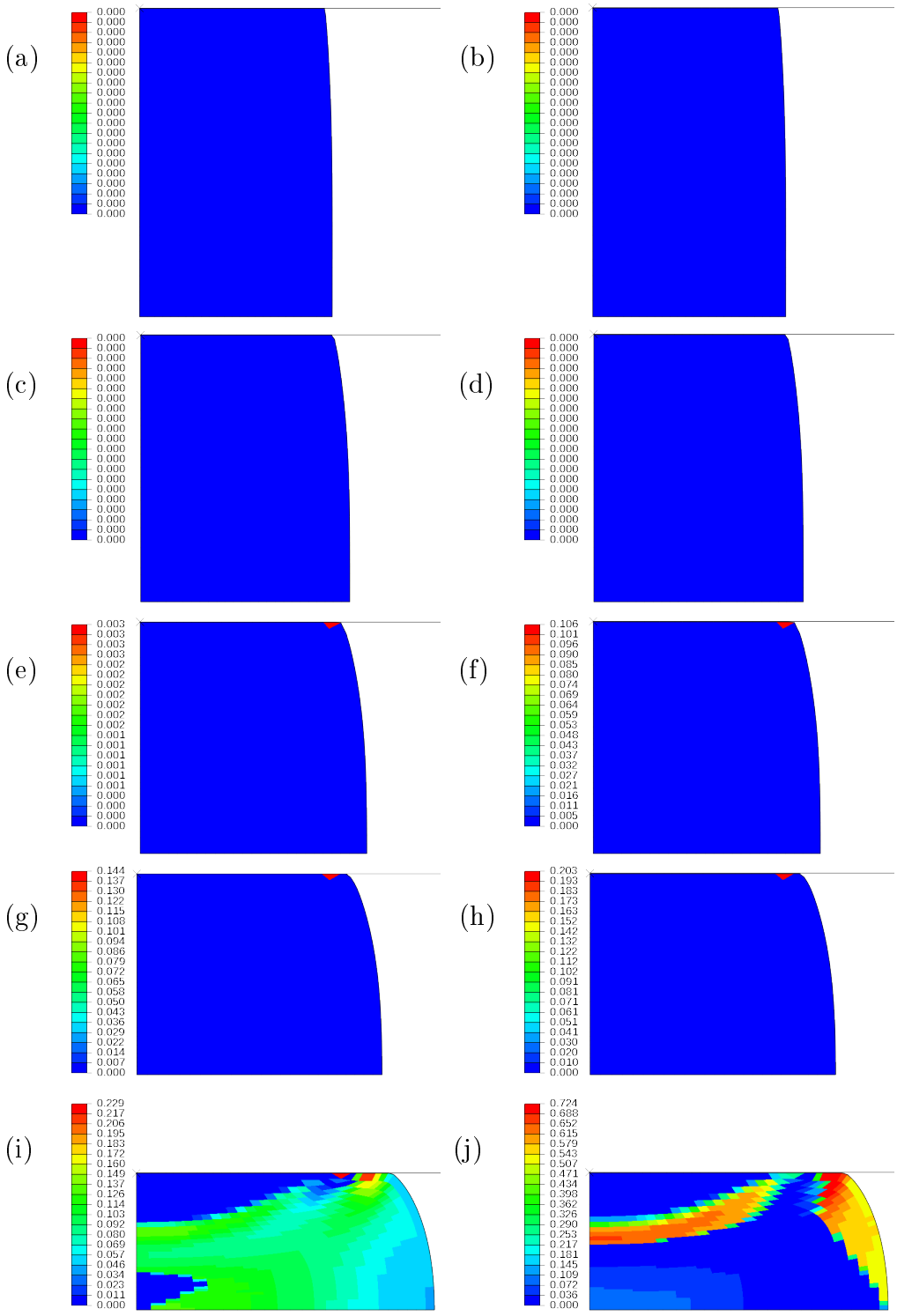

Figure G.9: Volume fraction recrystallised at least five times (f_{x_5}) in the axi-symmetric billet at (a) 0.5478s, (b) 10.1728s, (c) 10.5049s, (d) 19.9072s, (e) 20.1426s, (f) 29.4863s, (g) 29.6836s, (h) 38.999s, (i) 39.3994s and (j) 10 seconds after the final reduction. The discontinuous contours in (i) and (j) are as a result of a state variable shift once the original material f_{x_0}has fully recrystallised ($f_{x_1} \geq 0.999$).

Appendix H

Roll Schedule VI Internal State Evolution

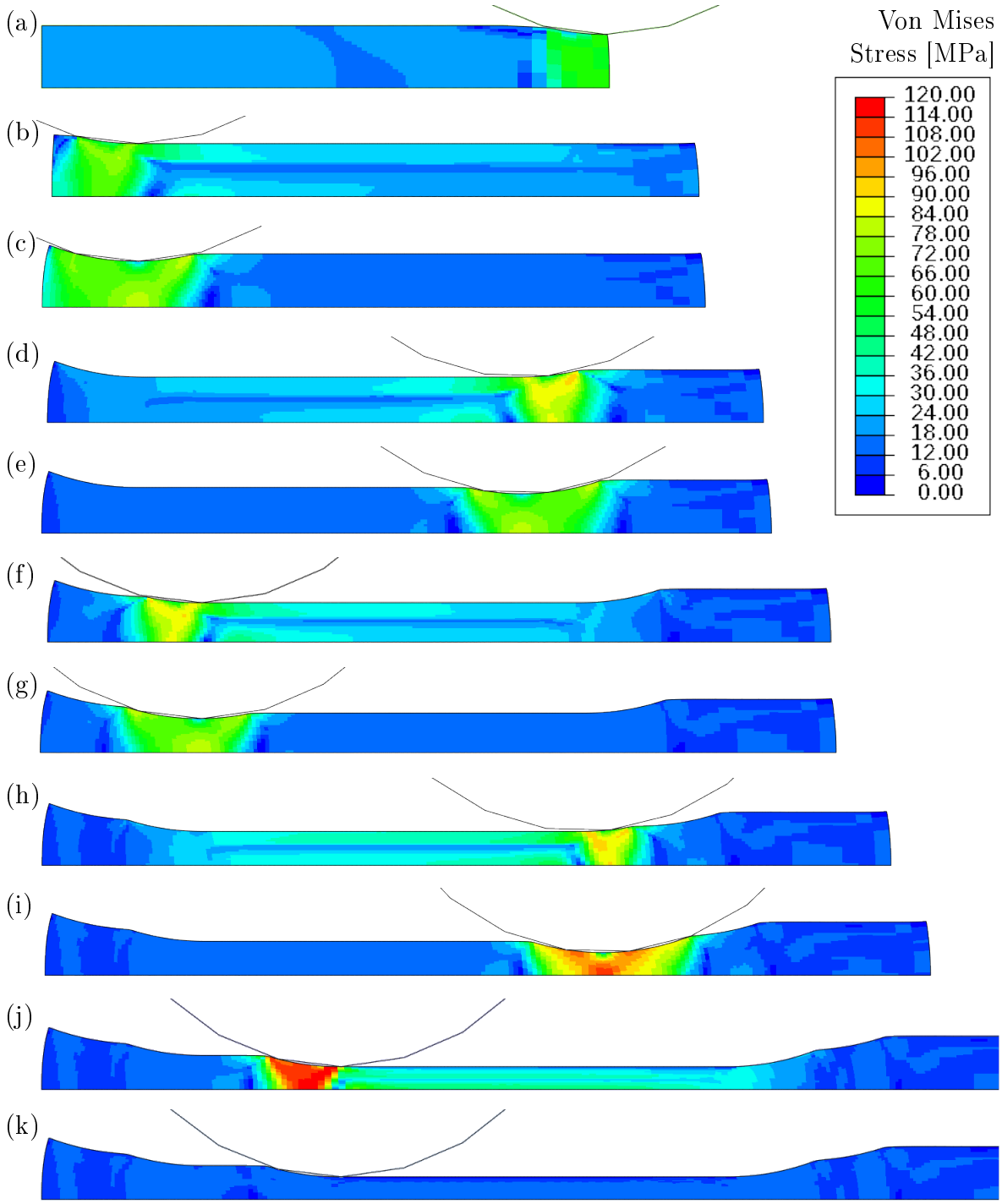

Figure H.1: Von Mises Stress contours for Schedule *IV* at (a) 1s, (b) 3.5s, (c) 13.5s, (d) 15s, (e) 25s, (f) 26.0714s, (g) 36.0714s, (h) 36.9047s, (i) 46.9047s, (j) 47.5864s and (k) 57.5865s

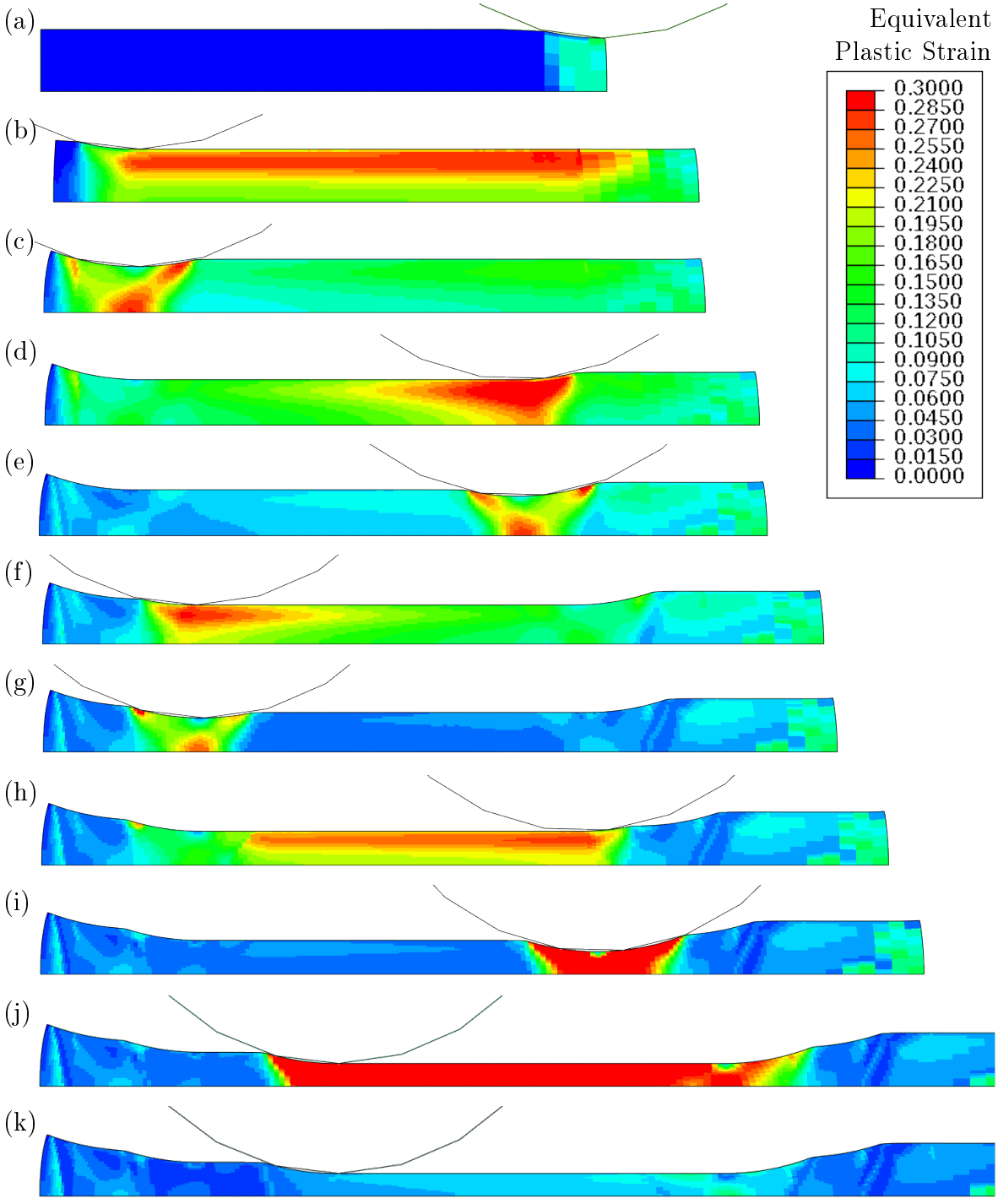

Figure H.2: Equivalent plastic strain contours for Schedule *IV* at (a) 1s, (b) 3.5s, (c) 13.5s, (d) 15s, (e) 25s, (f) 26.0714s, (g) 36.0714s, (h) 36.9047s, (i) 46.9047s, (j) 47.5864s and (k) 57.5865s

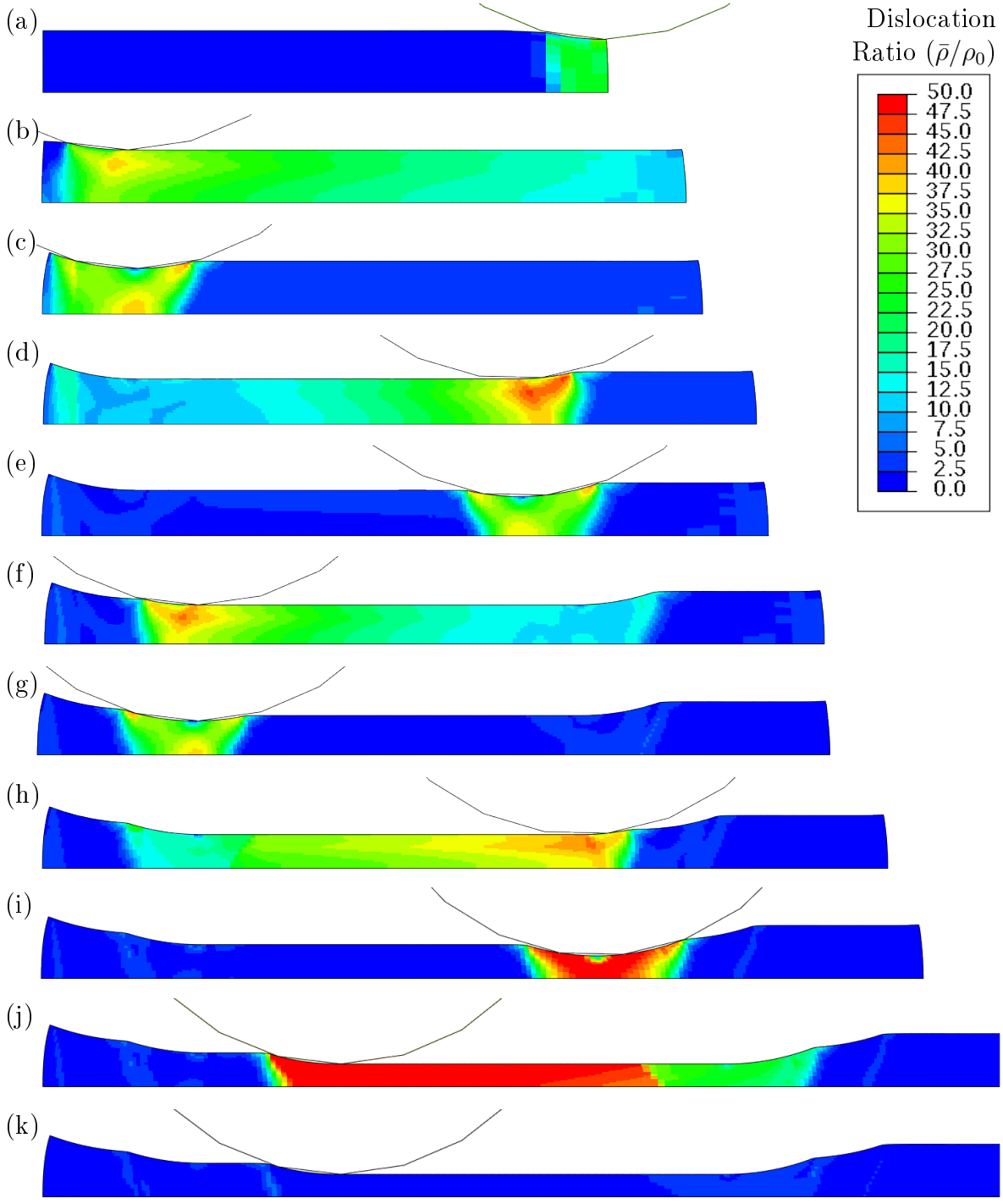

Figure H.3: Volume fraction averaged dislocation density ratio ($\bar{\rho}/\rho_0$) contours for Schedule *IV* at (a) 1s, (b) 3.5s, (c) 13.5s, (d) 15s, (e) 25s, (f) 26.0714s, (g) 36.0714s, (h) 36.9047s, (i) 46.9047s, (j) 47.5864s and (k) 57.5865s

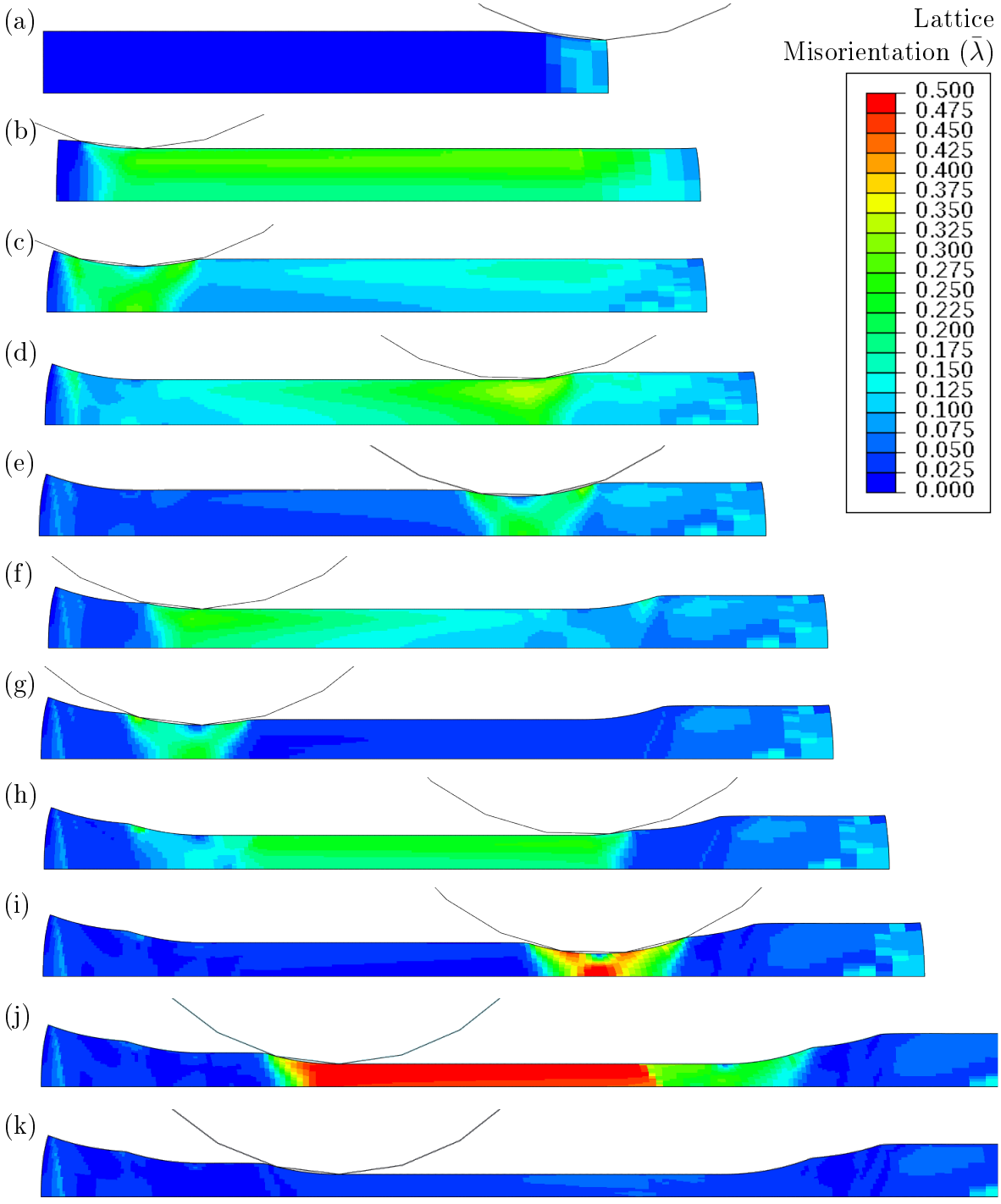

Figure H.4: Volume fraction averaged slip plane lattice misorientation ($\bar{\lambda}$) contours for Schedule *IV* at (a) 1s, (b) 3.5s, (c) 13.5s, (d) 15s, (e) 25s, (f) 26.0714s, (g) 36.0714s, (h) 36.9047s, (i) 46.9047s, (j) 47.5864s and (k) 57.5865s

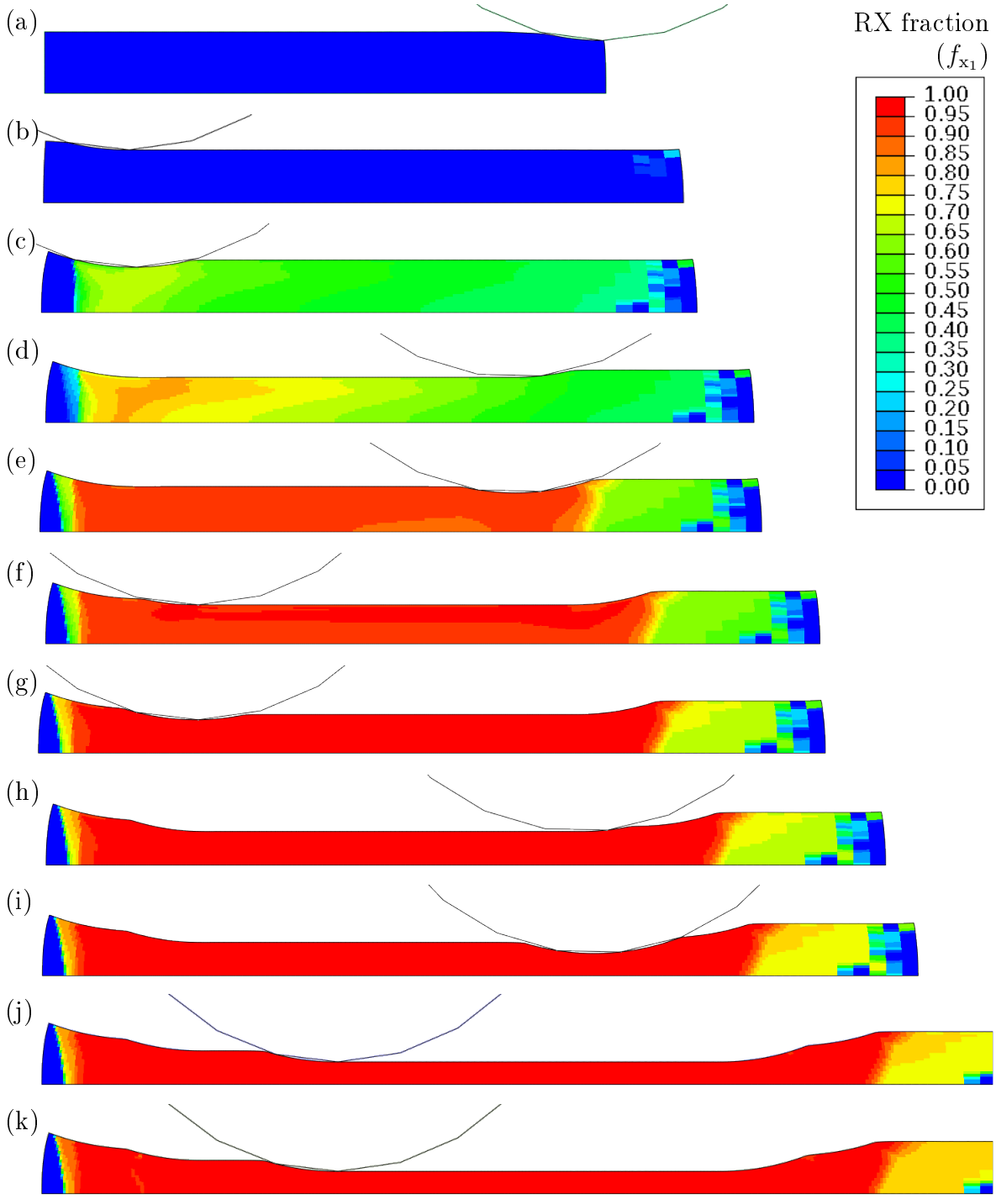

Figure H.5: Contours of f_{x_1} s for Schedule *IV* at (a) 1s, (b) 3.5s, (c) 13.5s, (d) 15s, (e) 25s, (f) 26.0714s, (g) 36.0714s, (h) 36.9047s, (i) 46.9047s, (j) 47.5864s and (k) 57.5865s

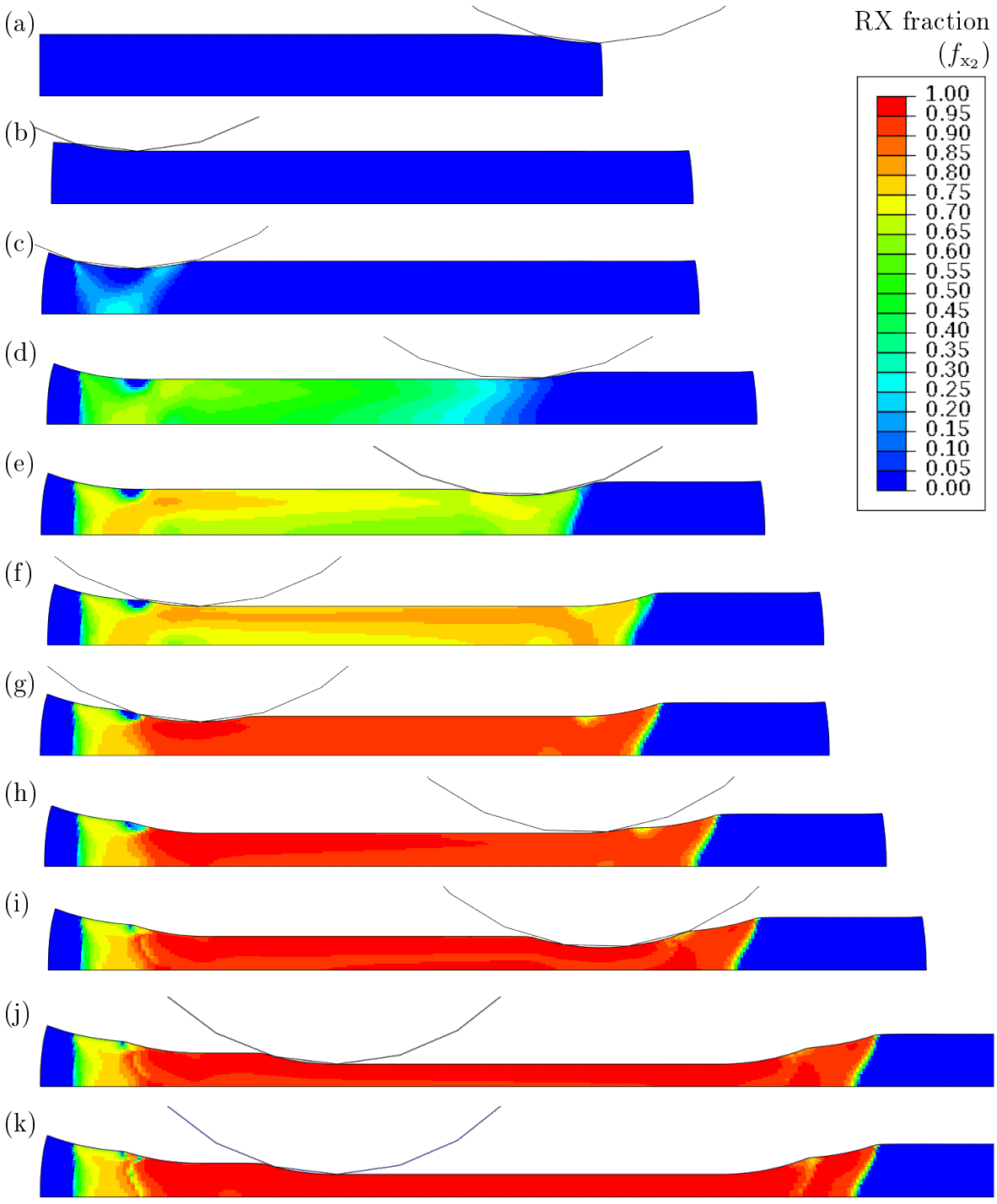

Figure H.6: Contours of f_{x_2} for Schedule *IV* at (a) 1s, (b) 3.5s, (c) 13.5s, (d) 15s, (e) 25s, (f) 26.0714s, (g) 36.0714s, (h) 36.9047s, (i) 46.9047s, (j) 47.5864s and (k) 57.5865s

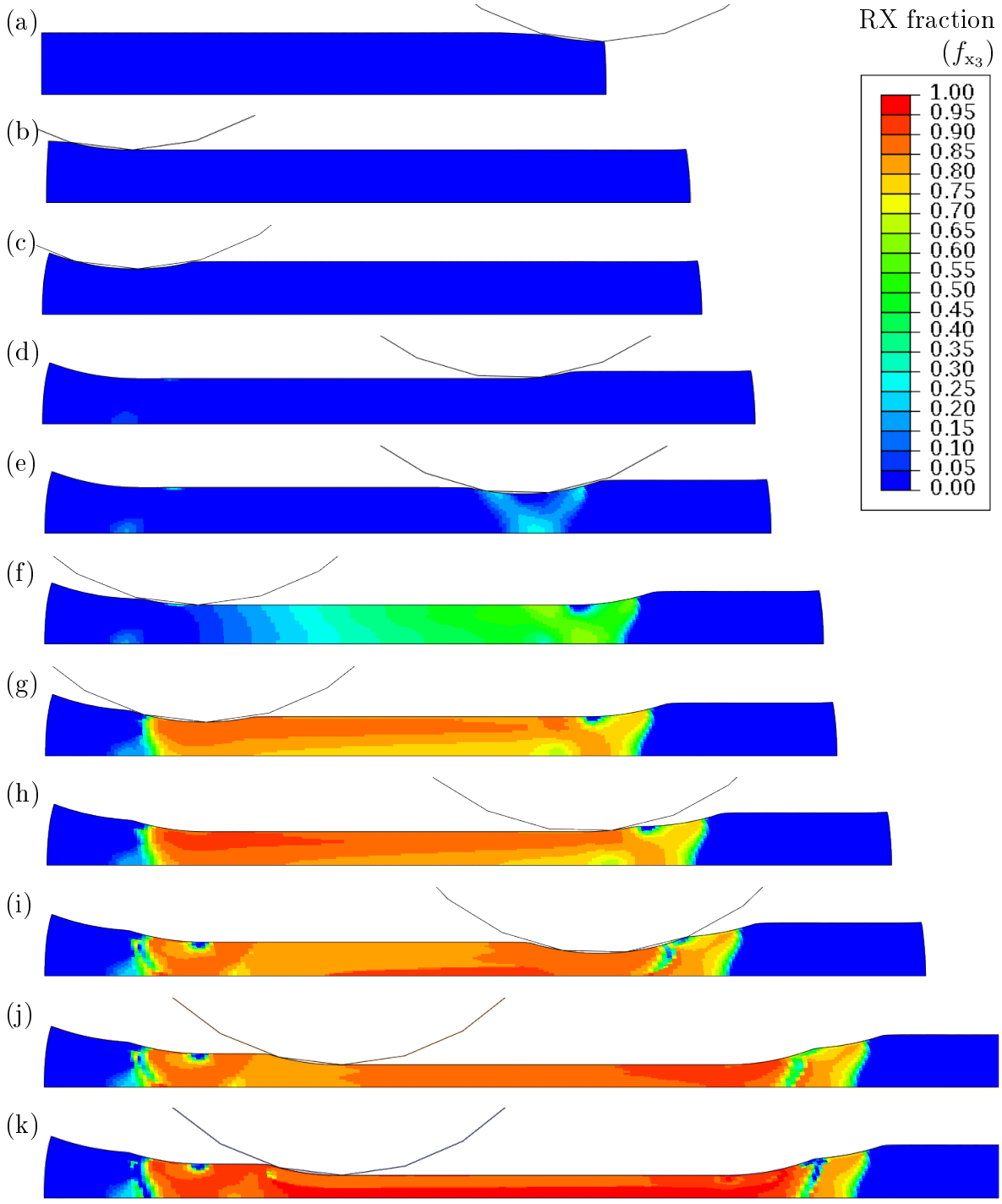

Figure H.7: Contours of f_{x_3} for Schedule *IV* at (a) 1s, (b) 3.5s, (c) 13.5s, (d) 15s, (e) 25s, (f) 26.0714s, (g) 36.0714s, (h) 36.9047s, (i) 46.9047s, (j) 47.5864s and (k) 57.5865s

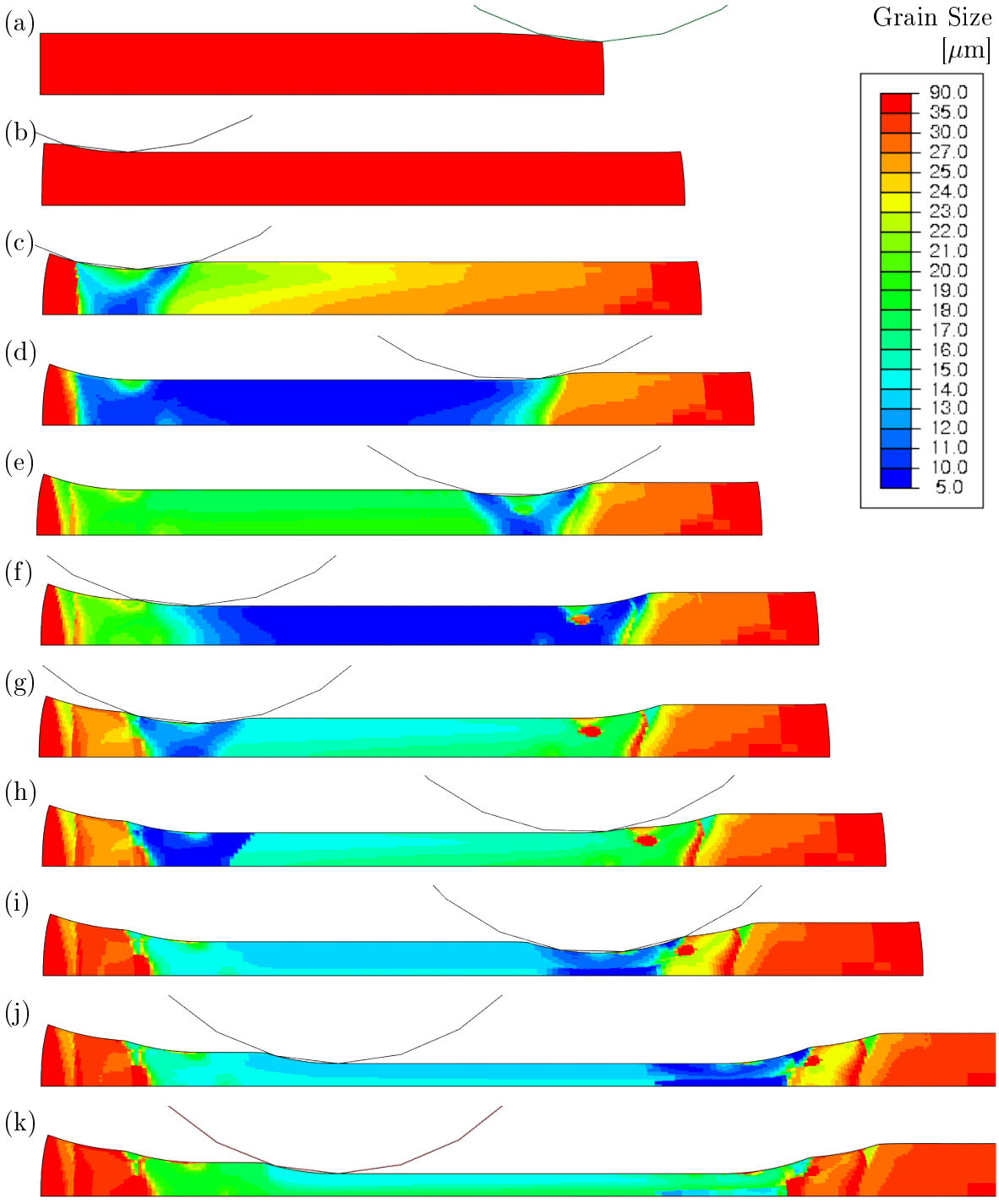

Figure H.8: Volume fraction averaged grain size contours for Schedule *IV* at (a) 1s, (b) 3.5s, (c) 13.5s, (d) 15s, (e) 25s, (f) 26.0714s, (g) 36.0714s, (h) 36.9047s, (i) 46.9047s, (j) 47.5864s and (k) 57.5865s

Appendix I

Through Thickness Variation of Simulated HSLA Steel Roughing Schedules

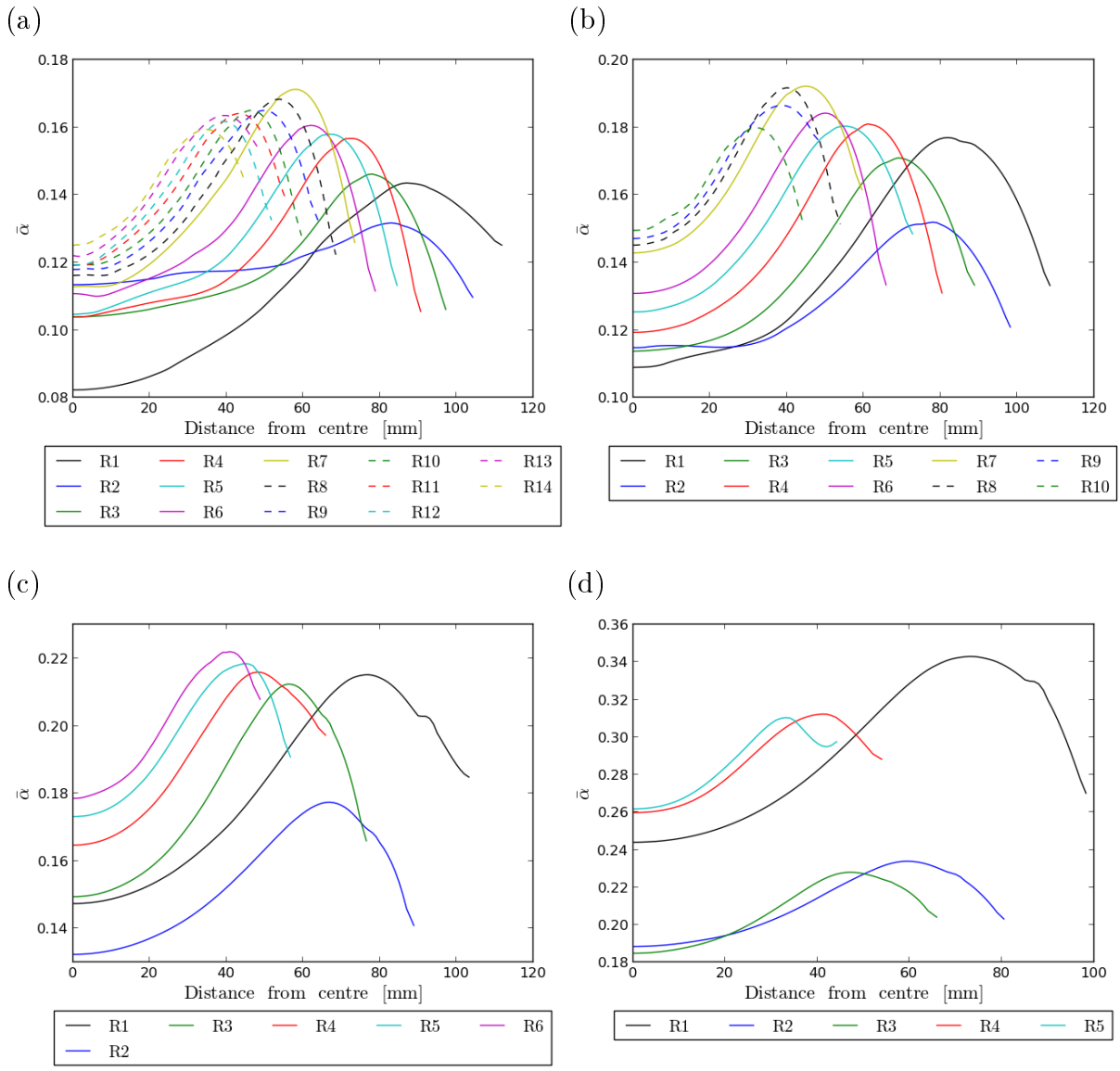

Figure I.1: Through thickness equivalent plastic strains 350mm away from the roller directly after each roll pass step modelled for (a) $14\times7\%$, (b)$10\times10\%$, (c) $6\times15\%$ and (d) $5\times20\%$ reduction roll pass sequences.

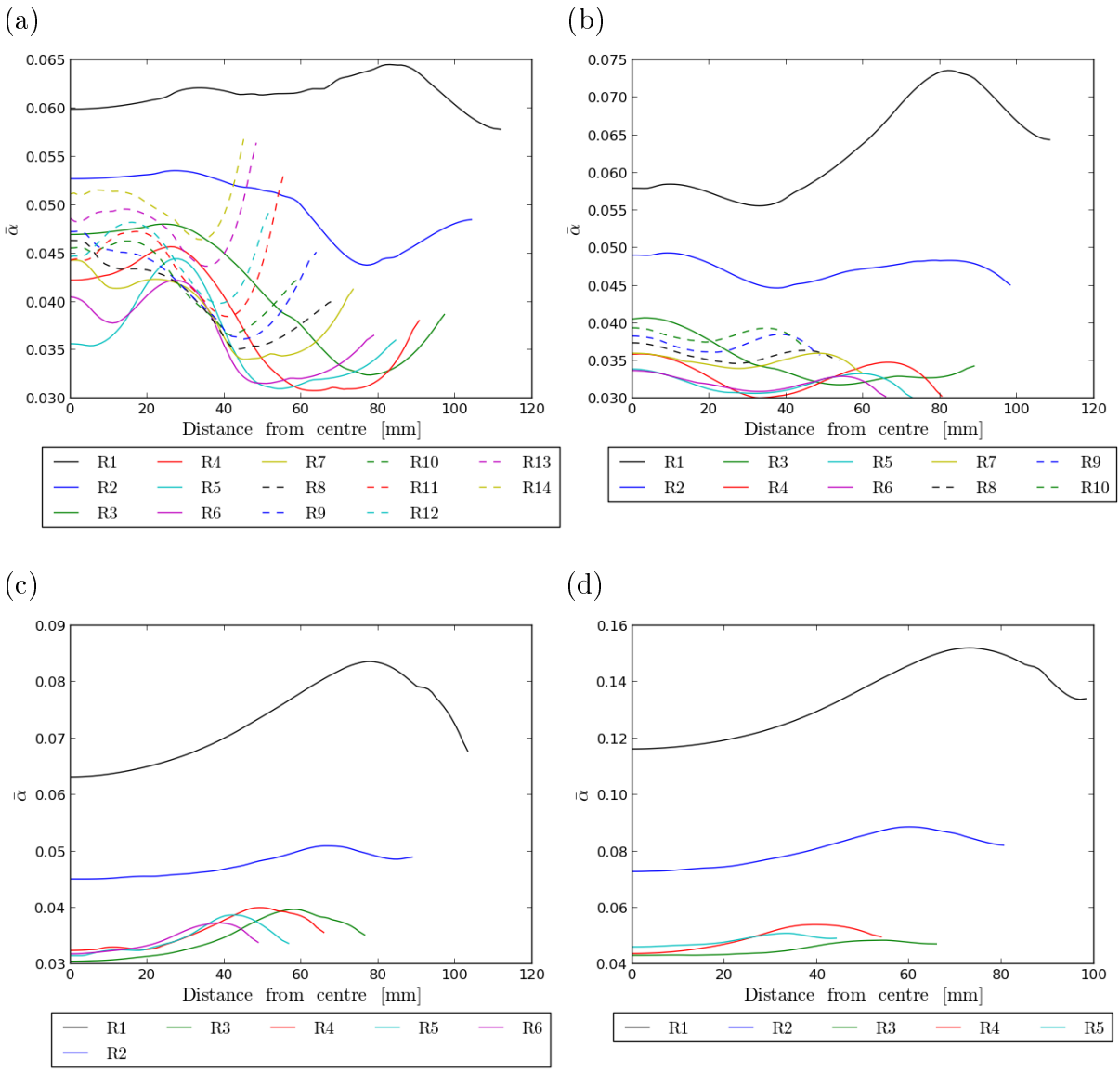

Figure I.2: Through thickness equivalent plastic strain 350mm away from the roller 10 seconds after each roll pass step modelled for (a) $14 \times 7\%$, (b)$10 \times 10\%$, (c) $6 \times 15\%$ and (d) $5 \times 20\%$ reduction roll pass sequences.

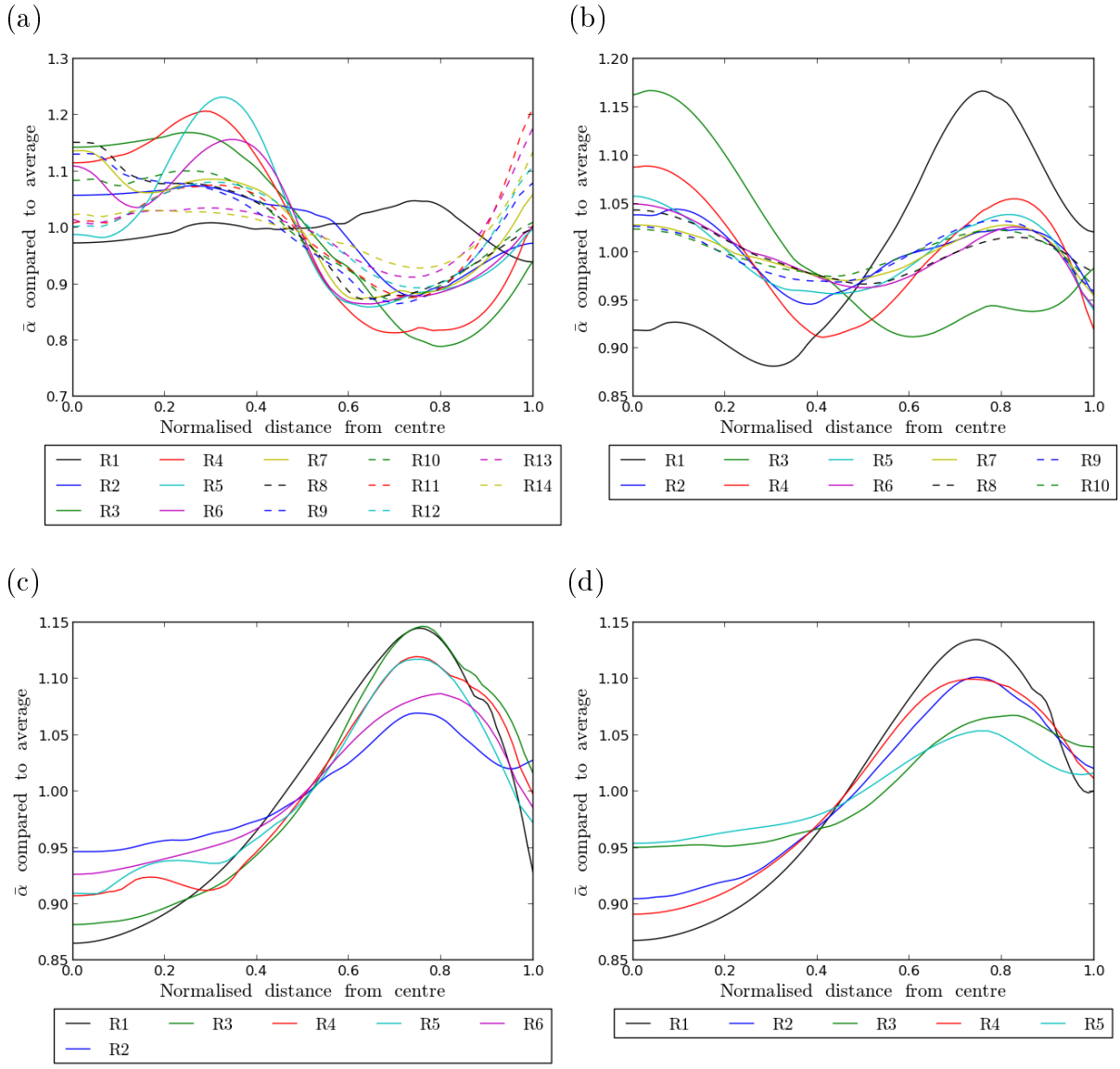

Figure I.3: The averaged data in Figure I.2 over the normalised distance from the centre. (a) $14 \times 7\%$, (b)$10\times10\%$, (c) $6\times15\%$ and (d) $5\times20\%$.

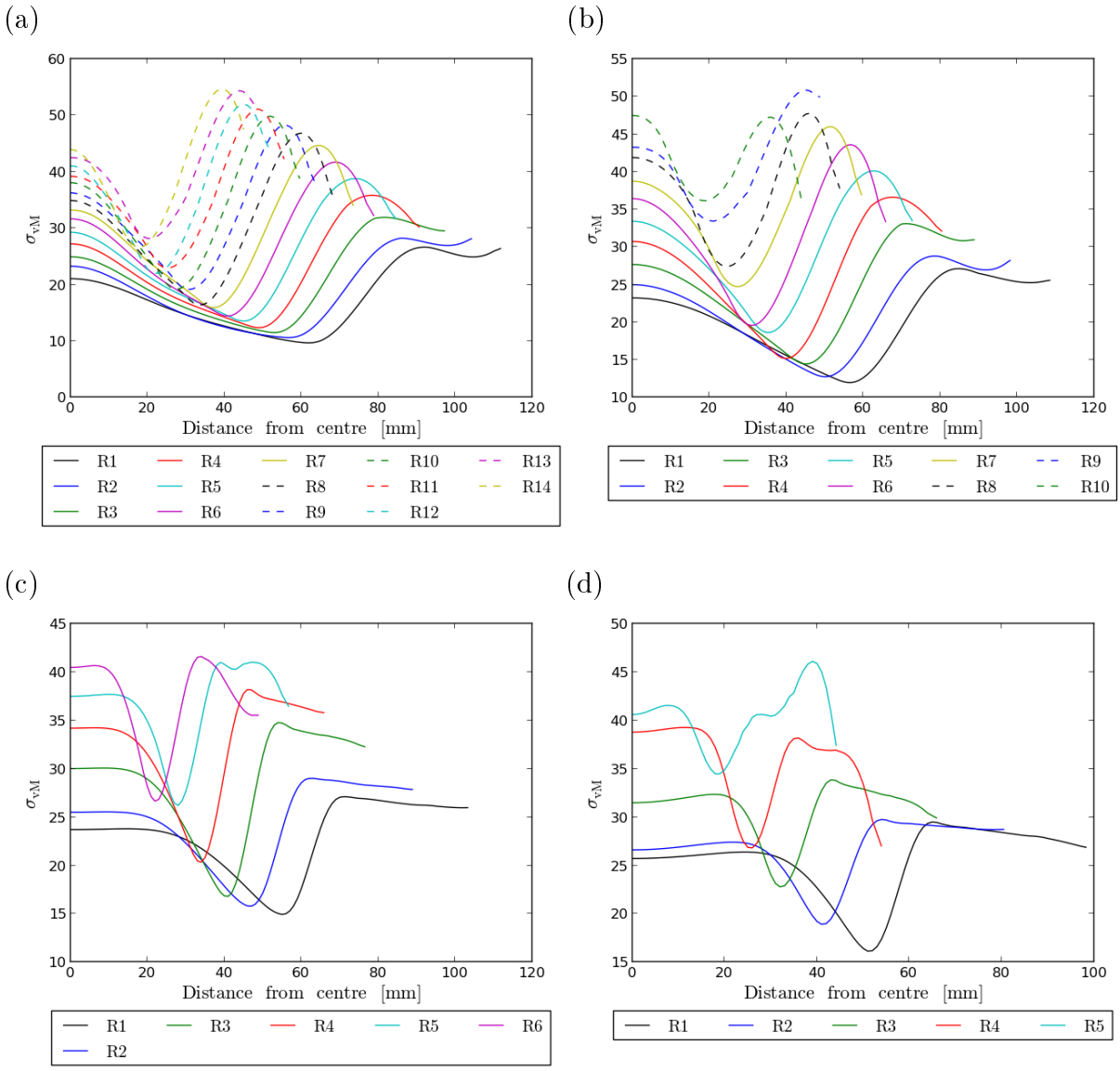

Figure I.4: Through thickness residual stresses 350mm away from the roller directly after each roll pass step modelled for (a) 14 × 7%, (b)10×10%, (c) 6×15% and (d) 5×20% reduction roll pass sequences.

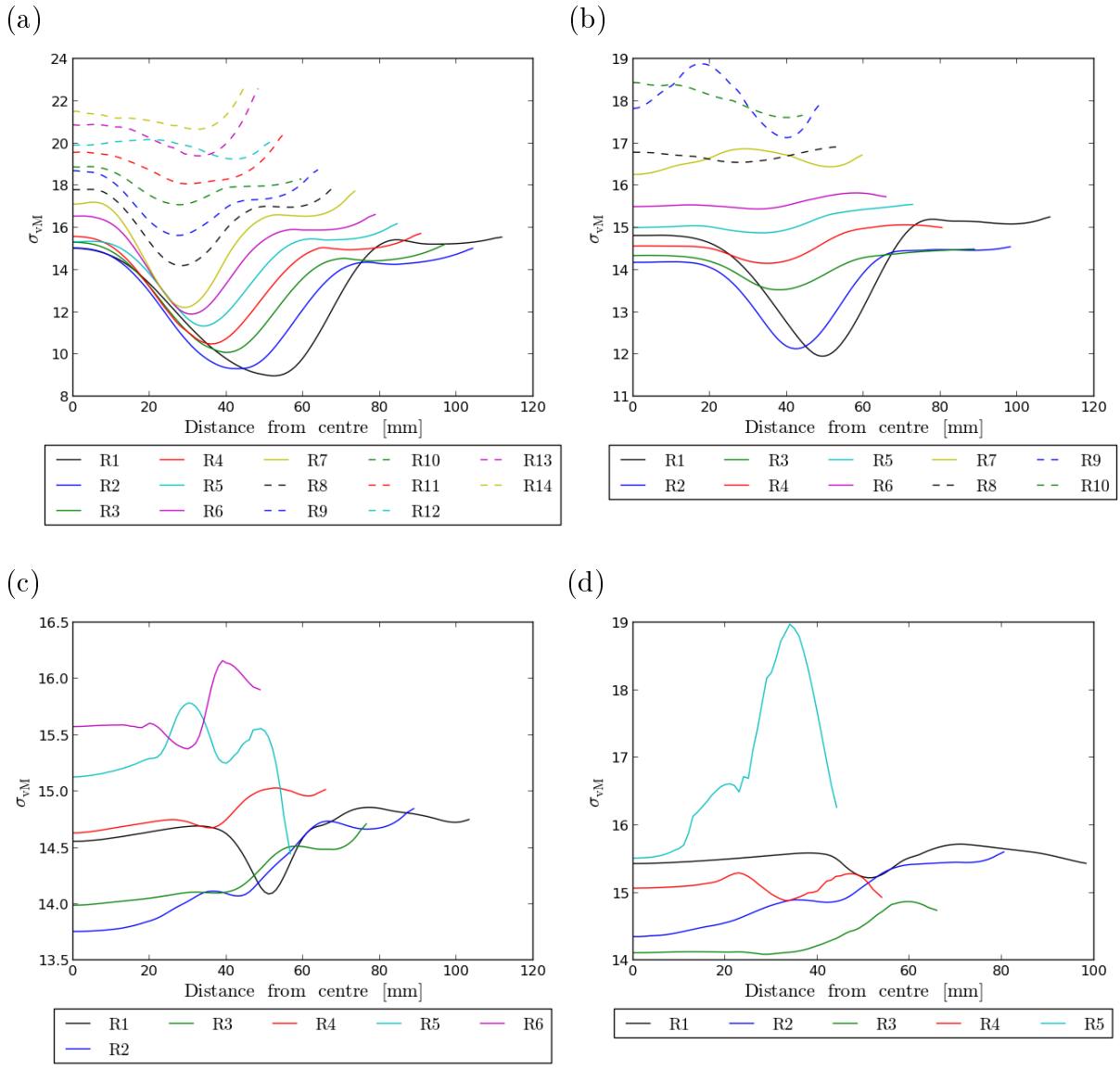

Figure I.5: Through thickness residual stresses 350mm away from the roller 10 seconds after each roll pass step modelled for (a) 14 × 7%, (b)10×10%, (c) 6×15% and (d) 5×20% reduction roll pass sequences.

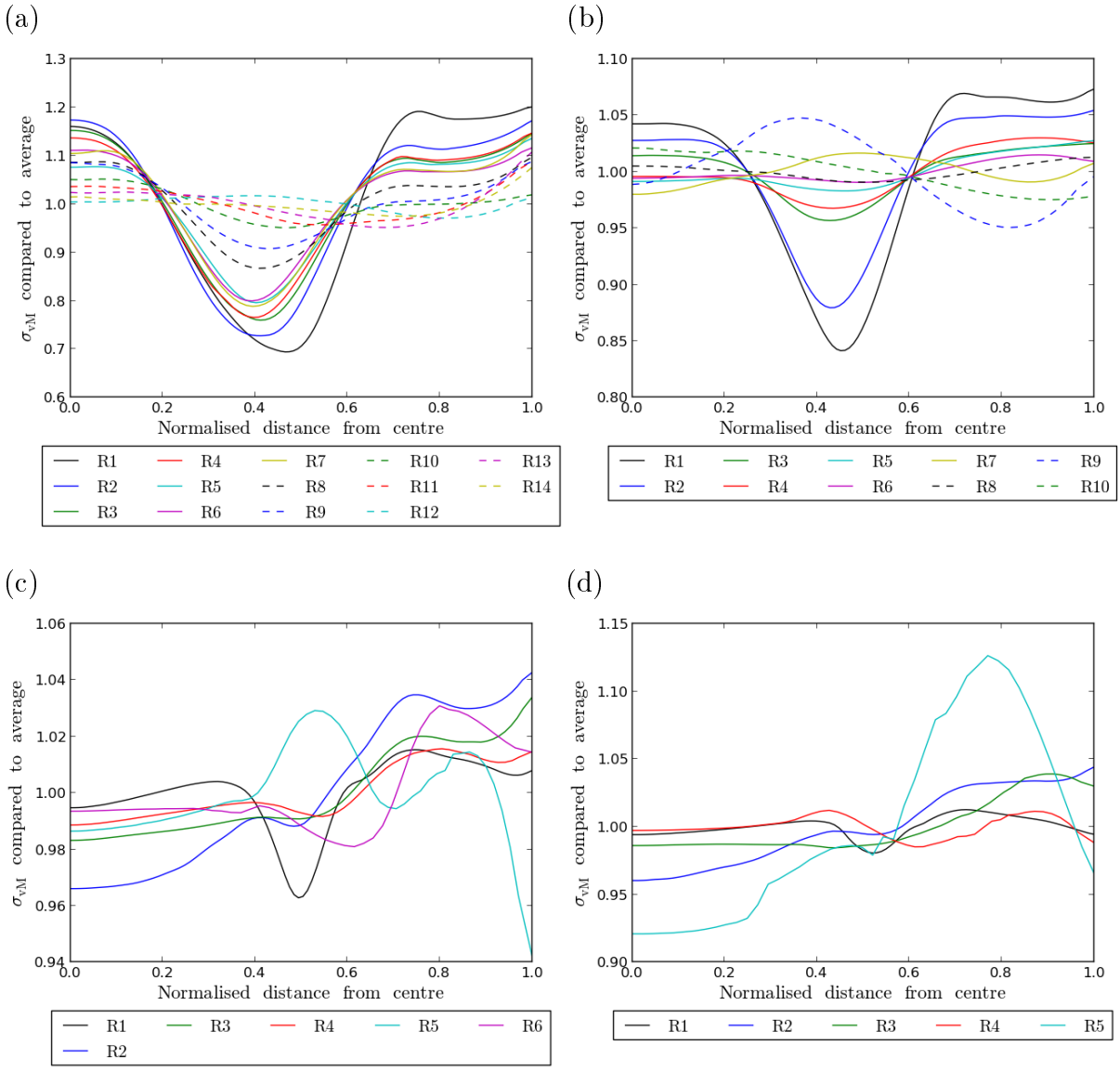

Figure I.6: The averaged data in Figure I.5 over the normalised distance from the centre. (a) $14 \times 7\%$, (b)$10\times10\%$, (c) $6\times15\%$ and (d) $5\times20\%$.

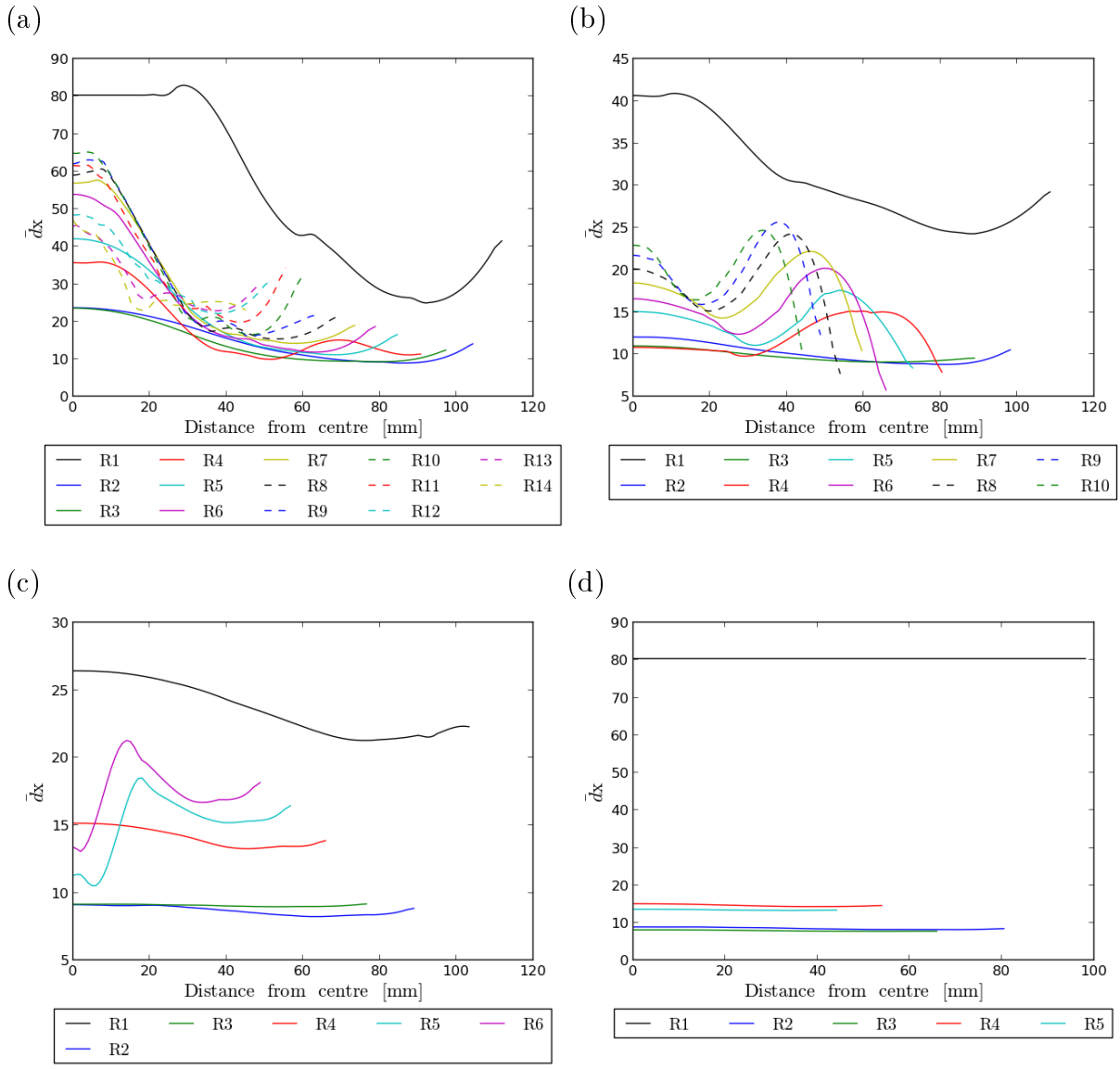

Figure I.7: Through thickness grain size estimates 350mm away from the roller directly after each roll pass step modelled for (a) 14 × 7%, (b)10×10%, (c) 6×15% and (d) 5×20% reduction roll pass sequences.

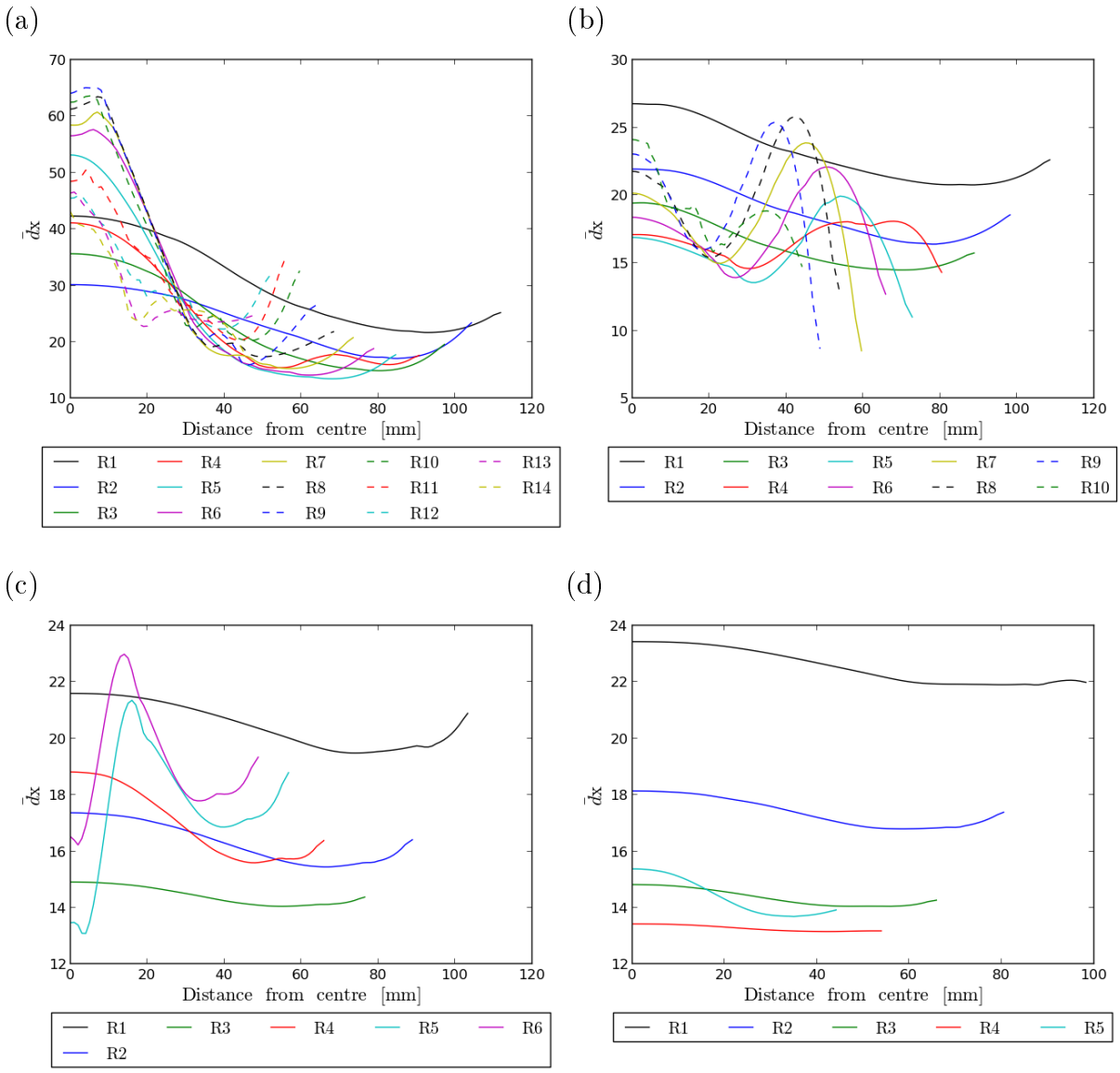

Figure I.8: Through thickness grain size estimates 350mm away from the roller 10 seconds after each roll pass step modelled for (a) $14 \times 7\%$, (b)$10\times10\%$, (c) $6\times15\%$ and (d) $5\times20\%$ reduction roll pass sequences.

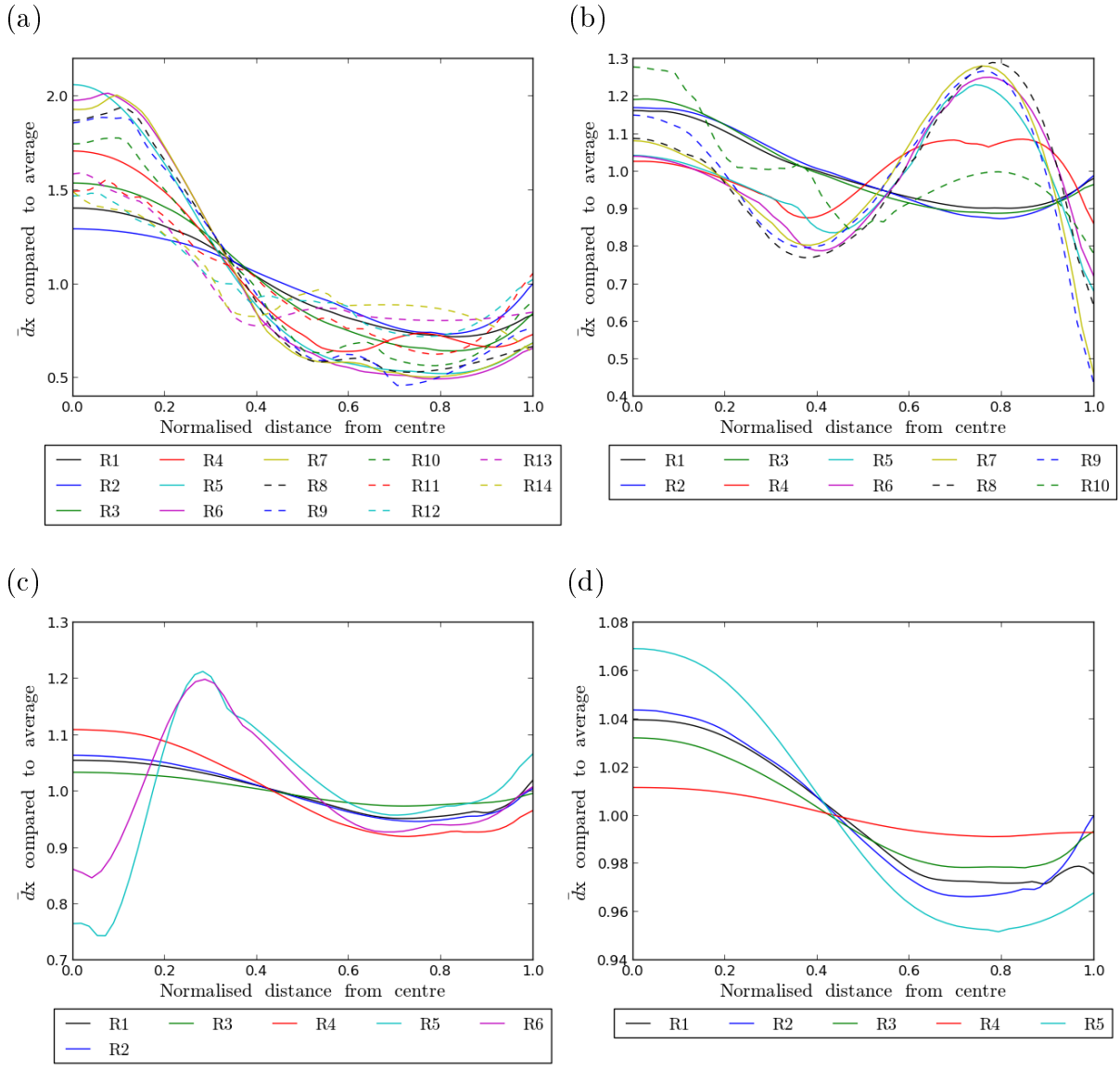

Figure I.9: The averaged data in Figure I.8 over the normalised distance from the centre. (a) $14 \times 7\%$, (b)$10\times10\%$, (c) $6\times15\%$ and (d) $5\times20\%$.